TECHNISCHE UNIVERSITÄT MÜNCHEN

TUM School of Engineering and Design

# A surface matching method in two orthogonal spaces for statistical shape analysis of abdominal aortic aneurysms

Marina M. T. Bassilious

Vollständiger Abdruck der von der TUM School of Engineering and Design der Technischen Universität München zur Erlangung des akademischen Grades einer

Doktorin der Ingenieurwissenschaften (Dr.-Ing.)

genehmigten Dissertation.

Vorsitzender: Prof. Dr.-Ing. habil. Christian U. Große

Prüfer der Dissertation:

1. Prof. Dr.-Ing. Michael W. Gee
2. Prof. Dr. rer. nat. Tim C. Lüth

Die Dissertation wurde am 19.04.2021 bei der Technischen Universität München eingereicht und durch die TUM School of Engineering and Design am 17.05.2022 angenommen.

# Abstract

Cardiovascular disease represent one of the leading causes of death in the modern world. One prominent pathology is that of the abdominal aortic aneurysm (AAA) which mainly occurs in the elderly male population and has caused 12.105 deaths in 2019 alone in Germany. The formation of an AAA usually progresses asymptomatically, often ending in fatal ruptures. If however detected by accident, the surgeon needs to weigh the treatment risk against the rupture risk if left untreated under regular screening. AAA treatments are performed either in open surgeries or in minimally invasive procedures via stent placement. Both treatment options carry risks, too, especially for the elderly patients.
Over the years, the rupture risk of an AAA was determined in the clinical daily practice by a geometric criterion, specifically the maximum diameter. If the maximum diameter exceeds $5.5$ mm, the risk of a rupture increases. However, this criterion is proven to not be accurate enough and so research has been conducted in the last years to develop more accurate rupture risk indicators incorporating further patient information, biomechanical modelings and extensive geometric analysis.

As artery wall composition changes accompany AAA formation and are manifested in its deformation, geometrical approaches are obviously beneficial for assessing the rupture risk and are easy to integrate in the clinical daily practice.
Therefore, in this work, a statistical shape analysis of abdominal aortic aneurysms is performed based on a patient-specific cohort of 142 abluminal AAA shapes. The examined dataset represents a cross-sectional cohort with different sizes, ages and stages of AAA progression. The AAA cases either are asymptomatic, symptomatic or known-ruptured. The shape analysis in this work is performed to understand the shape variability in the cohort and to generate a mathematically abstract representation for every AAA abluminal shape. In so doing, misinterpretations of concrete geometrical features are avoided and consistency in the measurements is achieved.

The input of the statistical shape analysis is generated in the Large Diffeomorphic Deformation Metric Mapping (LDDMM) framework where a constant reference geometry, in this case a cylindrical surface, is mapped to every AAA abluminal surface in the cohort. Statistical methods built on the principal component analysis are applied to the resulting mapping parameters to identify the principal deformation patterns among the 142 mapping parameters and generate the principal shape variations in the cohort.
In order to obtain representative mapping parameters for every AAA shape, a modular registration in two orthogonal spaces is developed in this work to extend the LDDMM framework. In short, the mapping of the reference cylindrical surface to the target AAA abluminal shape is carried out in a simultaneous transformation scheme, comprising a rigid translation and a non-rigid translation-free, diffeomorphic and geodesic deformation. Hence, the non-rigid transformation produces translation-free shape-descriptive mapping parameters which are used as input of the statistical shape analysis as described above.

In this work, the foundation for further examinations of AAA shape variability in specific groups of ages, gender or rupture risk is laid. Moreover, the obtained abstract shape descriptors are determined and could be incorporated in various applications, like automatic segmentations or the identification of biomechanical AAA wall properties.

# Zusammenfassung

Herz-Kreislauf-Erkrankungen gehören zur ersten Todesursache in der modernen Welt. Eine herausragende Pathologie ist das abdominale Aortenaneurysma (AAA), das hauptsächlich bei älteren Männern auftritt und allein im Jahre 2019 12.105 Todesfälle in Deutschland verursacht. Die Bildung eines AAA verläuft normalerweise asymptomatisch und endet häufig mit einer tödlichen Ruptur. Wenn das AAA zufällig entdeckt wird, muss der Arzt das Behandlungsrisiko und das Rupturrisiko verlgeichen, wenn das AAA unbehandelt bleibt. AAA-Behandlungen werden entweder in offenen Operationen oder minimal invasiv durch eine Stentplatzierung durchgeführt. Beide Behandlungsmöglichkeiten bergen auch Risiken, insbesondere für ältere Patienten.
Im Laufe der Jahre etablierte sich das Kriterium des maximalen Durchmessers für die Ermittlung des Rupturrisikos in der täglichen klinischen Praxis. Wenn der maximale Durchmesser $5.5$ mm überschreitet, steigt das Rupturrisiko. Dieses Kriterium ist jedoch nachweislich nicht genau genug. Daher wurden in den letzten Jahren Untersuchungen durchgeführt, um genauere Indikatoren für das Rupturrisiko zu entwickeln, die weitere Patienteninformationen, biomechanische Modellierungen und umfangreiche geometrische Analysen umfassen.

Da Änderungen der Wandkonstitution mit der AAA-Bildung einhergehen und sich in der Verformung manifestieren, sind geometrische Ansätze offensichtlich konstruktiv, um das Rupturrisiko zu bewerten, und lassen sich leicht in die klinische tägliche Praxis integrieren.
In dieser Arbeit wird eine statistische Formanalyse von AAA durchgeführt, die auf einer patientenspezifischen Kohorte von 142 abluminalen AAA-Formen basiert. Der untersuchte Datensatz repräsentiert eine Querschnittskohorte mit unterschiedlichen Größen, Altersgruppen und Stadien der AAA-Progression. Die AAA-Fälle sind entweder asymptomatisch, symptomatisch und bekanntermaßen rupturiert. Die Formanalyse in dieser Arbeit wird durchgeführt, um die Formvariabilität in der Kohorte zu verstehen und eine mathematisch abstrakte Darstellung für jede AAA-Ablumenform zu generieren. Auf diese Weise werden Fehlinterpretationen konkreter geometrischer Merkmale vermieden und Konsistenz bei den Messungen erreicht.

Die Eingabeparameter der statistischen Formanalyse werden mithilfe der Metrischen Abbildung der großen diffeomorphen Verformung (engl. Large Diffeomorphic Deformation Metric Mapping (LDDMM)) generiert, indem eine Referenzgeometrie, in diesem Fall eine zylindrische Oberfläche, auf jede AAA-Abluminalform in der Kohorte abgebildet wird. Statistische Methoden, die auf der Hauptkomponentenanalyse basieren, werden auf die resultierenden Abbildungsparameter angewandt, um die Hauptverformungsmuster unter den 142 Abbildungsparametern zu identifizieren und damit die Hauptformvariationen in der Kohorte zu erzeugen.
Um repräsentative Abbildungsparameter für jede AAA-Form zu erhalten, wird in dieser Arbeit eine modulare Registrierungsmethode in zwei orthogonalen Räumen entwickelt. Mithilfe dieser Methode wird die Abbildung der zylindrischen Referenzoberfläche auf die abluminale AAA-Zielform in einem simultanen Transformationsschema durchgeführt, das aus einer starren Translation und einer nicht starren translationsfreien, diffeomorphen und geodätischen Deformation besteht. Demzufolge erzeugt die nicht starre Transformation formbeschreibende translationsfreie Abbildungsparameter, die wie oben beschrieben als Eingabeparameter für die statistische Formanalyse eingesetzt werden.

In dieser Arbeit wird die Grundlage für weitere Untersuchungen der Formvariabilität von AAA in bestimmten Gruppen von Alter, Geschlecht oder Rupturrisiko gelegt. Darüber hinaus werden die erhaltenen abstrakten Formdeskriptoren geliefert, die in verschiedene Anwendungen wie automatische Segmentierungen oder die Identifizierung biomechanischer AAA-Wandeigenschaften integriert werden können.

# Contents

# Nomenclature

## Representation of scalars, tensors and other quantities

Geometric features

| | |
|---|---|
| $D_{\max}$ | maximum diameter of an AAA $[\mathrm{mm}]$ |
| $L_E$ | Euclidean centreline length of an AAA $[\mathrm{mm}]$ |
| $\alpha_s$ | asymmetry $[-]$ |
| $V$ | volume $[\mathrm{ml}]$ |
| $L_{\mathrm{CL}}$ | centreline length $[\mathrm{mm}]$ |
| $A_{c,\max}$ | maximum cross-section area $[\mathrm{mm}^2]$ |
| $A_T$ | surface area $[\mathrm{mm}^2]$ |
| $\zeta_{\max}$ | maximum curvature $[\mathrm{mm}^{-1}]$ |
| $\gamma$ | saccular index $[-]$ |
| $\Gamma$ | tortuosity $[-]$ |

Mathematical background

| | |
|---|---|
| LDDMM | large deformation diffeomorphic metric mapping |
| $\mathcal{G}$ | group of diffeomorphisms |
| $\mathfrak{g}$ | tangent-space of group $\mathcal{G}$ |
| $\varphi^{\underline{v}}(t)$ | time-dependent transformation element of group $\mathcal{G}$ generated by $\underline{v} \in \mathfrak{g}$ |
| $\mathcal{E}$ | Euclidean group for translation |
| $\mathfrak{e}$ | tangent-space of group $\mathcal{E}$ |
| $\underline{\tau}$ | translation velocity vector in $\mathfrak{e}$ |
| $\underline{r}$ | translation vector in $\mathcal{E}$ |
| $N$ | number of available observations, i.e. target shapes |
| $S$ | two-dimensional source/reference surface in $\mathcal{M}$ |
| $T$ | two-dimensional target surface in $\mathcal{M}$ |
| $\mathcal{M}$ | 3-dimensional manifold of $S$ and deformed configurations during registration |
| $\mathcal{X}$ | subset of $\mathbb{R}^3$ representing a 2-dimensional surface in $\mathcal{M}$, containing $\underline{q} \in \mathbb{R}^3$ |
| $n_x$ | number of vertices in triangular mesh of source surface $S$ in the discretized case |
| $\underline{q}$ | a vertex $\in \mathbb{R}^3$ on the manifold $\mathcal{X} \subset \mathbb{R}^3$ |
| $\underline{X}$ | initial configuration of $S$; is $\in \mathbb{R}^{3n_x}$ after spatial discretization |
| $\underline{x}$ | configuration of $S$ at time $t$; is $\in \mathbb{R}^{3n_x}$ after spatial discretization |
| $L_2$ | space of square-integrable functions |
| $\underline{n}$ | normal vector of a mesh triangle |
| $\underline{c}$ | center point of a mesh triangle |

| | |
|---|---|
| $k_{\underline{q}}$ | kernel functional in $\underline{q} \in \mathcal{X}$ |
| $\underline{v}_{\underline{q}}(\underline{q})$ | velocity vector in $\mathbb{R}^3$ of a vertex $\underline{q}$ at time $t$ |
| $\underline{v}(\underline{x}(t))$ | velocity vector field in $\mathcal{V}$ of configuration $\underline{x} \in \mathcal{M}$, consisting of the evaluations $\underline{v}_{\underline{q}}(\underline{q})$ |
| $\underline{\mu}$ | vector field in the dual space $\mathcal{V}^*$ for construction of $\underline{v} \in \mathcal{V}$ |
| $L$ | differential operator |
| $\mathcal{B}$ | Banach space |
| $\mathcal{H}$ | Hilbert space |
| $\mathcal{W}$ | Hilbert space with reproducing kernel (RKHS) for similarity measure defined on $\mathcal{X}$ |
| $\mathcal{W}^*$ | dual space of $\mathcal{W}$ |
| $\sigma_{\mathcal{W}}$ | kernel width for RKHS $\mathcal{W}$ |
| $\underline{K}_{\mathcal{W}}$ | kernel matrix of RKHS $\mathcal{W}$ with width $\sigma_{\mathcal{W}}$ |
| $\underline{\omega}$ | probing vector field in RKHS $\mathcal{W}$ |
| $d_{\mathcal{W}}$ | similarity measure of two shapes with metric in RKHS $\mathcal{W}$ |
| $\mathcal{V}$ | RKHS to embed $\underline{v} \in \mathfrak{g}$ for unconstrained non-rigid transformation in the original LDDMM |
| $\sigma_{\mathcal{V}}$ | kernel width for RKHS $\mathcal{V}$ |
| $k_{\mathcal{V}}$ | Gaussian kernel functional defined on $\mathcal{V}$ with width $\sigma_{\mathcal{V}}$ |
| $\underline{K}_{\mathcal{V}}$ | kernel matrix of RKHS $\mathcal{V}$ with width $\sigma_{\mathcal{V}}$ |
| $\underline{v}_0$ | initial velocity vector field in RKHS $\mathcal{V}$ defined on a surface in $\mathcal{M}$; $\in \mathbb{R}^{3n_x}$ after spatial discretization |
| $\underline{\mu}_0$ | initial momenta vector field in dual space $\mathcal{V}^*$ defined on a surface $\mathcal{X}$ in $\mathcal{M}$; $\in \mathbb{R}^{3n_x}$ after spatial discretization |
| $J_{\mathcal{V}}$ | cost function for matching in original LDDMM |
| $\gamma_E$ | weighing parameter between the data-fidelity and energy term |

## Method and Implementation

| | |
|---|---|
| $J_A$ | cost function for affine registration |
| $\underline{P}^{\perp}$ | projector used to construct the RKHS $\mathcal{V}^{\perp}$ |
| $\underline{B}$ | matrix used for projector construction |
| $\underline{v}^{\perp}$ | translation-free velocity vector field in RKHS $\mathcal{V}^{\perp}$ |
| $\mathcal{V}^{\perp}$ | RKHS of translation-free velocity vector fields $\underline{v}^{\perp}$ |
| $\mathcal{V}^{\perp *}$ | dual space of RKHS $\mathcal{V}^{\perp}$ |
| $J^{\perp}$ | cost function for surface matching problem in $\mathcal{V}^{\perp}$ |
| $\underline{K}_{\mathcal{V}^{\perp}}$ | Kernel matrix for metric definition of RKHS $\mathcal{V}^{\perp}$, incorporating $\underline{P}^{\perp}$ |
| $k_{\mathcal{V}^{\perp}}$ | kernel functional of RKHS $\mathcal{V}^{\perp}$ associated to $\underline{K}_{\mathcal{V}^{\perp}}$ |
| $J$ | cost function for modular matching problem |
| $\mathcal{F}$ | transformation group for modular registration method |
| $\varphi_{\mathcal{F}}$ | group transformation belonging to $\mathcal{F}$ |

Feature space of abdominal aortic aneurysms

| | |
|---|---|
| $HU$ | Hounsfield Units |
| $c_{\mathrm{M}}, c_{\mathrm{H_2O}}$ | attenuation values for material M and water $\mathrm{H_2O}$, respectively |
| $\bar{d}_{\mathcal{W}}$ | asymptotic value of similarity measure $d_{\mathcal{W}}$ |
| $d_{\mathcal{W}}^{\mathrm{norm}}$ | normalized similarity measure $d_{\mathcal{W}}$ using $\bar{d}_{\mathcal{W}}$ |
| $d_{cn}$ | local closest-node distance between two vertices measured with $L^2$ norm |
| $\bar{d}_{cn}$ | average of all local closest-node distances $d_{cn}$ for one AAA shape |
| $H_{\mathrm{cyl}l}$ | height of cylindrical reference geometry |
| $D_{\mathrm{cyl}}$ | diameter of cylindrical reference geometry |

Statistical analysis

| | |
|---|---|
| PCA | principal component analysis |
| SVD | singular value decomposition |
| $\underline{p}$ | feature vector |
| $\mathcal{P}$ | data set of all $\underline{P}$ |
| $p$ | dimension of $\underline{p}$ |
| $\tilde{p}$ | reduced dimension of $\underline{p}$ |
| $J_{\mathrm{PCA}}$ | cost function in PCA |
| $\underline{s}$ | vector of shape descriptors of dimension $\tilde{p}$ |
| $\underline{w}$ | identified basis vector in PCA |
| $\underline{\Sigma}_{\mathcal{P}}$ | covariance matrix of data set $\mathcal{P}$ |
| $\underline{\Sigma}_{\mathcal{P}}^{\mathrm{SVD}}$ | covariance matrix of data set $\mathcal{P}$ using SVD for PCA |
| $\underline{\Sigma}_{\mathcal{P}}^{\mathrm{LPCA}}$ | covariance matrix of data set $\mathcal{P}$ in linear PCA (LPCA) |
| $\pi$ | explained variance |
| $\underline{G}$ | Gram matrix |
| $\underline{g}$ | eigenvectors of $\underline{G}$ |
| $\underline{\phi}(\underline{p})$ | mapped feature vector $\underline{p}$ |
| $\underline{\tilde{\phi}}$ | reconstructed $\underline{\phi}(\underline{p})$ |
| $J_{\mathrm{recon}}$ | reconstruction cost function in kernel PCA |
| $\lambda$ | eigenvalue to the covariance matrix $\underline{\Sigma}$ |
| $\underline{m}$ | principal component |
| $m_{\mathrm{norm}}$ | normalization factor for $\underline{m}$ in kernel PCA |
| $\underline{m}^{\mathrm{norm}}$ | normalized $\underline{m}$ in kernel PCA |
| $\underline{\tilde{\mu}}_0^{\perp}$ | reconstructed initial momenta vector field $\underline{\mu}_0^{\perp}$ |
| $\underline{\bar{\mu}}_0^{\perp}$ | mean of initial momenta vector fields $\underline{\mu}_0^{\perp}$ |
| $\underline{m}^{+}, \underline{m}^{-}$ | modes for visualization of the associated $\underline{m}$ |
| $D_M$ | Mahalanobis distance |

# 1. Introduction

## 1.1. Motivation

In the present age of digitalization, advancing computational technologies, together with computer-assisted methods increasingly assist in medical procedures, be it in diagnosis, treatment decision, planning or completion. One pivotal facet of computer-assistance in medical procedures lies in the medical imaging field which benefits significantly from efficient computational technologies: higher resolution, shorter exposure to radiation, lower radiation doses and enhanced imaging accuracies are the outcome. From a broader perspective, medical images permit the digital codification of anatomical and biological information.

Medical images play an essential role in the young interdisciplinary domain of computational anatomy (CA) which is mainly concerned with the analysis of anatomical shapes and the distinction between healthy and pathological occurrences and progression scenarios. To that end, mathematical and statistical methods have been constantly developed for building the necessary models and simulation tools.
In CA, the extracted geometric information provided in medical images can be described in various ways : 1D fibres, 2D surfaces, 3D volumes or even simply the grey values on the medical images themselves in the case of a computed tomography (CT) dataset.

Although CA is an emerging discipline enabled primarily by advancing computational techniques, the concept of shape comparisons and the ”recognition” of one shape within another goes back to the beginning of the twentieth century with the work ”On growth and form” by the biologist and mathematician D’Arcy Thompson [173]. In his most famous book, Thompson incorporates physical laws and mechanics as fundamental elements to determine the shape evolution and form of living organisms. With his approach, Thompson established the field of mathematics in biology.

The modern definition of CA has been established with the Brown/Washington University model of anatomy based on Grenander’s pattern theory [70, 71]. With the availability of dense anatomical images, *typical* or *average* shapes of anatomical structures, so-called templates, are estimated. The templates are deformable and they are registered to patient-specific shape of the examined anatomical region. Thereupon, the cohort variability can be assessed. The brain structure was the first anatomical structure to be analyzed [123, 184].
Different anatomical mapping techniques have been an ongoing research field since then.

In the present, a novel method in CA is constructed to mainly analyse shapes of abdominal aortic aneurysms, with the goal of assisting the assessment of rupture risk. As exhibited in the following, morphologic features of abdominal aortic aneurysms have been established as a promising rupture risk predictor.

In the following, the medical background of abdominal aortic aneurysms is presented, including its pathological progression, common rupture risk assessment methods and treatment options. Afterwards, with a focus on morphology, the study population of the present work is introduced, concluding with challenges in related rupture risk assessment and the derived objectives of this work.

## 1.2. Medical background

According to the World Health Organization, cardiovascular diseases are one of the most frequent causes of death globally. In 2016 alone roughly 17.9 million people died due to a cardiovascular illness, thus representing $31\%$ of all deaths [195].
According to a study in 2002 [163], $45\%$ of men died between the age of 65 and 74 years due to cardiovascular problems. Here, the abdominal aortic aneurysm is one of the three major cardiovascular death causes. In Germany, according to [63], almost 12.105 men and women died of arterial diseases in 2019.

In this work, a serious cardiovascular illness, the abdominal aortic aneurysm (AAA) is addressed. An abdominal aortic aneurysm (AAA) is defined by a progressive dilation of the abdominal aorta with a maximum diameter greater than 3 cm. Other approaches diagnose an AAA if the maximum diameter is larger than $50\%$ of the healthy patient-specific diameter of abdominal aorta [96]. Figure 1.2.1 shows a manifestation of an infrarenal AAA which occurs between the renal arteries and the iliac bifurcation. Another AAA formation takes place completely proximal to the renal artery bifurcation and is classified as suprarenal AAA. A juxtarenal AAA extends between proximal renal artery bifurcation till and the aortic bifurcation to the iliac arteries. This work focuses on infrarenal AAA which constitute $90\%$ of all AAAs [83].

The morphological change decreases the ability of the abdominal aortic wall to withstand the mechanical forces exerted by the blood flow during a heartbeat [74]. Once the resulting wall stress exceeds the wall strength, rupture of the AAA occurs usually resulting in death.

The prevalence of AAA is higher in men than in women. All in all, about $30\%$ of all AAA cases show a maximum diameter of greater than 4.5 cm [163] which progress silently and present a high risk if ruptured. The associated high mortality rate and high prevalence make the AAA one of the leading cardiovascular causes of death in western societies.

### Clinical presentation

In clinical examination, with regard to the symptoms, AAA are divided in three groups: asymptomatic, symptomatic and ruptured. The majority of AAA cases, about $80\%$ of all cases, are clinically silent, i.e. asymptomatic, and are accidentally detected in abdominal medical images. Only $5-10\%$ of all cases show symptoms which mostly manifest themselves with a sudden

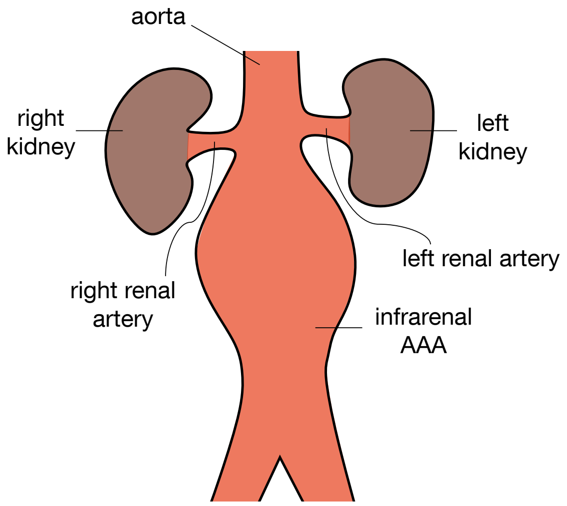

Figure 1.2.1.: Schematic representation of an infrarenal AAA formation which occurs between the renal arteries and the iliac bifurcation.

abdominal or back pain.

Once detected, asymptomatic AAA must be regularly monitored. The monitoring can be conducted using the fast, inexpensive and non-invasive ultrasound (US) imaging modality. According to [78, 110, 116], US is a valid and reliable screening method for AAA.

In case of symptomatic AAA, an urgent clinical intervention is necessary. Available treatment options are discussed later in this section. If a symptomatic AAA is left untreated, there is a $90\%$ chance of rupture within two years upon discovery as observed in [130].

The remaining group of ruptured AAA which make $10-15\%$ of all cases is the most life-threatening: $90\%$ of ruptured AAA cases end fatally before even reaching the hospital [136].

### Etiology and risk factors

The permanent structural deterioration of the abdominal aorta is induced by a degenerated aortic wall. A healthy aortic wall is illustrated in Figure 1.2.2 and consists of three main layers: the intima, the media and the adventitia, being separated with an external and an internal elastic membrane.

The intima is the thin luminal wall layer. It mainly consists of extracellular matrices (basement membranes) lined with endothelium which build a smooth semi-selective barrier of lumen to the aortic wall. Due to its fragile structure, it is the layer most exposed to injury or tear.

The aortic media is the middle layer and amounts to almost $80\%$ of aortic wall thickness. It mainly consists of elastic fibres, elastin, intertwined with smooth muscle cells. Hence, along with the bordering elastic membranes, this layer is largely responsible for the elastic behaviour of the abdominal aorta, allowing the propulsion of blood during a heartbeat and thus the pressure

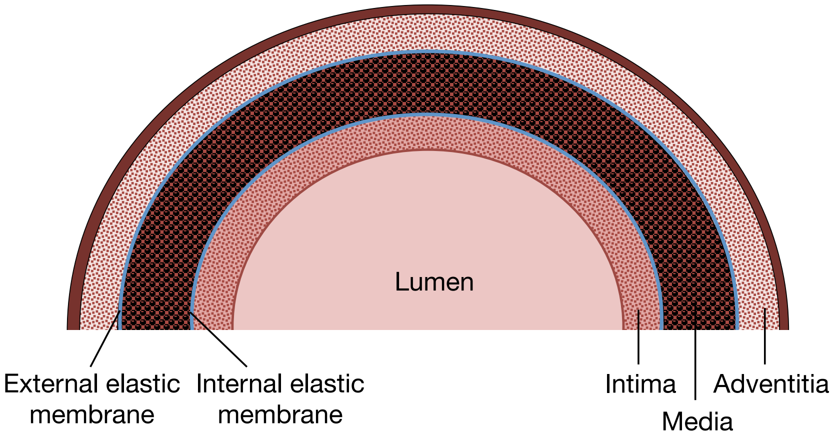

Figure 1.2.2.: Schematic representation of the composition of a healthy aortic wall which consists of an intima, media and adventitia, separated by the internal and external elastic membrane, respectively. This composition undergoes structural remodelling due to ageing and disease.

wave propagation.
Another connective tissue in the aortic wall, in addition to elastin, is collagen. The third and outermost thin layer, the aortic adventitia, mainly consists of collagen which grants great tensile strength [8]. Thus, the mechanical and structural properties of the aortic wall are determined by the interplay and balance of both constituents, collagen and elastin.

Tsamis et al. [180] presents an extensive study of structural remodelling during ageing and disease. So, naturally, throughout a lifetime and with progressing age, structural remodelling continually takes place in the aortic wall, causing an imbalance of collagen and elastin constituents and usually a loss in arterial compliance [106, 179, 201]. In particular, elastin concentration decreases within the aorta [50, 56] with age, while collagen undergoes an increase with age [69, 157]. The absence of elastin fibres leads to a pre-stretch change in the remaining aortic components, mainly collagen fibres and smooth muscle cells [193], while an overcompensatory collagen net occurrence stiffens the aortic wall and encourages aortic growth [18].

The structural remodelling takes different forms according to the wall layer and the region of aortic wall. Specifically, with regard to the abdominal aorta, the thickness and elastin and collagen amount of each layer differ between the regions. The different susceptibility is mainly due to distinct loading conditions [194].

Additionally, structural remodelling within the aortic wall can be triggered by disease, leading to an accelerated weakening and functional degradation of aortic wall, and especially the abdominal aortic wall [25]. An exact description thereof with connection to resulting mechanical properties has been conducted in [135] for three identified degradation stages.

Generally, false and true aneurysms are distinguished: The wall degeneration in a false AAA, also known as pseudo-aneurysm, is usually caused by a tear or injury in the vessel wall such that blood leaks and collects in the surrounding tissue, in particular between the media and the adventitia. An aortic dissection, on the other hand, is a tear in the intimal layer of the aorta, mechanically separating (dissecting) the wall layers and also leading to blood leakage into the vessel wall [33, 134]. False AAA occur mostly because of trauma or infection.
True AAA build the majority of AAA cases where all three vessel wall layers are involved. In this occurrence, the aortic wall degeneration takes place due to inner change of the microstructural composition of the wall, causing common structural deformation and mechanical alteration [9, 81].
True aneurysms can occur because of ageing-related disruptions, but also because of genetic disorders, like Marfan-Syndrome [75] or Ehlers-Danlos syndrome [30, 76].
Although the initial cause of pathogenic AAA development is not fully known yet, some factors strongly promote and correlate with the formation of true AAA, like male sex, age, smoking, hyptertension and hypercholestrolemia [55, 74].

## Treatment

Treatment guidelines are regularly provided and updated by the Society for Vascular Surgery, like the latest in [26]. Therein, based on various study results, suggestions to support the decision-making process of treatment options are given.

If the AAA should be treated, the treatment methods of AAA are usually of a surgical nature. The open repair surgical intervention has been the gold standard for operating ruptured and non-ruptured AAA. In this open repair intervention, the surgeon replaces the AAA with a prosthesis which is sutured to the adjoining healthy segments of the abdominal aorta.
Another meanwhile established and less invasive surgical treatment is endovascular aortic repair (EVAR). During this procedure, a graft with enclosed metal stent is placed transluminally into the AAA segment and attached on the luminal surface of the adjoining healthy aorta. To that end, a non-dilated and thrombus-free infrarenal neck is required.

Both surgical treatments carry life-threatening risks [161]. The various risks and scenarios have to be considered in the decision making process of a treatment. In some AAA cases, due to patient-specific intervention risks related to previous diseases or health status, a non-treatment is preferred. In such cases, AAA surveillance programs monitor the AAA growth rate and stability to allow for surgical intervention sufficiently in advance.

Consequently, a treatment decision includes a weighing of the patient-specific interventional risks against the rupture risk if left untreated. That is why clinical tools for rupture risk assessment has been the focus of interdisciplinary research efforts over the past decades.

## 1.3. Risk assessment and challenge

In the context of AAA treatment decisions, the rupture risk assessment is necessary in deciding for or against a treatment since treatments bear risks, too, as explained above. In the following, different approaches for AAA rupture risk assessment are presented.

### Biomechanical approaches

From a mechanical point of view, rupture occurs when the wall stress exceeds the wall strength. Biomechanical models help assess the aortic wall stress under certain loads and can help predict scenarios of possible rupture. Such models are generated on patient-specific geometries extracted from medical images. The challenges lie mainly in assigning patient-specific constitutive behaviour and in obtaining the wall strength.

To overcome these challenges, experiments have been conducted to make predictions on wall constitutive properties and laws, like in [152]. Based on these predictions, AAA biomechanical models have been constructed and studied [59, 61, 94, 114, 128, 129, 137, 187].
The wall strength is a more difficult parameter to estimate and it can vary in an AAA geometry depending on the tissue composition at a certain location. To overcome this challenge, an individual invasive wall strength distribution has been estimated in a stochastic model from non-invasive patient-specific parameters, specifically local thrombus thickness, local AAA diameter, sex and AAA family history [185]. Patient-specific wall strength values can be estimated retrospectively.

Integrating these biomechanical models in rupture risk assessment trials, it has been proven that the peak wall stress (PWS) is indeed an accurate rupture risk indicator [51, 52, 85, 113, 178].
Moreover, based on these mechanical and stochastic models, some rupture risk indices have been designed and introduced to the rupture risk estimation dilemma. One of the pioneers in this matter is the rupture potential index (RPI) by Vande Geest et al. [185]. The RPI is calculated as the quotient of wall stress and strength, both estimated with the previously mentioned methods.
The peak wall rupture risk (PWRR) index, another biomechanical rupture index, correlates strongly with PWS [59]. A probabilistic rupture risk index (PRRI) was later proposed by Polzer et al. and is shown to be superior to a purely deterministic approach [145]. Recently, in 2018, Leemans et al. investigate the added value of biomechanical indices to rupture risk assessment. In their study, they come to the conclusion that biomechanical indices may provide additional information concerning aneurysm growth, but they do not perform better than extracted patient-specific morphology features [107].

### Geometry

The integration of biomechanical rupture risk indices in daily clinical practice can turn out to be cumbersome due to expensive computations and the lack of patient-specific constitutive modelings. That is why research has been expansively conducted to understand the relation between the geometry, the biomechanical wall condition and the stage of disease. Aortic shape deformations can in fact be regarded as manifestations of disease-related weakening of aortic wall and

of changes in the wall stress distributions. If the shape deformations can be related to inner wall conditions and rupture risk, then these shape features can be favoured over biomechanical risk indices as they can be assessed quickly and non-invasively [151].
In this section, the importance of geometrical features with respect to rupture risk evaluation is highlighted, offering an understanding of common AAA shape variations and features.

Based on empirical evaluations, the widely accepted study of ”The U.K. Small Aneurysm Trial” [172] established in 1995 the common criterion of maximum transversal diameter $D_{\max}$ in daily clinical practice for rupture risk assessment. Other studies like [49] confirmed the findings. The core outcome of these studies takes a maximum diameter of $\approx 5.5$ cm as a threshold to identify rupture-prone AAA in men. The concept of a relation between the aortic diameter and a high wall stress is based on the mechanical Law of Laplace which relates the local wall stress in a thin-walled cylinder to the associated inner pressure and local diameter [99].
However, other studies like in [35, 164] or a more recent study in [101] show that the threshold does not apply to all cases. Also, with regard to growth prediction, the maximum diameter is not eligible as a surveillance parameter, but rather centreline-based diameter measurements along the entire centreline which relate to local growth rates [120, 121]. More patient-specific and more accurate rupture risk indicators have to be introduced consequently.

To that end, to take advantage of non-invasive geometrical predictors and advanced medical imaging technologies, ongoing research has identified multiple other geometric features which strongly correlate with an increased rupture risk. There, the direct relation between selected geometrical features and rupture risk is examined.

Comprehensive studies including multiple geometrical features, as in [167] or [53], pursue significant quantifications of AAA geometries for rupture risk prediction. Even, in [100], a statistical tool has been developed to generate a severity parameter of an AAA case based on morphology and general patient information. Nowadays, modern machine and deep learning techniques are employed toward that end. In [139], for instance, a decision-tree based classification of AAA based on their morphology is conducted. Also, in a most recent study in early 2020 [154], 53 geometric and 4 biomechanical markers, along with other general patient information data, are examined with regard to rupture prediction using different machine learning classification algorithms. So far, deep learning approaches have been developed to be directly applied on the medical image for classification. Hence, geometric features are not explicitly extracted for the analysis, but the learning is performed on the complete shape in the CT-image [88].
Additionally, studies have been performed to evaluate the relationship between PWS and AAA morphology, as in [144] to overcome complexity and long computation times of biomechanical models.

All these and similar studies conclude that morphology is relevant with regard to rupture risk assessment. With the help of modern data science techniques, promising results can be achieved. In the following, frequently analysed and promising geometric features are presented and discussed. These are usually categorized according to their dimension: 1D and 2D surrogates of 3D shape. Examples of 2D features are tortuosity and asymmetry.

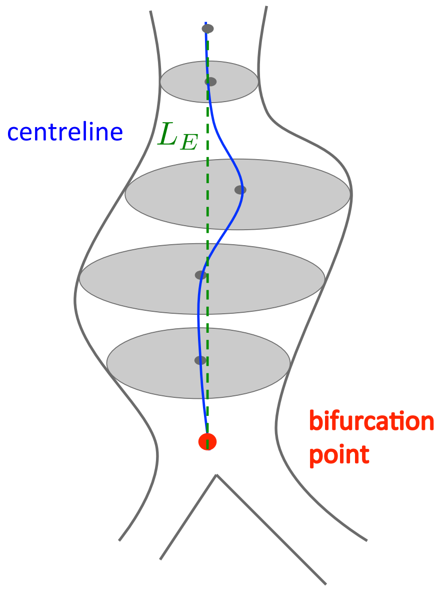

Figure 1.3.1.: Illustration of a centreline (blue) as a connecting line of all centre points of discrete aortic best fit circles (grey circles). $L_E$ describes the Euclidean length of the dashed green line which directly connects the top point with the bifurcation point in a straight line. $L_{\mathrm{CL}}$ describes the length of the centreline itself.

Before starting with the examination, an essential geometrical assessment tool, the centreline, is explained. A centreline is a line connecting all centre points of discrete aortic circular segments (see Figure 1.3.1). Based on an available centreline, geometrical features, like asymmetry or tortuosity, can be calculated. The euclidean length $L_E$ of the centreline describes the length of the straight line connecting the proximal and distal point of the centreline.

Cross-sectional diameter asymmetry morphologically characterizes AAA geometries. In this regard, two common AAA shapes can be differentiated, especially by physicians: fusiform (axis-symmetric) and saccular (asymmetric) describing mainly the bulge shape (see Figure 1.3.2). It is stated that most AAA are tortuous and asymmetric [41, 54]. This is due to the local boundary conditions given by neighbouring anatomical structures, like the spinal column in posterior direction [189]. That is why, in most cases, the AAA bulge grows further in anterior than in posterior direction [54], resulting in a thinner wall in the anterior part [100]. This implies that the AAA growth tendency can be anticipated from and is directed by surrounding anatomical limitations.

Nevertheless, since asymmetry vaguely describes a non-symmetric deformation in radial direction, different asymmetry measurements are introduced in literature. Finol et al. introduce in [54] an asymmetry index

$$\beta = \frac{r_p}{r_a}$$

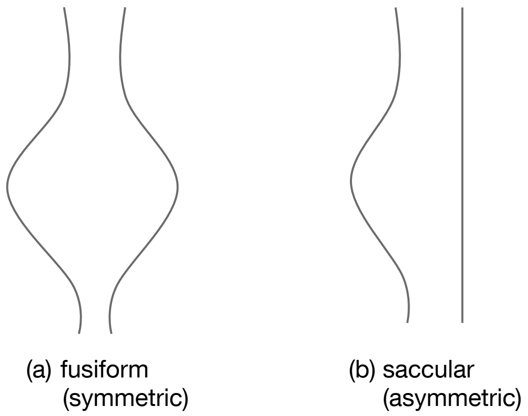

Figure 1.3.2.: Different bulge shapes (coronal view) with regard to asymmetry: (a) fusiform and (b) saccular.

with $r_p$ the posterior and $r_a$ the anterior radius in the cross-section with the maximum diameter $D_{\max}$ (see Figure 1.3.3). A symmetric AAA has an index of $\beta = 1$. It is stated that the higher the asymmetry, the higher the peak wall shear stress at peak blood flow. Additionally, with an increasing asymmetry, secondary flows occur more in late diastole.

In these studies, a strong correlation between asymmetry and wall stress, especially PWS, has been observed. Also, FSI simulations show in [165] a strong interaction between asymmetry and wall stress. Doyle et al. devote their research focus in [40] on asymmetry investigations, achieving similar conclusions: excessive bulging of one surface induces an increased PWS in the opposite site. An easily accessible asymmetry measure is found in [54] with

$$\alpha_s = r_{\max,OC} - r_{\max,IC},$$

the difference between the radius of outer circle (OC) and the radius of inner circle (IC) in the plane of maximum diameter $D_{\max}$. In this study, it has been revealed that ruptured AAA tend to have greater cross-sectional diameter asymmetry. Vorp et al. introduce a similar bulge factor based on the ration of $r_p$ and $r_a$ as well [191]. This study confirms that asymmetry has a role as significant as the maximum diameter on the wall stress distribution. In [155], the maximum radius $r_{\max}$ is incorporated in the asymmetry factor with

$$\alpha_r = \frac{e}{(\frac{r_{\max}}{r_{\text{sub}}} - 1)/r_{\max}}.$$

Curvature $\zeta$ is a frequently discussed geometrical feature of AAA as it is deduced from the common geometric feature, the diameter. In the AAA context, curvature is defined according to [64]. With this definition, in this study, the mean curvature along the AAA centreline has been found to correlate with the PWS. In [132] and [62], the relation between AAA curvature and PWS has been investigated likewise. However, the results are non-significant with respect to the analysis

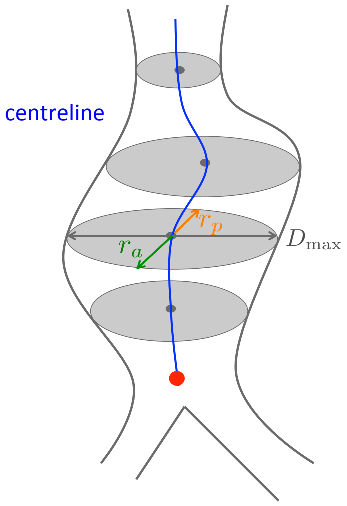

Figure 1.3.3.: Definition of asymmetry according to [54] as the difference of the radius of outer circle (OC) and the radius of inner circle (IC) in the plane of maximum diameter $D_{\max}$.

methods of [64] and can be therefore neglected. In [97], a more sophisticated approach is followed to analyse the role of only curvature in the rupture risk assessment. Therein, curvatures have been estimated using a biquintic Hermite finite element method which allows a reduction of curvature measurement to only ten global indices. Machine learning methods have been applied on the acquired indices, yielding a strong relation between rupture risk and curvature features.

Tortuosity $\Gamma$ is another common geometric feature. It is important to note that tortuosity and asymmetry do not refer to the same shape feature. A highly tortuous AAA does not necessarily show an asymmetry in the cross-section with the maximum diameter. However, in some AAA shapes, tortuosity can cause asymmetry. In this case, the asymmetry cannot be regarded independently from tortuosity.
Also for this geometrical feature, several measurements have been introduced in literature [53, 59, 62, 151, 167]. All these studies confirm that unstable rupture-prone AAA shapes tend to be less tortuous.

The list of relevant AAA geometric features has been extended with the saccular index defined in [100] with

$$\gamma = \frac{D_{\max}}{L_E},$$

the quotient of the maximum diameter $D_{\max}$ and the perpendicular centreline length $L_E$ (see Figure 1.3.1). Not only the expansion in radial direction is taken into account, but also the expansion in longitudinal direction. Although several studies have shown no correlation of saccular index with PWS [64, 167], other studies confirm the existing relation between saccular index and rupture risk [79, 100, 189] where the saccular index is even incorporated in the therein established rupture risk indices based on geometry and biomechanical factors.

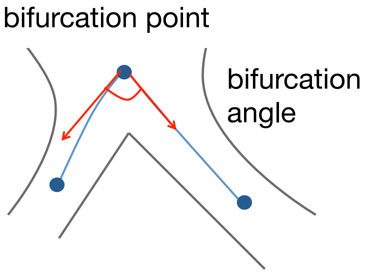

Figure 1.3.4.: Definition of bifurcation angle.

The bifurcation angle is also considered in the geometrical analysis [132]. The bifurcation angle is defined as the angle between the tangents on the centrelines between the bifurcation point and the iliac arteries in the bifurcation point (see Figure 1.3.4). Analysis show that the bifurcation angle does not influence the wall stress nor the rupture risk of an AAA and can be left out. This is a key fact which is made use of in the geometrical treatment of the available patient-specific AAA cohort in chapter 4.

More global geometrical features such as volume $V$ and surface area $A_T$ have been incorporated in most of the studies as well. An evident correlation between these features and the rupture risk has been determined in several studies. That is why it has been discussed whether the additional information of volume and surface area can enhance the rupture risk assessment or not. In [99] and [170], strong correlations between volume and PWS and surface area and PWS respectively have been determined. However, the volume and surface area and their correlation with PWS have been opposed to the maximum diameter and its accuracy as a rupture risk predictor [99]. On the other hand, no significant correlation of volume and PWS and surface area and PWS, respectively, have been found in other studies [64, 132].
Nonetheless, due to the correlation between volume and the maximum diameter, some research groups suggest substituting the maximum diameter with the volume. This aims at eliminating the ambiguity in the maximum diameter measurement, the choice of the measurement plane and to capture more global features of AAA shape.

Further global geometric features are centreline length $L_{\mathrm{CL}}$ and height $H$. The length is the real length of the centreline or centreline segment, whereas the height is the perpendicular distance between the specified points on the centreline. In general, the centreline has been often divided into a neck centreline segment and a sac centreline segment with corresponding lengths $(L_{\mathrm{neck}}, L_{\mathrm{sac}})$ and heights $(H_{\mathrm{neck}}, H_{\mathrm{sac}})$. Tang et al. [170] and Giannoglou et al. [64] found no significant correlation between any of the lengths and PWS. However, Shum et al. present in [167] a strong correlation between the sac length $L_{\text{sac}}$ and rupture risk. On the other hand, however, these findings are contradicted in [62].

Hence, as observed, some findings in the studies presented above contradict each other. These contradictions may occur due to inaccuracies in the measurements or to different choices of wall properties if the studies are based on mechanical modelings. Thus, a clear and consistent method definition is lacking among the studies.

Other geometric characteristics like bulge height, bulge location, torsion, deformation rate and several others have been also considered in the aforementioned studies, with an estimated relevance to rupture risk assessment [53, 64, 79, 98, 148, 167, 170, 189, 196].

### Challenge and requirements

However, as observed in the previous analysis, some challenges exist in rupture risk assessment based on AAA geometry:

- The evolved geometry indices include random disordered combinations of geometrical features. Still, not all geometrical features are covered in all of them.
- All in all, studies identify more than 40 relevant geometry features of which some are defined in a complex way and are not easily understood. The measurements are usually difficult to perform automatically on medical images, and therefore their manual clinical determination is tedious, inaccurate and time-consuming.
- Obviously, the more geometry features are considered, the more reliable and patient-specific the achieved rupture risk prediction is.
- Local geometry features are promising indicators of growth and should be incorporated in the analysis in a statistically significant way.
- There is a need to minimize the chances of misinterpretations of the many different, sometimes complex geometry features and measurements which can lead to inaccuracies in the diagnosis. This includes the widely used maximum diameter criterion.

As a result, the following requirements are deduced for a more accurate and easy accessible AAA shape description:

- It is difficult to determine and capture all relevant geometrical features in one measure. Therefore, a quantification of the complete AAA geometry should be considered as input for rupture risk analysis.
- The quantification should be performed automatically and quickly, without much effort in the clinical application, such that it can be smoothly integrated in the daily clinical workflow and can reliably contribute to the clinical decision making for AAA treatment.
- Moreover, chances of feature misinterpretations should be reduced.

## 1.4. Study population

The study population of the present work is a cross-sectional cohort of patient-specific infrarenal AAA cases. The available database has evolved during joint projects since 2006 between the Mechanics and High Performance Group, TUM, and the Vascular and Endovascular Surgery Department of university hospital Klinikum Rechts der Isar, TUM.
A relevant contribution to the construction of this database has been achieved in [114] with the cases collected between 2009 and 2011.

For this patient-specific cohort, invasive and non-invasive parameters have been recorded continuously, as far as feasible. Invasive parameters include mainly biomechanical characteristics and sample properties obtained in tensile tests. Non-invasive parameters include general information, medical history and clinical data of the associated patient case. Additionally, from acquired medical images, geometric features are extracted non-invasively.

### Earlier studies on the data set

In different stages of database growth, different studies have been conducted on the database. These studies were aimed mainly at understanding and modeling the pathological state of abdominal aortic aneurysms, seeking a reliable patient-specific prediction of rupture. The basis therefor is a patient-specific biomechanical model which is constructed from available medical images (CT images in most cases) [113, 114]. Required patient-specific material parameters can only be determined in a non-invasive fashion. Methods for their invasive measurements are presented in [152]. Methods for their non-invasive estimation have been addressed in [16, 94], including also an estimation of the aortic wall thickness which cannot be assessed with conventional medical imaging techniques.
An associated biomechanical rupture potential index (RPI) has been introduced in [113]. Therein, the importance of geometry integration in the rupture risk assessment is also highlighted and proven.
Accordingly, integrating further or more extensive geometrical parameters in the parameter estimation of biomechanical model or the rupture potential index RPI can be valuable and helpful.

### Cohort characteristics

The database examined in this work consists of $N = 142$ (119 male, 22 female, 1 unknown) cases with available CT images. $74$ cases thereof are asymptomatic and declared as stable. $56$ cases are symptomatic or known-ruptured, defined as unstable. The status of the rest of $12$ cases is unknown.

Table 1.1 presents the geometric characteristics of the study population which are discussed in section 1.3 and identified as relevant for rupture risk assessment in literature.
Looking at the statistics in Table 1.1, the available cohort covers a wide range of small and big AAA shapes with individual asymmetries and tortuosities. The mean maximum diameter, centreline length, volume and surface area indicate however that the cohort is slightly shifted to represent *big* AAA shapes. Nonetheless, the available AAA shapes build a representative cohort.

Table 1.1.: Descriptive cohort statistics for relevant geometric characteristics in literature. For all listed features, the values are extracted for the 142 cases.

| Geometric feature | *min* | *max* | *mean* ± *sd* |
|---|---|---|---|
| maximum diameter $D_{\max}$ [mm] | 31.0 | 95.0 | 57.9 ± 14.5 |
| centreline length $L_{\mathrm{CL}}$ [mm] | 41.5 | 187.61 | 99.9 ± 26.4 |
| Euclidean centreline length $L_E$ [mm] | 40.4 | 165.68 | 88.9 ± 21.1 |
| Tortuosity $\Gamma$ [-] | 1.01 | 1.59 | 1.12 ± 0.1 |
| maximum curvature $\zeta_{\max}$ $[\mathrm{mm}^{-1}]$ | 0.02 | 0.63 | 0.12 ± 0.1 |
| Asymmetry $\alpha_s$ [mm] | 0.7 | 22.1 | 3.6 ± 3.6 |
| Volume $V$ [ml] | 43.8 | 592.0 | 235.89 ± 135.27 |
| Surface area $A_T$ $[10^4 \cdot \mathrm{mm}^2]$ | 0.82 | 3.83 | 2.14 ± 0.76 |
| saccular index $\gamma$ [-] | 0.12 | 0.84 | 0.35 ± 0.14 |
| maximum cross-section area $A_{c,\max}[10^3 \cdot \mathrm{mm}^2]$ | 0.33 | 9.81 | 2.54 ± 1.59 |

Table 1.2.: A descriptive statistical interrelation of sex, AAA-status and maximum diameter as leading geometric feature in the examined cohort in the present work.

| Sex ($n = 141$) | Max diameter [mm] ($n = 141$) | AAA-status ($n = 130$) |
|---|---|---|
| female | $50.0 \pm 13.8$ | stable: 10, unstable: 9 |
| male | $59.4 \pm 14.3$ | stable: 64, unstable: 47 |

To create another impression of the cohort's composition, a categorization by AAA-status, sex and maximum diameter as a leading geometric feature is furthermore shown in Table 1.2.

The characteristics of the examined cohort correspond to a big extent with the findings in literature, specifically concerning the formation of AAA in the male and female population and the distinctive rupture risk which each population is exposed to.
Women are less exposed to an aortic dilation risk. In this cohort, only 19 of 141 cases belong to female patients. Moreover, the female population in this work possesses a smaller average maximum diameter which is also reported in literature. However, despite the low probability in the female cohort and the smaller maximum diameter, almost half of the female AAA cases either proceed symptomatic or rupture as existing also here in the cohort at hand. AAA formation in the male population, which is more probable, delivers bigger, but more stable AAA shapes.
Accordingly, with regard to capturing differences between male and female AAA formation, the cohort in this work is well representative.

In addition, with regard to the relation between relevant geometrical feature and the rupture risk (see section 1.3), box-and-whisker plots are employed in Figure 1.4.1 to visualize the relation of selected geometrical features and the rupture risk as they exist in the cohort without any outlier detection or processing. An examination of some wall properties which are invasively obtained and their relation with selected geometrical features is not performed here and beyond the scope of this work.

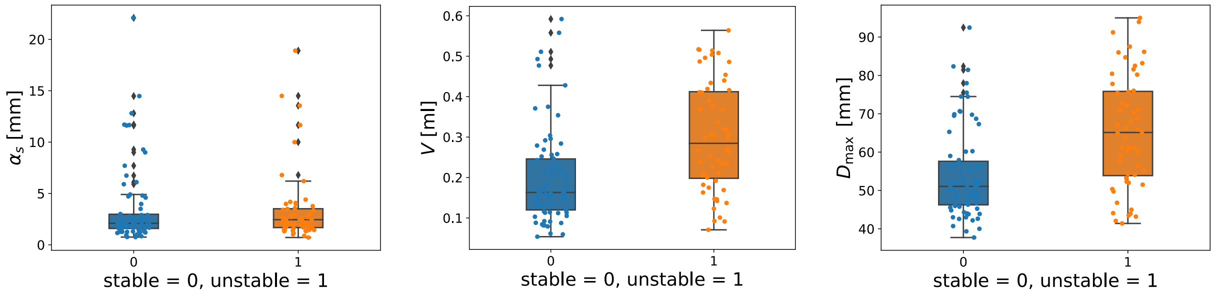

(a) asymmetry (b) volume (c) max. diameter

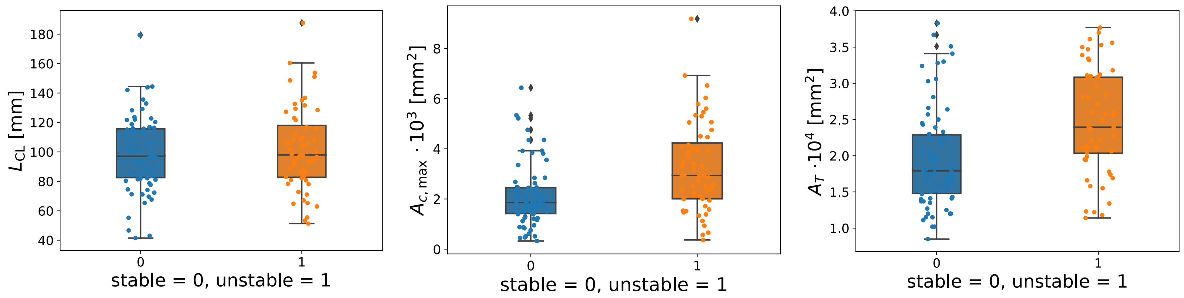

(d) centreline length (e) max. cross-section area (f) surface area

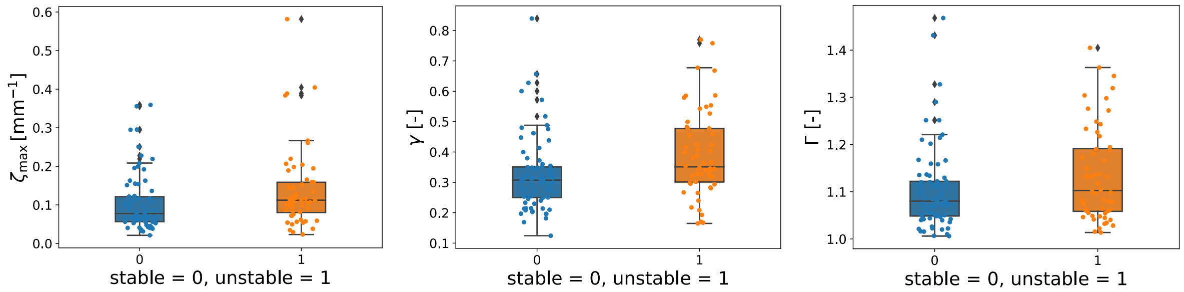

(g) max. curvature (h) saccular index (i) tortuosity

Figure 1.4.1.: Box-and-whisker plots to demonstrate the relation of selected geometrical features and the rupture risk as existing in the cohort without any outlier detection or processing.

The box-whisker plots in Figure 1.4.1 indicate that the selected relevant geometrical features cannot solely divide between the stable and unstable groups in the available cohort and are thus not reliable for rupture risk prediction.

## 1.5. Research objective and outline

The research objective of this work is deduced from the previously presented requirements for an appropriate AAA shape description, consisting of the following sub-objectives:

- More patient-specific, extensive, statistically significant and accurate AAA shape descriptors should be established. To that end, novel methods and techniques of CA are examined and modified.
- The generated shape descriptors should support a shape variability analysis to distinguish pathological and healthy AAA shape appearances.
- In order to avoid misinterpretations of geometrical features, the input of the method should be a complete AAA shape segmented from medical images.

To that end, two main methods are established in the present work. The first method belongs to the Large Deformation Diffeomorphic Metric Mapping (LDDMM) framework and generates for every AAA abluminal shape in the cohort a statistically more significant representation. This statistically more significant representation consists of a velocity vector field $\underline{v}$ which induces a mapping $\varphi$ of the cylindrical reference geometry $S$ to a AAA shape $T$ in the cohort. Figure 1.5.1 visualizes the procedure. The second required method statistically processes all obtained velocity vector fields $\underline{v}$ of all AAA shapes $T$. To that end, two forms of the principal component analysis (PCA) are employed to create a reduced system of shape descriptors $\underline{s}$. The previously displayed patient-specific AAA cohort is subject of examination.

In this work, a special structure of the registration parameter, the velocity vector field, $\underline{v}$ is developed to overcome AAA-specific challenges. In particular, $\underline{v}$ consists of two clearly separated components, namely a non-rigid translation-free $\underline{v}^{\perp}$ and a rigid translation $\underline{\tau}$. A modular registration method in two orthogonal spaces is thus created. The plain $\underline{v}^{\perp}$ is utilized then for the statistical analysis as $\underline{v}^{\perp}$ encodes the shape information, including the orientation.

Accordingly, the manuscript consists of two major parts which are visualized in Figure 1.5.2: The first part addresses the mathematical model behind the estimation of registration parameter $\underline{v}^{\perp}$ and includes Chapters 2, 3 and 4. Chapter 2 lays out the already existing mathematical concepts in CA which build the foundation of the novel registration method presented in Chapter 3. The registration method is applied in Chapter 4 on the examined patient-specific AAA cohort.

The shape descriptors are extracted from the computed registration parameters and elementarily interpreted in the second part that covers Chapters 5, 6 and 7 of this work. The required statistical foundation is presented in Chapter 5. Thereupon, in Chapter 6, the introduced statistical methods are adapted to the established framework with the computed registration parameters $\underline{v}^{\perp}$.

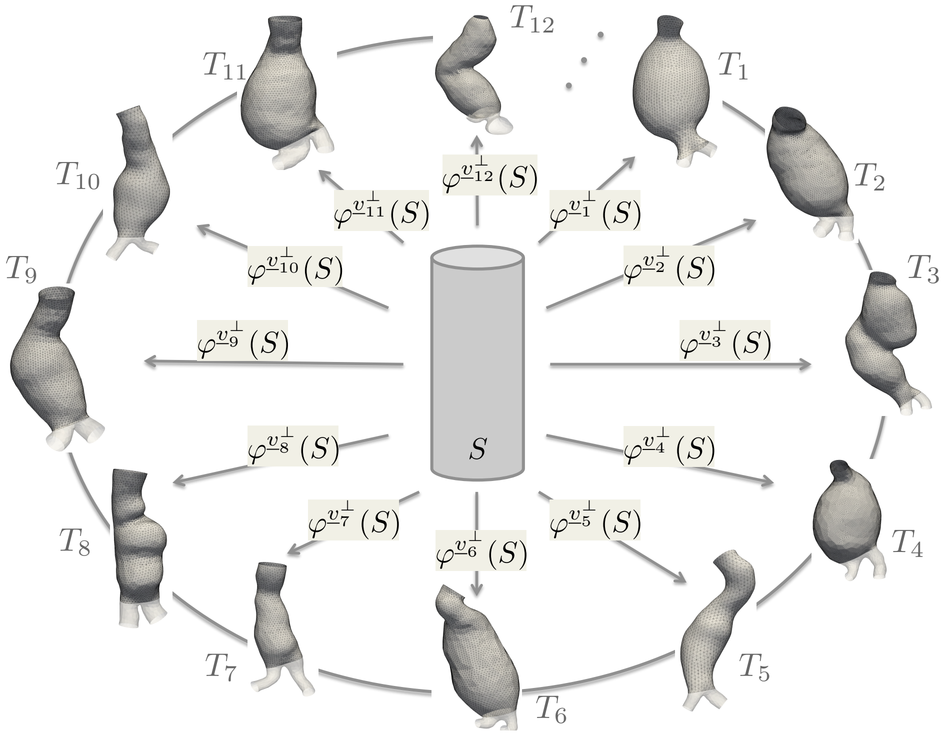

Figure 1.5.1.: Illustration of creating the statistically more significant representation of the AAA abluminal shapes in the cohort in the LDDMM framework. This statistically more significant representation consists of a velocity vector field $\underline{v}^\perp$ which induces a mapping $\varphi$ of the cylindrical reference geometry $S$ to a AAA shape $T$ in the cohort. Therein, the mapping is denoted with $\varphi^{\underline{v}_i^\perp}(S)$ with the velocity vector field $\underline{v}_i^\perp$ acquired for a target AAA surface $T_i$.

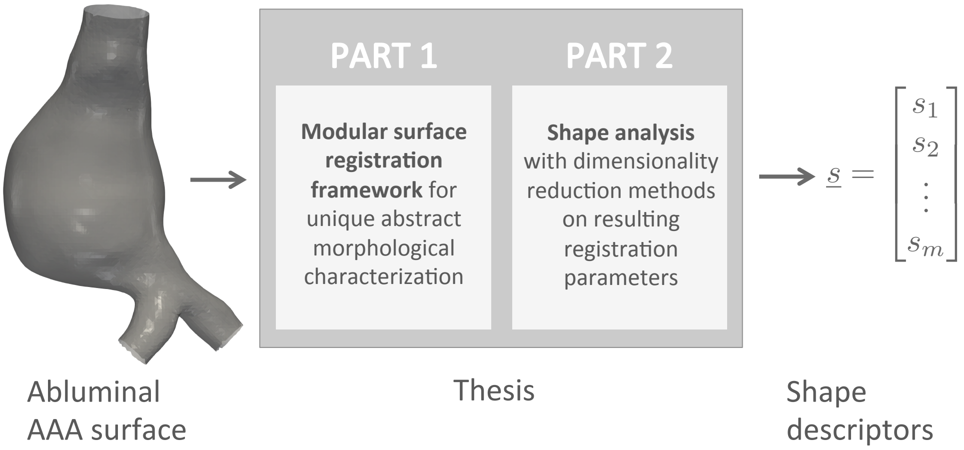

Figure 1.5.2.: Illustration of the composition of the present work. It consists of two major parts: The first part addresses the mathematical setup for the acquisition of representative registration parameters which are employed in the second part of the work for extracting the associated shape descriptors denoted with $\underline{s}$ for every AAA shape.

Finally, in Chapter 7, the shape descriptor vectors $\underline{s}$ for each AAA shape are determined using the introduced statistical methods. An elementary interpretation thereof concludes this chapter.

Chapter 8 is dedicated to the discussion and evaluation of the results achieved with the novel registration method and the subsequent statistical analysis that produces the shape descriptor vectors $\underline{s}$. An outlook closes this final chapter.

# Part I.

# Creation of the feature space

# 2. Mathematical background

In this mathematical introductory chapter, the Large Diffeomorphic Deformation Metric Mapping (LDDMM) [42, 72, 197] framework and its basic concepts are recapitulated. The LDDMM framework provides non-rigid registration methods for applications to anatomical shapes. In this work, the anatomical shapes are extracted from the 3D medical images and are represented by two-dimensional surfaces. Hence, these two-dimensional surfaces and their deformed configurations in the course of the registration are embedded in a three-dimensional Riemann manifold denoted with $\mathcal{M}$.

For the mentioned registration method, the underlying non-rigid deformation is denoted with $\varphi(t)$ and is defined within the group of diffeomorphisms $\mathcal{G}$ acting on the shape manifold $\mathcal{M}$. *Velocity* vector fields $\underline{v}$ determine these group transformations and are enclosed in a Reproducing Kernel Hilbert Space (RKHS) $\mathcal{V}$ which equips them with a smooth form.

In this work, the LDDMM registration aims at mapping a reference surface $S$ to a target surface $T$, both elements of the manifold $\mathcal{M}$. To that end, a cost function is minimized. This cost function consists of a (fictitious) energy term and of a similarity measure between the deformed reference surface $S$ and the target surface $T$. The optimization parameter is the velocity vector field $\underline{v} \in \mathcal{V}$ which achieves the deformation $\varphi(t)$ such that the deformed surface $S$ and target $T$ are similar with a minimal energy cost. The resulting velocity field $\underline{v}$ is thus characteristic for the associated target surface $T$ and can be regarded as a legitimate representation of $T$. The statistical analysis is performed then on the vector fields $\underline{v}$ which are individually obtained for the shapes in the cohort.

The specified similarity measure in the registration method is based on the concept of *surface currents*.

This work contributes with a modified structure of $\underline{v} \in \mathcal{V}$ such that rigid and non-rigid components are separated. The created registration framework is then applied to the displayed AAA cohort for further statistical analysis.

In this chapter, the necessary mathematical background for the definition of these spaces and actions is presented in the LDDMM framework. First, a short overview on reproducing kernel Hilbert spaces (RKHS) is given, as the structure of the velocity vector field $\underline{v}$ is determined by the properties of the embedding RKHS $\mathcal{V}$. Then, the group of diffeomorphisms $\mathcal{G}$ of $\varphi(t)$ with the associated parameterization by the characteristic vector field $\underline{v}$ and their action on the shape manifold $\mathcal{M}$ are introduced. The chapter concludes with the similarity measure computation using surface currents [46, 183]. Based on this background, the contributed method and its implementation are addressed in chapter 3.

Beforehand, a clarifying remark on the employed notations for the two-dimensional surfaces in $\mathcal{M}$ needs to be made. $\mathcal{X} \subset \mathbb{R}^3$ is a subset of the 3D space and represents a surface in $\mathcal{M}$. $\mathcal{X}$ comprises hence the vertices $\underline{q} \in \mathbb{R}^3$ that form the surface. The collection of all vertices is denoted with $\underline{x} \in \mathbb{R}^{3n_x}$, with $n_x$ the number of vertices. In the continuous case, $n_x$ is infi-

nite; in the discretized case, it is the number of vertices of the associated triangular mesh. Thus, $\underline{x} = [\underline{q}_1, \dots, \underline{q}_{n_x}]^{\mathrm{T}}$. The initial configuration of $\underline{x}(t = 0)$ is denoted with $\underline{X}$.
Accordingly, the vector field $\underline{v}$ comprises the velocity vectors in all vertices $\underline{q}$ and is therefore of the dimension $3n_x$. A single velocity vector is $\underline{v}_q$, Thus, $\underline{v} = [\underline{v}_{q_1}, \dots, \underline{v}_{q_{n_x}}]^{\mathrm{T}}$. This notation is applied to other vector fields, too, which are introduced in the course of this work.

## 2.1. Large Diffeomorphic Deformation Metric Mapping (LDDMM)

The Large Diffeomorphic Deformation Metric Mapping, or shortly LDDMM, is a registration method that allows the matching of an object $S$ to another object $T$ of the same group. In continuum mechanics, registration problems usually represent sophisticated ill-posed inverse problems where for example constitutive models are developed and optimally parameterized [95].

In the general unconstrained LDDMM framework, the underlying registration model does not assume a specific deformation behaviour, but is generally formulated to suit as many registration groups as possible. There, usually only a parameter fitting leads to the desired deformation behaviour.
Although the LDDMM framework does not explicitly incorporate models of continuum mechanics, the description of particle velocity relies on an Eulerian perspective, i.e. the velocity of a surface vertex is calculated from the position of the vertex at time $t$. Moreover, some non-rigid transformation models employed in the LDDMM framework are formulated based on Euler-Lagrange equations which ensure momentum conservation along the transformation path in $t \in [0, 1]$ [87, 119, 131].

However, LDDMM preceding matching methods are mostly derived from or based on mechanical models. The mechanical approaches realize registration problems using mechanical deformations, like works of Christensen et al. [28, 29] where *small* displacements achieve the image registration. There, the displacement fields are constrained with viscous-fluid PDE stimulated by body force, not attempting however to model the realistic growth of anatomical structures.
Another mechanical approach is followed in [115] for instance to achieve a 3D image matching. The approach builds on potentials of attraction. The source image creates such a potential of attraction, driving the deformation of the second image towards an optimal registration position. J. Gee et al. also develop in [60] a method to handle 3D image data as elastic continua, extending therewith the works of Bajcsy et al. on 2D CT images [10]. In this approach, the region of interest in an image is deformed to match the target object in the second image employing continuum mechanics principles of linear elasto-statics and volume forces generated from voxel data. In [11], Bajcsy et al. refines the presented elastic matching process with a multi-resolution, i.e. coarse-to-fine, strategy to improve local similarity results and global coherence. To that end, the mechanical registration problem is generally realized with minimizing the cost

$$\mathrm{cost} = \mathrm{cost}(\mathrm{deformation}) - \mathrm{cost}(\mathrm{similarity}).$$

The similarity is measured using normalized correlations with computed displacements.

At the same time, with the pioneering works of Brookstein in 1978 [20], anatomical mapping problems have been conducted on specific anatomical geometrical features, like landmarks (points) [21] or contours (lines).

Towards the development of the recent LDDMM framework, Younes innovates in [197] an elastic curve matching formulation. Instead of using a finite collection of geometrical points or features for the matching process, the similarity measure is based on the whole continuous outline as a plane curve. The curves are parameterized by the Euclidean arc-length which assumes regularity of compared curves and are embedded in continuous manifolds. The deformation of curves is realized with diffeomorphic group actions adopted from Lie group theory. The distance between curves is then measured with the energy that results from deformation of the one curve to the other, mathematically realized with the metric of the vector space of the velocity vector fields $\underline{v}$.
In [176, 177], Trouvé examines other geometrical shape manifolds and other infinite-dimensional Lie group transformations. The matching problem departs from the mechanical formulation to a more generic realization based on mathematical group actions.

The method of the Large Diffeomorphic Metric Mapping (LDDMM) was first introduced in 1998 to solve image matching problems in computational anatomy [42, 72, 197]: The proposed mapping consists of mapping a reference geometry or source $S$ to a target shape $T$. The deformations correspond to the group of diffeomorphisms $\mathcal{G}$ and the associated deformation parameter $\underline{v} \in \mathcal{V}$. In this manner, the aim is to find a vector field $\underline{v}$ that transports $S$ to $T$.

### 2.1.1. Group of diffeomorphisms $\mathcal{G}$

The group of diffeomorphisms $\mathcal{G}$ in this work consists of non-rigid, invertible, one-to-one and diffeomorphic deformations $\varphi(t)$ which only depend on time $t$, turning the group $\mathcal{G}$ to a one-parameter subgroup. This is the case in this work as the ODE governing the group transformation $\varphi(t)$ is autonomous. At $t = 0$, the transformation $\varphi(0)$ represents the identity $id$.

In this work, elements of the three-dimensional Riemann shape manifold $\mathcal{M}$ are parameterized by two-dimensional surfaces in the $\mathbb{R}^3$ space over $t \in [0, 1]$. The action of $\varphi \in \mathcal{G}$ on the shape manifold $\mathcal{M}$ results therefore in coordinate transformations of elements in $\mathcal{M}$. This group action of $\mathcal{G}$ on $\mathcal{M}$ can be written as

$$(\varphi, S) \mapsto \varphi \circ S \in \mathcal{M} \tag{2.1.1}$$

with $\varphi \in \mathcal{G}$ and $S \in \mathcal{M}$ [127].

The tangent-space $\mathfrak{g}$ in an element $\varphi(t) \in \mathcal{G}$ represents the vector space which determines the temporal evolution of the elements in $\mathcal{G}$ according to

$$\frac{\mathrm{d}\varphi(t)}{\mathrm{d}t} = \underline{v} \circ \varphi(t). \tag{2.1.2}$$

Consequently, the vector space $\mathfrak{g}$ generates the infinitesimal transformation of an element $\varphi(t) \in \mathcal{G}$. Obviously, $\mathfrak{g}$ can be then regarded as a tangent-space of elements in $\mathcal{G}$ [111].

The vector space of $\mathfrak{g}$ is usually a Riemann manifold such that a metric is defined. Also, the defined inner product $p$ thereof has the convenient feature of varying smoothly from a $\varphi$ to another in $\mathcal{G}$. Given two vector fields $\underline{v}^1 \in \mathfrak{g}$ and $\underline{v}^2 \in \mathfrak{g}$ in an element $\varphi \in \mathcal{G}$, the inner product is defined with $\varphi \mapsto p(\underline{v}^1, \underline{v}^2)$ and is a smooth function [58, 146]. In this work, this vector space represents a Reproducing Kernel Hilbert Space (RKHS) which is handled in the course of the present work.

Coming back to the diffeomorphic transformations in $\mathcal{G}$, a transformation $\varphi(t) \in \mathcal{G}$ evolves in time as described with the ODE in Equation 2.1.2 which is determined by $\underline{v}$. The solution of such an ODE can be given with

$$\varphi(t) = e^{(t\underline{v})} \quad \forall t \in \mathbb{R}. \tag{2.1.3}$$

Hence, starting at identity in $\mathcal{G}$ and with the tangent vector field $\underline{v} \in \mathfrak{g}$, the transformation $\varphi(t)$ at time $t > 0$ is achieved with $e^{(t\underline{v})}$ which belongs to $\mathcal{G}$.The element $\varphi \in \mathcal{G}$ is accordingly mapped along the tangent vectors $\underline{v} \in \mathfrak{g}$ [57, 168].

Figure 2.1.1 illustrates the transformation $\varphi(t) \in \mathcal{G}$ when acting on the shape manifold $\mathcal{M}$. In $\mathcal{M}$, the initial shape configuration $S$ is represented with an infinite number of surface points $\underline{X}$. The deformed configurations therein are denoted with $\underline{x}(t)$. The transformation $\varphi(t)$ is generated by $\underline{v} \in \mathfrak{g}$. The identity element $\varphi(0) \in \mathcal{G}$ resides in the initial surface configuration $\underline{X} \in \mathcal{M}$ where the vector field $\underline{v} \in \mathfrak{g}$ exists. With the temporal evolution in $t \in [0, 1]$, the transformation $\varphi(t)$ evolves in $\varphi_1^{\underline{v}}$ at $t = 1$. When acting on the shape manifold $\mathcal{M}$, this transformation $\varphi_1^{\underline{v}}$ transports $\underline{X}$ to its deformed configuration $\underline{x}(t = 1) = \varphi_1^{\underline{v}}(\underline{X})$ at $t = 1$. According to the definition of the shape manifold $\mathcal{M}$, $\mathcal{M}$ consists of the initial shape configuration $\underline{X}$ and its deformed configurations $\underline{x}(t)$ in $t \in [0, 1]$. Thus, the resulting $\underline{x}(t) = \varphi_1^{\underline{v}}(\underline{X})$ belongs to $\mathcal{M}$. Hence, the transformation $\varphi_1^{\underline{v}}$ produces the diffeomorphism

$$\varphi_1^{\underline{v}} : \underline{X} \to \underline{x}(1) \in \mathcal{M} \tag{2.1.4}$$

when acting on $\mathcal{M}$.

The transport produced by $\varphi_t^{\underline{v}}$ of initial shape configuration $\underline{X} \in \mathcal{M}$ can be thus formulated with

$$\frac{\mathrm{d}\underline{x}}{\mathrm{d}t} = \underline{v}(\underline{x}(t)) \circ \underline{x}(t) \tag{2.1.5}$$

with $\underline{x}$ as the current configuration at time $t$ in $\mathcal{M}$ and the vector field $\underline{v}$ defined on the current configuration $\underline{x}(t)$. The generated $\underline{x}(t)$ configurations represent a trajectory that is unique and determined by the initial conditions of $\underline{v}$ in $\underline{X}$. Hence, $\varphi(t)$ defines the time-dependent transformation which generates the path of a surface $S$ and its deformed configurations in $\mathcal{M}$ over $t \in [0, 1]$

In the following, the notion $\varphi^{\underline{v}}(t)$ describes the diffeomorphic transformation that is produced by a vector field $\underline{v}$. Also, in the following, the RKHS $\mathcal{V}$ represents the space where $\underline{v}$ is embedded. As mentioned before, it is defined on the subset $\mathcal{X} \subset \mathbb{R}^3$, comprising the vertices $\underline{q} \in \mathbb{R}^3$ which belong to a surface in $\mathcal{M}$. All vertices $\underline{q} \in \mathcal{X}$ together represent the current configuration $\underline{x}(t)$ of the shape at a time $t$. The RKHS $\mathcal{V}$ is thus the space of vector fields $\underline{v}$ defined on the subset $\mathcal{X}$.

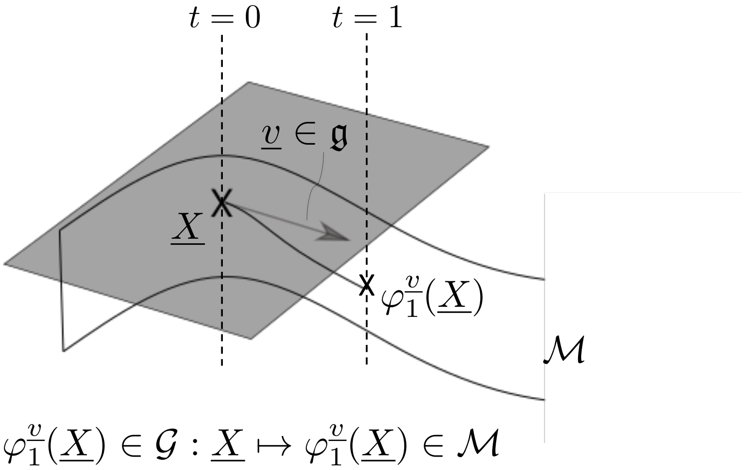

Figure 2.1.1.: Illustration of the transformation $\varphi(t) \in \mathcal{G}$ when acting on the shape manifold $\mathcal{M}$. Starting at $t = 0$ in the initial shape configuration $\underline{X}$, the velocity vector field $\underline{v} \in \mathfrak{g}$ produces the corresponding transformation $\varphi \in \mathcal{G}$. The transformation $\varphi_1^{\underline{v}}(\underline{X}) \in \mathcal{G}$ at end point $t = 1$ yields the deformed shape $\underline{x}(t = 1) \in \mathcal{M}$.

In this context, the notation $\underline{v}_q(\underline{q}(t))$ evaluates the velocity vector in a single point $\underline{q}(t) \in \mathcal{X}$ and is element of $\mathbb{R}^3$, while the notation $\underline{v}(\underline{x}(t))$ stands for the velocity vector field of all vertices $\underline{q}$, i.e. the configuration $\underline{x}(t)$.

In all cases, a norm $\|\underline{v}\|^2_{\mathcal{V}}$ can be computed and exists. The exact description of this norm and of the RKHS $\mathcal{V}$ is handled in the course of this section. According to the construction guidelines of Dupuis et al. in [42], if $\int_0^1 \|\underline{v}(\underline{x}(t))\|^2_{\mathcal{V}}\, \mathrm{d}t < \infty$, then the mapping $\varphi_1 : \mathcal{M} \mapsto \mathcal{M}$ is a diffeomorphism of $\mathcal{M}$ to $\mathcal{M}$. To that end, the vector fields $\underline{v} \in \mathcal{V} = \{\underline{v} : \int_0^1 \|\underline{v}\|^2_{\mathcal{V}}\, \mathrm{d}t < \infty\}$ have to fulfill

$$\varphi^{\mathcal{V}} = \left\{ \varphi(t) : \frac{\partial \varphi(t)(t)}{\partial t} = \underline{v}(\underline{x}(t)),\, t \in [0,1] : \int_0^1 \|\underline{v}(\underline{x}(t))\|^2_{\mathcal{V}}\, \mathrm{d}t < \infty,\, \underline{v} \in \mathcal{V} \right\} \tag{2.1.6}$$

to produce a diffeomorphism.

Additionally, a diffeomorphic change $\dot{\varphi}(t) = \underline{v}(\underline{x}(t))$ along $\varphi(t)$ has to be stationary. The vector field $\underline{v}$ in each time step in $t \in [0,1]$ does not depend on time, but only on a current configuration $\underline{x}(t)$. The stationary ODE should accordingly generate a flow of $\underline{x}(t) \in \mathcal{M}$ with the transformation $\varphi(t)$ such that for a fixed $\underline{x}(0)$ the one-parameter mapping $t \mapsto \varphi_t^{\underline{v}}(\underline{x}(0))$ is the unique solution of the stationary ODE with initial conditions $\underline{x}(0) = \underline{X}$ and $\dot{\underline{x}}(0) = \underline{v}_0$ at time $t = 0$ [6]. According to [171], one-parameter subgroups of diffeomorphisms are always achieved by flows of stationary ODE. The vector field $\underline{v}$ is the *infinitesimal generator* of the subgroup. These

ODEs were already provided with Equation 2.1.2, defining the forward and inverse maps of the group transformations.

### Definition of optimal path $\varphi(t)$

The optimal solution path for $\varphi(t)$ connecting the objects $S$ and $T$ in $\mathcal{M}$ with the minimal cost is determined from the group of diffeomorphisms in Equation 2.1.6 by the geodesic property. The requirement of geodesy is necessary to produce a *unique* and *energetically* minimal path $\varphi^{\underline{v}}(t)$ from $S$ to $T$. This requirement gives rise to the need of an appropriate description of the *cost* or *energy* $||\underline{v}(\underline{x}(t))||^2_{\mathcal{V}}$ along the path $\varphi^{\underline{v}}(t)$ for $t \in [0,1]$. Also, the diffeomorphic transport of $S$ to $T$ along $\varphi(t)$ needs to represent realistic physically possible deformations of the examined shape group in $\mathcal{M}$.

### Construction of the vector field $\underline{v}$

As a consequence, the choice of an appropriate norm $||\underline{v}(\underline{x}(t))||^2_{\mathcal{V}}$ for energy quantification along $\varphi(t)$ for $t \in [0,1]$ is essential. Hence, a choice of an appropriate normed space $\mathcal{V}$ becomes essential to describe the transformation $\varphi(t)$ which generates the flow of the transformed configurations of source shape $S$ over $t \in [0,1]$. With regard to the physically possible deformations, it seems obvious to adopt the form of flow $\varphi(t)$ from transport equations from continuum or fluid mechanics, as described in [177]. Consequently, in order to identify a suitable model for $\varphi(t)$, a qualified space $\mathcal{V}$ has to be established.

In [44, 48], Durlemann et al. choose a reproducing kernel Hilbert space (RKHS) as a suitable space to construct the vector field $\underline{v}$. This choice is built on the works [42, 125, 198] where a generalized approach to define a suitable space is followed. In these works, Sobolev spaces are proven to be appropriate for the specified task and are the basis from where employing RKHS is deduced. In particular, Sobolev spaces provide the integration of a differential operator $L$ which can be employed to model $\varphi(t)$ as desired. The integration of operator $L$ and its norm $||\cdot||_L$ in the context of Sobolev spaces provides conditions on the norm $||\cdot||_L$ that ensure regularity properties for functions on $L$ as functions on $\mathcal{X}$.

According to [48] and inspired by [200], the differential operator $L$ can be implicitly determined, while the Green's function or kernel $k$ sets the metric. This is achieved by formulating the operations on $\mathcal{V}$ as a regularizing *convolution*, instead of explicitly determining a (numerically unstable) differential operator $L$. The kernel convolution with $k$ is only in space. The space $\mathcal{V}$ becomes a reproducing kernel Hilbert space (RKHS) where the metric is controlled by Gaussian kernel $k$. A Gaussian kernel is chosen, thus $k_{\mathcal{V}}$ represents the kernel of $\mathcal{V}$ with kernel width $\sigma_{\mathcal{V}}$, according to

$$k_{\mathcal{V}}(\underline{q}_1, \underline{q}_2) := \exp\big(-\frac{||\underline{q}_1 - \underline{q}_2||^2_{\mathcal{X}}}{\sigma^2_{\mathcal{V}}}\big). \tag{2.1.7}$$

Therein, $\sigma_{\mathcal{V}}$ represents the kernel width and determines the smoothing radius of the kernel.

In this setting, the vectors $\underline{\mu}$ belong to the dual space $\mathcal{V}^*$ and the kernel $k_{\mathcal{V}}$ realizes the mapping from $\underline{\mu} \in \mathcal{V}^*$ to $\underline{v} \in \mathcal{V}$. The mapping between $\mathcal{V}$ and its dual space $\mathcal{V}^*$ is realized with $k_{\mathcal{V}}$

as $k_{\mathcal{V}} : \mathcal{V}^* \mapsto \mathcal{V}$.

The tangent vector $\underline{v}_q(\underline{q}(t))$ in $\underline{q}(t) \in \mathcal{X}$ is subsequently constructed from the vectors $\underline{\mu}_q \in \mathcal{V}^*$ with

$$\underline{v}_q(\underline{q}(t)) = \int_{\mathcal{X}} k_{\mathcal{V}}(\underline{q}(t), \underline{y}(t))\underline{\mu}_q(\underline{y}(t))\, d\underline{y}. \tag{2.1.8}$$

The RKHS $\mathcal{V}$ is defined over the shape manifold $\mathcal{M}$ and is a space of functions $\underline{v}_q(\underline{q})$. The evaluation of velocity vector field $\underline{v}(\underline{x}(t))$ for a shape configuration $\underline{x}(t) \in \mathcal{M}$ at time $t$ is constructed of the evaluation in Equation 2.1.8 of every velocity vector $\underline{v}_q(\underline{q}(t))$ in a vertex $\underline{q}(t)$. Hence, the tangent vector field $\underline{v}(\underline{x}(t)) \in \mathcal{V}$ is evaluated at time $t$ for a configuration $\underline{x} \in \mathcal{M}$ in the Eulerian frame.

At this point, the introduction of the spatial discretization of surfaces in $\mathcal{M}$ is beneficial. To that end, a surface in $\mathcal{M}$ is spatially discretized with a triangular mesh of $n_x$ vertices. Hence, the initial surface configuration $\underline{X} \in \mathcal{M}$ and the associated deformed configurations $\underline{x}(t)$ become vectors of $\mathbb{R}^{3n_x}$. Also, the velocity vector field $\underline{v}$ is now of dimension $\mathbb{R}^{3n_x}$. Moreover, the subset $\mathcal{X} \subset \mathbb{R}^3$ consists of $n_x$ vertices $\underline{q} \in \mathbb{R}^{3n_x}$ and the Hilbert space $\mathcal{V}$ becomes finite-dimensional on $\mathcal{X}$.

For the discretized description of the vector field $\underline{v}(\underline{x}(t)) \in \mathbb{R}^{3n_x}$, the formulation

$$\underline{v}(\underline{x}(t)) = \underline{K}_{\mathcal{V}} \cdot \underline{\mu}(t) \tag{2.1.9}$$

is introduced with $\underline{v}, \underline{x}, \underline{\mu} \in \mathbb{R}^{3n_x}$ and $\underline{K}_{\mathcal{V}} \in \mathbb{R}^{3n_x \times 3n_x}$. A matrix complex $\underline{K}_{\mathcal{V},ij}$ in kernel matrix $\underline{K}_{\mathcal{V}} \in \mathbb{R}^{3n_x \times 3n_x}$ consists of

$$\underline{K}_{\mathcal{V},ij} = k_{\mathcal{V}}(\underline{q}_i, \underline{q}_j) \cdot \underline{I}^{3\times3} \tag{2.1.10}$$

with $k_{\mathcal{V}}$ the kernel function of vertices $\underline{q}_i$ and $\underline{q}_j$ and $\underline{I}^{3\times3}$ a $3 \times 3$ identity matrix $\underline{I}$. More information regarding discretization, especially in context of current implementation, can be found in subsection 3.3.1.

### Flow model

Having established a suitable space and structure for $\underline{v}$, an optimal path generated by a $\underline{v}$ has to be derived. With the demonstrated $\underline{v}$ in RKHS $\mathcal{V}$, the path length or energy norm can be evaluated for the configuration $\underline{x} \in \mathcal{M}$ with

$$E(\varphi) = \int_0^1 \|\underline{v}(\underline{x}(t))\|^2_{\mathcal{V}} \,\mathrm{d}t = \int_0^1 \langle \underline{K}_{\mathcal{V}}\underline{\mu}(t), \underline{\mu}(t)\rangle_{\mathcal{V}} \,\mathrm{d}t \tag{2.1.11}$$

or written out

$$E = \int_0^1 \underline{\mu}(t)^{\mathrm{T}} \underline{K}_{\mathcal{V}} \underline{\mu}(t) \,\mathrm{d}t. \tag{2.1.12}$$

Consequently, the new control variable is $\underline{\mu}$. With the variational principle also applied on Equation 2.1.11, the ODEs governing the temporal evolution of $\underline{\mu}$ are derived as follows:

$$\delta E = \int_0^1 \left(\underline{\dot{x}}^{\mathrm{T}} \delta\underline{\mu} + \underline{\mu}^{\mathrm{T}} \delta\underline{\dot{x}}\right) \mathrm{d}t \tag{2.1.13}$$

$$= \int_0^1 \left(2\underline{\mu}^{\mathrm{T}} \delta\underline{\dot{x}} - \underline{\mu}^{\mathrm{T}} d_{\underline{x}}(\underline{K}_{\mathcal{V}}\underline{\mu})\delta\underline{x}\right) \mathrm{d}t \tag{2.1.14}$$

With $\delta\underline{x}(0) = \delta\underline{x}(1) = \underline{0}$ :

$$\delta E = -\int_0^1 \left(2\underline{\dot{\mu}} + d_{\underline{x}}(\underline{K}_{\mathcal{V}}\underline{\mu})^{\mathrm{T}}\underline{\mu}\right)^{\mathrm{T}} \delta\underline{x}\, \mathrm{d}t \tag{2.1.15}$$

For arbitrary $\delta\underline{x}$ and $\delta E \overset{!}{=} 0$:

$$2\underline{\dot{\mu}} + d_{\underline{x}}\left(\underline{K}_{\mathcal{V}}\underline{\mu}\right)^{\mathrm{T}}\underline{\mu} \overset{!}{=} 0 \tag{2.1.16}$$

Consequently:

$$\underline{\dot{\mu}} = -\frac{1}{2} d_{\underline{x}}\left(\underline{K}_{\mathcal{V}}\underline{\mu}\right)^{\mathrm{T}}\underline{\mu}. \tag{2.1.17}$$

With an established temporal behaviour of control variable $\underline{\mu}$, a geodesic mapping with the shortest path length is established in $t \in [0,1]$. In other words, starting with appropriate initial momenta $\underline{\mu}(t=0) = \underline{\mu}_0$, Equation 2.1.17 gives corresponding $\underline{\mu}(\underline{x})$ and $\underline{v}(\underline{x})$ at every $t \in [0,1]$, generating a transformation $\varphi(t)$ with the shortest length to the final configuration $\underline{x}(1) \in \mathcal{M}$.

Therewith, the energetically shortest (= geodesic) path in the space of diffeomorphisms is ensured, when solving the dynamic equations with given initial conditions $\underline{x}(0) = \underline{X}$ and $\underline{\mu}(0) = \underline{\mu}_0$ [48].

### Momentum conservation

The (fictituous) energy of the system is given by Equation 2.1.11 which can be interpreted from a mechanical point of view as the kinetic energy of the system. The derivation of the associated momentum formulation in Eulerian coordinates and the proof of momentum conservation are extensively explained in [126]. In the following, a short introduction is provided.

The kinetic energy or the energy term Equation 2.1.11 with ODE Equation 2.1.17 describes the path of the shortest energy. At the initial time, the energy of the system is determined with the velocity $\underline{v}_0$. Then, without further system activation, the system dynamics follow Equation 2.1.17. The resulting path $\underline{x}(t) \in \mathcal{M}$ generated by $\varphi(t)$ is naturally the path with the minimal energy, as stated by the least action principle of Lagrangian mechanics. The momentum is conserved along any energy minimizing path which is a law from classical mechanics.

Accordingly, the energy of the system can be very well given by just considering the initial time $t = 0$ with $\underline{v}_0$ determining the total energy of the system. That is why, following [48], the registration problem can be reformulated with regard to $\underline{v}_0 = \underline{v}(0)$.

### 2.1.2. Surface matching problem

In the matching problem, two objects $S, T \in \mathcal{M}$ are given. The geodesic diffeomorphic path $\varphi^{\underline{v}}(t)$ is to be determined that connects $S$ to $T$. In other words, the corresponding vector field $\underline{v}$ which parameterizes the deformation $\varphi$ needs to be determined. With the proven momentum conservation, it suffices to estimate the initial velocity vector field $\underline{v}_0$.
Consequently, a matching optimization problem is at hand. To that end, the cost function

$$J_{\mathcal{V}}(\underline{v}_0) = \gamma_E \cdot \|\underline{v}_0\|_{\mathcal{V}}^2 + d_{\mathcal{W}}(\varphi_1^{\underline{v}_0}(S), T). \tag{2.1.18}$$

needs to be minimized with regard to the initial tangent vectors $\underline{v}_0 \in \mathcal{V}$, or in particular with regard to the underlying momenta $\underline{\mu}_0$. Thus, with minimizing Equation 2.1.18, the optimal initial velocity vector field $\underline{v}_0$ is estimated that induces with the temporal evolution in Equation 2.1.17 the corresponding geodesic path connecting $S$ to $T$. The parameter $\gamma_E$ is a weighing parameter between the data-fidelity and energy term.
The energy minimizing term also ensures a regularization on the control variable $\underline{v}_0$ and thereby on the total energy of the system.

The second term in Equation 2.1.18 is a similarity metric between the deformed source $\varphi_1^{\underline{v}_0}(S)$ and the target object $T$ also known as the data attachment term. It penalizes the difference between the deformed $S$ and target $T$, leading to the estimation of the optimal initial velocity vector field $\underline{v}_0$. Arsigny et al. present a detailed formulation and proofs for the existence of a solution in the LDDMM framework in [6].

### 2.1.3. Similarity measure of shapes

This section is devoted to the definition of a convenient manifold $\mathcal{M}$ where the deforming objects are embedded. In the previous section 2.1, the LDDMM paradigm has been introduced, allowing a geodesic matching between two shapes. In order to perform the matching procedure and to solve the inverse problem, it is necessary to extend the energy term Equation 2.1.11 with a similarity measure $d_{\mathcal{W}}(\varphi_1^{\underline{v}_0}(S), T)$ as in Equation 2.1.18. Consequently, the general LDDMM problem in Equation 2.1.18 consists of two terms. The first term ensures that the path with the minimal energy, i.e. geodesic path, is found, and the second term is the data-fidelity term. In this section, a suitable shape representation for similarity measurement is introduced and analyzed.

Since the introduction of diffeomorphisms in anatomical analysis, the matching has been performed on landmark data, like in [1, 21]. In 2000, Joshi et al. introduced landmark matching to the LDDMM framework [93].
However, landmark matching requires point-correspondence which is often cumbersome to provide. That is why, in [65], the LDDMM framework was applied on unlabelled point-sets and submanifolds from which the most recent LDDMM formulation has been developed in [46, 183]. There, the surface currents method has been integrated in the LDDMM framework based on the works of [38].

Other approaches to eliminate point-correspondence in matching problems are followed in [192] for instance where the matching is based on local geometry comparisons and in [66] where the matching is based on different parameterizations of planar shapes.

The surface representation with surface currents relaxes the similarity measure from finding point-wise correspondences between two compared surfaces. In particular, the proposed method considers the whole boundary of both shapes to be compared, without any prior correspondence establishment, but based on a global measure. Thus, it is more robust to shape irregularities.
To that end, the matching objects are embedded a linear space which is designed as a RKHS $\mathcal{W}$. By doing so, a computable norm is provided which enables a more robust comparison between surfaces in the matching procedure.

### Surface description in differential geometry

In this context, it is now imperative to mathematically establish a definition of a surface. So far, the term *surface* has been employed to describe the boundary of an object in 3D space. Formally, adopting the definition from [39], a surface is understood as a two-dimensional differential manifold in the three-dimensional Euclidean space $\mathbb{R}^3$. Additionally, in this work, the surfaces are assumed to be regular and are parameterized according to the standards of differential geometry. Therefore, a parameterization can be used with $\underline{\phi}(\underline{q})(u_1, u_2)$ where $\underline{\phi}$ is a vector-valued function of $(u_1, u_2)$ and represents an infinitesimally small surface on $S$.
The first derivatives with regard to the parameters $(u_1, u_2)$ are expressed with $\underline{\phi}_{u_1} := \frac{\partial \underline{\phi}}{\partial u_1}$ and $\underline{\phi}_{u_2} := \frac{\partial \underline{\phi}}{\partial u_2}$, respectively. For a regular surface, the vector-valued derivatives are linearly independent and span a tangent space in $\underline{q}$ on the surface determined by the parameters $(u_1, u_2)$. They can be denoted with tangent vectors. The cross product of the tangent vectors is the unit normal vector

$$\underline{n} = \frac{\underline{\phi}_{u_1} \times \underline{\phi}_{u_2}}{|\underline{\phi}_{u_1} \times \underline{\phi}_{u_2}|}$$

orthogonal to the tangent space in $\underline{q}$.

Only with this representation can the surface currents concept be applied to a surface $S$ in $\mathcal{M}$. The interested reader should refer to [94].

### Concept of surface *currents*

For the introduction of the surface currents concept, two surfaces $S_1$ and $S_2$ are considered, with the parameterizations $\underline{\phi}^1(u_1, u_2)$ and $\underline{\phi}^2(t_1, t_2)$, respectively. These surfaces are embedded in a vector field $\underline{\omega} \in \mathbb{R}^3$ which passes through the surfaces $S_1$ and $S_2$. The vector field thus creates a flux through each surface $S_1$ and $S_2$. The similarity $d_{\mathcal{W}}(S_1, S_2)$ between $S_1$ and $S_2$ is then measured as the difference of these two fluxes.
The same concept is similarly applied with 3D scanners which digitally acquire the geometry of 3D objects with laser beams. The light beams probe the geometry and their diffraction on the geometry surface is employed to reconstruct the geometry computationally. This analogy is illustrated in [118]. In the same manner, the vector field $\underline{\omega}$ characterizes the similarity $d_{\mathcal{W}}(S_1, S_2)$ of surface $S_1$ and $S_2$.

The flux of the vector field $\underline{\omega}$ through a surface $S$ is defined as the integral of vector field $\underline{\omega}$ through the surface $S$ and denoted with $S(\underline{\omega})$. It is evaluated according to

$$S(\underline{\omega}) = \int_{u_1} \int_{u_2} \underline{\omega}(\underline{\phi}(\underline{q})(u_1, u_2))(\underline{\phi}_{u_1}, \underline{\phi}_{u_2}) \,\mathrm{d}u_2 \,\mathrm{d}u_1, \tag{2.1.19}$$

with $\underline{\phi}_{u_1}$ and $\underline{\phi}_{u_2}$ as the tangent vectors in $\underline{\phi}(\underline{q})$, and $\mathrm{d}\underline{\phi}(\underline{q})$ as the element of surface area [46, 47], or reformulated as

$$S(\underline{\omega}) = \int_{u_1} \int_{u_2} \underline{\omega}(\underline{\phi}(u_1, u_2))^{\mathrm{T}}(\underline{\phi}_{u_1}(u_1, u_2) \times \underline{\phi}_{u_2}(u_1, u_2)) \,\mathrm{d}u_2 \,\mathrm{d}u_1. \tag{2.1.20}$$

With the previously introduced parameterization for a surface $S$ as objects embedded in the Euclidean three-dimensional space, the integral form Equation 2.1.19 belongs to the differential 2-forms of such objects [183]. The differential 2-form action on objects consists in the differential 2-form mapping $\underline{q} \to \underline{\omega}(\underline{q})$ where the function $\underline{\omega}(\underline{q})$ is a skew-symmetric bilinear function on $\mathbb{R}^3$. Therewith, the surface $S$ is a linear functional on the space of 2-forms. The notation $S$ represents in this sense a *surface* consisting of the vertices $\underline{q} \in \mathbb{R}^3$.

### Construction of vector field $\underline{\omega}$

In this work, the vector field $\underline{\omega}$ is chosen to be embedded in a RKHS $\mathcal{W}$ with Gaussian kernel $k_{\mathcal{W}}$. The kernel width is noted with $\sigma_{\mathcal{W}}$. This guarantees spatial smoothness for the similarity evaluation as the kernel functions as a low-pass filter on the spatial frequencies of the underlying vector fields. The underlying vector field is chosen to consist of centers and normals of the examined surfaces respectively [47], as follows:

$$\underline{\omega}(\underline{q}) = \int_{u_1} \int_{u_2} k_{\mathcal{W}}(\underline{q}, \underline{\phi}^1(u_1, u_2)) \cdot \underline{n}^{S_1}(u_1, u_2) \mathrm{d}u_2 \mathrm{d}u_1 - \int_{t_1} \int_{t_2} k_{\mathcal{W}}(\underline{q}, \underline{\phi}^2(t_1, t_2)) \cdot \underline{n}^{S_2}(t_1, t_2) \mathrm{d}t_1 \mathrm{d}t_2. \tag{2.1.21}$$

The vector field $\underline{\omega}$ depends therefore on the examined surfaces $S_1$ and $S_2$ with their parameterizations $\underline{\phi}^1(u, v)$ and $\underline{\phi}^2(t_1, t_2)$ and the associated normal vectors $\underline{n}^{S_1}$ and $\underline{n}^{S_2}$ respectively.

### Evaluation of similarity measure in RKHS $\mathcal{W}$

Consequently, the similarity measure $\Delta S(\underline{\omega}) = S_1(\underline{\omega}) - S_2(\underline{\omega})$ can be written with Equation 2.1.21 to

$$\Delta S(\underline{\omega}) = \int_{u_2} \int_{u_1} \underline{\omega}(\underline{\phi}^1(u_1, u_2))^{\mathrm{T}} \cdot \underline{n}^{S_1}(u_1, u_2) \mathrm{d}u_1 \mathrm{d}u_2 - \int_{t_2} \int_{t_1} \underline{\omega}(\underline{\phi}^2(t_1, t_2))^{\mathrm{T}} \cdot \underline{n}^{S_2}(t_1, t_2) \mathrm{d}t_1 \mathrm{d}t_2. \tag{2.1.22}$$

From Equation 2.1.22, the following relations can be deduced:

$$\begin{aligned} \Delta S(\underline{\omega}) = & \int_{u_2} \int_{u_1} \int_{u_2} \int_{u_1} k_{\mathcal{W}}(\underline{\phi}^1(u_1, u_2), \underline{\phi}^1(u_1, u_2)) \, \underline{n}^{S_1}(u_1, u_2)^{\mathrm{T}} \cdot \underline{n}^{S_1}(u_1, u_2) \, \mathrm{d}u_1 \mathrm{d}u_2 \mathrm{d}u_1 \mathrm{d}u_2 \\ & - 2 \cdot \int_{u_2} \int_{u_1} \int_{t_2} \int_{t_1} k_{\mathcal{W}}(\underline{\phi}^1(u_1, u_2), \underline{\phi}^2(t_1, t_2)) \, \underline{n}^{S_1}(u_1, u_2)^{\mathrm{T}} \cdot \underline{n}^{S_2}(t_1, t_2) \, \mathrm{d}t_1 \mathrm{d}t_2 \mathrm{d}u_1 \mathrm{d}u_2 \\ & + \int_{t_2} \int_{t_1} \int_{t_2} \int_{t_1} k_{\mathcal{W}}(\underline{\phi}^2(t_1, t_2), \underline{\phi}^2(t_1, t_2)) \, \underline{n}^{S_2}(t_1, t_2)^{\mathrm{T}} \cdot \underline{n}^{S_2}(t_1, t_2) \, \mathrm{d}t_1 \mathrm{d}t_2 \mathrm{d}t_1 \mathrm{d}t_2. \end{aligned} \tag{2.1.23}$$

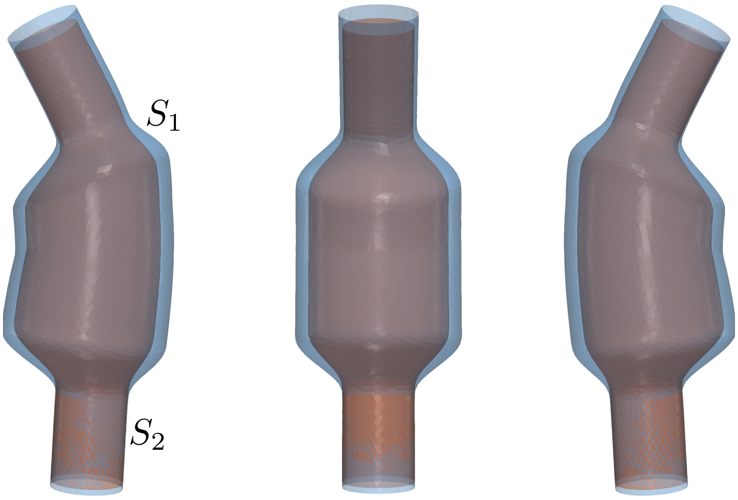

Figure 2.1.2.: Exemplary shapes $S_1$ and $S_2$ for which the vector field $\underline{\omega}$ from Equation 2.1.21 is evaluated and visualized in Figure 2.1.3. $S_1$ is coloured in blue, $S_2$ in red. The shapes $S_1$ and $S_2$ are shown from three different views.

The latter formulation can be identified as the decomposition of the natural scalar product

$$\|\Delta S\|^2_{\mathcal{W}^*} = \|S_1 - S_2\|^2_{\mathcal{W}^*} =< S_1 - S_2, S_1 - S_2 >_{\mathcal{W}^*} \tag{2.1.24}$$

of the current-matching norm that is reformulated according to

$$\|\Delta S\|^2_{\mathcal{W}^*} =< S_1, S_1 >_{\mathcal{W}^*} -2 < S_1, S_2 >_{\mathcal{W}^*} + < S_2, S_2 >_{\mathcal{W}^*} . \tag{2.1.25}$$

With regard to Equation 2.1.23, the relation in Equation 2.1.25 can be rewritten with

$$\|\Delta S\|^2_{\mathcal{W}^*} = \|S_1\|^2_{\mathcal{W}^*} - 2\cdot < S_1, S_2 >_{\mathcal{W}^*} + \|S_2\|^2_{\mathcal{W}^*}.$$

Also, as stated in [47], the norm of the vector field $\underline{\omega}$ in the test space $\mathcal{W}$ is an isometric map to the current-matching norm in $\mathcal{W}^*$

$$\|\underline{\omega}\|^2_{\mathcal{W}^*} = \|\Delta S(\underline{\omega})\|^2_{\mathcal{W}^*}. \tag{2.1.26}$$

The test vector field $\underline{\omega}$ in Equation 2.1.21 which is used to compute the similarity measure $\|\Delta S\|^2_{\mathcal{W}^*}$ of $S_1$ and $S_2$ from Figure 2.1.2 is shown in Figure 2.1.3. The vector field $\underline{\omega}$ is computed in the vertices of a mesh grid around $S_1$ and $S_2$ with a mesh space of $8\,\mathrm{mm}$ and a kernel width $\sigma_{\mathcal{W}} = 10\,\mathrm{mm}$. Figure 2.1.3 shows the behaviour of vector field $\underline{\omega}$ that is used to measure the similarity between $S_1$ and $S_2$ of Figure 2.1.2 according to Equation 2.1.21 with kernel width $\sigma_{\mathcal{W}} = 10\,\mathrm{mm}$. Where $S_1$ and $S_2$ are very similar, like at the lower neck, the vector field vanishes; where $S_1$ and $S_2$ differ a lot, $\underline{\omega}$ is big to maximize the dissimilarity between them, like in the center with the different diameters.

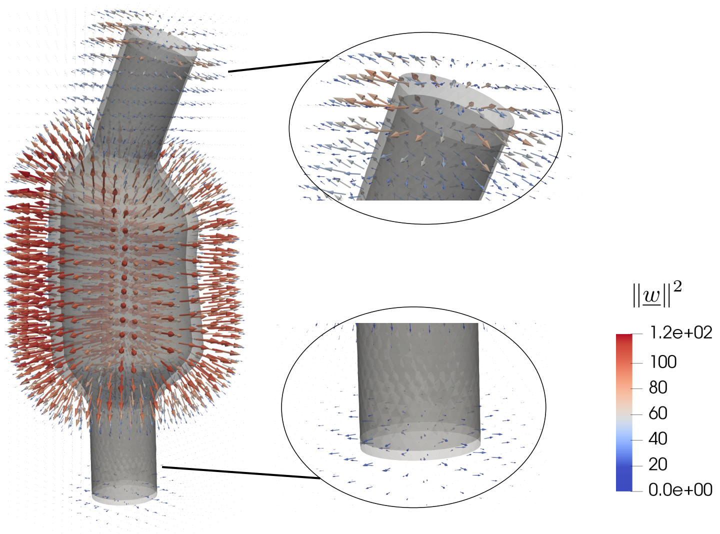

Figure 2.1.3.: The test vector field $\underline{\omega}$ that can capture the similarity between surfaces $S_1$ and $S_2$ computed on vertices of a mesh grid with $\sigma_{\mathcal{W}} = 10\,\mathrm{mm}$. The mesh grid encloses both surfaces. The form of $\underline{\omega}$ here shows how the vector field changes to adapt to the shapes' similarity: where the two surfaces are very similar, like in the bottom outlet, the vector field is almost zero. Where the similarity decreases, like in the middle, the vector $\underline{\omega}$ increases to capture the dissimilarities.

### Diffeomorphism on currents

After the introduction of the surface representation with currents, the question now becomes how the currents behave under the action of the diffeomorphic transformations.
Vaillant et al. presented in [183] the incorporation of a currents-based similarity measure in the LDDMM framework. There, they explained the push forward and pull back of currents under deformations.
The main outcome is the relation $S(\varphi^{\#}\underline{\omega}) = \varphi(S)(\underline{\omega})$ for the push forward action. This relation states that the surface integral $S(\underline{\underline{\omega}})$ can be computed either by first deforming the ambient space with the vector field $\underline{\omega}$ and then computing the integral through the surface $S$, or deforming the surface $S$ and computing the integral of non-changed $\underline{\omega}$ through the deformed surface $\varphi S$ afterwards. The resulting surface integral $S(\underline{\omega})$ is equal in both cases.

In this work, the latter case is used. The surface is transformed with the velocity vector field $\underline{v} \in \mathcal{V}$. When the surface is represented via surface currents in $\mathcal{W}$, the currents $\delta_{\underline{q}}$ are transported as surface representers.

## 2.2. Summary

In this chapter, the mathematical foundation of the present work is laid out, starting with the introduction of the group of diffeomorphisms and the corresponding parameterization. Then reproducing kernel Hilbert spaces are presented. Having established these two fundamental concepts, the large diffeomorphic deformation metric mapping (LDDMM) framework builds on them and is detailed afterwards. The chapter concludes with an appropriate similarity measure in the LDDMM framework for surfaces in 3D space.

Based on that, in the following chapter, the contribution of this work is exhibited, adapting the LDDMM framework to be used for the anatomical region of abdominal aortic aneurysms later on.

# 3. Method and Implementation

The previous chapter 2 provided a fundamental overview of the group of diffeomorphisms transformations and the corresponding parameterizatioin with $\underline{v}$. Based on that, a non-rigid transformation framework, the (unconstrained) LDDMM framework, has been deduced to produce the associated diffeomorphic deformations.
In the current chapter, a novel modular method is developed in the LDDMM framework in two orthogonal spaces. It consists of a translation-free non-rigid registration and a rigid translational registration part - each with independent parameterizations and in orthogonal spaces. The orthogonal spaces are achieved by two orthogonal group transformations, produced by the associated orthogonal group parameterizations.

By doing so, a clear separation of rigid translational and non-rigid transformations and their parameterizations is achieved. This procedure has two main advantages:

- The matching procedure is independent of the initial relative position of source $S$ and target $T$, which resolves the initial rigid alignment question.
- The statistical analysis can be performed solely on the non-rigid component parameters which are translation-free. In general, the translational transformation does not contain shape variability information and therefore might only perturb the non-rigid information.

The separation is performed solely on the rigid translation, and not on the rigid rotation, too. Due to the anatomical arrangement in the abdominal area, the development and growth of an AAA is restricted by the neighbouring anatomical structures, mainly the spine in posterior direction. That is why the rigid rotation is characteristic and unique to a the shape of a specific AAA and should remain in the shape-descriptive non-rigid component.

This chapter begins with the presentation of a translation-free LDDMM framework, followed by the creation of a joint registration method. Then implementation techniques and experimental results are discussed.

## 3.1. Translation-free non-rigid deformation in LDDMM

The unconstrained diffeomorphic geodesic mapping in the LDDMM framework has been introduced in section 2.1. Therein, the construction of the velocity vector field $\underline{v}$ is described in a RKHS $\mathcal{V}$ determined by kernel $\underline{K}_{\mathcal{V}}$ such that it also fulfills the diffeomorphic and geodesic deformation requirements.

In the novel LDDMM framework presented here, a RKHS $\mathcal{V}^{\perp}$ is designed with corresponding velocity vector fields $\underline{v}^{\perp}$ which are free of rigid translation components. To that end, an appropriate kernel $\underline{K}_{\mathcal{V}^{\perp}}$ has to be established for the desired structure of $\mathcal{V}^{\perp}$.

The development of a translation-free $\underline{K}_{\mathcal{V}^{\perp}}$ for RKHS $\mathcal{V}^{\perp}$ is inspired by works of Arguillère et al. who extend the unconstrained RKHS $\mathcal{V}$ with possible manipulations of operator $L$ or $\underline{K}_{\mathcal{V}}$ [3]. This section begins with a short introduction of this generally formulated extension which enables the construction of the required translation-free RKHS $\mathcal{V}^{\perp}$. This section concludes with an appropriate definition of an $\underline{K}_{\mathcal{V}^{\perp}}$ for diffeomorphic translation-free non-rigid deformations.

## Motivation

In the original LDDMM framework, the deformation parameter $\underline{v}(\underline{x}(t))$ belongs to the RKHS $\mathcal{V}$ which is embedded in $C_0^p$. Therefore, the vector fields $\underline{v}$ vanish at infinity. They cannot incorporate rigid alignments even if rigid transformations exist between source $S$ and target $T$ during diffeomorphic deformation [3]. As a consequence, these existing rigid transformations are carried out under non-rigid deformation. The estimated non-rigid deformation is therefore perturbed with rigid components.

So far, a pre-alignment step is usually performed prior to diffeomorphic matching to discard these linear rigid differences between source $S$ and target $T$. Several approaches have been established to perform the rigid pre-alignment step before non-rigid registration in the LDDMM framework. These approaches usually comprise an optimization step to find the optimal configuration according to some cost function:

- Durrleman et al. pre-orient white matter fibre bundles by employing a simple empirical procedure. The procedure consists of determining the longest fibre in the cohort and connecting its extremities to define the orientation vector to which all other cohort fibres are aligned.In some cases, a manual correction is necessary [47].

- Prior to a multi-scale, multi-kernel shape matching procedure of human brain datasets, Pai et al. deploy an affine registration with 12 degrees of freedom in the pre-alignment step [138].

- Mansi et al. employ a standard least-square method [7] for rigid-body alignment in a preprocessing step before non-rigid surface registration of heart shapes [117]. The alignment of shapes is accomplished to a representative patient of the dataset. As the shape meshes are resampled, point-correspondence is guaranteed between the cohort shapes and enables the applied rigid registration method.

- A similar approach is followed by Liang et al. who also uniformly remesh the cohort shapes to first establish mesh correspondence [108]. The mesh alignment to a common coordinate system is achieved by Generalized Procrustes Analysis (GPA) [68] which is applied in an iterative manner. In a subsequent pre-processing step, a standard least-square optimization method is also deployed [181]. The following non-rigid diffeomorphic registration is for the analysis of morphometric risk features of ascending aortic aneurysms.

- Also Durrleman et al. perform a co-registration of cohort shapes by affine transformations [48]. The examined anatomical region is that of deep brain structures in context of a neuroimaging study.
- Standard iterative-closest point (ICP) procedures are also employed, like in [24] for the first stage of an iterative two-stages pre-processing. There, all input shapes are rigidly aligned to an initial reference shape. In the second stage of pre-processing, the reference shape is updated and used in the recurring first stage in the ICP method. The process is repeated until an update of reference shape is not necessary. ICP algorithms do not require point-correspondence. However, as pointed out in [95], such point-wise least-square problems are ill-posed and depend much on mesh quality and regularizing strategies. The point-wise behaviour also imposes non-realistic and non-existing spatial constraints on the rigid registration problem.

Consequently, an approach relying on the current-based similarity measure in $\mathcal{W}$ (Equation 2.1.25) is beneficial for rigid registration without point-correspondence. The cost function is formulated as

$$J_A(\underline{A}) = \|T - \underline{A} \circ S\|^2_{\mathcal{W}^*}. \tag{3.1.1}$$

The matrix $\underline{A}$ typically contains a rotation matrix and a translation vector and acts on a surface $S$ in the shape manifold $\mathcal{M}$, producing the corresponding coordinate change on $S$. The optimal rigid transformation $\underline{A}$ is then the transformation that minimizes the *distance* in the shape space $\mathcal{W}^*$. Such an implementation is generically found in [19].

However, although the above mentioned preprocessing rigid registration techniques are widely used, the quality of fit for each shape depends on the registration method and the quality of the input mesh. Consequently, some residual rigid linear differences may remain, creating a bias. The remaining rigid difference is subsequently compensated for during the non-rigid matching algorithm which results in a deformation consisting of non-rigid and rigid components.
There, the drawback lies in the fact that both components are described in the non-rigid deformation parameterization $\underline{\mu}_0$ without clear separation. As the present work mainly relies on the non-rigid deformation parameters as a shape descriptor for further statistical analysis, the unintended und irrelevant rigid components in the parameterization might influence and decrease the statistical significance.

## Challenge and solution

The anatomical structure examined in this work is the abdominal aortic aneurysm (AAA) as portrayed in the introductory chapter. The healthy and pathological shape variations are to be determined using techniques from computational anatomy, in particular the non-rigid diffeomorphic registration in the LDDMM framework.
As examined in chapter 1, the growth direction of the AAA bulge is determined by the surrounding organs. In fact, a dilation in anterior direction is more common as the spine constrains the expansion in posterior direction. The bulge direction characterizes therefore the patient-specific AAA occurrence and should be somewhat integrated in the upcoming statistical shape analysis. As the statistical shape analysis will be based on the non-rigid deformation parameters, the orientation information should be comprised in the non-rigid registration process. Consequently,

any rigid alignment of AAA shapes should only cover rigid translation in this work and the orientation should be kept.
Furthermore, any rigid alignment of AAA shapes in this work should be performed according to Equation 3.1.1 as no point-correspondence is established among the input meshes. Additionally, the current-based rigid-body optimization can be easily incorporated in the LDDMM framework. The matrix $\underline{A}$ is reduced to the translation vector $\underline{r} \in \mathbb{R}^3$ and incorporated in the registration scheme.

Still, after an initial rigid alignment, some linear differences between reference and input AAA shape can still remain. These differences should be identified and eliminated from the non-rigid diffeomorphic registration during the whole registration process.
To that end, in this section, a translation-free non-rigid geodesic diffeomorphic matching framework is introduced. This novel diffeomorphic matching method is subsequently supplemented by a separate rigid translation module in a modular framework in the next section.

The proposed translation-free deformation method is primarily built upon the general matching framework of Arguillère et al. in [4] and Younes et al. in [198]. Younes et al. introduced a generalized constrained LDDMM deformation module where mainly object-dependent constraints determine the space of possible motions at a given time. This space is built on a set of suitable basis-functions which compose Eulerian velocities in a subspace of the originally established RKHS $\mathcal{V}$. This approach is similar to finite-element methods.
In [4], Arguillère et al. reformulate the constrained LDDMM framework into a control theory formulation which helps to impose constraints on the Eulerian velocities without explicitly specifying basis-functions. Therein, the constraints are applied onto the RKHS where the Eulerian velocities for diffeomorphic evolutions exist. Additionally, based on that, inequality constraints are introduced for the first time in relation to a LDDMM framework.

In this work, the translation-free restriction is applied to the control variable $\underline{v}(\underline{x}(t))$ in a suitable RKHS as it finally parameterizes the non-rigid transformation and builds the basis for the further statistical analysis. In the proposed setting, the adjustment is not formulated as a constraint on the governing ODE in Equation 2.1.17 of the control variable $\underline{v}(\underline{x}(t))$, but is realized with the construction of a translation-free RKHS $\mathcal{V}^\perp$ where the control velocity vector field $\underline{v}^\perp(t)$ resides at every $t \in [0,1]$. In other words, the constructed space $\mathcal{V}^\perp$ is orthogonal to rigid translations: in each time step $t$, $\underline{v}^\perp$ is free of components parallel to the rigid translations with regard to the axes of a global Euclidean coordinate system. As a result, translational displacements are eliminated and $\underline{v}^\perp$ does not contain information about rigid translations.
In the same manner, also rotational rigid transformations could excluded from $\underline{v}^\perp$. However, as explained, the rotation information should be preserved in $\underline{v}^\perp$.

Before the construction of the translation-free $\mathcal{V}^\perp$ is presented, projector $\underline{P}^{\parallel}$ and its orthogonal complement $\underline{P}^\perp$, which are employed in the construction, are introduced.

### 3.1.1. Projector formulation

In Linear Algebra, a projector $\underline{P}$ is a linear mapping operator from a vector space $V$ into itself $\underline{P} : V \mapsto V$, fulfilling the projection property

$$\underline{P}^2 = \underline{P} \tag{3.1.2}$$

with $\underline{P}$ called idempotent.

In the finite-dimensional case of vector space $V = \mathbb{R}^n$, the projector $\underline{P}$ is a $n \times n$ matrix and is composed of

$$\underline{P} = \underline{B}(\underline{B}^{\mathrm{T}}\underline{B})^{-1}\underline{B}^{\mathrm{T}} \qquad \mathbb{R}^{n\times n} \tag{3.1.3}$$

with matrix $\underline{B} \in \mathbb{R}^{n\times m}$. Matrix $\underline{B}$ comprises the $m$ basis vectors $\underline{b} \in \mathbb{R}^n$ which are projected onto and builds the associated subspace $U \subseteq V$. The product $\underline{B}^{\mathrm{T}}\underline{B}$ is assumed invertible which implies that matrix $\underline{B}$ has full rank.

Projector $\underline{P}$ is also idempotent as stated with

$$\begin{aligned}\underline{P}^2 &= \left(\underline{B}(\underline{B}^{\mathrm{T}}\underline{B})^{-1}\underline{B}^{\mathrm{T}}\right) \cdot \left(\underline{B}(\underline{B}^{\mathrm{T}}\underline{B})^{-1}\underline{B}^{\mathrm{T}}\right)\\ &= \underline{B}(\underline{B}^{\mathrm{T}}\underline{B})^{-1}\cancel{\underline{B}^{\mathrm{T}}\underline{B}(\underline{B}^{\mathrm{T}}\underline{B})^{-1}}\underline{B}^{\mathrm{T}}\\ &= \underline{B}(\underline{B}^{\mathrm{T}}\underline{B})^{-1}\underline{B}^{\mathrm{T}} = \underline{P}.\end{aligned}$$

Projection matrix $\underline{P}$ with a composition as in Equation 3.1.3 is an orthogonal projector. Also, projector $\underline{P}$ is symmetric since

$$\begin{aligned}\underline{P}^{\mathrm{T}} &= \left(\underline{B}(\underline{B}^{\mathrm{T}}\underline{B})^{-1}\underline{B}^{\mathrm{T}}\right)^{\mathrm{T}}\\ &= \left(\underline{B}^{\mathrm{T}}\right)^{\mathrm{T}}\left((\underline{B}^{\mathrm{T}}\underline{B})^{-1}\right)^{\mathrm{T}}\underline{B}^{\mathrm{T}}\\ &= \underline{B}(\underline{B}^{\mathrm{T}}\underline{B})^{-1}\underline{B}^{\mathrm{T}} = \underline{P}.\end{aligned}$$

Figure 3.1.1 illustrates the projection of a vector $\underline{a} \in \mathbb{R}^n$ onto the subspace $U \subseteq V$ with

$$\underline{a}_{\|} = \underline{P}^{\|} \cdot \underline{a} \qquad \in \mathbb{R}^n.$$

The projector $\underline{P}^{\|} \in \mathbb{R}^{n\times n}$ is built according to Equation 3.1.3 with corresponding matrix $\underline{B} \in \mathbb{R}^{n\times m}$ consisting of $m$ basis vectors $\underline{b}_i \in \mathbb{R}^n$ for $i = (1, \dots, m)$ as

$$\underline{B} = [\underline{b}_1, \dots, \underline{b}_m] \qquad \mathbb{R}^{n\times m}. \tag{3.1.4}$$

The available property of orthogonality allows for the direct sum

$$V = U \oplus U_{\perp} \tag{3.1.5}$$

with the disjoint orthogonal complementary subspace $U_{\perp}$. Also, $U \cap U_{\perp} = 0$ follows. As a result, a vector $\underline{a} \in V \subseteq \mathbb{R}^n$ can be uniquely decomposed into

$$\underline{a} = \underline{a}_{\|} + \underline{a}_{\perp} \qquad \in \mathbb{R}^n, \tag{3.1.6}$$

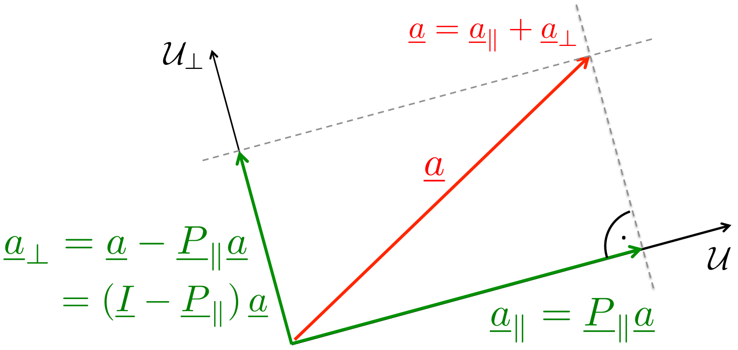

Figure 3.1.1.: Illustration of projector $\underline{P}^{\|}$ functionality on vector $\underline{a}$. The projection decomposes $\underline{a}$ in a component $\underline{a}_{\|}$ in $\mathcal{U}$ and $\underline{a}_{\perp}$ in complementary space $\underline{U}_{\perp}$, yielding $\underline{a} = \underline{a}_{\|} + \underline{a}_{\perp}$.

with $\underline{a}_{\|} \in U$ and $\underline{a}_{\perp} \in U_{\perp}$. In other words, $\underline{a}_{\|}$ is the projection of $\underline{a}$ into $U$ and $\underline{a}_{\perp}$ the respective projection of $\underline{a}$ into $U_{\perp}$ [12] with

$$
\begin{aligned}
\underline{a}_{\|} &= \underline{P}^{\|}\underline{a}, \\
\underline{a}_{\perp} &= \underline{a} - \underline{a}_{\|} \\
&= (\underline{I} - \underline{P}^{\|})\,\underline{a}.
\end{aligned}
\tag{3.1.7}
$$

The expression $\underline{I} - \underline{P}^{\|}$ projects $\underline{a}$ into the orthogonal complementary space $U_{\perp}$ and is denoted from now on with $\underline{P}^{\perp} = \underline{I} - \underline{P}^{\|}$. The projector $\underline{P}^{\perp}$ is also idempotent with

$$
\begin{aligned}
\underline{P}^{\perp 2} &= (\underline{I} - \underline{P}^{\|})^2 \\
&= \underline{I}^2 - 2 \cdot \underline{P}^{\|} + \underline{P}^{\|2} \\
&= \underline{I} - 2 \cdot \underline{P}^{\|} + \underline{P}^{\|} \\
&= \underline{I} - \underline{P}^{\|} = \underline{P}^{\perp},
\end{aligned}
$$

since $\underline{P}^{\|2} = \underline{P}^{\|}$. Also, the projector $\underline{P}^{\perp}$ is symmetric since

$$
\begin{aligned}
(\underline{P}^{\perp})^{\mathrm{T}} &= \left(\underline{I} - \underline{P}^{\|}\right)^{\mathrm{T}} \\
&= \underline{I} - \underline{P}^{\|}
\end{aligned}
\tag{3.1.8}
$$

using the symmetry of $\underline{P}^{\|}$.

So far, finite-dimensional general vector spaces, which are subspaces of $n$-dimensional Euclidean spaces $\mathbb{R}^n$, have been addressed. In the following, the projection theory is expanded to Hilbert spaces and then to RKHS.

### Projections in Hilbert spaces

The RKHS $\mathcal{V}$, which is a Hilbert space, is a vector space with a defined inner product. The inner product defines the notion of orthogonality. Two vectors $\underline{u}, \underline{w} \in \mathcal{V}$ are orthogonal or perpendicular if and only if $\langle \underline{u}, \underline{w} \rangle = 0$.
As for the finite-dimensional vector spaces, Hilbert spaces also allow for orthonormal bases. To that end, and to be able to apply the methods developed in the finite-dimensional case, the Hilbert space $\mathcal{V}$ is defined on the discretized subspace $\mathcal{X}$ and includes a countable orthonormal basis, namely a Schauder basis. Thus, the Hilbert space $\mathcal{V}$ is (topologically) separable. Therefore, the orthonormal basis consists of a linearly independent collection of vectors. The interested reader is referred to [12, 105].

Since the orthogonal projector $\underline{P}^{\|}$ is a constant function, it represents a continuous symmetric linear operator. Subsequently, a vector $\underline{v} \in \mathcal{V}$ is projected onto $\underline{P}^{\|}\underline{v} = \underline{u} \in \mathcal{U} \subseteq \mathcal{V}$. Therewith, the subspace $\mathcal{U}$ builds the image $\mathrm{Im}(\underline{P}^{\|})$ of $\underline{P}^{\|}$. In this work, $\mathcal{V}$ is closed. Therefore, $\mathcal{U}$ is also closed.
Also, the unique orthogonal complementary subspace $\mathcal{U}^{\perp}$ comprises all vectors $\underline{u}_{\perp}$ and builds therewith the kernel $\mathrm{Ker}(\underline{P}^{\|})$ of $\underline{P}^{\|}$. Thus, the orthonormal subspace $\mathcal{U}^{\perp}$ is a closed subspace of $\mathcal{V}$, too.
As a consequence, the vector $\underline{v}$ can be uniquely decomposed as $\underline{v} = \underline{u} + \underline{u}_{\perp}$ where $\underline{u} \in \mathcal{U}$ and $\underline{u}_{\perp} \in \mathcal{U}^{\perp}$. The direct sum can be formulated with $\mathcal{V} = \mathcal{U} \oplus \mathcal{U}^{\perp}$.
Projector $\underline{P}^{\perp}$ can be additionally defined to map the vector $\underline{u} \in \mathcal{U}$ directly to the orthogonal complementary subspace $\mathcal{U}^{\perp}$ with $\underline{P}^{\perp} = \underline{I} - \underline{P}^{\|}$.

In summary, according to [12], a continuous linear operator $\underline{P}$ on RKHS $\mathcal{V}$ generates an orthogonal projection to a closed linear subspace $\mathcal{U}$ of Hilbert space $\mathcal{V}$ only if it satisfies $\underline{P}^2 = \underline{P}$ and is symmetric. This can be achieved by the projector introduced in Equation 3.1.3.

### Hilbert projection theorem

The Hilbert projection theorem states the uniqueness of the projection for each $\underline{v} \in \mathcal{V}$ onto the subspace $\mathcal{U}$. Let the subspace $\mathcal{U}$ be a closed subset of $\mathcal{V}$ and let $\underline{u}$ denote the projection of $\underline{v}$ onto $\mathcal{U}$. For determining the appropriate $\underline{u}$, the error vector $\underline{v} - \underline{u}$ has to be orthogonal to the base vectors of $\mathcal{U}$. By doing so, the shortest distance of $\underline{v}$ and $\underline{u}$ is established. Only then, $\underline{u}$ is the orthogonal projection of $\underline{w}$ onto $\mathcal{U}$.

By choosing the orthogonal projector $\underline{P}^{\|}$ as in Equation 3.1.3, the structure and basis vectors of subspace $\mathcal{U}$ are determined [12].

### Projector $\underline{P}^{\perp}$ to eliminate parallel components in $\mathcal{V}$

In this section, the expanded orthogonal projection is applied to the velocity vector field $\underline{v}(\underline{x}(t))$ in RKHS $\mathcal{V}$. Still assuming a finite-dimensional description of surface $S$ with $n_x$ vertices, the velocity vector field $\underline{v}$ becomes a vector field of dimension $\mathbb{R}^{3n_x}$ (more on spatial discretization in subsection 3.3.1). The illustrated vector field $\underline{v}$ in the left in Figure 3.1.2 is such a discretized velocity vector field on $n_x$ surface vertices.

As a result of the discretization, the RKHS $\mathcal{V}$ becomes a Hilbert space of vector fields $\underline{v}(\underline{x}(t))$ on $\mathbb{R}^{3n_x}$. The associated reproducing kernel $\underline{K}_{\mathcal{V}}$ is the mapping defined by the $3n_x \times 3n_x$ matrix applied to the $n_x$ vertices of shape $S$.
Consequently, the previously deduced requirements and properties of orthogonal projections on Hilbert spaces are applied for $\underline{v} \in \mathbb{R}^{3n_x}$.

In order to eliminate rigid translations produced by integration of $\underline{v}(\underline{x}(t))$ over a time $t \in [0, 1]$, the components of $\underline{v}$ which are parallel to global Euclidean directions in 3D space should be eliminated by projection. These are denoted with $\underline{v}^{\parallel}$ and the associated closed subspace is $\mathcal{V}^{\parallel} \subseteq \mathcal{V}$.
Accordingly, the orthonormal basis vectors of subspace $\mathcal{V}^{\parallel} \subseteq \mathcal{V}$ are the global Euclidean axes in 3D. The corresponding basis matrix $\underline{B}$ consists hence of three basis vectors $\underline{b}_i \in \mathbb{R}^{3 \cdot n_x}, i = (1, \dots, 3)$. The resulting matrix $\underline{B} = [\underline{b}_1, \dots, \underline{b}_3]$ is of dimension $\mathbb{R}^{3n_x \times 3}$ and can be written as

$$\underline{B} = \begin{bmatrix} 1 & 0 & 0 \\ 0 & 1 & 0 \\ 0 & 0 & 1 \\ 1 & 0 & 0 \\ 0 & 1 & 0 \\ 0 & 0 & 1 \\ \vdots & \vdots & \vdots \end{bmatrix} \quad \in \mathbb{R}^{3n_x \times 3}. \tag{3.1.9}$$

In order to project the velocity vector field $\underline{v}(\underline{x}(t)) \in \mathcal{V}$ onto the subspace $\mathcal{V}^{\parallel} \subseteq \mathcal{V}$ with basis vectors $\underline{B}$, a projector $\underline{P}^{\parallel}$ is constructed with the established $\underline{B}$ in Equation 3.1.9 according to Equation 3.1.3.

Thus, the resulting projection $\underline{P}^{\parallel}\underline{v} = \underline{v}^{\parallel} \in \mathcal{V}^{\parallel} \subseteq \mathcal{V}$ yields the components $\underline{v}^{\parallel}$ of $\underline{v}$ which are parallel to the global Euclidean axes given in $\underline{B}$.

Now, the orthogonal complementary component $\underline{v}^{\perp} \in \mathcal{V}^{\perp}$ is the required one for the desired translation-free non-rigid deformation. To that end, the projector $\underline{P}^{\perp} = \underline{I} - \underline{P}^{\parallel}$ is applied on $\underline{v} \in \mathcal{V}$ to directly acquire $\underline{v}^{\perp} \in \mathcal{V}^{\perp} \subseteq \mathcal{V}$.
The projector $\underline{P}^{\perp}$ satisfies the properties and requirements for an orthogonal projection and allows for a unique decomposition into the two subspaces. The direct sum $\mathcal{V} = \mathcal{V}^{\parallel} \oplus \mathcal{V}^{\perp}$ and $\underline{v} = \underline{v}^{\parallel} + \underline{v}^{\perp}$ follow.

Figure 3.1.2 illustrates the achieved decomposition of the velocity vector field $\underline{v} \in \mathcal{V}$ to its components $\underline{v}^{\parallel}$ and $\underline{v}^{\perp} = \underline{P}^{\perp} \cdot \underline{v}$ after the application of projection matrix $\underline{P}^{\perp}$ onto it.

Thus, the subspace $\mathcal{V}^{\perp} \subseteq \mathcal{V}$ includes the required component $\underline{v}^{\perp}$ which is free of components parallel to the Euclidean axes in the 3D space. Consequently, when $\underline{v}^{\perp}$ is integrated over $t = [t_1, t_2]$, it does not generate rigid translational displacements.

In the next part, the projector $\underline{P}^{\perp}$ is integrated in a RKHS formulation such that the resulting

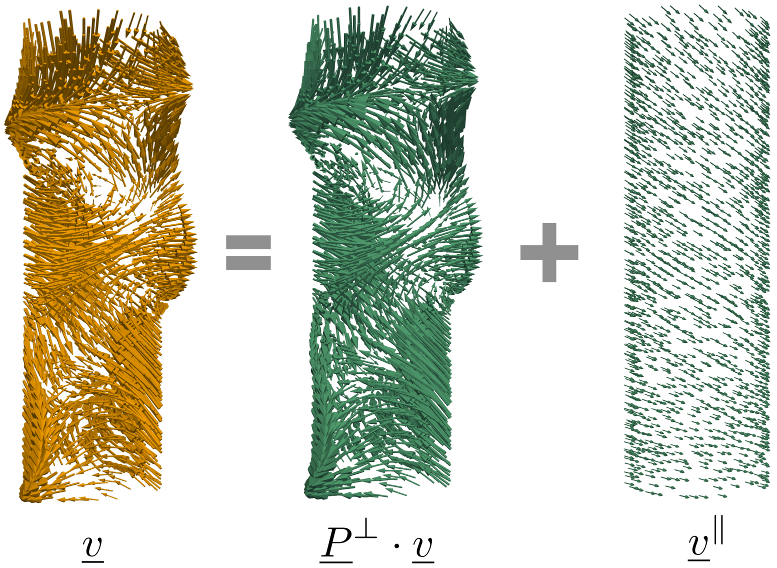

Figure 3.1.2.: Visualization of projector $\underline{P}^{\perp}$ application on a vector field $\underline{v} \in \mathcal{V}$. Projector $\underline{P}^{\perp}$ is defined with regard to the Euclidean axes. When multiplying $\underline{v}$ with $\underline{P}^{\perp}$, the parallel components to global 3D axes are extracted and eliminated, denoted with $\underline{v}^{\parallel}$. The vector field $\underline{P}^{\perp} \cdot \underline{v}$ is free of rigid translation components and equals $\underline{v}^{\perp}$.

$\underline{v}^{\perp}(t)$ over the temporal evolution in $t \in [0, 1]$ still produces diffeomorphic non-rigid deformations without rigid translations.

### 3.1.2. Construction of translation-free RKHS $\mathcal{V}^{\perp}$

In this section, a valid RKHS $\mathcal{V}^{\perp}$ with corresponding kernel $\underline{K}_{\mathcal{V}^{\perp}}$ is constructed to embed only translation-free velocity vector fields $\underline{v}^{\perp}(\underline{x}(t))$ such that $\dot{\underline{x}}(t) = \underline{P}^{\perp}\, \underline{v}(\underline{x}(t)) =: \underline{v}^{\perp}(\underline{x}(t))$. The derivation is based on the already introduced $\underline{v}$ in the unconstrained RKHS $\mathcal{V}$ and the projector $\underline{P}^{\perp}$.

#### Incorporation of the projector $\underline{P}^{\perp}$

The incorporation of the projector $\underline{P}^{\perp}$ in the original LDDMM framework relies on the extended formulation of the original LDDMM non-rigid deformation from Arguillère et al. [3]. As mentioned before, the final temporal evolution of $\underline{x}(t)$ should look somewhat like $\dot{\underline{x}}(t) = \underline{P}^{\perp}\, \underline{v}(\underline{x}(t)) =: \underline{v}^{\perp}(\underline{x}(t))$ with the new formulation $\underline{v}^{\perp} \in \mathcal{V}^{\perp}$. The challenge now lies in the proper formulation of the associated $\mathcal{V}^{\perp}$. Following the extensive derivation of the original RKHS $\mathcal{V}$ in subsection 2.1.1, a starting point is therefore the determination of kernel $\underline{K}_{\mathcal{V}^{\perp}}$.

To that end, let $\mathcal{X}$ be a subspace of $\mathcal{V}$ that the operator $\underline{P}^{\perp}$ maps to according to

$$\underline{P}^{\perp} : \mathcal{V} \rightarrow \mathcal{U}. \tag{3.1.10}$$

The form of $\mathcal{U}$ depends obviously on the structure of operator $\underline{P}^{\perp}$. As $\underline{P}^{\perp}$ produces a linear continuous mapping, the space $\mathcal{X}$ is a subset of vector space $\mathcal{V}$ with dimension $\mathbb{R}^{3n_x}$. Hence, the deformations it produces act on the same finite-dimensional shape manifold $\mathcal{M}$.
In this context, the subspace $\mathcal{X}$ is the translation-free RKHS $\mathcal{V}^{\perp}$ and builds the kernel $\mathrm{Ker}(\underline{P}^{\perp})$ of projector $\underline{P}^{\perp}$. Equation 3.1.10 can be therefore formulated directly with

$$\begin{aligned} &\underline{P}^{\perp} : \mathcal{V} \mapsto \mathcal{V}^{\perp} \\ &\underline{P}^{\perp} : \underline{v} \mapsto \underline{v}^{\perp} := \underline{P}^{\perp}\, \underline{v}. \end{aligned} \tag{3.1.11}$$

The corresponding dual spaces to Equation 3.1.11 are defined by the transpose $(\underline{P}^{\perp})^{\mathrm{T}}$ with

$$\begin{aligned} &(\underline{P}^{\perp})^{\mathrm{T}} : \mathcal{V}^{\perp *} \mapsto \mathcal{V}^{*} \\ &(\underline{P}^{\perp})^{\mathrm{T}} : \underline{\mu}^{\perp} \mapsto \underline{\mu} := (\underline{P}^{\perp})^{\mathrm{T}}\, \underline{\mu}^{\perp}. \end{aligned} \tag{3.1.12}$$

The space $\mathcal{V}^{*}$ denotes the already established dual space of the RKHS $\mathcal{V}$. Elements of $\mathcal{V}^{\perp *}$ will be denoted with $\underline{\mu}^{\perp}$. The pull back of $\underline{\mu}^{\perp} \in \mathcal{V}^{\perp *}$ to $\mathcal{V}^{*}$ is defined with Equation 3.1.12 and is achieved via the transpose $(\underline{P}^{\perp})^{\mathrm{T}}$, i.e. $(\underline{P}^{\perp})^{\mathrm{T}}\underline{\mu}^{\perp}$ lies in $\mathcal{V}^{*}$. Accordingly, the relation

$$\langle (\underline{P}^{\perp})^{\mathrm{T}}\underline{\mu}^{\perp}, \underline{v} \rangle_{\mathcal{V}} = \langle \underline{\mu}^{\perp}, \underline{P}^{\perp}\underline{v} \rangle_{\mathcal{V}^{\perp}} \tag{3.1.13}$$

between the spaces $\mathcal{V}^{\perp}$ and $\mathcal{V}$ and their dual spaces is established for every $\underline{v} \in \mathcal{V}$.

The inclusion of the kernel matrix $\underline{K}_{\mathcal{V}}$ yields

$$\langle (\underline{P}^{\perp})^{\mathrm{T}}\underline{\mu}^{\perp}, \underline{v} \rangle_{\mathcal{V}} = (\underline{K}_{\mathcal{V}}(\underline{P}^{\perp})^{\mathrm{T}}\underline{\mu}^{\perp}, \underline{v})_{\mathcal{V}}. \tag{3.1.14}$$

According to [140], the *momentum map* is realized with the mapping $(\underline{x}, \underline{\mu}^{\perp}) \in \mathcal{M} \times \mathcal{V}^{\perp *} \mapsto (\underline{P}^{\perp})^{\mathrm{T}}\underline{\mu}^{\perp} \in \mathcal{V}^{*}$.

Assuming the image $\mathrm{Im}(\underline{P}^{\perp})$ to be closed, there exists a unique $\underline{\mu}^{\perp} \in \mathcal{V}^{\perp *}$ for every $\underline{v} \in \mathcal{V}$ such that the resulting $\underline{v}(\underline{x}(t)) = \underline{K}_{\mathcal{V}}(\underline{P}^{\perp})^{\mathrm{T}}\underline{\mu}^{\perp}$ has the minimal norm over all elements $\underline{v}'(t) \in \mathcal{V}$.

Subsequently, the former unconstrained control variable $\underline{v} \in \mathcal{V}$ in Equation 2.1.9 can be replaced in a discretized fashion with

$$\underline{v}(\underline{x}(t)) = \underline{K}_{\mathcal{V}}(\underline{P}^{\perp})^{\mathrm{T}}\underline{\mu}^{\perp}(t). \tag{3.1.15}$$

The required velocity vector field $\underline{v}^{\perp} \in \mathcal{V}^{\perp}$ is thus constructed from $\underline{v}(\underline{x}(t))$ with

$$\underline{v}^{\perp} = \underline{P}^{\perp}\, \underbrace{\underline{K}_{\mathcal{V}}\, \underbrace{(\underline{P}^{\perp})^{\mathrm{T}}\, \underbrace{\underline{\mu}^{\perp}}_{\in \mathcal{V}^{\perp *}}}_{\in \mathcal{V}^{*}}}_{\in \mathcal{V}} \qquad \in \mathcal{V}^{\perp}. \tag{3.1.16}$$

Figure 3.1.3 visualizes the mappings and the associated operators. Starting with the momenta $\underline{\mu}^{\perp} \in \mathcal{V}^{*}$, the operator $(\underline{P}^{\perp})^{\mathrm{T}}$ transports it to the dual space $\mathcal{V}^{*}$ of RKHS $\mathcal{V}$ to become $\underline{\mu} \in \mathcal{V}^{*}$

$$\begin{tikzcd}
\text{dual spaces} & \mathcal{V}^* \arrow[d, "\underline{K}_{\mathcal{V}}"'] & \mathcal{V}^{\perp *} \arrow[l, "(\underline{P}^{\perp})^{\mathrm{T}}"'] \arrow[ld, "\underline{K}_{\mathcal{V}} \cdot (\underline{P}^{\perp})^{\mathrm{T}}"'] \arrow[d, "\underline{K}_{\mathcal{V}^{\perp}}"] \\
\text{RKHS} & \mathcal{V} \arrow[r, "\underline{P}^{\perp}"'] & \mathcal{V}^{\perp}
\end{tikzcd}$$

Figure 3.1.3.: Visualization of relation of spaces and the isometric mappings. The construction of an appropriate $\underline{K}_{\mathcal{V}^{\perp}}$ is displayed. The reconstruction of $\underline{K}_{\mathcal{V}^{\perp}}$ can be thus achieved with $\underline{P}^{\perp}\,\underline{K}_{\mathcal{V}}(\underline{P}^{\perp})^{\mathrm{T}}$, following the blue arrows which depict the construction steps $(\mathcal{V}^{\perp *} \rightarrow \mathcal{V} \rightarrow \mathcal{V}^{\perp})$. The grey arrows show the isometric mapping between the RKHS and its associated dual space.

according to Equation 3.1.12. This transformation allows the subsequent transformation onto $\mathcal{V}$ with $\underline{K}_{\mathcal{V}}$, which generates $\underline{v} \in \mathcal{V}$. Then, by the projection with projector $\underline{P}^{\perp}$, $\underline{v} \in \mathcal{V}$ becomes $\underline{v}^{\perp} \in \mathcal{V}^{\perp}$ according to Equation 3.1.11.

Hence, the control system $\dot{\underline{x}}(t) = \underline{P}^{\perp}\,\underline{v}(\underline{x}(t))$ in conjunction with Equation 3.1.16 yields the system

$$\dot{\underline{x}}(t) = \underline{P}^{\perp}\underline{K}_{\mathcal{V}}(\underline{P}^{\perp})^{\mathrm{T}}\underline{\mu}^{\perp}(t). \tag{3.1.17}$$

The new kernel formulation can be thus written as

$$\underline{K}_{\mathcal{V}^{\perp}} := \underline{P}^{\perp}\,\underline{K}_{\mathcal{V}}(\underline{P}^{\perp})^{\mathrm{T}} \tag{3.1.18}$$

for every $\underline{x} \in \mathcal{M}$.

The operator $\underline{K}_{\mathcal{V}^{\perp}}$ is symmetric and continuous and generates the mapping

$$\underline{K}_{\mathcal{V}^{\perp}} : \mathcal{V}^{\perp *} \rightarrow \mathcal{V}^{\perp}, \tag{3.1.19}$$

establishing the connection between the space $\mathcal{V}^{\perp}$ and its dual space $\mathcal{V}^{\perp *}$. The kernel satisfies $\langle \underline{\mu}^{\perp}, \underline{K}_{\mathcal{V}^{\perp}}\underline{\mu}^{\perp} \rangle_{\mathcal{V}^{\perp}} = \|\underline{K}_{\mathcal{V}}(\underline{P}^{\perp})^{\mathrm{T}}\underline{\mu}^{\perp}\|_{\mathcal{V}}^2$ for every $\underline{\mu}^{\perp} \in \mathcal{V}^{\perp}$.
Consequently, the kernel matrix $\underline{K}_{\mathcal{V}^{\perp}}$ can be regarded as the Green's function of the differential operator $L$ as described for the mapping in Equation 2.1.7.

The temporal evolution of $\mathcal{V}^{\perp}$ over $t \in [0,1]$ follows

$$\dot{\underline{x}}(t) = \underline{K}_{\mathcal{V}^{\perp}} \underline{\mu}^{\perp}(t) \tag{3.1.20}$$

for $t \in [0,1]$.

As the projector $\underline{P}^{\perp}$ has been proven to be symmetric in Equation 3.1.8, $(\underline{P}^{\perp})^{\mathrm{T}} = \underline{P}^{\perp}$ follows. Consequently, the kernel $\underline{K}_{\mathcal{V}^{\perp}}$ can be written with

$$\underline{K}_{\mathcal{V}^{\perp}} := \underline{P}^{\perp}\, \underline{K}_{\mathcal{V}} \underline{P}^{\perp}. \tag{3.1.21}$$

As $\underline{P}^{\perp}$ is just a constant matrix, the produced $\underline{K}_{\mathcal{V}^{\perp}}$ benefits from the smooth qualities of the original kernel $\underline{K}_{\mathcal{V}}$, thus creating a RKHS $\mathcal{V}^{\perp}$.

Summarizing, the temporal evolution of $\underline{x}(t)$ is thus formulated as

$$\dot{\underline{x}}(t) = \underline{v}^{\perp}(t) = \underline{P}^{\perp}\, \underline{v}(\underline{x}(t)) = \underline{K}_{\mathcal{V}^{\perp}} \underline{\mu}^{\perp}(t) \tag{3.1.22}$$

at every $t \in [0,1]$, with constant $\underline{P}^{\perp}$ in all configurations $\underline{x}(t), t \in [0,1]$.

### 3.1.3. Surface matching in $\mathcal{V}^{\perp}$

As the orthogonal complementary space $\mathcal{V}^{\perp}$ is a closed subspace of the original RKHS $\mathcal{V}$, the space $\mathcal{V}^{\perp}$ defines a RKHS acting on the finite-dimensional surface manifold $\mathcal{M} \subset \mathbb{R}^{3n_x}$. The associated mapping results in

$$\varphi_1^{v^{\perp}}(\underline{X}) \in \mathcal{G} : \underline{X} \mapsto \varphi_1^{v^{\perp}}(\underline{X}) \in \mathcal{M} \tag{3.1.23}$$

with the defined action of the group $\mathcal{G}$ (see Equation 2.1.4). Consequently, with the introduction of $\underline{v}^{\perp} \in \mathcal{V}^{\perp}$, the transformation produced by the diffeomorphic group action $\mathcal{G}$ does not change in nature; solely the structure of the vector field in the tangent space $\mathfrak{g}$ is changed. The characteristics of transformation $\varphi$ are preserved as defined in subsection 2.1.1. More details concerning this are discussed in the course of this section.

Accordingly, in order to produce geodesic connections of source $S$ and a target $T$ like in the original formulation of Equation 2.1.18, the surface matching problem in $\mathcal{V}^{\perp}$ minimizes the cost function

$$J^{\perp}(\underline{\mu}^{\perp}(t)) = \gamma_E \cdot \int_0^1 \langle \underline{\mu}^{\perp}(t), \underline{K}_{\mathcal{V}^{\perp}} \underline{\mu}^{\perp}(t) \rangle_{\mathcal{V}^{\perp}}\, \mathrm{d}t + \| \varphi_1^{\underline{\mu}_0^{\perp}}(S) - T \|_{\mathcal{W}^*}^2 \tag{3.1.24}$$

such that $\dot{\underline{x}}(t) = \underline{K}_{\mathcal{V}^{\perp}} \underline{\mu}^{\perp}(t) \in \mathcal{V}^{\perp}$ for $t \in [0,1]$. In this formulation, the vector field $\underline{v}_0$ is replaced by the underlying momenta vector field $\underline{\mu}_0$ as these are optimized in the minimization of $J^{\perp}$. The expression $\varphi_1^{\underline{\mu}_0^{\perp}}(S)$ is equivalent to $\varphi_1^{\underline{v}_0^{\perp}}(S)$ as the momenta vector field $\underline{\mu}_0^{\perp}$ represents $\underline{v}_0^{\perp}$ in the dual space $\mathcal{V}^{\perp *}$.

The cost function consists of an energy term and a data-fidelity term. The energy term is determined by the metric $\int_0^1 \langle \underline{\mu}^\perp(t), \underline{K}_{\mathcal{V}^\perp}\underline{\mu}^\perp(t)\rangle_{\mathcal{V}^\perp}$ in the new RKHS $\mathcal{V}^\perp$. Also here, the parameter $\gamma_E$ achieves the weighing between the data-fidelity and energy term.

To generate a temporal evolution of $\underline{\mu}^\perp(t)$ which produces a $\underline{v}^\perp(t)$ for a diffeomorphic deformation in $t \in [0,1]$, the same approach is followed as in the unconstrained case in Equation 2.1.13 and Equation 2.1.16, with the symmetric and positive semi-definite kernel matrix $\underline{K}_{\mathcal{V}^\perp}$. In this setting, the temporal evolution of $\underline{\mu}^\perp(t)$ results in

$$\dot{\underline{\mu}}^\perp(t) = -\frac{1}{2}\nabla_{\underline{x}}((\underline{\mu}^\perp)^{\mathrm{T}}(t)\underline{K}_{\mathcal{V}^\perp}\underline{\mu}^\perp(t)) \tag{3.1.25}$$

for $t \in [0,1]$ with $\underline{x}(0) = \underline{X}$ and $\underline{\mu}^\perp(0) = \underline{\mu}_0^\perp$. Hence, the group deformation $\varphi(t) \in \mathcal{G}$ presented in subsection 2.1.1 is retained.

As for all geodesic evolutions, momentum conversation also applies in $\mathcal{V}^\perp$. As a consequence, the surface matching cost function in Equation 3.1.24 becomes

$$J^\perp(\underline{\mu}_0^\perp) = \gamma_E\langle \underline{\mu}_0^\perp, \underline{K}_{\mathcal{V}^\perp}\underline{\mu}_0^\perp\rangle_{\mathcal{V}^\perp} + \|\varphi_1^{\underline{\mu}_0^\perp}(S) - T\|^2_{\mathcal{W}^*}, \tag{3.1.26}$$

denoting with $\underline{\mu}_0^\perp$ the momenta $\underline{\mu}^\perp(t_0) \in \mathcal{V}^{\perp *}$ at the initial time $t(0) = t_0$.

### Existence of solution

Obviously, there is a correspondence between the surface matching problem in the unconstrained and the translation-free case, and also between the minimizers $\underline{v}_0 \in \mathcal{V}$ and $\underline{v}_0^\perp \in \mathcal{V}^\perp$. As stated before, the application of the projector $\underline{P}^\perp$ on RKHS $\mathcal{V}$ results in the direct sum of the subspaces with $\mathcal{V} = \mathcal{V}^\parallel \oplus \mathcal{V}^\perp$. The velocity vector field $\underline{v} \in \mathcal{V}$ is given by $\underline{v}(\underline{x}(t)) = \underline{v}^\parallel(\underline{x}(t)) + \underline{v}^\perp(\underline{x}(t))$ with $\underline{v}^\parallel \in \mathcal{V}^\parallel$ and $\underline{v}^\perp \in \mathcal{V}^\perp$. From this, it follows

$$\int_0^1 \|\underline{v}^\perp(\underline{x}(t))\|_{\mathcal{V}}^2 \,\mathrm{d}t \leq \int_0^1 \|\underline{v}(\underline{x}(t))\|_{\mathcal{V}}^2 \,\mathrm{d}t.$$

Accordingly, if $\underline{v}_0^\perp$ is inserted in the original cost function $J_{\mathcal{V}}$ (see Equation 2.1.18), it follows that $J_{\mathcal{V}}(\underline{v}_0^\perp) \leq J_{\mathcal{V}}(\underline{v}_0)$ and $\inf J^\perp \leq \inf J_{\mathcal{V}}$.

As a consequence, with these established relations and with the closed $\mathcal{V}^\perp = \mathrm{Im}(\underline{P}^\perp)$, the surface matching problems defined with $J_{\mathcal{V}}$ and $J^\perp$ are equivalent in the sense that $\inf J_{\mathcal{V}} = \inf J^\perp$ over the respective constraints and setups. A one-to-one correspondence between the minimizers of both optimization problems exist:
If $\bar{\underline{v}}_0$ minimizes $J_{\mathcal{V}}$, then there exists an associated $\bar{\underline{v}}_0^\perp$ which minimizes $J^\perp$ and vice versa.

The existence of a solution to Equation 3.1.24 is thus proven as well: If a solution exists to match source $S$ to target $T$ with a geodesic path induced by $\underline{v}_0 \in \mathcal{V}$, then there is an equivalent geodesic path induced by $\underline{v}_0^\perp \in \mathcal{V}^\perp$ with the applied projection matrix $\underline{P}^\perp$. The existence of the solution to the original matching problem $J_{\mathcal{V}}$ has been proven before in [198].

Additionally, according to [198], finding the geodesic path connecting source $S$ to target $T$ with a constrained velocity vector field $\underline{v}^{\perp} \in \mathcal{V}^{\perp} \subset \mathcal{V}$ is equivalent to minimizing the energy

$$\int_0^1 \|\underline{v}(\underline{x}(t))\|_{\mathcal{V}}^2 \,\mathrm{d}t$$

which is subject to $\frac{\partial \varphi}{\partial t} = \underline{v} \circ \varphi, \underline{x}(t) = \varphi(t) \circ \underline{X}$ and the pivotal condition of $\underline{v}(t, \cdot) \in \mathcal{V}^{\perp}$.

The key requirement for a solution to exist lies in [198] as in the unconstrained LDDMM framework. This requirement also ensures that the resulting path $\varphi^{(n)}$ of $\underline{v}^{(n)}$ converges uniformly in time and space to the optimal geodesic path $\varphi$ that belongs to $\underline{v}$.
As a result, for the constrained as well as the unconstrained geodesic deformation, it is assumed that the action $\varphi \circ \underline{x}$ for all $\underline{x} \in \mathcal{M}$ is continuous in $\varphi$ which is originally derived in subsection 2.1.1. In addition, particularly in the constrained framework, $\mathcal{V}^{\perp}$ must depend continuously on $\underline{x} \in \mathcal{M}$ which implies that the projector $\underline{P}^{\perp}$ has to be continuous in $\underline{x} \in \mathcal{M}$ which is given with the constant $\underline{P}^{\perp}$.
As a consequence, the following applies

$$\begin{aligned} \varphi^{(n)}(1) \circ \underline{X} = \underline{x}(1) \quad &\rightarrow \quad \varphi(1) \circ \underline{X} = \underline{x}(1) \\ \underline{P}^{\perp}(\underline{v}^{(n)}(t), \varphi^{(n)} \circ \underline{X}) = \underline{v}^{\perp(n)}(t) \quad &\rightarrow \quad \underline{P}^{\perp}(\underline{v}(\underline{x}(t)), \varphi \circ \underline{X}) = \underline{v}^{\perp}(t). \end{aligned}$$

The last relation confirms $\underline{v}^{\perp}(t) \in \mathcal{V}^{\perp}$.

If the above assumptions are satisfied, then there exists a minimizing geodesic path between $S$ and $T$ with finite energy. If also the evaluation of the similarity term $d_{\mathcal{W}}$ with every $\underline{x}(t)$ is continuous, then a solution to Equation 3.1.24 exists.

As in the unconstrained case, the shape manifold $\mathcal{M}$ is connected. As a result, there is a geodesic path $\varphi(t)$ that connects source $S$ and $T$. This means that every configuration $\underline{x}(t)$ of source $S$ with initial parameterization $\underline{x}(0) = \underline{X}$ has to lie in the shape manifold $\mathcal{M}$ in every $t \in [0, 1]$. To that end, the velocity vector field $\underline{v}_0^{\perp}$ has to generate a transformation $\varphi(t) \in \mathcal{G}$ whose resulting flow of surface configuration $\underline{x}(t)$ lies in $\mathcal{M}$ in every $t \in [0, 1]$. Moreover, the vector field $\underline{v}_0^{\perp} \in \mathcal{V}^{\perp}$ is as smooth as $\underline{v}_0 \in \mathcal{V}$ which guarantees that the resulting $\underline{x}(t)$ from the action $\varphi_1^{v_0^{\perp}}$ on $\underline{X}$ are the shape manifold $\mathcal{M}$.
A sufficient condition is given with Chow's theorem. The theorem states that in a connected manifold any two points can be connected by a path in the manifold. As there are no boundary conditions on the shape manifold $\mathcal{M}$, any two configurations $S$ and $T$ can be connected in it.
To that end, the parameterization of the group $\mathcal{G}$ with transformations $\varphi(t)$, i.e. the tangent space on $\mathcal{M}$ in every $\underline{x}(t)$, has to contain the required velocity vector field $\underline{v}^{\perp}(t)$ such that $\underline{v}^{\perp}(t) \cdot \underline{x}(t)$ is defined and lies in $\mathcal{M}$. If this is satisfied, then the induced path $\varphi^{\underline{v}_0^{\perp}}(t)$ completely lies in $\mathcal{M}$ [13].

## 3.2. Matching framework in orthogonal spaces

As developed in the preceeding section 3.1, the non-rigid deformation is performed in the translation-free RKHS $\mathcal{V}^{\perp}$ and is parameterized with $\underline{v}^{\perp} \in \mathcal{V}^{\perp}$ or more precisely the under-

lying $\underline{\mu}^{\perp} \in \mathcal{V}^{\perp *}$. The corresponding group transformation remains $\varphi \in \mathcal{G}$, but with the non-rigid component $\underline{v}^{\perp} \in \mathcal{V}^{\perp}$ in the associated tangent space $\mathfrak{g}$.
However, the translation-free attribute only applies to the form of the deformation, and not to the actual necessary deformation of source $S$ to target $T$ which might include a rigid translational component as well. In such a case, the deformation has to be extended with a further rigid transformation module as the non-rigid deformation in $\mathcal{V}^{\perp}$ cannot perform the rigid translational module in an energetically efficient way.

For that reason, in this section, a modular matching framework is introduced that incorporates two modules:

- a rigid translational transformation module,
- a non-rigid translation-free deformation module according to the translation-free LDDMM framework in $\mathcal{V}^{\perp}$ (see section 3.1).

Due to the nature of the resulting registration setup, the parameterization of both transformations has to be realized in two orthogonal spaces: one space contains only the rigid translations, while the other space contains the non-rigid translation-free deformation parameters. The obtained transformations therefore take place in two orthogonal spaces. Thus, for this modular transformation, the modular transformation group $\mathcal{F}$ is defined and comprises an Euclidean group $\mathcal{E}$ and the group $\mathcal{G}$ of diffeomorphisms. The tangent space of transformation group $F$ is denoted with $\mathfrak{f}$. In this work, the transformation group $\mathcal{E}$ is determined with a translation velocity vector field $\underline{\tau}$ in tangent space $\mathfrak{e}$ associated to the group $\mathcal{E}$. The generated translation vector is denoted with $\underline{r}(t)$ at time $t$ and is element of the tranformation group $\mathcal{E}$.

As a result, the tangent space $\mathfrak{f}$ of the transformation group $\mathcal{F}$ combines $\mathfrak{e}$ and $\mathfrak{g}$ and produces a mapping with $\underline{\tau} \in \mathfrak{e}$ and $\underline{v}^{\perp} \in \mathfrak{g}$. Figure 3.2.1 illustrates the application of the joined transformation group $\mathcal{F}$ on the shape manifold $\mathcal{M}$ and how the orthogonal transformations act: At every point in time $t$, the final $\underline{v}^{\mathcal{F}} \in \mathfrak{f}$ in the tangent-space of a configuration $\underline{x}$ in manifold $\mathcal{M}$ is a result of two separate velocity fields in two orthogonal spaces, namely the non-rigid parameterization $\underline{v}^{\perp} \in \mathcal{V}^{\perp}$ and $\underline{\tau} \in \mathfrak{e}$ which produces the rigid translation. For a discretized source surface $S$ with $n_x$ vertices, $\underline{x}, \underline{v}, \underline{v}^{\perp}, \underline{\tau} \in \mathbb{R}^{3n_x}$ follows. The associated transformation $\varphi_{\mathcal{F}}$ consists of a rigid translation produced by the rigid transformation $\mathcal{E}$ and a non-rigid translation-free deformation of $\varphi^{\underline{v}_0^{\perp}}(t)$ at every $t \in [0,1]$. Therefore, the temporal evolution $\varphi_{\mathcal{F}}$ can be written as

$$\frac{\mathrm{d}\varphi_{\mathcal{F}}(t)}{\mathrm{d}t} = \underline{v}^{\perp}(t) + \underline{\tau}. \tag{3.2.1}$$

The associated coordinate change is obviously

$$\frac{\mathrm{d}\underline{x}(t)}{\mathrm{d}t} = \underline{v}^{\perp}(t) + \underline{\tau}. \tag{3.2.2}$$

according to derivation in Equation 2.1.5.

Several modular approaches in the LDDMM framework have been introduced in literature. Similar to this work, the goal is always to model the deformation and growth process of anatomical

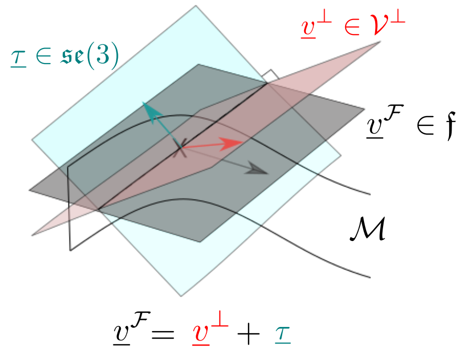

Figure 3.2.1.: An abstract representation of the modular group action in two orthogonal spaces on the shape manifold $\mathcal{M}$. The final $\underline{v}^{\mathcal{F}} \in \mathfrak{f}$ in the tangent-space (grey plane) at a configuration $\underline{x}$ of source surface $S$ in manifold $\mathcal{M}$ is a result of two separate velocity fields in two orthogonal spaces, namely the non-rigid $\underline{v}^{\perp} \in \mathcal{V}^{\perp}$ (red plane) and $\underline{\tau} \in \mathfrak{e}$ (blue) which produces the rigid translation and lies in the orthogonal plane (blue) to $\mathcal{V}^{\perp}$ (red plane). For a discretized source surface $S$ with $n_x$ vertices, $\underline{x}, \underline{v}^{\mathcal{F}}, \underline{v}^{\perp}, \underline{\tau} \in \mathbb{R}^{3n_x}$ follows.

shapes in the most accurate way, subject to constraints and external factors. There, constraints are imposed on LDDMM diffeomorphisms by constricting the deformation to be a combination of local deformation modules, thus creating together a global smooth velocity vector field $\underline{v} \in \mathcal{V}$, like in [73] with the definition of sub-Riemann metrics as [2]. Compared to the presented modular approach, the rigid module is only a rigid transport of the diffeomorphism which is completely achieved in $\mathcal{V}^{\perp}$, eliminating complicated sub-Riemann computations.

### 3.2.1. Non-rigid and rigid transformations in the orthogonal spaces

Figure 3.2.2 illustrates the interaction of both transformations during registration. Starting at $t = 0$ (state I), the vertices $\underline{X}$ are transported simultaneously by the rigid and non-rigid transformations at every $t$. The deformed configuration $\underline{x}(t)$ is subsequently achieved by the rigid translation $\underline{r}(t)$ (state II) and the non-rigid deformation $\varphi_t^{\mu_0^{\perp}}(\underline{X} + \underline{r}(t))$ (state III) which is orthogonal to the rigid transformation. The rigid translation velocity $\underline{\tau}$ is constant for every $t \in [0, 1]$ and it does not evolve from a prescribed acceleration $\dot{\underline{\tau}}(t) = 0$.

The state variable $\underline{x}(t)$ is accordingly computed using

$$\underline{x}(t) = \varphi_t^{\mu_0^{\perp}}(\underline{X}) + \underbrace{\int_0^t \underline{\tau}(t)\,\mathrm{d}t}_{:=\underline{r}(t)} \tag{3.2.3}$$

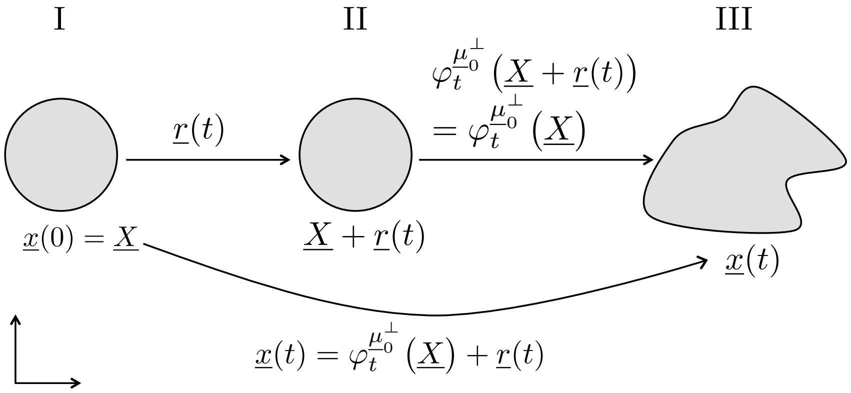

Figure 3.2.2.: Visualization of the transformation in the modular framework. Starting at time $t=0$ with $\underline{x}(0)=\underline{X}$, $\underline{\mu}^{\perp}(0)=\underline{\mu}_0^{\perp}$ and $\underline{\tau}=\underline{\tau}_0$, the rigid and non-rigid transformation take place simultaneously in two orthogonal spaces. The deformed $\underline{X}$ at time $t$ results in $\underline{x}(t)=\varphi_t^{\underline{\mu}_0^{\perp}}(\underline{X})+\underline{r}(t)$. The notations $\varphi_t^{\underline{\mu}_0^{\perp}}$ and $\varphi_t^{\underline{v}_0^{\perp}}$ are equivalent.

and its temporal evolution using

$$\frac{\partial \underline{x}(t)}{\partial t}=\underline{v}^{\perp}(t)+\underline{\tau}(t) \tag{3.2.4}$$

at every $t \in [0,1]$ with $\underline{x}(0)=\underline{X}, \underline{v}^{\perp}(0)=\underline{v}_0^{\perp}$ and $\underline{\tau}(0)=\underline{\tau}_0$.

In this general form, at each time $t$, the transformation of the state variable $\underline{x}(t)$ consists of transformations of the non-rigid translation-free LDDMM module (first term) and the rigid translational module (second term).

The structure of the RKHS $\mathcal{V}^{\perp}$ brings with it a very useful feature for the new control variables $(\underline{v}^{\perp}(t), \underline{\tau}(t))$: the parameterization of the non-rigid deformation component with $\underline{v}^{\perp}(t)$ and the parameterization of the rigid deformation component with $\underline{\tau}(t)$ do not only belong to two orthogonal spaces, but are independent of each other. This feature is owed to the structure of kernel $\underline{K}_{\mathcal{V}^{\perp}}=\underline{P}^{\perp}\,\underline{K}_{\mathcal{V}}(\underline{P}^{\perp})^{\mathrm{T}}$. Therein, the projection operators $\underline{P}^{\perp}$ and $(\underline{P}^{\perp})^{\mathrm{T}}$ are independent of any configurations $\underline{x}(t)$ and are referenced with respect to the global $x-, y-$ and $z-$ axes. Also, the kernel $\underline{K}_{\mathcal{V}}$ is independent of rigid transformations of the underlying structure. This is guaranteed by the radial Gaussian kernel function $k_{\mathcal{V}}(\underline{x}, \underline{y})=\exp(-\frac{\|\underline{x}-\underline{y}\|^2}{\sigma_{\mathcal{V}}^2})$ in $\underline{K}_{\mathcal{V}}$ which is invariant to Euclidean rigid transformations.

In this context, the Euclidean transformations act as isometries on $\mathcal{V}^{\perp}$: The velocity $\underline{v}^{\perp}(t)$ is independent of the translational transformation as $\hat{\underline{v}} := \underline{v}^\perp(\underline{x} + \Delta\underline{x})$ also belongs to the same RKHS $\mathcal{V}^\perp$ as $\underline{v}^\perp(\underline{x})$. This is due to the rigid invariance of metric kernel $\underline{K}_{\mathcal{V}^\perp}$. Consequently, the same norm $\|\hat{\underline{v}}\|^2_{\mathcal{V}^\perp} = \|\underline{v}^\perp\|^2_{\mathcal{V}^\perp}$ is generated by $\hat{\underline{v}}$ at every $t \in [0, 1]$.

Consequently, the non-rigid deformation $\varphi_t^{\underline{\mu}_0^\perp}(\underline{X})$ is independent of the rigid translation $\underline{r}(t)$, yielding two independent group actions. Starting with the diffeomorphic transformation in Equation 2.1.2, the aforementioned isometry with regard to rigid transformations can be proven by

$$\begin{aligned}
\varphi_t^{\underline{\mu}_0^\perp}(\underline{X} + \underline{r}(t)) &= \int_0^t \underline{v}^\perp(\underline{X} + \underline{r}(t))\,\mathrm{d}t + \underline{X} + \underline{r}(t) \\
&= \underbrace{\int_0^t \langle \underline{K}_{\mathcal{V}^\perp}\underline{\mu}^\perp, \underline{\mu}^\perp\rangle_{\mathcal{V}^\perp}\,\mathrm{d}t + \underline{X}}_{\varphi_t^{\underline{\mu}_0^\perp}(\underline{X})} + \underline{r}(t) \\
&= \varphi_t^{\underline{\mu}_0^\perp}(\underline{X}) + \underline{r}(t).
\end{aligned} \tag{3.2.5}$$

Equation 3.2.5 simply integrates Equation 2.1.2. The proof is only achieved with the isometric property of the Gaussian kernel in $\underline{K}_{\mathcal{V}^\perp}$.

### 3.2.2. Surface matching in the orthogonal spaces

To realize the presented modular transformation in the two orthogonal groups, the cost function takes the form

$$\begin{aligned}
J(\underline{v}^{\mathcal{F}}) &= \gamma_E \cdot \|\underline{v}^{\mathcal{F}}\|^2 + \|\varphi_1^{\underline{v}^{\mathcal{F}}}(S) - T\|^2_{\mathcal{W}^*} \\
&= \gamma_E \cdot E_{\varphi_{\mathcal{F}}} + d_{\mathcal{W}}.
\end{aligned} \tag{3.2.6}$$

The velocity vector field $\underline{v}^{\mathcal{F}}$ comprises the non-rigid transformation parameter $\underline{v}_0^\perp$ and the translation velocity vector field $\underline{\tau}$. The term $\|\underline{v}^{\mathcal{F}}\|^2$ ensures the geodesic property and decomposes into $\|\underline{v}_0^\perp\|^2_{\mathcal{V}^\perp}$ and $\|\underline{\tau}\|_2^2$. As the rigid translation vector $\underline{\tau}$ is constant in $t \in [0, 1]$ and no bounding is necessary, the energy term of $\underline{\tau}$ is omitted. For the regularization of the non-rigid transformation and the guarantee of a geodesic mapping, the path energy $\|\underline{v}_0^\perp\|^2_{\mathcal{V}^\perp}$ is kept. Hence, only the similarity term (latter term) depends on the rigid velocity vector $\underline{\tau}(t)$.
The cost function for the matching becomes then

$$\begin{aligned}
J(\underline{\mu}_0^\perp, \underline{\tau}) &= \gamma_E \cdot \|\underline{\mu}_0^\perp\|^2_{\mathcal{V}^{\perp *}} + \|\varphi_1^{\underline{v}^{\mathcal{F}}}(S) - T\|^2_{\mathcal{W}^*} \\
&= \gamma_E \cdot E_{\mathcal{V}^\perp} + d_{\mathcal{W}}
\end{aligned} \tag{3.2.7}$$

with regard to

$$\begin{aligned}
\frac{\mathrm{d}\underline{\mu}^\perp(t)}{\mathrm{d}t} &= -\frac{1}{2}\nabla_{\underline{x}}((\underline{\mu}^\perp)^{\mathrm{T}}(t)\underline{K}_{\mathcal{V}^\perp}\underline{\mu}^\perp(t)) := \underline{F}(\underline{\mu}(t)) \qquad \in \mathbb{R}^{3n_x}, \\
\frac{\mathrm{d}\underline{x}(t)}{\mathrm{d}t} &= \underline{v}^\perp(t) + \underline{\tau}(t) := \underline{G}(\underline{\mu}(t), \underline{x}(t)) + \underline{\tau}(t) \qquad \in \mathbb{R}^{3n_x}.
\end{aligned} \tag{3.2.8}$$

according to Equation 3.1.25 and Equation 3.2.4. The cost function $J$ is minimized with regard to the control variables $\underline{\mu}_0^\perp$ and $\underline{\tau}(t) = \text{const.}$ for $t \in [0, 1]$. The initial momenta vector field $\underline{\mu}_0^\perp$ is minimized for the optimal $\underline{v}_0^\perp$. The notation $\varphi_1^{\underline{v}^{\mathcal{F}}}(S)$ represents the transformed source surface $S$ at final time step $t = 1$ and is achieved with transformations $\varphi_1^{\underline{\mu}_0^\perp}(\underline{X}) + \underline{\tau}(1)$. The parameter $\gamma_E$ represents the weighing factor.

The introduced form of the cost function $J(\underline{\mu}_0^\perp, \underline{\tau})$ creates rigid and non-rigid transformation paths of specific behaviour:

- The non-rigid deformation in $\mathcal{V}^\perp$ is totally determined by the initial momenta vector $\underline{\mu}_0^\perp$ at time $t_0$. The temporal course of the non-rigid deformation follows the ODE of Equation 3.1.22 which guarantees a geodesic path from $S$ to $T$ in RKHS $\mathcal{V}^\perp$. A complete geodesic shooting is obtained by including the translation vector $\underline{\tau}$ as in Equation 3.2.4. Only by doing so, can the correct final $\underline{v}^{\mathcal{F}}$ be built (see Figure 3.2.1).
- The rigid translational transformation is performed with one straight line starting at $\underline{X}$ at $t = 0$ and ending at $t = 1$.
- The temporal evolution of the non-rigid deformation and the rigid transformation are followed independently as this does not involve energy minimization in each time step $t$. That is also why the rigid transformation results in one straight line connecting $S$ to $T$.
- However, there is still an indirect connection between the optimal initial momenta $\underline{\mu}_0^\perp$ and the optimal $\underline{\tau}$: The optimal $\underline{\tau}$ is determined such that the similarity measure with the resulting non-rigid deformation $\varphi_1^{\underline{\mu}^\perp}$ at time $t = 1$ is minimized. As a result, from an energy efficiency standpoint, the necessary translational rigid transformation along the non-rigid path in $t \in [0, 1]$ is comprised in the optimal $\underline{\tau}$.

### Existence of solution

The minimization problem in Equation 3.2.7 of the modular framework estimates the optimal variables $\underline{\tau}$ and $\underline{\mu}_0^\perp$ to register the source $S$ to the target $T$. As the RKHS $\mathcal{V}^\perp$ is invariant to affine alignment, the properties of the RKHS and the existence of its solution are preserved. The added translational velocity $\underline{\tau}$ only affects the dissimilarity term $d_{\mathcal{W}}$ in Equation 3.2.7. Consequently, the energy term is not affected and the optimal translational velocity $\underline{\tau}$ is determined only by the dissimilarity term, independently from the optimal non-rigid transformation parameterized with $\underline{\mu}_0^\perp$.

### Gradient in the control variables

The cost function in Equation 3.2.7 is evaluated at the last time step $t = 1$. However, the optimization variables $\underline{\mu}_0^\perp$ and $\underline{\tau}$ of non-rigid and rigid module exist at the initial time step $t = 0$. In [32, 43, 48, 188], approaches are introduced to tackle similar registration problems. Therein, the gradient is evaluated at $t = 1$ and transported to $t = 0$ where it is deployed to update the optimization variables according to the chosen gradient method. The transport is achieved with backward integration in time of the spatially discretized ODEs.

To that end, a variational approach is followed. A perturbation of the initial value $\underline{\mu}_0^\perp$ denoted as $\delta\underline{\mu}_0^\perp$ results in a perturbation of time evolution of momenta $\underline{\mu}^\perp(t)$ and source vertices $\underline{x}(t)$. The resulting perturbations denoted with $\delta\underline{\mu}^\perp(t)$ and $\delta\underline{x}(t)$ generate a perturbation $\delta J$ of the cost function $J$ of Equation 3.2.7 so that

$$\delta J = \big(\nabla_{\underline{x}(1)} d_{\mathcal{W}}\big)^{\mathrm{T}} \delta\underline{x}(1) + \gamma_E \cdot \big(\nabla_{\underline{\mu}_0^\perp} E_{\mathcal{V}^\perp}\big)^{\mathrm{T}} \delta\underline{\mu}_0. \tag{3.2.9}$$

The associated perturbed linearized ODE in Equation 3.2.8 is written as:

$$\begin{aligned} \delta\dot{\underline{\mu}}^\perp(t) &= \mathrm{d}_{\underline{\mu}^\perp(t)}\underline{F}\delta\underline{\mu}^\perp(t) & \delta\underline{\mu}^\perp(0) &= \underline{\mu}_0^\perp \\ \delta\dot{\underline{x}}(t) &= \partial_1\underline{G}\delta\underline{x}(t) + \partial_2\underline{G}\delta\underline{\mu}^\perp(t) & \delta\underline{x}(0) &= \underline{0}. \end{aligned} \tag{3.2.10}$$

As the source vertices $\underline{x}(0) = \underline{X}$ are not to be optimized in this registration procedure, the corresponding perturbation is simply $\underline{0}$.
Additionally, in $\delta\dot{\underline{x}}(t)$, as the translational component $\underline{\tau}$ depends neither on $\underline{x}(t)$ nor on $\underline{\mu}^\perp(t)$, it does not appear in the perturbed ODE of $\underline{x}(t)$ and is not influenced by the perturbation of $\underline{\mu}_0^\perp$.

The solutions of the perturbed ODE are respectively

$$\begin{aligned} \delta\underline{\mu}^\perp(t) &= \exp\Big(\int_0^t \mathrm{d}_{\underline{\mu}^\perp(s)}\underline{F}\,ds\Big)\delta\underline{\mu}_0^\perp \\ \delta\underline{x}(t) &= \int_0^t \exp\Big(\int_s^t \partial_1\underline{G}(s)ds\Big)\partial_2\underline{G}(s)\delta\underline{\mu}^\perp(s)\,ds. \end{aligned} \tag{3.2.11}$$

Substituting $\delta\underline{\mu}^\perp(t)$ in $\delta\underline{x}(t)$ delivers

$$\delta\underline{x}(t) = \int_0^t \underbrace{\exp\Big(\int_n^t \partial_1\underline{G}(s)\,ds\Big)}_{\underline{V}_{nt}}\,\partial_2\underline{G}(n)\cdot\underbrace{\exp\Big(\int_0^n \mathrm{d}_{\underline{\mu}^\perp(n)}\underline{F}dn\Big)}_{\underline{R}_{0n}}\,\delta\underline{\mu}_0 dn \tag{3.2.12}$$

which then respectively replaces $\delta\underline{x}(1)$ in Equation 3.2.9 with $t = 1$. The resulting gradient with regard to $\underline{\mu}_0^\perp$ is thus

$$\nabla_{\underline{\mu}_0^\perp} J = \int_0^1 \big(\underline{R}_{0t}^{\mathrm{T}}\,\partial_2\underline{G}(\underline{x}(t),\underline{\mu}^\perp(t))^{\mathrm{T}}\,\underline{V}_{t1}^{\mathrm{T}}\nabla_{\underline{x}(1)}d_{\mathcal{W}}\big)\,\mathrm{d}t + \gamma_E\cdot\nabla_{\underline{\mu}_0^\perp}E_{\mathcal{V}^\perp} \tag{3.2.13}$$

with

$$\begin{aligned} \underline{R}_{0t} &= \exp\Big(\int_0^t \mathrm{d}_{\underline{\mu}^\perp(s)}\underline{F}\,ds\Big), \\ \underline{V}_{t1} &= \exp\Big(\int_t^1 \partial_1\underline{G}(\underline{x}(s),\underline{\mu}^\perp(s))\,ds\Big). \end{aligned}$$

With the introduction of two further auxiliary variables $\underline{g}(t)$ and $\underline{p}(t)$ as

$$\begin{aligned} \underline{g}(t) &= \partial_2\underline{G}(t)^{\mathrm{T}}\big(\underline{V}_{t1}^{\mathrm{T}}\nabla_{\underline{x}(1)}d_{\mathcal{W}}\big), \\ \underline{p}(t) &= \int_t^1 \underline{R}_{ts}^{\mathrm{T}}\,\underline{g}(s)\,ds \end{aligned}$$

the gradient Equation 3.2.13 can be formulated accordingly as

$$\begin{aligned}\nabla_{\underline{\mu}_0^\perp} J &= \int_0^1 \underline{R}_{0s}^{\mathrm{T}} \underline{g}(s)\, ds + \gamma_E \cdot \nabla_{\underline{\mu}_0^\perp} E_{\mathcal{V}^\perp} \\ &= \underline{p}(0) + \gamma_E \cdot \nabla_{\underline{\mu}_0^\perp} E_{\mathcal{V}^\perp}.\end{aligned} \tag{3.2.14}$$

Starting from this form and applying some reformulations given in [48], the auxiliary variable $\underline{p}(t)$ becomes the time-dependent gradient of optimization variable $\underline{\mu}_0$. Its temporal evolution has been derived to fulfill

$$\dot{\underline{p}}(t) = -\underline{g}(t) - \mathrm{d}_{\underline{\mu}^\perp(t)} \underline{F}^{\mathrm{T}} \underline{p}(t) \qquad\qquad \underline{p}(1) = \underline{0}. \tag{3.2.15}$$

As a result, for the gradient computation $\nabla_{\underline{\mu}_0^\perp} J$, starting with $\underline{p}(1) = \underline{0}$, a backward integration in time takes place with Equation 3.2.15 to deliver $\underline{p}(0)$ which is used in Equation 3.2.14. The initial condition $\underline{\mu}_0^\perp$ is accordingly updated in $t = 0$.

The second term of Equation 3.2.14 is the partial derivative $\frac{\partial E_{\mathcal{V}^\perp}}{\partial \underline{\mu}_0^\perp}$ which is straightforward, and results in

$$\nabla_{\underline{\mu}_0^\perp} E_{\mathcal{V}^\perp} = 2 \cdot \underline{K}_{\mathcal{V}^\perp} \underline{\mu}_0^\perp.$$

Regarding the rigid module, only the similarity term $d_{\mathcal{W}}$ depends on $\underline{\tau}$ as the energy term $E_{\mathcal{V}^\perp}$ only depends on $\underline{v}^\perp$ which is invariant to rigid transformations, resulting in

$$\frac{\partial J}{\partial \underline{\tau}} = \frac{\partial d_{\mathcal{W}}}{\partial \underline{\tau}} + \cancelto{0}{\frac{\partial E_{\mathcal{V}^\perp}}{\partial \underline{\tau}}}.$$

Also in the rigid module, the gradient with regard to $\underline{\tau}$ is evaluated at the last time step $t = 1$. As the velocity vector is constant over $t \in [0, 1]$, the associated displacement at $t = 1$ is $\underline{r}(1) = 1s \cdot \underline{\tau}$. Subsequently, at $t = 1$, the final configuration is $\underline{x}(1) = \varphi_1^{\underline{v}_0}(\underline{X}) + \underline{r}(1)$, as described in Equation 3.2.3. As a result, the term $\frac{\partial d_{\mathcal{W}}}{\partial \underline{\tau}}$ is computed as

$$\frac{\partial d_{\mathcal{W}}}{\partial \underline{\tau}} = \frac{\partial d_{\mathcal{W}}}{\partial \underline{x}(1)} \cdot \cancelto{1}{\frac{\partial \underline{x}(1)}{\partial \underline{r}(1)}} \cdot \cancelto{1}{\frac{\partial \underline{r}(1)}{\partial \underline{\tau}}}. \tag{3.2.16}$$

The remaining term $\frac{\partial d_{\mathcal{W}}}{\partial \underline{x}(1)}$ is calculated by incorporating the original formulation for $d_{\mathcal{W}}$ from Equation 2.1.25 and building the gradient of every term with regard to a $\underline{q}(1)$.

### Solving the minimization problem

In summary, the gradients w.r.t. the optimization variables $\underline{\tau}$ of the rigid module and $\underline{\mu}_0^\perp$ of the non-rigid module are computed independently and simultaneously at the last time step $t = 1$ and transported back to the initial time step $t = 0$ where the optimization variables exist.

To update the optimization variables, a Limited-memory Broyden-Fletcher-Goldfarb-Shanno (L-BFGS) optmization algorithm is employed. This algorithm is a modified line search steepest descent method and enhances the simple steepest gradient descent method for unconstrained non-linear minimization problems. More details on the minimization algorithm can be found in [23].

## 3.3. Implementation

The modular matching framework has been incorporated in the open-source software Deformetrica 4 [19]. Deformetrica is primarily developed in the context of computational anatomy and supports statistical shape analysis of anatomical 2D fibres or 3D volumes. The supported statistical shape analysis is based on a registration of a reference geometry to every shape in the examined cohort in a LDDMM framework.
To that end, Deformetrica provides an object-oriented skeleton in Python [186] with different registration options, kernel choices and computational settings and algorithms with computationally efficient modules and libraries.
In Deformetrica's current implementation, non-rigid registrations take place in the LDDMM framework with unconstrained diffeomorphic geodesic paths. The modular registration method presented in this work has been added as a further registration module to Deformetrica software.

In this section, a more detailed description of Deformetrica is given, along with the integration of the presented modular matching framework.
Before that, the numerical setup of the modular matching framework and the corresponding optimization algorithms and gradients are displayed. The section concludes with some exemplary results which serve as validation of the novel method.

### 3.3.1. Numerical presentation of modular transformation

The dynamical *control* system of the presented modular transformation framework is determined by the temporal evolution of the control variable $\underline{v}^{\perp}(t) \in \mathcal{V}^{\perp}$ (or more precise $\underline{\mu}^{\perp}(t) \in \mathcal{V}^{\perp *}$) and $\underline{\tau}(t) \in \mathbb{R}^{3n_x}$. The resulting temporal evolution of the state variable $\underline{x}(t) \in \mathcal{M}$ is given by the initial conditions $\underline{X}$, $\underline{\mu}_0^{\perp}$ and $\underline{\tau}$ to realize with the ODE in Equation 3.2.8 the diffeomorphic mapping.

In the following, the spatial and temporal discretizations of the implemented diffeomorphic mapping are presented, followed by the numerical solution of the registration problem.

#### Spatial discretization

The spatial discretization is relevant for different areas in the modular transformation framework. The first area concerns the computational representation of source $S$ and target $T$ with a triangular mesh and the associated representation with surface currents in the similarity measure $d_{\mathcal{W}}$. To that end, the integral $S(\underline{\omega})$ in Equation 2.1.19 is approximated by the sum

$$S(\underline{\omega}) \approx \sum_{i=1}^{n_f} (\underline{n}_i)^{\mathrm{T}} k_{\mathcal{W}}(\underline{c}_i, \underline{c}_k) \underline{n}_k$$

with $n_f$ the number of faces of the triangular $S$ in 3D space, the center $\underline{c}_i \in \mathbb{R}^3$ and normal vector $\underline{n}_i \in \mathbb{R}^3$ of each mesh triangle.

Accordingly, the inner product of two surfaces $S_1$ and $S_2$ in $\mathcal{W}^*$ can be derived as

$$< S_1, S_2 >_{\mathcal{W}^*} \approx \sum_{i=1}^{n_f^1} \sum_{k=1}^{n_f^2} (\underline{n}_i^1)^{\mathrm{T}} k_{\mathcal{W}}(\underline{c}_i^1, \underline{c}_k^2) \underline{n}_k^2 \tag{3.3.1}$$

with $k_{\mathcal{W}}$ being the scalar kernel function with kernel width $\sigma_{\mathcal{W}}$. With the spatial discretization, the flux of $\underline{\omega}$ through a face $i$ is bundled through the center point $\underline{c}_i$ of face $i$ along the associated normal $\underline{n}_i$.

The mesh size plays thus an important role in the accuracy of the probing vector field and its ability to assess dissimilarities. The accuracy is furthermore determined by the kernel width $\sigma_{\mathcal{W}}$ of Gaussian kernel $k_{\mathcal{W}}$. Consequently, the mesh size and the kernel width $\sigma_{\mathcal{W}}$ have to be adjusted with regard to one another. There is no golden rule for the appropriate relation. However, $\sigma_{\mathcal{W}}$ should be bigger than the mesh size.
The chosen mesh length is $\approx 1.5\mathrm{mm}$. An accurate similarity measure does not necessitate a fine mesh; a coarse mesh is sufficient. The accuracy depends more on the chosen $\sigma_{\mathcal{W}}$. Later in this section, a parameter analysis is performed to analyse the dependence of similarity measure on $\sigma_{\mathcal{W}}$.
The computation of center point $\underline{c}_i$ and normal vector $\underline{n}_i$ of a mesh face $i$ follows:

$$\begin{aligned} \underline{c}_i &= \frac{1}{3}(\underline{q}_i^1 + \underline{q}_i^2 + \underline{q}_i^3), \\ \underline{n}_i &= \frac{1}{2}(\underline{q}_i^2 - \underline{q}_i^1) \times (\underline{q}_i^3 - \underline{q}_i^1). \end{aligned} \tag{3.3.2}$$

The vertices $\underline{q}_i^1, \underline{q}_i^2, \underline{q}_i^3$ represent the vertices of a mesh $i$.

The second area relevant to the spatial discretization is the computational representation of the control variable $\underline{v}^{\perp}(t) \in \mathcal{V}^{\perp}$. In this work, the velocity vector field $\underline{v}^{\perp}(t)$ is defined on the vertices $\underline{x}(t)$ of the triangular mesh of 3D source surface $S$ as already introduced in subsection 3.1.2 with $\underline{\mu}^{\perp} \in \mathcal{V}^{\perp *}$. This spatial discretization facilitates the realization of the translation-free LDDMM with RKHS $\mathcal{V}^{\perp}$ in Equation 3.1.22 with kernel $\underline{K}_{\mathcal{V}^{\perp}}$ in Equation 3.1.18

$$\underline{v}_q^{\perp}(\underline{q}(t)) = \sum_{k=1}^{n_x} k_{\mathcal{V}^{\perp}}(\underline{q}, \underline{q}_k(t)) \underline{\mu}_{q,k}^{\perp}(t) \qquad \in \mathbb{R}^3. \tag{3.3.3}$$

Herein, $n_x$ denotes the number of mesh vertices where the momenta vectors $\underline{\mu}_q^{\perp} \in \mathcal{V}^{\perp *}$ reside and $k_{\mathcal{V}^{\perp}}$ represents the kernel function associated to $\underline{K}_{\mathcal{V}^{\perp}}$, incorporating the projector $\underline{P}^{\perp}$.
The velocity vector field $\underline{v}^{\perp} \in \mathbb{R}^{3n_x}$ containing all velocity vectors Equation 3.3.3 is summarized by

$$\underline{v}^{\perp}(\underline{x}(t)) = \underline{K}_{\mathcal{V}^{\perp}} \cdot \underline{\mu}^{\perp}(t) \qquad \text{with } \underline{v}^{\perp}, \underline{x}, \underline{\mu}^{\perp} \in \mathbb{R}^{3n_x}, \underline{K}_{\mathcal{V}^{\perp}} \in \mathbb{R}^{3n_x \times 3n_x}, \tag{3.3.4}$$

compare to Equation 2.1.9.

Because the initial velocity vector field $\underline{v}_0^\perp$ is defined on the control points $\underline{X}$ of the triangular mesh, the mesh length is relevant for the choice of an appropriate $\sigma_{\mathcal{V}^\perp}$. Again, there is no golden rule for the best relation between mesh length and $\sigma_{\mathcal{V}^\perp}$. However, $\sigma_{\mathcal{V}^\perp}$ should be bigger than the mesh length $\ell$.

Moreover, there is also no formula for an appropriate relation between the kernel widths $\sigma_{\mathcal{W}}$ and $\sigma_{\mathcal{V}^\perp}$. Results have nonetheless shown that $\sigma_{\mathcal{V}^\perp}$ should be equal to or smaller than $\sigma_{\mathcal{W}}$: With $\sigma_{\mathcal{W}}$ the similarity is measured and guides the optimization to find an appropriate $\underline{v}_0^\perp$ to minimize the dissimilarity. In order to achieve this, the non-rigid deformation should be *elastic* enough to produce the necessary deformation. The elasticity is determined with $\sigma_{\mathcal{V}^\perp}$. In [48], a good estimate is $\sigma_{\mathcal{V}^\perp} = \frac{1}{2}\sigma_{\mathcal{W}}$. In the present work, a relation of $\sigma_{\mathcal{V}^\perp} = \sigma_{\mathcal{W}}$ has been found to be suitable for the examined surface shapes.

### Temporal discretization

The modular transformation of non-rigid and rigid transformations is performed in a pseudo-time interval $t \in [0, 1]$. Depending on the fixed number of time steps $N_t$, a time step $\Delta t$ is computed with

$$\Delta t = \frac{1}{N_t} s.$$

With the previously detailed spatial discretization, the ODEs of the dynamical system result in

$$\begin{aligned} \frac{\partial \underline{x}(t)}{\partial t} &= \underbrace{\underline{K}_{\mathcal{V}^\perp} \underline{\mu}^\perp(t)}_{=\underline{v}^\perp(t)} + \underline{\tau} & \qquad \underline{x}(0) &= \underline{X} \\ \frac{\partial \underline{\mu}^\perp(\underline{x}, t)}{\partial t} &= -\nabla_{\underline{x}} \underline{K}_{\mathcal{V}^\perp} \underline{\mu}^\perp(t)^{\mathrm{T}} \underline{\mu}^\perp(t) & \qquad \underline{\mu}^\perp(0) &= \underline{\mu}_0^\perp \end{aligned}$$

for $t \in [0, 1]$ and with $\underline{v}^\perp, \underline{x}, \underline{\mu}^\perp \in \mathbb{R}^{3n_x}$ and $\underline{K}_{\mathcal{V}^\perp} \in \mathbb{R}^{3n_x \times 3n_x}$. The first ODE describes the temporal evolution of the state variable $\underline{x}(t)$ which represents the path of the vertices of a triangular mesh of source $S$ during the registration. The control variable $\underline{v}(\underline{x}(t))$ is also time-dependent and is computed from the momenta $\underline{\mu}^\perp(t)$ whose temporal change is given above in the second ODE.

The numerical integration of the presented ODEs of the system is addressed in the following. The solution of $\underline{x}_{k+1}$ and $\underline{\mu}_{k+1}^\perp$ at time step $k + 1$ is linked and approximated with the explicit single mid-point second order Runge-Kutta method. The mid-points are computed according to

$$\begin{aligned} \underline{x}_{\mathrm{mid}} &:= \underline{x}_k + \frac{\Delta t}{2} \underline{K}_{\mathcal{V}^\perp}(\underline{x}_k, \underline{x}_k) \underline{\mu}^\perp + \frac{\Delta t}{2} \underline{\tau} \\ \underline{\mu}_{\mathrm{mid}}^\perp &:= \underline{\mu}_k^\perp - \frac{\Delta t}{2} \nabla_{\underline{x}} \underline{K}_{\mathcal{V}^\perp}(\underline{x}_k, \underline{x}_k) \underline{\mu}_k^\perp. \end{aligned}$$

The term $\frac{\Delta t}{2}\underline{\tau}$ in $\underline{x}_{\mathrm{mid}}$ can be *left out* as the further steps with kernel $\underline{K}_{\mathcal{V}^\perp}$ and its Jacobian $\nabla \underline{K}_{\mathcal{V}^\perp}$ are isometric with regard to rigid transformations. Accordingly, $\underline{\mu}_{\mathrm{mid}}^\perp$ is used to explicitly compute the control variable $\underline{\mu}_{k+1}^\perp$ at time step $k + 1$ with

$$\underline{\mu}_{k+1}^\perp = \underline{\mu}_k^\perp - \Delta t \nabla_{\underline{x}} \underline{K}_{\mathcal{V}^\perp}(\underline{x}_{\mathrm{mid}}, \underline{x}_{\mathrm{mid}}) \underline{\mu}_{\mathrm{mid}}^\perp$$

which generates the non-rigid transformation velocity field

$$\underline{v}_{k+1}^{\perp} = \underline{K}_{\mathcal{V}^{\perp}}(\underline{x}_{\mathrm{mid}}, \underline{x}_{\mathrm{mid}})\underline{\mu}_{k+1}^{\perp}. \tag{3.3.5}$$

On that basis, incorporating the translational displacement with $\underline{\tau}$, the state variable $\underline{x}_{k+1}$ is

$$\underline{x}_{k+1} = \underline{x}_k + \Delta t\, \underline{v}_{k+1}^{\perp} + \Delta t\, \underline{\tau}. \tag{3.3.6}$$

With the given initial conditions $\underline{X}$ and $\underline{\mu}_0^{\perp}$, the integration according to Equation 3.3.6 produces a geodesic path transporting $\underline{X}$ to the end state $\underline{x}(t = 1)$.

## 3.3.2. Numerical solution to the minimization problem

The discretized cost function $J$ (Equation 3.2.7) can be thus formulated as

$$\begin{aligned} J(\underline{\mu}_0^{\perp}, \underline{\tau}) = & \sum_{i=1}^{n_f^S}\sum_{k=1}^{n_f^S} (\underline{n}_i^S[1])^{\mathrm{T}} k_{\mathcal{W}}(\underline{c}_i^S[1], \underline{c}_k^S[1])\underline{n}_k^S[1] + \sum_{i=1}^{n_f^T}\sum_{k=1}^{n_f^T} (\underline{n}_i^T)^{\mathrm{T}} k_{\mathcal{W}}(\underline{c}_i^T, \underline{c}_k^T)\underline{n}_k^T \\ & - 2 \cdot \sum_{i=1}^{n_f^S}\sum_{k=1}^{n_f^T} (\underline{n}_i^S[1])^{\mathrm{T}} k_{\mathcal{W}}(\underline{c}_i^S[1], \underline{c}_k^T)\underline{n}_k^T + \gamma_E \cdot (\underline{\mu}_0^{\perp})^{\mathrm{T}} \underline{K}_{\mathcal{V}^{\perp}}(\underline{X}, \underline{X})\underline{\mu}_0^{\perp} \end{aligned} \tag{3.3.7}$$

and subject to

$$\begin{aligned} \dot{\underline{x}}[t] &= \underline{K}_{\mathcal{V}^{\perp}}(\underline{x}[t], \underline{x}[t])\underline{\mu}^{\perp}[t] + \underline{\tau}[t] & \underline{x}[0] &= \underline{X} \\ \dot{\underline{\mu}}^{\perp}[t] &= -\frac{1}{2}\underline{\mu}^{\perp}[t]^{\mathrm{T}}\underline{\mu}^{\perp}[t]\nabla_{\underline{x}}\underline{K}_{\mathcal{V}^{\perp}}(\underline{x}[t], \underline{x}[t]) & \underline{\mu}^{\perp}[0] &= \underline{\mu}_0^{\perp} \end{aligned} \tag{3.3.8}$$

with regard to the control variables $\underline{\tau}$ and $\underline{\mu}_0^{\perp}$ which are already spatially discretized. The superscripts $S$ and $T$ refer to the associated surface: $S$ stands for source, $T$ for target surface. The denoted center points $\underline{c}$ and normals $\underline{n}$ are evaluated in the last time step $t = 1$. $n_f$ is the number of corresponding faces, $n_x$ the number of mesh vertices of source $S$ surface.
The last term of Equation 3.3.7 expresses the path energy in $\mathcal{V}^{\perp}$. The momenta $\underline{\mu}^{\perp}(t)$ reside in the vertices $\underline{x}(t)$ of source $S$.

In the minimization procedure of $J$ for registration, the estimation of the optimal discretized variables $(\underline{\mu}^{\perp}, \underline{\tau})$ is performed simultaneously as both control variables are independently computed. In the following, the implementation of the minimizing algorithm is presented.

### Minimization algorithm

The minimization technique was introduced in section 3.2. The procedure is detailed in algorithm 1, below.

The initialization step includes:

- Initializing the optimization parameters $\underline{\tau}_0$ and $\underline{\mu}_{0,0}$ to $\underline{0}$, Algorithm 1: Optimization algorithm for the registration problem in the modular transformation framework.

```
   Input  : triangular mesh of source $S$ and target $T$, stored each as a list of mesh vertices
            and the corresponding face matrix
1  initialization;
2  while $i \leq N_{\mathrm{it}}$ do
3      compute a geodesic shooting with $\underline{\mu}^{\perp}_{0,i}, \underline{\tau}_i$ and evaluate $J(\underline{\mu}^{\perp}_{0,i}, \underline{\tau}_i)$ (Equation 3.3.7);
4      if $J(\underline{\mu}^{\perp}_{0,i}, \underline{\tau}_i) \leq \epsilon$ then
5          break;
6      else
7          compute the gradients (Equation 3.2.14, Equation 3.2.16);
8          update optimization variables $\underline{\mu}^{\perp}_{0,i}, \underline{\tau}_i$ according to the LBFG-S method;
9          $\underline{\mu}^{\perp}_{0,i+1}, \underline{\tau}_{i+1} \leftarrow \underline{\mu}^{\perp}_{0,i}, \underline{\tau}_i$;
10         $i + 1 \leftarrow i$ ;
11     end
12 end
   Output: Optimal values for $\underline{\mu}^{\perp}_{0}, \underline{\tau}$ that achieve a geodesic diffeomorphic registration of $S$
           to $T$
```

- Bringing source $S$ and target $T$ surfaces to an initial position where they overlap such that the similarity measure $d_{\mathcal{W}}$ can determine initial dissimilarities. This is achieved by moving source $S$ to target $T$ with a rigid translation

  $$\Delta \underline{r} = \overline{\underline{X}} - \overline{\underline{X}}_T$$

  with $\overline{\underline{X}}$ as the *mean* vector of the initial vertices $\underline{X}$ of source $S$ and $\overline{\underline{X}}_T$ as the mean vector of vertices of target $T$.

- Offline computing and storing of projector $\underline{P}^{\perp}$ (Equation 3.1.11) for the registration problem. Projector $\underline{P}^{\perp}$ is constant for all configurations $\underline{x}(t)$ of the source surface $S$ in all $t \in [0, 1]$.

$N_{\mathrm{it}}$ is the number of iterations. In this work, it is set to $N_{\mathrm{it}} = 100$. The error tolerance $\epsilon$ is set to $\epsilon = 10^{-6}$.

The gradients computation in line 7 and the subsequent update in line 8 are performed in parallel since both optimization variables are independent of each other.

The presented implementation of the modular registration method is supported and realized with the PyTorch library within Deformetrica, as addressed in the following section.

### 3.3.3. Implementation framework in *PyTorch*

In Deformetrica, the implemented registration in the LDDMM framework exploits the features of PyTorch, as does the implemented modular registration method - for both, the forward geodesic

shooting and the inverse problem.
In this setting, the PyTorch library basically provides algorithms to build the forward geodesic model, especially for the expensive and very frequent kernel convolutions. Based on the forward model, the PyTorch library offers automatic differentiation techniques which allow for a very convenient gradient computation. The gradient can be further used for update of optimization variables in a L-BFGS implementation.

The PyTorch library was initially developed by Facebook's AI Research lab in 2016. It is an open-source, free deep- and machine-learning library implemented with high-performance capabilities and is based on the original Torch library for machine-learning. However, since 2018, Torch is not in active development anymore and has been replaced by PyTorch. PyTorch is widely used because of the enabled accelerated tensor computations on GPUs. In a way, it is similar to the NumPy library but using the power of GPUs [142].
PyTorch has an interface for python as well as for C++ although it has been primarily developed for Python use. According to [142], the interface to Python has been kept as simple and as broad as possible. That is why, for instance, during the development of PyTorch, the interoperability and extensibility within Python libraries was a priority to ensure an easy integration with already existing Python libraries. For instance, tools are implemented to easily convert between NumPy arrays and PyTorch tensors. Also the memory sharing between Python and PyTorch modules has been enabled and simplified.

### Kernel convolutions with KeOps library

In almost every evaluation, be it in the geodesic shooting or the gradient computation, the kernel convolution has to be evaluated several times. Such convolution computations grow quadratically with the number of considered points. Also, memory requirements for the differential computations increase quadratically with the size of the input data. Consequently, the matching problem in the modular framework demands huge computational power.

In Deformetrica, the computational challenge is met with the integration of accelerating parallel computation components based on PyTorch libraries. In this work, a KeOps library is used in a PyTorch-compatible wrapper in Python. This library is used for kernel-efficient computations and the corresponding derivatives.

For the computationally demanding kernel operations, the KeOps library allows generic reductions of very large arrays which are defined with mathematical formulae, such as

$$\underline{a}_i = \underset{j=1\ldots N}{\text{Reduction}}[f(\underline{p}_j, \underline{x}_i, \underline{y}_j)], \qquad i = 1\ldots M \tag{3.3.9}$$

with the vector-valued function $f$, parameter vectors $\underline{p}_i \in \mathbb{R}^{n_p}$ and input vectors or variables $\underline{x}_i \in \mathbb{R}^n$ and $\underline{y}_j \in \mathbb{R}^{n_y}$. Also the derivatives of Equation 3.3.9 with regard to any parameters or variables can be computed efficiently [27].

Usually, the reduced functions are kernel dot products of the form $\underline{K}(\underline{x}_i, \underline{y}_j) \cdot \underline{b}_j$ that are summed to approximate a kernel convolution as seen in the numerical discretizations earlier. KeOps handles this summation relying on online map-reduce schemes using CUDA. These online reductions sum the coefficients $\underline{K}(\underline{x}_i, \underline{y}_j) \cdot \underline{b}_j$ as they are computed, without ever storing the full kernel matrix $\underline{K}$ in memory like as in standard array-centric frameworks. As a consequence, reduced memory usage is achieved, in addition to a speed-up of kernel computations with efficient simple map-reduce operations.

In this work, the function $f$ of Equation 3.3.9 is the approximated kernel convolution with

$$\underline{a}_i = \sum_j \underline{K}(\underline{q}_i, \underline{q}_j)\underline{b}_j \qquad i = 1 \dots M \tag{3.3.10}$$

for the computation of the similarity measure $d_{\mathcal{W}}$ with scalar product in Equation 3.3.1 and the velocity vector field $\underline{v}^{\perp}(t) \in \mathcal{V}^{\perp}$ in Equation 3.3.3 with kernel $\underline{K}_{\mathcal{W}}$ and $\underline{K}_{\mathcal{V}^{\perp}}$ respectively.

With a Gaussian kernel, the generic reduction for Equation 3.3.10 is realized with the generic function

$$\begin{aligned} \text{gaussianConv} = \text{genericSum}\,(&\text{"Exp}\,(-G * \text{SqDist}(\underline{q}_i, \underline{q}_j)) * B\text{"},\\ &\text{"}A = Vx(3)\text{"}, \text{"}G = Pm(1)\text{"},\\ &\text{"}X = Vx(3)\text{"}, \text{"}Y = Vy(3)\text{"}, \text{"}B = Vy(3)\text{"}). \end{aligned}$$

$A$ describes the resulting vector $a_i$. In this case, it is a vector of dimension 3. $G$ is a scalar and describes the square kernel width $\frac{1}{\sigma_{\mathcal{W}}^2}$ or $\frac{1}{\sigma_{\mathcal{V}}^2}$ respectively. Also, $B$ is three-dimensional and represents the $\underline{b}_j$'s in Equation 3.3.10. The summation takes place over $j$-elements $(\underline{q}_j, \underline{b}_j)$. The basic generic function genericSum is supplied in the PyKeops library for torch computations, i.e., pykeops.torch. The generic function is then called with

$$A = \text{gaussianConv}\,(G, \underline{q}_i, \underline{q}_j, B).$$

### KeOps for evaluation of $\underline{v}^{\perp}$

In the case of the kernel convolution to compute the velocity vector field $\underline{v}^{\perp}$ from the momenta vectors $\underline{\mu}^{\perp}$ (Equation 3.3.3) with kernel $\underline{K}_{\mathcal{V}^{\perp}}$, the presented generic function is employed in the defined kernel convolution function

$$\underline{v}_q^{\perp}(\underline{q}_j) = \text{kernelConv}(\frac{1}{\sigma_{\mathcal{V}}^2}, \underline{q}, \underline{q}_j, \underline{\mu}_{q,j}^{\perp}, \underline{P}^{\perp})$$

which incorporates the projector $\underline{P}^{\perp}$ and the associated kernel $\underline{K}_{\mathcal{V}^{\perp}}$ in the Gaussian convolution. The kernelConv function incorporates the generic gaussianConv according to

$$\underline{v}_q^{\perp}(\underline{q}_i) = \underline{P}_i^{\perp} \cdot \text{gaussianConv}(\frac{1}{\sigma_{\mathcal{V}}^2}, \underline{q}_i, \underline{q}, \underline{P}^{\perp}\,\underline{\mu}_q^{\perp})$$

with constant projector $\underline{P}^{\perp}$ that is computed offline and loaded only once in the model object as mentioned earlier, to compute

$$\underline{v}_q^{\perp}(\underline{q}_i) = \underline{P}_i^{\perp} \cdot \sum_j k_{\mathcal{V}}(\underline{q}_i, \underline{q}_j)\underline{P}_{ij}^{\perp}\,\underline{\mu}_{q,j}^{\perp}.$$

### KeOps for evaluation of similariy measure $d_{\mathcal{W}}$

In the case of the similarity measure $d_{\mathcal{W}}$ with kernel $\underline{K}_{\mathcal{W}}$ in the discretized numerical form of Equation 3.3.1, the generic $\mathrm{gaussianConv}$ is embedded in the computation of the scalar product

$$\langle S_1, S_2 \rangle_{\mathcal{W}^*} = \mathrm{scalarProduct}(\underline{c}^1, \underline{c}^2, \underline{n}^1, \underline{n}^2, \frac{1}{\sigma_{\mathcal{W}}^2}).$$

The $\mathrm{scalarProduct}$ generic function is also composed of a $\mathrm{gaussianConv}$ generic function according to

$$\mathrm{scalarProduct} = (\underline{n}^1)^{\mathrm{T}} \cdot \mathrm{gaussianConv}(\frac{1}{\sigma_{\mathcal{W}}^2}, \underline{c}^1, \underline{c}^2, \underline{n}^2).$$

### Torch tensors

In order to profit from the automatic differentiation and accelerated computations in PyTorch, all employed vectors $\underline{x}, \underline{\mu}^{\perp}, \underline{c}$ or $\underline{n}$ and the parameter $\sigma$ in the previous reduction functions must be torch tensors. The torch tensor belongs to the PyTorch library and is a multi-dimensional matrix of elements of a single data type. The conversion of numpy arrays to torch tensors is easily achieved by the well-established torch-numPy interface in both directions:

$$\begin{aligned} \underline{x}_{\mathrm{TORCH}} &= \mathrm{torch.tensor}(\underline{x}, \mathrm{dtype} = \mathrm{torch.float}), \\ \underline{x} &= \underline{x}_{\mathrm{TORCH}}.\mathrm{numpy}(). \end{aligned}$$

In the PyTorch library, some essential functions are provided for a torch tensor, like dot, diagonal, inverse, zero, rand, eye, add and many others which are comparable to array functions in NumPy. The PyTorch backend provides GPU acceleration of the tensor operations which is beneficial for KeOps generic functions.

Moreover, the declaration of the vectors as torch tensors enables the automatic differentiation. Then, the gradient of a loss or cost function with respect to the tensor variable can be easily computed.

### PyTorch module for automatic differentiation

With the previously displayed generic functions for torch tensors, the construction of the cost function $J$ creates a graph of the forward model. Figure 3.3.1 shows the graph of constructing the cost function $J$ at the final time step $t = 1$, denoted with $t_1$. The optimization variables are $\underline{\mu}_0^{\perp}$ and $\underline{\tau}$ (in blue circles). $\underline{X}$ is the initial configuration of source $S$. Through the geodesic shooting $\varphi_1^{\underline{\mu}_0^{\perp}}(\underline{X})$ and rigid translation of $\underline{X}$, the end configuration $\underline{x}(t_1) = \underline{x}(1)$ is achieved. Thus, the similarity measure term $d_{\mathcal{W}}$ can be computed. The energy metric term in $J(1)$ is also computed with the initial momenta $\underline{\mu}_0^{\perp}$ to $\|\underline{v}_0^{\perp}\|_{\mathcal{V}^{\perp}}^2$. The PyTorch module for automatic differentiation is part of the previously presented PyTorch library which is equipped with *reverse-mode* automatic differentiation. The automatic differentiation is based on *autograd mechanics* [141].

Back-propagation is only possible if a forward model exists. This requirement is fulfilled with

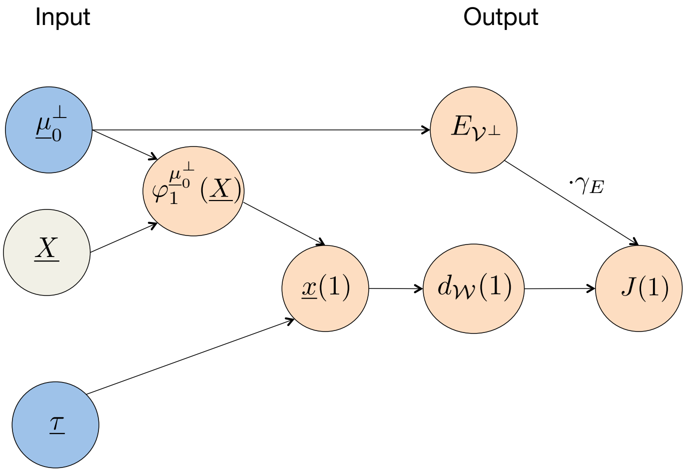

Figure 3.3.1.: Computational graph of the forward computational model. The control variables $\underline{\mu}_0^\perp$ and $\underline{\tau}$ are the input variables (blue), along with the initial position $\underline{X}$ of source $S$ (grey). At the final time step $t_1$ the end position $\underline{x}(1) = \underline{x}(t = 1)$ (orange) is computed from the input according to $\underline{x}(1) = \varphi_1^{\underline{\mu}_0^\perp}(\underline{X}) + \underline{r}$, with displacement $\underline{r} = 1s \cdot \underline{\tau}$. The cost function (orange) is calculated with $\underline{x}(1)$ and the energy term $\|\underline{v}_0^\perp\|^2_{\mathcal{V}^\perp}$ depending on the initial momenta $\underline{\mu}_0^\perp$.

the previously described forward model implementation. The gradient of a torch tensor Variable can be obtained with

$$\frac{\partial J(1)}{\partial \underline{\mu}_0^\perp} = \underline{\mu}_{0,\mathrm{TORCH}}^\perp.\mathrm{grad}().$$

The loss function $J(1)$ must be specified as a loss function and this is achieved with $J(1).\mathrm{backward}()$.

The resulting back-propagation of $J(1)$ to the optimization variable $\underline{\mu}_0^\perp$ is achieved by the chain rule and can be tracked in Figure 3.3.2. Starting at the output $J(1)$ of forward model, the node paths are followed backward with partial differentiations till the node of the desired optimal variable is reached.

Hence, indirectly, the gradient of $\frac{\partial J(1)}{\partial \underline{x}(1)}$ is transported to the initial time step $t = 0$ where the optimization variables reside.
The resulting gradients with respect to $\underline{\tau}$ and $\underline{\mu}_0^\perp$ are then used in the L-BFGS scheme in the optimization process.

### Minimization scheme in Python

With the SciPy module [190], Python delivers packages for numerical computations in the fields of mathematics, engineering, data analysis and science. The core package SciPy of this module supports, with its optimize library, the implementation and solution of optimization problems.
In Deformetrica, the optimize library is taken advantage of in solving the minimization problem

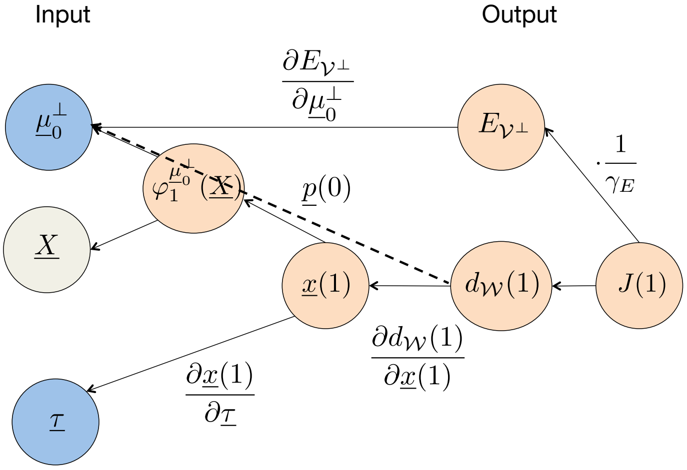

Figure 3.3.2.: Chain rule for automatic differentiation using PyTorch tensors. To that end, the backward model of the function is used.

of cost function $J$, specifically with the function $\mathrm{minimze}$ of this library.
With the computed gradients, the update of the optimization variables is performed by the L-BFGS method at every iteration step. For further details on the minimize function, the reader is referred to [190].

## 3.4. Experimental results

For a better method understanding and as a proof of concept of the method, some simple cases are considered in this section. In all cases, a cylindrical reference geometry is registered to different targets $T_i$, illustrating the possible applications of the implemented method. The possible cases covered, the corresponding models and the expected registration results can be understood as follows:

1. independence of the non-rigid deformation from the initial positions of reference geometry and target surface. To examine this behaviour, the cylindrical reference geometry is registered to the same target surface $T$ which is then placed in different initial locations $\underline{b}_1$ and $\underline{b}_2$ (see Figure 3.4.1), creating the two targets $T_1$ and $T_2$ respectively. The registration results should consist of different rigid transformations, but of the same non-rigid deformations. The plotted existing $\Delta\underline{b}$ should also result between $1s \cdot \underline{\tau}_1$ and $1s \cdot \underline{\tau}_2$. Also the non-rigid deformation is to be proven to be translation-free.

2. *right* employment of the rigid and non-rigid transformations. The examination of this feature is achieved by the registration of the cylindrical reference geometry to the same cylindrical geometry in different locations. The expected registration results should only consist of the correct rigid translation vector and of no non-rigid deformation at all.

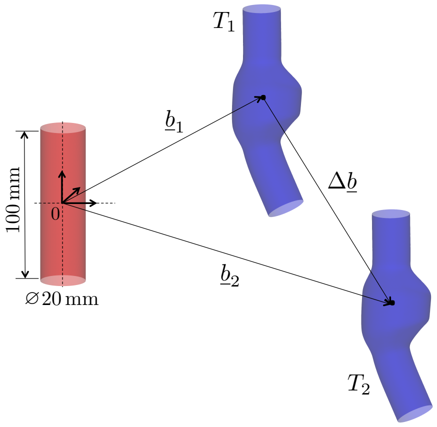

Figure 3.4.1.: Setup of method validation. The same target surface $T$ is placed initially in two different positions relative to the origin of coordinate system and center of cylindrical source, creating two targets $T_1$ and $T_2$ respectively.

The rigid translations $\underline{b}_1$ and $\underline{b}_2$ in Figure 3.4.1 are given between the origin of global coordinate system (= center point of cylinder) and the zero point of the parameterized AAAs. The zero point of the parameterized AAAs is consistent for all parameterized AAAs and is given by the construction rules in [84]. The evaluation tools of the registration results are:

- measurement of the registration quality measured in $L^2$ using the closest-node method which delivers the node-wise distances $d_{cn}$,
- visualization of rigid and non-rigid transformation parameters $\underline{\tau}$ and $\underline{\mu}_0^{\perp}$ as vector field.

These evaluation tools are consistently used throughout the work at hand.

In the discussion on the parameter choice, the overall surface area $A$ of a geometry is compared to triangular mesh precision $\ell_f[\mathrm{mm}]$, the approximate edge length of one face, and the number of vertices $n_x$. The area of a mesh face $A_f$ is computed with

$$A_f \approx A/n_f \tag{3.4.1}$$

with $n_f$ the number of mesh faces. Assuming regular triangular mesh and uniform edge length $\ell_f$, the edge length $\ell_f$ is computed with

$$\ell_f \approx \sqrt{\frac{A_f \cdot 4}{\sqrt{3}}}. \tag{3.4.2}$$

The cylindrical reference geometry is chosen to have a number of faces $n_f$ and an approximate edge length $\ell_f$ similar to the mean of those of all target surfaces.

The corresponding registration parameters $\sigma_{\mathcal{V}}$ and $\sigma_{\mathcal{W}}$ are adjusted to the chosen precision of the mesh. According to [44, 48], $\sigma_{\mathcal{V}}$ is related to the feature variation that needs to be captured

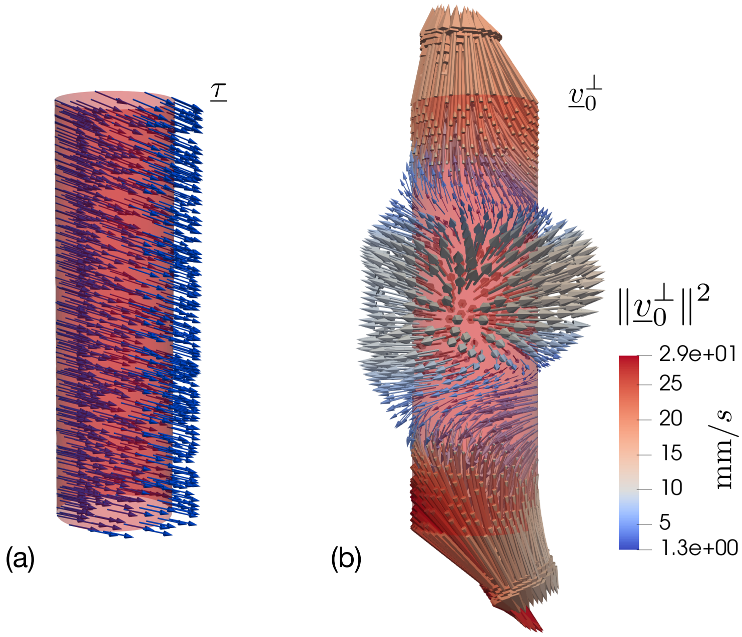

Figure 3.4.2.: Visualization of resulting optimal control variables for described matching problem. (a) The optimal rigid translation vector $\underline{\tau}$. (b) The optimal initial velocity vector field $\underline{v}_0^{\perp} \in \mathcal{V}^{\perp}$ with magnitude $\|\underline{v}_0^{\perp}\|^2$ of case 1.

and determines the deformation *elasticity*. The smaller $\sigma_{\mathcal{V}}$, the more independent is the flow of neighboured vertices. Also, the smaller $\sigma_{\mathcal{V}}$, the less integrated are bigger anatomical differences. A finer sampling also creates a redundant parameterization of the velocity fields $\underline{v}_0^{\perp}$ which is unfavourable for the subsequent statistical analysis.
Good parameters for the examined cases have proven to be $\sigma_{\mathcal{W}} = \sigma_{\mathcal{V}} = 15\,\mathrm{mm}$ and $\gamma_E = 0.0001$.

### Case 1: rigid and non-rigid transformation

The first displayed example is the registration of the cylindrical reference geometry to the parameterized AAA geometry $T_1$ with initial relative translation $\underline{b}_1$. The correct registration is expected to result in a rigid translation velocity vector and a corresponding translation-free non-rigid parameterization $\underline{v}_0^{\perp}$.
The rigid and non-rigid results are shown in Figure 3.4.2. The left figure shows the registration result $\underline{\tau}$ of the rigid translational module, the right figure shows the registration result $\underline{v}_0^{\perp}$ of the non-rigid transformation module. The resulting non-rigid vector field $\underline{v}_0^{\perp}$ is free of translational components. This can be examined by multiplying the flattened vector field $\underline{v}_0^{\perp} \in \mathbb{R}^{3 \cdot n_x \times 1}$ by the matrix $\underline{B} \in \mathbb{R}^{3 \cdot n_x \times 3}$ from Equation 3.1.9

$$\underline{a} = \underline{v}^{\mathrm{T}}_{\perp,0} \cdot \underline{B} \;\; \in \mathbb{R}^{1\times 3}, \tag{3.4.3}$$

which results in a vector denoted by $\underline{a}$. Each component of $\underline{a}$ indicates the scalar product of the corresponding global axis $x, y, z$ with the flattened vector field.
For the examined case 1, the vector $\underline{a}$ equals $[11.0, -4.1, 60.6] \cdot 10^{-5} \approx \underline{0}$.

The quality of fit is evaluated by computing the node-wise distance $d_{cn}$ in the Euclidean $L^2$. This distance is selected since the accepted error tolerance is computed in the Euclidean $L^2$ and equals the segmentation precision of $2\,\text{mm}$. In this case, the maximum distance is $0.79\,\text{mm}$ and occurs at the lower outlet of the parameterized AAA. Figure 3.4.3 shows the results for the performed registration.
The optimization behaviour is depicted in Figure 3.4.4 where the cost function $J$ is plotted against the iterations.

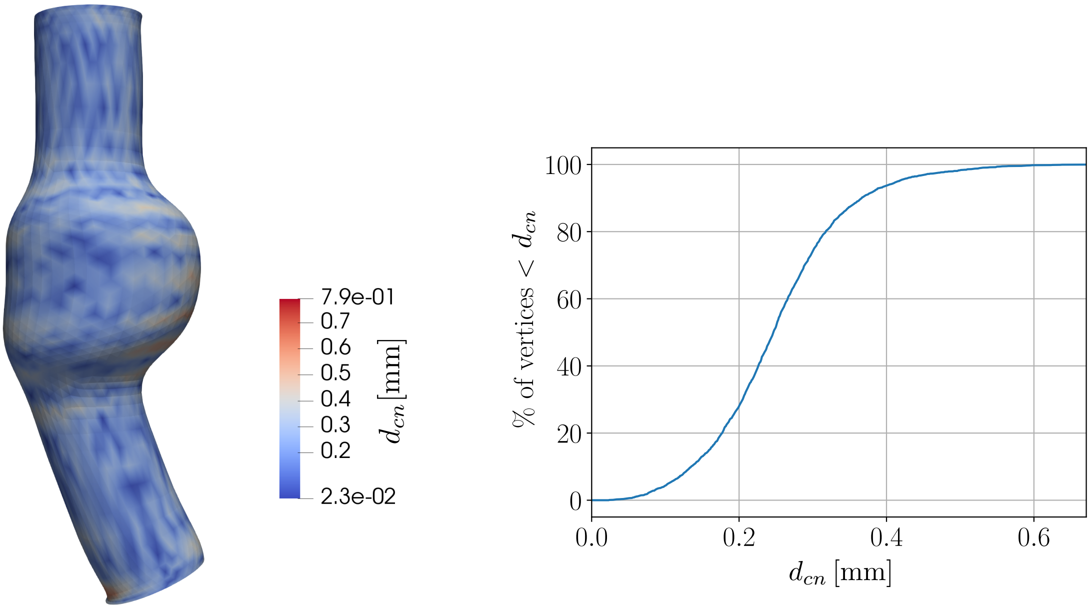

Figure 3.4.3.: (a) Quality of registration result depicted in point-wise distance $d_{cn}$ of transformed reference geometry $S$ to target $T$ measured with the $L^2$ norm. (b) Node-wise distance graph.

### Case 2: rigid and non-rigid transformation

Case 2 builds on Case 1 and aims at demonstrating the independence of the non-rigid transformation results from the initial translational relative position of cylindrical source $S$ and the target surface. To that end, the cylindrical reference is registered to target $T_2$ as in Figure 3.4.1. In this case, the rigid result can be validated: The resulting difference between $1s \cdot \underline{\tau}_1$ and $1s \cdot \underline{\tau}_2$ should be equal to the true $\Delta \underline{b}$. Apart from that, the optimal $\underline{v}_0^{\perp}$ should be translation-free.
Figure 3.4.5 shows results of the registration problem of $S$ to $T_2$. The multiplication of the flattened $\underline{v}_0^{\perp}$ with the matrix $\underline{B}$ gives $[-0.33, -1.2, 2.5] \cdot 10^{-4} \approx \underline{0}$.
Figure 3.4.2 and Figure 3.4.5 state visually that the optimal non-rigid parameter $\underline{v}_0^{\perp}$ in case 1 and case 2 are the same. Computationally, the difference $\|\underline{v}_0^{\perp,1} - \underline{v}_0^{\perp,2}\|_2^2$ in $L^2$ equals $0.0005\frac{\text{mm}}{s}$.

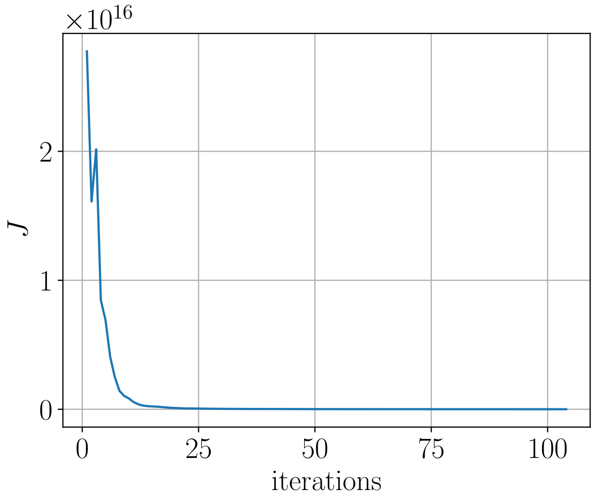

Figure 3.4.4.: Plot of cost function $J$ over iterations of registration problem in case 1.

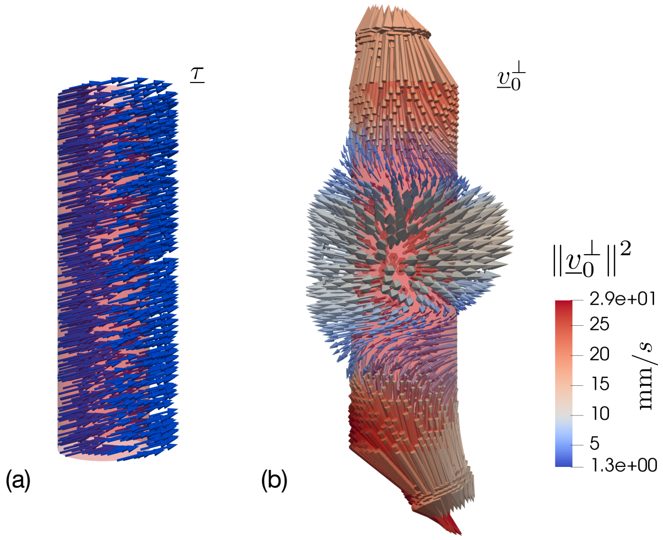

Figure 3.4.5.: Visualization of registration results of $S$ to $T_2$. (a) The optimal rigid translation vector $\underline{\tau}$. (b) The optimal initial velocity vector field $\underline{v}_0^\perp \in \mathcal{V}^\perp$ with magnitude $\|\underline{v}_0^\perp\|^2_{\mathcal{V}^\perp}$ of case 2.

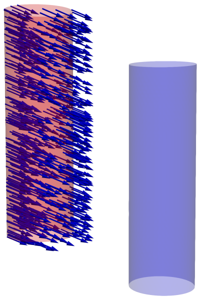

Figure 3.4.6.: The cylindrical source geometry (red) is shown with the resulting optimal $\underline{\tau} = [52.1, 17.5, -23.4]^{\mathrm{T}} \frac{\mathrm{mm}}{1s}$ as a vector field. The color of the vectors is uniform as the rigid translation is uniform for all vertices. The blue surface is the target.

### Case 3: rigid transformation

Case 3 is aimed at demonstrating that the method identifies the suitable employment of the non-rigid and rigid module. For instance, if the positions of source $S$ and target $T$ differ with translation, the method should only perform the rigid transformation. In order to test this, the target $T$ is just the translated cylindrical surface $S$ to a random position. The expected registration result is the estimation of the correct translational $\underline{\tau}$ without the involvement of the non-rigid module. Hence, the non-rigid parameter $\underline{v}_0^{\perp}$ should be $\underline{0}$.
Figure 3.4.6 shows the registration result of the translational rigid module. The non-rigid module has been correctly and automatically self-deactivated in the registration with $\underline{v}_0^{\perp} = \underline{0}$.

## 3.5. Summary

In this chapter, a registration method was introduced which incorporates a translational and a non-rigid translation-free transformation in a modular framework. The implementation using the PyTorch module in Python has been also displayed, followed by some numerical results. These results validated the intended behaviour of the method which includes amongst others:

- a clear separation of rigid and non-rigid transformations,
- independence from a pre-alignment step,
- a translation-free non-rigid transformation which is parameterized by tangent-space parameters.

In the next chapter, the application of the method to the available AAA cohort is performed, building the basis for the subsequent shape analysis in the second part of the present work.

# 4. Feature space of abdominal aortic aneurysms

After the introduction of the modular registration framework in the previous chapter, its application to the shapes of abdominal aortic aneurysms (AAAs) is presented in this chapter. To that end, the study population is discussed in detail, starting with the geometry extraction from CT images. Afterwards, the novel modular registration method is applied to the extracted AAA geometries. The chapter concludes with depictions of the registration results with an appropriate choice of parameters.
The resulting initial momenta for each AAA case are together the basis for the subsequent statistical analyses in the second part of this work.

## 4.1. AAA study population

In the introductory chapter 1, the complete cohort of real abdominal aortic aneurysm cases is displayed. This section focuses on this cohort and its preparation for the modular registration.

### 4.1.1. Data preparation

As the statistical shape analysis is built upon 3D abluminal surfaces of the examined AAA shapes in the database, the construction of the corresponding 3D models from computed tomography (CT) scans plays a crucial role and is addressed in the following.

#### Medical images

In the examined database, all geometrical information is retrieved from patient-specific CT scans which were provided by the clinical partner at the university hospital Rechts der Isar, TUM [114]. The scans are obtained with a Philips Brilliance 64 channel CT Scanner (Philips Healthcare, DA Best, The Netherlands) using contrast-enhanced thoraco-abdominal multi-slice CT angiography. The reconstruction takes place with a spatial resolution of 0.6 mm. The captured anatomy represents the diastolic state with a blood pressure of $p \approx 87\,\mathrm{mmHg}$ [153].

CT attenuation values are given in Hounsfield Units (HU) according to a linear density scale. The HU is a measure of the radio-density which is a physical property of the imaged material. Consequently, the different anatomical structures in a CT image can be identified by the corresponding HU values [89].
Water has been arbitrarily assigned the value of 0 HU. The HU values of all other materials are

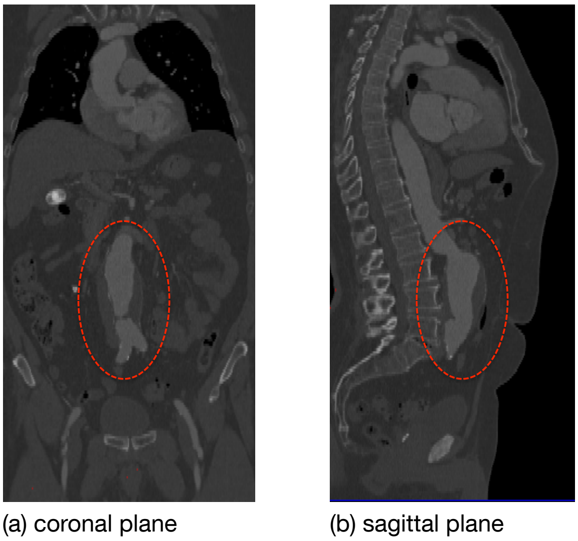

(a) coronal plane (b) sagittal plane

Figure 4.1.1.: AAA representation in the (a) coronal and (b) sagittal 2D plane. The 2D views are obtained from a 3D CT scan of the abdominal region. The AAA region is encircled with a red dashed line.

calculated relative to water according to

$$HU = \frac{c_{\mathrm{M}} - c_{\mathrm{H_2O}}}{c_{\mathrm{H_2O}}}$$

with the CT attenuation values $c_{\mathrm{M}}$ for material and $c_{\mathrm{H_2O}}$ for water. The HU values of the human body range between $-1000$ HU for air to approx. $3000$ HU for bones [102].

Figure 4.1.1 shows a CT image of the abdominal region with a common presentation of an AAA. The AAA region is presented in the coronal and sagittal plane and is encircled by a red dashed line. In the ideal case, the HU values identify the different attenuation: contrast-enhanced blood $150$ HU $-500$ HU, ILT $28$ HU $-45$ HU and calcifications $200$ HU $-1000$ HU [37, 77]. However, the fourth component, the aortic wall, cannot be recognized in the CT image due to its small thickness which is comparable to the available CT resolution [114, 153].
The material-specific HU values facilitate the differentiation between the abdominal organs and the extraction of the anatomical structure of interest, the AAA, which is addressed in the next step. The treatment of missing wall thickness information is also described.

### 3D AAA geometry model

The aforementioned partitioning of medical images based on HU values is known as segmentation. Maier presents in [114] a detailed segmentation protocol which has been followed to construct AAA 3D geometry models from the available CT images in the database. In the following, the relevant steps to the work at hand are recapitulated. Based on that, further preparation

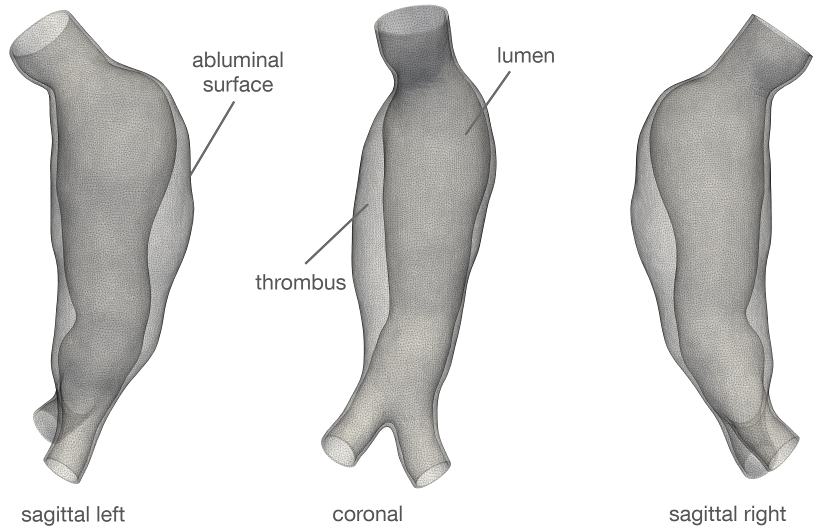

Figure 4.1.2.: The AAA 3D geometric model resulting from the outlined segmentation process. The reconstructed 3D model consists of a lumen and thrombus.

steps complete the pre-processing of the AAA geometries.

The segmentation process of the whole AAA geometry roughly consists of

1. semi-automatic segmentation of blood lumen,
2. segmentation of the complete AAA geometry,
3. construction of the ILT 3D geometry with a 3D boolean separation of the lumen from the complete AAA geometry,
4. filtering and smoothing operations.

After the described segmentation process, the segmented parts are uniformly cut 2 cm distal to the aortic bifurcation and at the branching of the renal arteries (see Figure 4.1.2).

Since it is impossible to recognize and segment the patient-specific aortic wall from CT-images, an idealized AAA wall is extruded conformly to the abluminal ILT surface by one pixel which is 1 mm. The whole presented procedure is conducted with the commercial software Simpleware™ ScanIP (Version M-2017.06-SP2; Synopsis, Inc., Mountain View, USA).

According to literature, despite the uniform AAA wall reconstruction, the resulting geometry depicts the 3D AAA geometry with great accuracy. Other inaccuracies are introduced to the 3D model reconstruction by the concluding filtering and smoothing steps of the segmentation procedure described above. However, all in all, the estimated inaccuracy of all contributing factors in the 3D geometry reconstruction is roughly $2\,\mathrm{mm}$.

### Abluminal surface preparation

The resulting segmented 3D AAA volumes build the basis for further pre-processing steps which are necessary for the attempted shape analysis. According to the literature review in chapter 1, relevant AAA shape characterizations are related to the AAA abluminal surface. That is why in this work, only the abluminal surface of the reconstructed 3D AAA model is taken into consideration for shape analysis. To that end, the further pre-processing steps comprise the following:

1. extraction of abluminal surface of 3D AAA (Trelis™ 15.1, Csimsoft, Utah),
2. automatic spatial discretization of the abluminal surface with an element length between $1-2$ mm (Trelis™ 15.1, Csimsoft, Utah),
3. automatic generation of centreline of AAA abluminal surface (Simpleware™ ScanIP, Version M-2017.06-SP2; Synopsis, Inc., Mountain View, USA),
4. automatic assessment of selected shape features (section 1.4) using the centreline (Simpleware™ ScanIP, Version M-2017.06-SP2; Synopsis, Inc., Mountain View, USA),
5. calculation of derived morphologic features based on step 3 (Simpleware™ ScanIP, Version M-2017.06-SP2; Synopsis, Inc., Mountain View, USA),
6. assessment of bifurcation point and corresponding tangent along centreline,
7. cut of the abluminal surface with a plane perpendicular to the centreline at bifurcation point.

The procedure is illustrated in Figure 4.1.3.

To facilitate the computation of the similarity measure with surface currents as in subsection 2.1.3, the abluminal surface is spatially discretized with a triangular mesh. The mesh size is chosen to be between 1 - 2 mm. A finer mesh creates higher dimensional deformation parameters $\underline{\mu}_0^{\perp}$ with redundant shape information which overloads the subsequent shape analysis. Moreover, the kernel widths $\sigma_{\mathcal{V}}$ and $\sigma_{\mathcal{W}}$ are adapted to the mesh size later on. So, a finer mesh is not advantageous as in a biomechanical analysis of the 3D model where a finer mesh is beneficial.

Without any rigid alignment steps, the results of the cutting pre-processing step are the final abluminal shapes which are examined in the shape analysis. Selected final cut abluminal shapes are shown in Figure 4.1.4 with the cut off bifurcation arteries underneath.
As seen in Figure 4.1.4, relevant shape features are preserved despite excluding the iliac arteries which do not provide relevant shape information and exhibit random appearances. The orientation and spatial information of each AAA is also preserved. Moreover, with absent bifurcation arteries, the deformation parameters describe more the form of the AAA shape and are not disturbed by the arteries which might expend unnecessary deformation energy and influences the shape analysis.

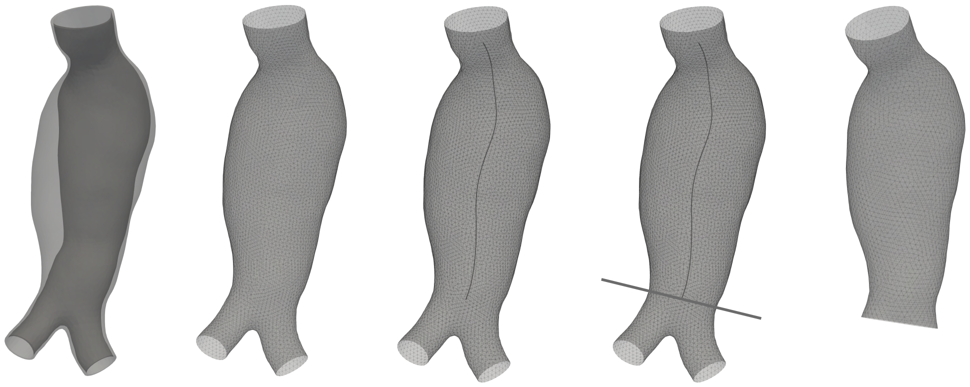

segmented 3D volume

extracted & discretized abluminal surface

generated centerline

definition of plane in bifurcation point

final cut abluminal surface

Figure 4.1.3.: Illustration of further pre-processing steps of segmented 3D AAA volumes to generate the final abluminal AAA surface.

## 4.2. Modular registration

For shape analysis, the entire cohort 142 AAA abluminal surfaces is taken into consideration. In this section, the corresponding mathematical abstract representation of each surface is retrieved for shape analysis. To that end, a reference geometry is registered to each abluminal surface of the cohort according to the established modular registration framework. The abstract shape representation is obtained with the parameter of the non-rigid module, the initial momenta $\underline{\mu}_0^{\perp}$. Amongst others, the aim of this section is to determine appropriate registration parameters $\sigma_{\mathcal{V}}$ and $\sigma_{\mathcal{W}}$ for this cohort.

### 4.2.1. Settings

### Reference geometry

In some statistical shape analysis methods in CA, an optimized reference geometry is estimated such that it has the minimum distance to all shapes in the cohort. The cost function consists of the similarity measure and the energy term, too, as in Equation 3.2.7. The minimum distance refers therefore to the distance both energetically in $\mathcal{V}^{\perp}$ and with regard to the similarity measure in $\mathcal{W}^*$. During the optimization procedure, the vertices of the reference geometry are added as an optimization variable and are updated respectively while staying connected.

In this work, a cylindrical surface is the reference geometry. Consequently, the reference geometry is not estimated in an optimization algorithm for the following reasons:

- A healthy aorta has a roughly cylindrical shape. When taking a cylindrical surface as the reference geometry for AAA shape analysis, the resulting registration captures the morphology difference between the diseased aorta and a healthy one. Consequently, the non-rigid registration parameter $\underline{v}_0^\perp \in \mathcal{V}^\perp$ or the underlying $\underline{\mu}_0^\perp \in \mathcal{V}^{\perp *}$ is a valid basis for shape analysis and captures statistically significant and useful shape information.

- Since the iliac arteries are cut off, the remaining shapes of AAA are deformed cylinders. The deformation goes in every direction, especially without a prior orientation alignment which is omitted in this work. That is why, with enough AAA samples, the mean geometry would be a cylinder.

- From a probabilistic point of view, by setting the mean geometry to that of a healthy aorta, both stable and unstable AAA shapes are regarded as observations or samples around the healthy aorta, without any bias to a certain AAA shape or AAA class. This yields a more descriptive AAA shape parameterization with $\underline{v}_0^\perp \in \mathcal{V}^\perp$ or the underlying $\underline{\mu}_0^\perp \in \mathcal{V}^{\perp *}$ compared with a mean AAA shape which would already show some deformations since the data set is not big enough. With a *neutral* mean geometry, the stable and unstable cohort can be better identified later in the shape analysis. A *more general* distribution of AAA shapes is generated therewith.

- As the stable and unstable AAA cohorts show too much variation, a *fair* mean geometry is also hard to obtain without a bias, especially with the unequal number of stable and unstable observations which would distort the mean geometry estimation.

On these grounds, the cylindrical reference geometry is shown in Figure 4.2.1 with the displayed dimensions and is generated in Trelis™ 15.1 (Csimsoft, Utah). The spatial discretization is automatically generated as a triangular mesh with an element length of 1 mm.

## Parameter choice

As there is no golden rule for the parameter choice $\sigma_\mathcal{W}$ and $\sigma_\mathcal{V}$ for spatial resolution, the mapping is performed first with several pairs $(\sigma_\mathcal{W}, \sigma_\mathcal{V})$ to identify an appropriate parameter combination with regard to accuracy.

For the parameter choice, the only applicable rule is that the deformation parameter $\sigma_\mathcal{V}$ shall be equal to or smaller than the similarity parameter $\sigma_\mathcal{W}$ such that a registration is possible (see subsection 3.3.1).
Preceding explanatory modular registrations of the reference geometry to AAA shapes in the cohort revealed that appropriate values range from $\sigma_\mathcal{W} = [12\,\text{mm}, \dots, 30\,\text{mm}]$ and $\sigma_\mathcal{V} = [10\,\text{mm}, \dots, 25\,\text{mm}]$. The probing pairs $(\sigma_\mathcal{W}, \sigma_\mathcal{V})$ are selected within these ranges.

The trade-off parameter $\gamma_E$ is chosen such that the non-rigid deformation is as elastic as possible, i.e. the energy term in Equation 3.2.7 does not have a big impact on the registration quality and the registration allows for *large* deformations. Therefore, the parameter $\gamma_E$ is always set to $0.0001$.

In this context, an appropriate parameter pair $(\sigma_{\mathcal{W}}, \sigma_{\mathcal{V}})$ is a pair for which the registration is the most accurate and its parameterization depicts the associated AAA case as accurately as possible. Mathematically speaking, it is the parameter pair which achieves a registration characterized with a low similarity measure $d_{\mathcal{W}}$. The similarity measure assesses the achieved registration's quality of fit.

It is important to note that different similarity measures $d_{\mathcal{W}}$ of different kernel widths $\sigma_{\mathcal{W}}$ cannot be compared to each other. The $d_{\mathcal{W}}$ is a norm which is only valid for a $\sigma_{\mathcal{W}}$ in the associated RKHS $\mathcal{W}$. For a chosen $\sigma_{\mathcal{W}}$, the larger $\sigma_{\mathcal{V}}$ becomes, the closer comes $d_{\mathcal{W}}$ to its asymptotic value $\bar{d}_{\mathcal{W}}$ where the undeformed cylinder $S$ is compared to the target $T$ according to

$$\bar{d}_{\mathcal{W}} = \|\varphi_1^{\mu_0^{\perp}}(S) - T\|^2_{\mathcal{W}^*}. \tag{4.2.1}$$

This can be explained by the fact that for larger $\sigma_{\mathcal{V}}$ the non-rigid module produces an increasingly rigid deformation. So, for one $\sigma_{\mathcal{W}}$ and increasing $\sigma_{\mathcal{V}}$, the similarity measure $d_{\mathcal{W}}$ gets larger towards $\bar{d}_{\mathcal{W}}$.
The defined asymptotic value $\bar{d}_{\mathcal{W}}$ is used for normalizing $d_{\mathcal{W}}$ to achieve dimensionless comparable values among different $\sigma_{\mathcal{W}}$.

In Table 4.1, the mean values of normalized similarity measures $d_{\mathcal{W}}^{\text{norm}} = d_{\mathcal{W}}/\bar{d}_{\mathcal{W}}$ for various pairs $(\sigma_{\mathcal{W}}, \sigma_{\mathcal{V}})$ are displayed.

Table 4.1.: Mean values of normalized similarity measure $d_{\mathcal{W}}^{\text{norm}} = d_{\mathcal{W}}/\bar{d}_{\mathcal{W}}$ [-] over all AAA cases for every pair $(\sigma_{\mathcal{W}}, \sigma_{\mathcal{V}})$. The values for $\sigma_{\mathcal{W}}$ and $\sigma_{\mathcal{V}}$ are given in mm.

| $\sigma_{\mathcal{V}}$<br>$\sigma_{\mathcal{W}}$ | 10.0 | 12.0 | 15.0 | 18.0 | 20.0 | 25.0 |
|---|---|---|---|---|---|---|
| 12.0 | 0.0343 | 0.0138 | 0.0075 | 0.0023 | 0.0071 | 0.0056 |
| 15.0 | 0.1586 | 0.0417 | 0.0048 | 0.0006 | 0.0009 | 0.0022 |
| 18.0 | 0.368 | 0.2934 | 0.0853 | 0.0223 | 0.0004 | 0.001 |
| 20.0 | 0.7369 | 0.5051 | 0.1713 | 0.038 | 0.0003 | 0.0008 |
| 25.0 | 1.1632 | 1.0535 | 0.6638 | 0.3265 | 0.1353 | 0.0759 |
| 30.0 | 1.6167 | 1.6305 | 1.3244 | 0.7814 | 0.5843 | 0.2344 |

It is obvious that for successful cases and with a constant $\sigma_{\mathcal{W}}$, the bigger the kernel width $\sigma_{\mathcal{V}}$, the bigger the normalized similarity measure $d_{\mathcal{W}}^{\text{norm}}$. This is due to the fact that with bigger $\sigma_{\mathcal{V}}$, the stiffer the deformation, the more neglected are the small shape details in the registration procedure.

For some cases, e.g. for case no. 132, different parameter pairs $(\sigma_{\mathcal{W}}, \sigma_{\mathcal{V}})$ significantly impact the registration results as displayed in Figure 4.2.2. Consequently, for the parameter choice, a parameter pair $(\sigma_{\mathcal{W}}, \sigma_{\mathcal{V}})$ is chosen where more or less all AAA cases are matched accurately enough. In the case of AAA shapes, these inaccuracies arise at the boundaries.

According to Table 4.1, the following pairs produce the smallest mean of the similarity value for every similarity kernel $\sigma_{\mathcal{W}}$ and have in this regard the best registration results:

- $\sigma_{\mathcal{W}} = 15.0$ mm and $\sigma_{\mathcal{V}} = 18.0$ mm,
- $\sigma_{\mathcal{W}} = 18.0$ mm and $\sigma_{\mathcal{V}} = 20.0$ mm,
- $\sigma_{\mathcal{W}} = 20.0$ mm and $\sigma_{\mathcal{V}} = 20.0$ mm,
- $\sigma_{\mathcal{W}} = 20.0$ mm and $\sigma_{\mathcal{V}} = 25.0$ mm.

This implies that for the available study population the best registration results are achieved in the modular registration framework with similar or even equal kernel lengths for similarity measure and deformation.

In the same manner, comparison of registration results obtained with different $(\sigma_{\mathcal{W}}, \sigma_{\mathcal{V}})$ is carried out based on the deformation energy $\|\underline{v}_0^\perp\|^2_{\mathcal{V}^\perp}$ (as in Equation 3.2.7).

The calculated mean values in Table 4.2 indicate that for a constant $\sigma_{\mathcal{V}}$, the deformation energy is almost the same. However, for a small similarity kernel $\sigma_{\mathcal{W}}$, like 12.0 mm, the deformation energy is relatively higher than for the other $\sigma_{\mathcal{W}}$ since the similarity measure is *stricter* and requires high accuracies. The bigger $\sigma_{\mathcal{V}}$, the less elastic the non-rigid deformation, the smaller the required energy for deformation.

Table 4.2.: Mean values of deformation energy $\|\underline{v}_0^\perp\|^2_{\mathcal{V}^\perp}$ $[\frac{\mathrm{mm}}{s}]$ over all AAA cases for every pair $(\sigma_{\mathcal{W}}, \sigma_{\mathcal{V}})$. The values for $\sigma_{\mathcal{W}}$ and $\sigma_{\mathcal{V}}$ are given in mm.

| $\sigma_{\mathcal{W}}$<br>$\sigma_{\mathcal{V}}$ | 12.0 | 15.0 | 18.0 | 20.0 | 25.0 | 30.0 |
|---|---|---|---|---|---|---|
| 10.0 | 21187.98 | 19861.37 | 17701.84 | 17149.65 | 17008.08 | 16985.32 |
| 12.0 | 18873.6 | 15526.88 | 13807.51 | 13428.62 | 13264.12 | 13180.06 |
| 15.0 | 14922.65 | 11943.85 | 10520.79 | 10269.29 | 10136.05 | 10014.32 |
| 18.0 | 12863.74 | 10334.76 | 8600.72 | 8455.89 | 8312.28 | 8209.5 |
| 20.0 | 11679.56 | 9568.67 | 7855.64 | 7720.51 | 7579.77 | 7448.11 |
| 25.0 | 10650.14 | 8608.35 | 6983.8 | 6834.48 | 6641.6 | 6685.08 |

Nevertheless, to determine the most suitable pair of the identified four pairs, the similarity measure is taken into account. From the identified four appropriate parameter pairs $(\sigma_{\mathcal{W}}, \sigma_{\mathcal{V}})$, the most appropriate one is determined with regards to the mean values of similarity in $L^2$ over all AAA cases. This measure is also employed in the explanatory example of the previous chapter and represents the *visual accuracy assessment*.

Table 4.3 reveals the optimal parameter pair which is $(\sigma_{\mathcal{V}} = 20\,\mathrm{mm}, \sigma_{\mathcal{W}} = 20\,\mathrm{mm})$. For this pair, all registration cases succeed and deliver an overall accuracy of only 0.52 mm. Appendix A

Table 4.3.: Mean values of closest-node distances $\bar{d}_{cn}$ [mm] over all AAA cases for every pair $(\sigma_{\mathcal{W}}, \sigma_{\mathcal{V}})$ The values for $\sigma_{\mathcal{W}}$ and $\sigma_{\mathcal{V}}$ are given in mm.

| $\sigma_{\mathcal{V}}$<br>$\sigma_{\mathcal{W}}$ | 10.0 | 12.0 | 15.0 | 18.0 | 20.0 | 25.0 |
|---|---|---|---|---|---|---|
| 12 | 2.10E+16 | 1.515 | 0.915 | 0.748 | 0.706 | 0.741 |
| 15 | 7.09E+17 | 1.48E+17 | 0.636 | 0.547 | 0.597 | 0.639 |
| 18 | 1.61E+18 | 1.24E+18 | 2.95E+17 | 1.15E+17 | 0.496 | 0.582 |
| 20 | 3.14E+18 | 2.26E+18 | 5.88E+17 | 1.57E+17 | 0.522 | 0.603 |
| 25 | 5.57E+18 | 5.73E+18 | 2.35E+18 | 1.00E+18 | 3.66E+17 | 1.71E+17 |
| 30 | 8.91E+18 | 9.39E+18 | 6.87E+18 | 4.01E+18 | 2.60E+18 | 1.18E+18 |

shows the registration results for this parameter pair for every AAA abluminal surface in the cohort. Therein, the normalized similarity measure $d_{\mathcal{W}}^{norm}$, the path energy $\|\underline{v}_0^{\perp}\|^2_{\mathcal{V}^{\perp}}$ in $\mathcal{V}^{\perp}$ and the average closest-node distance $\bar{d}_{cn}$ are listed for every AAA surface.

In the following, the registration results for the selected parameter pair are discussed.

### 4.2.2. Results and discussion

With the identified optimal parameter pair $(\sigma_{\mathcal{W}} = 20\,\mathrm{mm}, \sigma_{\mathcal{V}} = 20\,\mathrm{mm})$, all registrations succeed with an average accuracy of 0.52 mm, as assessed by mean $d_{cn}$ distance measurements between the deformed source $S$ and the target $T$. The success for all registration problems is one of the main reasons for the optimal parameter pair selection.

The achieved mean $\bar{d}_{cn}$ distance is small and readily acceptable. However, it is only a mean value. For some AAA cases, the registration results are better or worse than the mean. For almost all cases, due to the relatively big kernel widths $\sigma_{\mathcal{W}}$ and $\sigma_{\mathcal{V}}$, detailed shape features or segmentation artefacts are not captured in the registration, see Figure 4.2.3. Simply said, the function cost, especially the similarity measure, does not *see* these details.

For the same case no. 85 and the selected parameter pair, the corresponding $d_{cn}$ distance distribution over the whole deformed surface $\varphi_1^{v_0^{\perp}}(S)$ is displayed in Figure 4.2.4, along with the percentage of vertices over distance.

The corresponding vertex percentage over the distance $d_{cn}$ is additionally displayed in the graph of Figure 4.2.5. Nevertheless, for some AAA cases, in most cases smaller ones, the achieved registration results are of high accuracy, like for case no. 55. For this case and the selected parameter pair, the mean $\bar{d}_{cn}$ distance is 0.42 mm. The deformed source $\varphi_1^{v_0^{\perp}}(S)$, the corresponding $d_{cn}$ distribution over $\varphi_1^{v_0^{\perp}}(S)$ and the percentage of points over distance $d_{cn}$ are displayed in Figure 4.2.6 and in Figure 4.2.7.

Corresponding percentage of points over distance $d_{cn}$ are displayed in Figure 4.2.8. In summary,

the employed registration methods requires a constant parameter pair $(\sigma_{\mathcal{W}}, \sigma_{\mathcal{V}})$ for all registered AAA cases. By doing so, a consistency is achieved for further statistical analysis. However, for a cohort with widely spread geometrical features, the selected pair $(\sigma_{\mathcal{W}}, \sigma_{\mathcal{V}})$ cannot achieve the same registration quality and accuracy.
For the examined AAA cohort, the selected parameter pair $\sigma_{\mathcal{W}} = \sigma_{\mathcal{V}} = 20$ guarantees successful registrations for all cases. Due to the relatively big kernel widths, segmentation artefacts are filtered out in the resulting deformed source $\varphi_1^{v_0^\perp}(S)$ and small shape alternations are not captured in $\varphi_1^{v_0^\perp}(S)$, too. This can be regarded as a benefit to eliminate local, irrelevant shape information in the following statistical analysis.

### 4.2.3. Summary

In this chapter, the focus was on the available database and on its preparation for shape analysis. To that end, a reference geometry was chosen and registered to every AAA shape in the cohort with an identified suitable pair of kernel parameters $(\sigma_{\mathcal{W}}, \sigma_{\mathcal{V}})$. With the resulting AAA-specific non-rigid registration parameter $\underline{\mu}_0^\perp$, the required abstract shape description for every individual AAA shape was obtained.

The selected parameter pair is $\sigma_{\mathcal{W}} = \sigma_{\mathcal{V}} = 20$ mm, which guarantees successful registrations and the best registration results with regard to $d_{\mathcal{W}}$ and the $d_{cn}$ distance with $L^2$ norm which represents the visual inspection. For this parameter pair, the registration results have a mean accuracy error of $0.52$ mm which is assessed with the $d_{cn}$ distance measured with the $L^2$ norm. Due to the different size and shape evolutions of examined AAA cases, the registration results slightly show different registration accuracies and quality with the selected parameter pair.

Nonetheless, the obtained abstract shape-specific parameter $\underline{\mu}_0^\perp$ depicts the associated shape with an appropriate accuracy. Building on all obtained case-specific $\underline{\mu}_0^\perp$, the shape statistical analysis is conducted in the second part of this thesis. A dimensionality reduction method is applied on these shape parameters, allowing for a statistically significant description of shapes using a so-called shape descriptor $\underline{s}$.

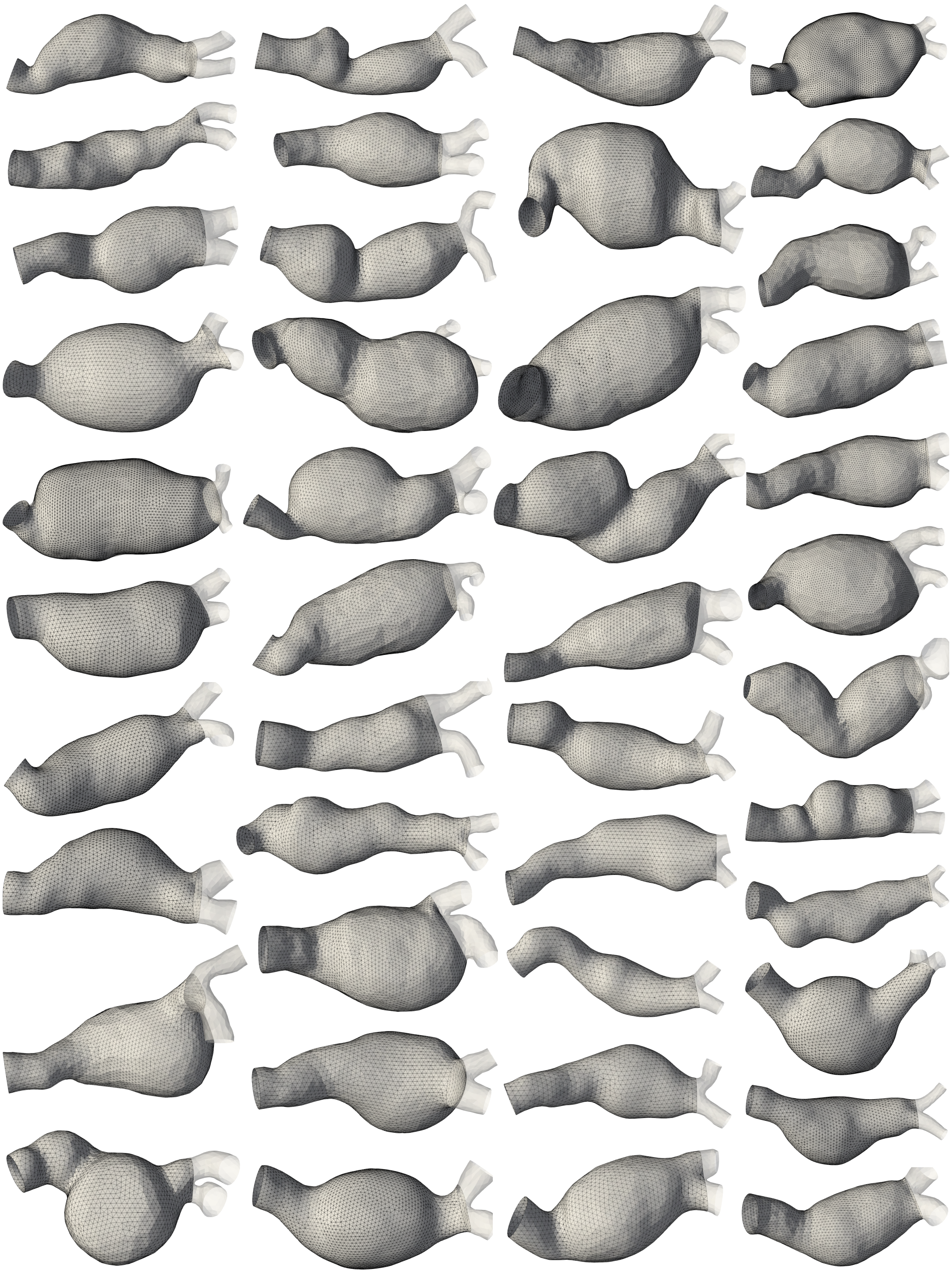

Figure 4.1.4.: Final results of pre-processing of case-specific AAA abluminal surface for shape analysis. The bifurcation arteries which are cut in the illustrated pre-processing steps are also shown underneath the final cut shapes.

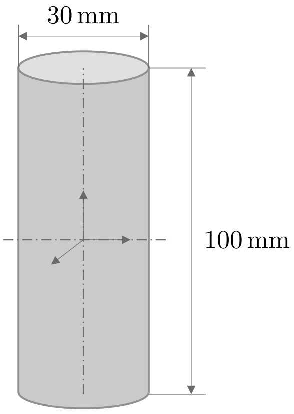

Figure 4.2.1.: The selected cylindrical reference geometry has a height of $H_{cyl} = 100$ mm and a diameter of $D_{\mathrm{cyl}} = 30$ mm.

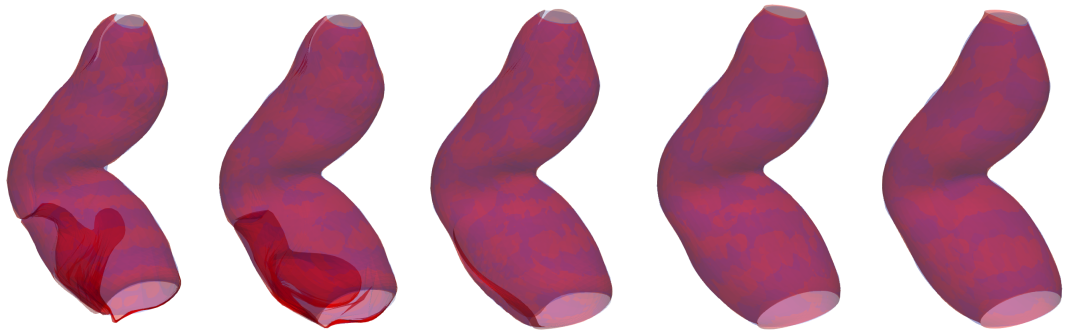

$\sigma_{\mathcal{V}} = 10\,\mathrm{mm}$ $\quad \frac{d_{\mathcal{W}}}{\bar{d}_{\mathcal{W}}} = 0.0017$

$\sigma_{\mathcal{V}} = 12\,\mathrm{mm}$ $\quad \frac{d_{\mathcal{W}}}{\bar{d}_{\mathcal{W}}} = 0.0017$

$\sigma_{\mathcal{V}} = 15\,\mathrm{mm}$ $\quad \frac{d_{\mathcal{W}}}{\bar{d}_{\mathcal{W}}} = 0.0005$

$\sigma_{\mathcal{V}} = 20\,\mathrm{mm}$ $\quad \frac{d_{\mathcal{W}}}{\bar{d}_{\mathcal{W}}} = 0.0005$

$\sigma_{\mathcal{V}} = 25\,\mathrm{mm}$ $\quad \frac{d_{\mathcal{W}}}{\bar{d}_{\mathcal{W}}} = 0.0008$

Figure 4.2.2.: Registration results of AAA case no. 132 with $\sigma_{\mathcal{W}} = 12$ mm and different $\sigma_{\mathcal{V}}$. The great impact of parameter choice $(\sigma_{\mathcal{W}}, \sigma_{\mathcal{V}})$ is observed for this case.

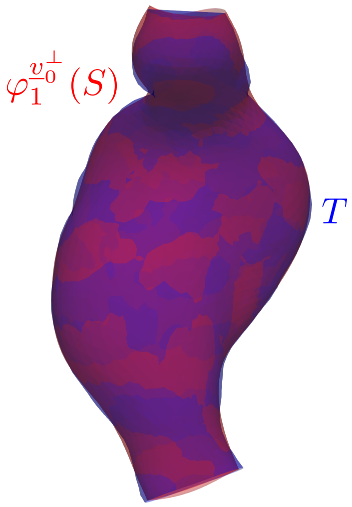

Figure 4.2.3.: Registration result of AAA case no. 85 with $\sigma_{\mathcal{W}} = \sigma_{\mathcal{V}} = 20$ mm in sagittal view. For this selected parameter pair, segmentation artefacts and detailed shape features are not captured in the registration process.

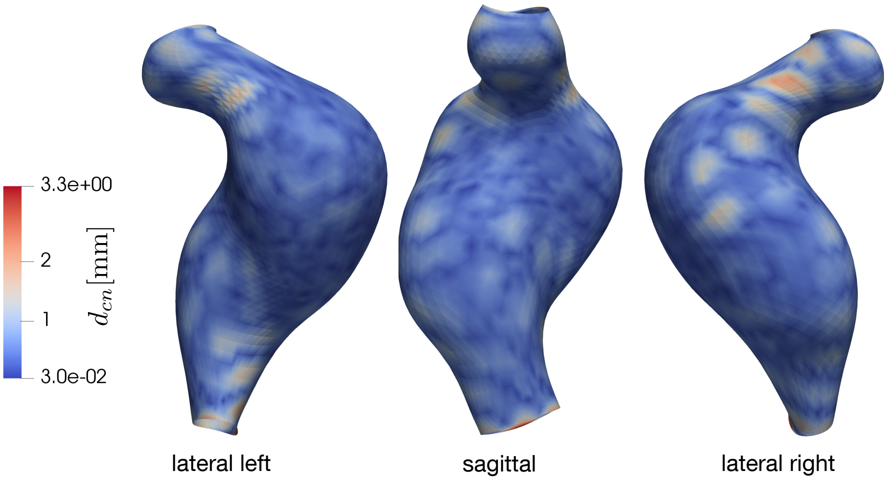

Figure 4.2.4.: The closest-node $d_{cn}$ distance distribution of $\varphi_1^{v_0^\perp}(S)$ for AAA case no. 85 with $\sigma_{\mathcal{W}} = \sigma_{\mathcal{V}} = 20$ mm in sagittal, lateral left and lateral right view. The mean $\bar{d}_{cn}$ distance of all points is 0.589 mm. The displayed graph on the right shows the $d_{cn}$ distance distribution over deformed $\varphi_1^{v_0^\perp}(S)$. The largest $d_{cn}$ distances are found in the neck and inlet boundaries.

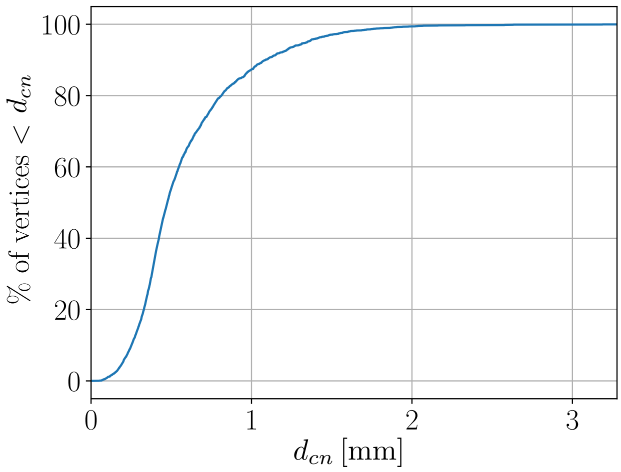

Figure 4.2.5.: Plot of percentage of points over the $d_{cn}$ distance. For case no. 85 and the selected parameter pair, 100 $\%$ of vertices have 2 mm or less distance error.

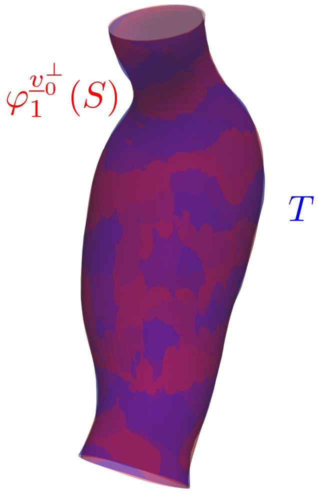

Figure 4.2.6.: Registration result of AAA case no. 55 with $\sigma_{\mathcal{W}} = \sigma_{\mathcal{V}} = 20$ mm in sagittal view. For this selected parameter pair, the registration result for case no. 55 captures the detailed shape features. Segmentation artefacts are still filtered.

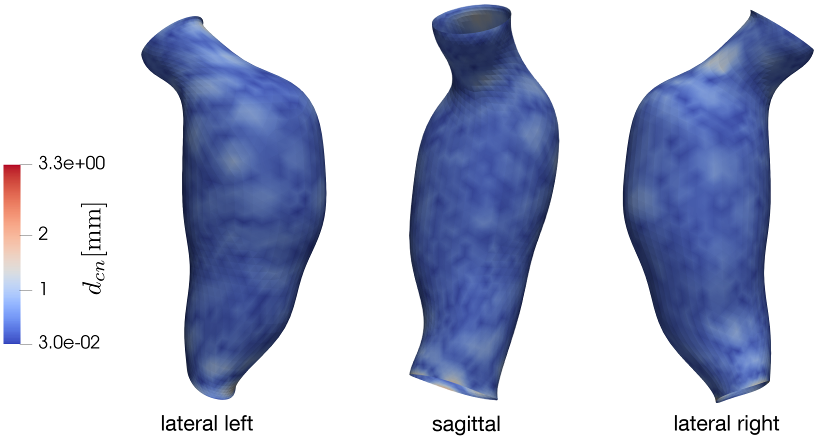

Figure 4.2.7.: Closest-node distance $d_{cn}$ distribution of $\varphi_1^{v_0^\perp}(S)$ for AAA case no. 55 with $\sigma_{\mathcal{W}} = \sigma_{\mathcal{V}} = 20$ mm in sagittal, lateral left and lateral right view. The mean $\bar{d}_{cn}$ distance of all points is 0.42 mm. The displayed graph on the right side shows the $d_{cn}$ distance distribution over deformed $\varphi_1^{v_0^\perp}(S)$. The largest $d_{cn}$ distances are found on inlet boundaries.

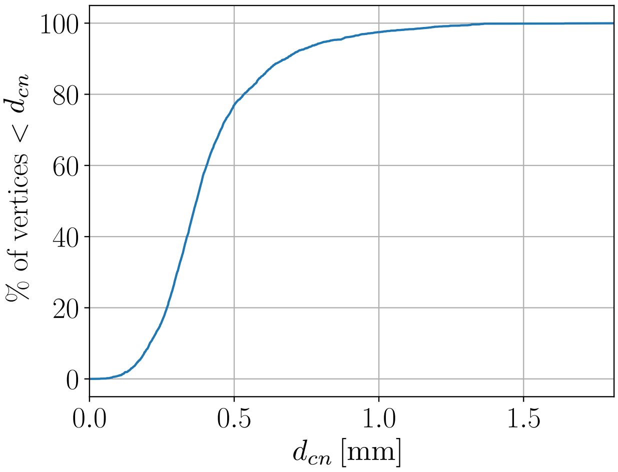

Figure 4.2.8.: Plot of percentage of points over the $d_{cn}$ distance measured with the $L^2$ norm. For case no. 55 and the selected parameter pair, 100 % of vertices have 1.1 mm or less distance error.

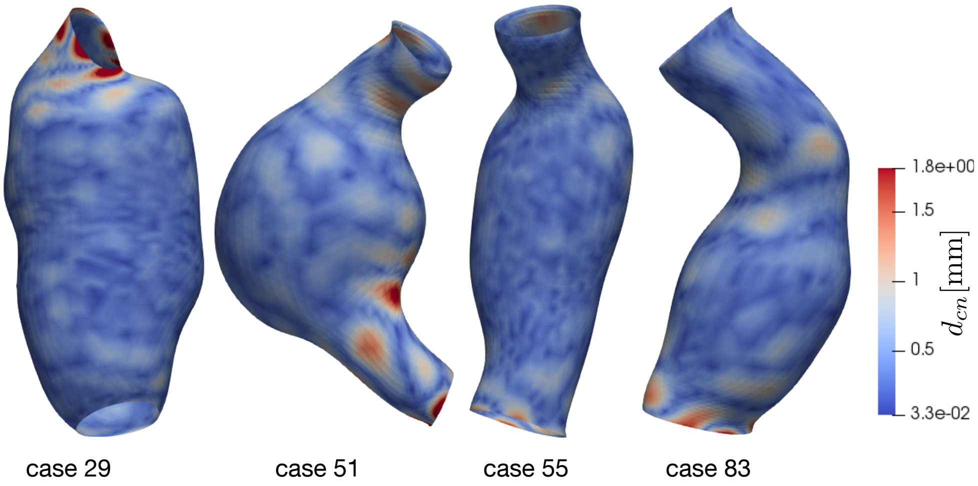

Figure 4.2.9.: Visualization of registration results of some patient-specific AAA abluminal surfaces from the coronal view. The results are represented with the closest-node $d_{cn}$ distance in mm which is measured between the registration result at $t = 1$ and the associated original shape $T$.

# Part II.

# Statistical shape analysis

# 5. Mathematical background

The second part of the present work is concerned with the statistical interpretation of the initial momenta $\underline{\mu}_0^{\perp}$ that was acquired for each AAA in the cohort at the end of the first part. Thanks to the momentum conservation given for the geodesic paths starting with initial momenta $\underline{\mu}_0^{\perp}$ (review subsection 2.1.1), the AAA-specific initial momenta provide a legitimate representation of the individual AAA shape in the tangent-space.
According to Vaillant et al. [182] who first introduced statistical analysis on diffeomorphisms in 2004, the tangent vectors $\underline{\mu}_0^{\perp}$ span a linear space and parameterize the diffeomorphism of reference geometry $S$ to N target AAA shapes $T$. The thereby created tangent space representation enables Log-Euclidean statistical applications on diffeomorphisms following vectorial statistics, and consequently statistical analysis of shapes.
Employing dimensionality-reduction techniques on this linear shape space achieves an abstract and low-dimensional geometrical characterization of each AAA shape with so-called shape descriptors $\underline{s}$.

Consequently, the statistical shape analysis conducted in the tangent-space opens up new possibilities for shape understanding compared to shape analysis in the non-linear shape space. With the established approximated linear shape representation in the tangent-space, mean shape appearances and the variabilities can be calculated with standard vectorial methods. Also, point correspondences and noise in the shape space can be overcome.
Following this concept, shape variability of several anatomical surface models has been conducted over the past years. Durrleman et al. examine for instance the brain structure variability based on diffeomorphisms [45], while Bruse et al. benefit from statistics in tangent-space to determine biomarkers of repaired aortic coarctation arches for potential functional relevance [24]. Also, Mansi et. al employ this technique to develop a quantification and prediction model of the cardiac remodelling in the case of Fallot [117].

The rigid parameterization with $\underline{\tau}$ is not incorporated in the statistical analysis as the rigid registration component does not involve shape information. That is why it is important to clearly separate the non-rigid and rigid components in a diffeomorphism.

In this work, the statistical analysis builds on principal component analysis (PCA). The application of this method in the field of shape analysis goes back to 1995 when Cootes et al. employ it in their active shape models [31]. In the field of shape analysis, the PCA is used to extract principal shape features that are defined as the shape features with the maximum variance. Furthermore, it is used to create abstract dimensionally reduced shape descriptors which are acquired in the generated reduced systems of PCA. Two forms of PCA are examined in this work: linear/classical and kernel PCA which are presented in the following.

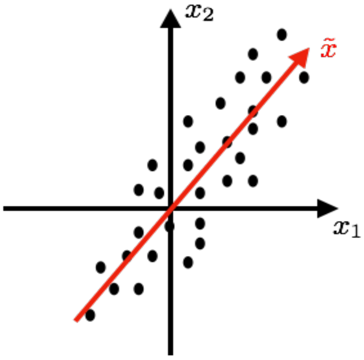

Figure 5.1.1.: Visualization of PCA concept of dimensionality reduction. The red direction represents the direction identified by PCA which possesses the maximum variance when the data are mapped onto it. Subsequently, a datum can be represented with one variable, namely $\tilde{x}$ in the PCA dimensionality reduced space.

## 5.1. Principal component analysis

The principal component analysis method (PCA) belongs to the most widely used techniques for dimensionality reduction and was introduced by Karl Pearson in 1901 [143]. The PCA is effectively a linear orthogonal transformation of input data to a new coordinate system where the input data can be expressed with remarkably fewer variables and without a significant loss of information. The new basis is unique for an examined data set and can meet different requirements. Its determination is subject of this section.

PCA represents an unsupervised learning technique such that no class information or similar knowledge is integrated in the procedure. The PCA is usually a preprocessing step of dimensionality reduction and is solely based on data variances. It helps eliminate dimensions with low variance.

### 5.1.1. Linear principal component analysis

For the explanation of the PCA method, let $\underline{p}$ be one datum or feature vector of the data set $\mathcal{P}$. The vector $\underline{p}$ of dimension $\mathbb{R}^p$ contains hence all $p$ features that belong to one observation. The collection of all $(\underline{p}_1, \ldots, \underline{p}_N)$ builds the data set $\mathcal{P}$ and includes $N$ observations.

Figure 5.1.1 shows the concept of PCA in 2D. The PCA identifies one dimension (in red) with the maximum variance. This means that when the data points (black dots) are projected onto this dimension, they are not mapped on top of each other.

## Optimization problem

According to [91], an appropriate basis with a dimension $\tilde{p} \ll p$ is estimated with a least-square optimization problem. The aim is to find as few orthogonal directions as possible that can capture most of the variance of the input data as possible. In addition, the reconstructed $\underline{\tilde{p}}$ from the low-dimensional basis should be as close as possible to the original data set $\mathcal{P}$. This goal can be achieved by minimizing the error in

$$J_{\text{PCA}} = E\{\|\underline{p} - \underline{\tilde{p}}\|^2\}. \tag{5.1.1}$$

The reconstructed $\underline{\tilde{p}}$ is carried out with

$$\underline{\tilde{p}} = \sum_{i}^{\tilde{p}} \langle \underline{w}_i, \underline{p} \rangle \underline{w}_i. \tag{5.1.2}$$

The vectors $\underline{w}_i \in \mathbb{R}^p$ are the basis vectors of the new coordinate system and are constructed so as to be orthonormal. The scalar product $\langle \underline{w}_i, \underline{p} \rangle$ is the orthogonal projection of original feature vector $\underline{p}$ onto one new basis vector $\underline{w}_i$. The resulting scalar $s_i$ is called score. For a basis of dimension $\tilde{p}$, the reduced vector $\underline{s}$ has $\tilde{p}$ scores, one for the projection onto each axis $\underline{w}$

$$\underline{s} = [\langle \underline{w}_1, \underline{p} \rangle, \ldots, \langle \underline{w}_{\tilde{p}}, \underline{p} \rangle]^{\mathrm{T}}.$$

The vector $\underline{s} \in \mathbb{R}^{\tilde{p}}$ is the low-dimensional representation of original observation vector $\underline{p}$. Thus, the reconstructed $\underline{\tilde{p}}$ can be formulated with

$$\underline{\tilde{p}} = \sum_{i}^{\tilde{p}} s_i \cdot \underline{w}_i. \tag{5.1.3}$$

If the orthonormal basis vectors are grouped in the basis matrix $\underline{W} \in \mathbb{R}^{p \times \tilde{p}}$ with $\underline{W} = [\underline{w}_1, \ldots, \underline{w}_{\tilde{p}}]$, the reduction can be simplified to

$$\underline{s} = \underline{W}^{\mathrm{T}} \underline{p}. \tag{5.1.4}$$

Hence, the matrix $\underline{W}$ is responsible for the linear orthogonal transformation of high-dimensional $\underline{p}$ to a lower dimensional representation $\underline{s}$. As $\underline{W}$ is an orthonormal matrix, $\underline{W}^{\mathrm{T}} \underline{W} = \underline{I}$ is given. Additionally, the reconstructed $\underline{\tilde{p}}$ can be computed with $\underline{\tilde{p}} = \underline{W}\,\underline{W}^{\mathrm{T}} \underline{p}$. Integrating this reformulation in Equation 5.1.1 yields

$$J_{\text{PCA}} = E\{\|\underline{p} - \underline{W}\,\underline{W}^{\mathrm{T}} \underline{p}\|^2\}. \tag{5.1.5}$$

The questions of how to determine appropriate principal directions $\underline{W}$ and of how to assess the variance captured with one direction $\underline{w}_i$ are answered in the following.

## Variance and covariance

First, some variance-related terms need to be clarified. The variance is a measure of how spread out the data $\underline{p}$ is. It measures therewith the variability of the data set $\mathcal{P}$ according to

$$var(\underline{p}) = \frac{1}{N} \sum_{i}^{N} (\underline{p}_i - \underline{\hat{p}})^{\mathrm{T}} (\underline{p}_i - \underline{\hat{p}})$$

with $\hat{\underline{p}}$ as the mean vector $\hat{\underline{p}} = \frac{1}{N}\sum_i^N \underline{p}_i$ of data set $\mathcal{P}$. The corresponding covariance matrix $\underline{\Sigma}_{\mathcal{P}}$ of the data set $\mathcal{P}$ is formulated with

$$\underline{\Sigma}_{\mathcal{P}} = \frac{1}{N-1}\big(\underline{P}_{\mathcal{P}} - \hat{\underline{P}}_{\mathcal{P}}\big)\big(\underline{P}_{\mathcal{P}} - \hat{\underline{P}}_{\mathcal{P}}\big)^{\mathrm{T}} \qquad \in \mathbb{R}^{p\times p}. \tag{5.1.6}$$

The flattened vector $\underline{P}_{\mathcal{P}} \in \mathbb{R}^{p\cdot N\times 1}$ contains all $N$ observations of the data set $\mathcal{P}$ as $\underline{P}_{\mathcal{P}} = [\underline{p}_i, \dots, \underline{p}_N]$, but in a flattened representation. $\hat{\underline{P}}_{\mathcal{P}}$ represents the mean in the flattened form.

The covariance reveals the correlation between two random data sets $\mathcal{P}$ and $\mathcal{U}$ with

$$cov(\underline{p}, \underline{u}) = \frac{1}{N}\sum_i^N (\underline{p}_i - \hat{\underline{p}})^{\mathrm{T}}(\underline{u}_i - \hat{\underline{u}}).$$

$\hat{\underline{u}}$ represents the mean of $\mathcal{U}$. If $cov(\underline{p}, \underline{u})$ is zero, there is no correlation between both data sets.

## Solution

According to [82], the PCA objective function in Equation 5.1.5 can be reformulated to

$$J_{\mathrm{PCA}} = \mathrm{Tr}\big\{\underline{W}^{\mathrm{T}}\underline{\Sigma}_{\mathcal{P}}\underline{W}\big\}. \tag{5.1.7}$$

According to [91, 92], $J_{\mathrm{PCA}}$ in Equation 5.1.7 is minimized if the $\tilde{p}$ basis vectors $\underline{w}$ in basis $\underline{W}$ are the $\tilde{p}$ eigenvectors associated with the $\tilde{p}$ largest eigenvalues of the covariance matrix $\underline{\Sigma}_{\mathcal{P}}$.

The eigenvalue decomposition of orthonormal $\underline{\Sigma}$ delivers

$$\underline{\Sigma}_{\mathcal{P}} = \underline{V}\,\underline{\Lambda}\,\underline{V}^{\mathrm{T}} \tag{5.1.8}$$

with unitary matrix $\underline{V} \in \mathbb{R}^{p\times p}$ of $p$ eigenvectors $\underline{v}_e$ and diagonal matrix $\underline{\Lambda} \in \mathbb{R}^{p\times p}$ of $p$ eigenvalues $(\lambda_1, \dots, \lambda_p)$. The eigenvalues are arranged by value $\lambda_1 \geq \lambda_2 \geq \dots \geq \lambda_p$.

Consequently, after choosing the number of necessary $\tilde{p}$ eigenvectors, the reduction in Equation 5.1.4 can be written with

$$\underline{s} = \underline{\Lambda}^{-\frac{1}{2}}\underline{V}^{\mathrm{T}}\underline{p} \qquad \in \mathbb{R}^{\tilde{p}}$$

with the decreased diagonal matrix $\underline{\Lambda} \in \mathbb{R}^{\tilde{p}\times\tilde{p}}$ with $\tilde{p}$ eigenvalues $\lambda$ and the corresponding $\tilde{p}$ eigenvectors $\underline{v}_e$ in $\underline{V} \in \mathbb{R}^{p\times\tilde{p}}$. The input vector $\underline{p}$ is expected to be a centered, i.e. zero-mean, vector which can be easily achieved by substracting the mean vector $\hat{\underline{p}}$.

The resulting projection on each basis vector $\underline{w}_i$ is the so-called score and generates the new variable $s_i$ in a reduced $\underline{s}$. As the basis vectors are orthonormal, the scores $s_i$ in a $\underline{s}$ are uncorrelated.

Therewith, the original datum $\underline{p}$ can be approximated with

$$\tilde{\underline{p}} \approx s_1 \cdot \underline{w}_1 + \dots + s_{\tilde{p}} \cdot \underline{w}_{\tilde{p}} \tag{5.1.9}$$

in the reduced basis according to Equation 5.1.3.

### Singular value decomposition for PCA

If the size of a datum exceeds the number of available observations in the dataset, then the eigenvalue decomposition of $\underline{\Sigma}_{\mathcal{P}}$ in Equation 5.1.8 can become difficult due to the null eigenvalues. Another more appropriate approach to the PCA problem is in this case the Singular Value Decomposition (SVD) which can handle null eigenvalues [67]. The SVD is performed directly on the (centered) data matrix $\underline{P}_{\mathcal{P}}$ with

$$\underline{P}_{\mathcal{P}} = \underline{U}\,\underline{D}\,\underline{V}^{\mathrm{T}} \tag{5.1.10}$$

with $\underline{P}_{\mathcal{P}} \in \mathbb{R}^{p \times N}$, $\underline{D}$ is a diagonal matrix of size $p \times N$, $\underline{U} \in \mathbb{R}^{p \times p}$ and $\underline{V} \in \mathbb{R}^{N \times N}$.

In this case, the principal axes are the columns of $\underline{V}$ and have the same directions as the axes found by the eigenvalue decomposition on $\underline{\Sigma}_{\mathcal{P}}$ in Equation 5.1.8. The only difference lies in the scaled eigenvalues. The scale is determined if the expression in Equation 5.1.10 for input space $\underline{P}_{\mathcal{P}}$ is embedded in the covariance matrix (Equation 5.1.6) with

$$\begin{aligned}
\underline{\Sigma}_{\mathcal{P}}^{\mathrm{SVD}} &= (\underline{U}\,\underline{D}\,\underline{V}^{\mathrm{T}})^{\mathrm{T}}\underline{U}\,\underline{D}\,\underline{V}^{\mathrm{T}}/(n-1) \\
&= \underline{V}\,\underline{D}\,\underline{U}^{\mathrm{T}}\underline{U}\,\underline{D}\,\underline{V}^{\mathrm{T}}/(n+1) \\
&= \underline{V}\,\frac{\underline{D}^2}{n-1}\,\underline{V}^{\mathrm{T}}.
\end{aligned} \tag{5.1.11}$$

The comparison of the last expression of Equation 5.1.11 and the original PCA covariance matrix (Equation 5.1.8) yields the scaling difference according to

$$\lambda_i^2 = \frac{d_i^2}{n-1}$$

with $d_i$ the eigenvalues of $\underline{\Sigma}_{\mathcal{P}}^{\mathrm{SVD}}$.

As mentioned, the SVD can handle null eigenvalues. Hence, SVD can generate eigenvalues equal to or very close to 0. This would mean that one dimension is linearly dependent on another dimension and thus can be totally represented by the first one.
In a 2D case with two linear dependent dimensions, all (centered) data points would already lie on the first principal component with an eigenvalue $\lambda_1 \neq 0$. The second identified principal component would be orthogonal to the first one with an eigenvalue $\lambda_2 = 0$. The mapping of the centered data points onto the second component would always generate a zero.

## Outliers and PCA

The presented PCA method represents the classic PCA approach. A disadvantage of the classic PCA is its sensitivity to outliers. It follows from the nature of the minimization problem in Equation 5.1.1. Therein, the cost function consists of a sum of quadratic norms of original data and reconstructed data. If outliers are present, they would dominate the total sum and manipulate the resulting principal axes of the method.
In chapter 6, the outlier detection is covered for the present work.

In literature, derived robust PCA methods were recently developed [90, 133]. These are not covered in this work, but represent a further interesting development of this work.

### 5.1.2. Kernel principal component analysis

The kernel PCA is a non-linear method which makes use of the relation between multidimensional scaling and PCA. It has been mainly brought forward by Scholkopf et al. in the late nineties [158, 160]. The kernel PCA transforms the input data $\underline{p}$ with a transformation $\underline{\Phi}$ into a higher dimensional space where the resulting mapped vectors $\underline{\Phi}(\underline{p})$ have a shape which can be captured by linear PCA. The linear PCA is thus applied to $\underline{\Phi}(\underline{p})$ in the higher dimensional space. The corresponding reduced representation of input $\underline{P}_{\mathcal{P}}$ is obtained.

#### Multidimensional scaling

Another equivalent, classic linear dimensionality reduction method is multidimensional scaling (MDS). Therein, instead of a covariance matrix, a Gram matrix $\underline{G}$ is analysed. A Gram matrix is constructed with inner products

$$\underline{G} = \underline{P}_{\mathcal{P}}^{\mathrm{T}} \underline{P}_{\mathcal{P}} \qquad\qquad \in \mathbb{R}^{N \times N} \tag{5.1.12}$$

with N the number of observations $\underline{p}$ included in $\underline{P}_{\mathcal{P}}$. The $i-, j-$ component of $\underline{G}$ is calculated from the inner product of observation $\underline{p}_i$ and $\underline{p}_j$. Since the Gram matrix $\underline{G}$ is a real, symmetric matrix, its eigen-decomposition results in

$$\underline{G} = \underline{W}_N \underline{D}_N \underline{W}_N^{\mathrm{T}} \tag{5.1.13}$$

with eigenvectors in $\underline{W}_N$ and corresponding eigenvalues in $\underline{D}_N$ [22, 103, 104]. The space spanned by the MDS eigenvectors corresponds to the space spanned by the linear PCA, and also the eigenvalues are the same [92]. These eigenvectors are orthogonal to one another in the input space of $\underline{p}$.

#### Multidimensional scaling in kernel PCA

Similar to classic linear PCA, the covariance matrix of mapped $\underline{\Phi}(\underline{p})$ has to be calculated, a definition of mapping $\underline{\Phi}$ is therefore required. Finding an appropriate $\underline{\Phi}$ for every data set is tedious and not straightforward. At this point, the correspondence to MDS comes into play. There, for building the Gram matrix, only the inner product between the input data is required, a precise knowledge of $\underline{\Phi}(\underline{p})$ is not necessary. Also in the kernel PCA method, the Gram matrix is assembled to perform the non-linear dimensionality reduction: With the defined form of the inner product, the explicit definition of mapping $\underline{\Phi}$ is obviated. Usually, kernel functions $k$ are used to establish these inner products, according to

$$\langle \underline{\Phi}(\underline{p}_1), \underline{\Phi}(\underline{p}_2) \rangle = k(\underline{p}_1, \underline{p}_2). \tag{5.1.14}$$

The Gram matrix is consequently composed with

$$\underline{G} = \begin{bmatrix} \langle \underline{\Phi}(\underline{p}_1), \underline{\Phi}(\underline{p}_2) \rangle & \dots & \langle \underline{\Phi}(\underline{p}_1), \underline{\Phi}(\underline{p}_N) \rangle \\ \vdots & \vdots & \vdots \\ \langle \underline{\Phi}(\underline{p}_N), \underline{\Phi}(\underline{p}_1) \rangle & \dots & \langle \underline{\Phi}(\underline{p}_N), \underline{\Phi}(\underline{p}_N) \rangle \end{bmatrix} = \begin{bmatrix} \langle k(\underline{p}_1, \underline{p}_1) & \dots & k(\underline{p}_1, \underline{p}_N) \\ \vdots & \vdots & \vdots \\ k(\underline{p}_N, \underline{p}_1) & \dots & k(\underline{p}_N, \underline{p}_N) \end{bmatrix} \quad \in \mathbb{R}^{N \times N}. \tag{5.1.15}$$

The use of a kernel to expand the dimensionality of the feature space to attain more linear representations thereof is known as the kernel trick and was first introduced in [158] for mappings. The kernel trick is used in various machine learning and data analysis applications [17, 86, 159, 166]. For the interested reader, further developments and applications of kernel PCA can be found in [15, 34, 150].
The input space is mapped to a higher dimensional space where linear PCA or the equivalent MDS can be employed. As an exact definition of a mapping $\underline{\Phi}$ is complicated, the MDS method is preferred to obtain the principal components. To that end, the eigen-decomposition of the Gram matrix $\underline{G}$ produces $N$ eigenvalues $\lambda_i^{\underline{G}}$ and corresponding eigenvectors $\underline{g}_i$ for $i = (1, \ldots, N)$, with $N$ the number of observations in $\underline{P}_{\mathcal{P}}$. The introduced cost function (Equation 5.1.5) for linear PCA is also minimized here, but in the higher dimensional space. The eigenvectors are perpendicular in the higher dimensional space, too.

The principal components are reconstructed from the resulting eigenvalues $\underline{g}_i$ for $i = (1, \ldots, N)$ of matrix $\underline{G}$ with

$$\underline{w}_i = \sum_{k=1}^{N} \underline{g}_{i[k]} \underline{\Phi}(\underline{p}_k) \qquad \in \mathbb{R}^{3n_x}. \tag{5.1.16}$$

The expression $\underline{g}_{ik}$ denotes the $k$-th element of eigenvector $\underline{g}_i$. Hence, the orthogonal principal components $\underline{w}_i$ are a linear composition of mapped observations $\underline{\Phi}(\underline{p})$ in the high dimensional space.

Finally, the reduced representation $\tilde{\underline{p}}$ is obtained by projecting the original $\underline{p}$ onto the considered $\tilde{p}$ principal components in the high dimensional space. Consequently, the projection becomes

$$\tilde{\underline{\Phi}}(\underline{p})_{[i]} = \sum_{k=1}^{N} \underline{g}_{i[k]} \underline{\Phi}(\underline{p}_k)^{\mathrm{T}} \underline{\Phi}(\underline{p}) \qquad k = (1, \ldots, \tilde{p}) \tag{5.1.17}$$

with $\tilde{\underline{\Phi}}(\underline{p})_{[i]}$ the $i$-th element of reduced mapped vector $\tilde{\underline{\Phi}}(\underline{p})$, $\underline{g}_{i[k]}$ the $k$-th element of eigenvector $\underline{g}_i$.

The original mapped data $\underline{\Phi}(\underline{p})$ can therefore be approximated in the higher dimensional space from $\tilde{\underline{\Phi}}(\underline{p})_{[i]}$ with

$$\underline{\Phi}(\underline{p}) \approx \tilde{\underline{\Phi}}(\underline{p})_{[1]} \cdot \underline{w}_1 + \ldots + \tilde{\underline{\Phi}}(\underline{p})_{[\tilde{p}]} \cdot \underline{w}_{\tilde{p}} \tag{5.1.18}$$

with $\tilde{\underline{\Phi}}(\underline{p})_{[1]}$ the first component of $\tilde{\underline{\Phi}}(\underline{p})$, $\underline{w}_1$ the first principal component in the higher dimensional space. $\tilde{p}$ is the dimension of reduced model.

However, the reconstruction of $\underline{p}$ in the original input space is often required than in the higher dimensional space. Retrieving approximated $\tilde{\underline{p}} \in \mathbb{R}^{\tilde{p}}$ from $\tilde{\underline{\Phi}}(\underline{p})$ is not straightforward and computationally demanding. Usually, an optimization problem generates an estimation of $\tilde{\underline{p}}$ by minimizing the cost function

$$J_{\text{recon}} = \|\underline{\Phi}(\tilde{\underline{p}}) - \tilde{\underline{\Phi}}(\underline{p})\|^2. \tag{5.1.19}$$

Depending on the selected inner product and the associated space, this optimization problem is solved by a gradient descent scheme. In the case of employing kernels for scalar products as displayed above in Equation 5.1.14, a straightforward derivation of gradient of $J_{\text{recon}}$ serves as input for the gradient descent for instance and is described in [122].

Compared to linear PCA, kernel PCA is computationally more expensive. However, the expensive component extraction pays off when kernel PCA is integrated in further statistical methods, like support vector machines (SVM). Combining kernel PCA with linear SVM achieves an accurate decision boundary of a non-linear dataset much faster than non-linear SVM [158]. .

## 5.1.3. Quality assessment of dimensionality reduction

As with dimensionality reduction methods, accuracy errors when retrieving the original data in the dimensionally reduced model occur. In the following, the relevant reconstruction errors and their definition in this chapter are presented. Additionally, methods to evaluate the statistical performance of the principal component analysis are introduced.

### Reconstruction Errors

In this work, the principal component analysis is performed on the initial momenta vector fields in the tangent-space of the examined shapes. The dimensionally reduced model is created subsequently in the tangent-space. The reconstruction error however is measured in the shape space, i.e. the shape corresponding to the dimensionally reduced momenta vector field is generated with geodesic shooting and is compared to the original shape. As the reduction does not include the translation vector $\underline{\tau}$, the optimal $\underline{\tau}$ which has resulted in the registration step is taken in the geodesic shooting. The modular registration method requires both inputs to generate indicative results. The error is then measured in Euclidean $L^2$ with the node-wise distance and in $\mathcal{W}$ using the normalized dissimilarity measure as in subsection 4.2.1.

### Evaluation of statistical performance

In this work, two main statistical qualities play an important role in the evaluation of principal component analysis performance. One is generalization and the other is compactness.

The generalization error describes the behaviour of a reduced model applied to unseen data. The question here is if the model can accurately predict or reconstruct unseen data. To that end, in a Leave-One-Out-Cross-Validation (LOOCV) process, one datum is left out and the reduced model is built from the remaining $N-1$ data. The left-out datum is then passed to the generated reduced model, i.e. mapped onto the dimensionally reduced PCA model. The ability of the PCA model to accurately represent the left-out shape is assessed in the shape space using the reconstruction error.

The compactness error describes the dimensionality of the reduced system: The lower the dimension for a comparable reconstruction error, the more compact the reduction.

## 5.2. Summary

In this chapter, the mathematical background for the upcoming statistical shape analysis is outlined, focusing on the principal component analysis (PCA) with two different approaches, the linear and kernel PCA method. With both PCA methods, a reduced system for shape representation is generated. For each method, the derivation is displayed. Additionally, quantifications of the reduced system qualities are discussed.

In the following, the methods are adapted to the shape representation generated in this work using the modular matching framework.

# 6. Method and implementation

This chapter focuses on the final methods, specifically the linear and kernel PCA, used for statistical analysis of the resulting initial momenta $\underline{\mu}_0^{\perp}$ in chapter 4 and the associated implementation. An exemplary synthetic cohort is generated and examined with regard to its shape by using the implemented methods. The examinations should provide a better understanding of linear and kernel PCA when applied to the feature space generated by the modular registration method in this work.

## 6.1. Principal component analysis

In this work, principal component analysis (PCA) forms the basis of the statistical analysis. The mathematical concept of linear and kernel PCA were presented in section 5.1. In the following, their integration in this work is layed out.

### 6.1.1. Linear principal component analysis

In this work, linear principal component analysis (LPCA) operates in $\mathcal{V}^{\perp *}$ where the initial momenta vector fields $\underline{\mu}_0^{\perp}$ reside. The space $\mathcal{V}^{\perp *}$ represents the dual space of RKHS $\mathcal{V}^{\perp}$ of $\underline{v}_0^{\perp}$.

### Singular value decomposition

The LPCA employed here is based on singular value decomposition (SVD) for constructing the covariance matrix due to the high dimensionality of flattened initial momenta vector field $(3n_x)$. The resulting covariance matrix $\underline{\Sigma}_{\mathcal{P}}^{\mathrm{LPCA}}$ subsequently comprises $N$ initial momenta vector fields $\underline{\mu}_0^{\perp} \in \mathbb{R}^{3n_x}$ building its columns. $N$ represents the number of observations, i.e. examined AAA cases.
Accordingly, the final covariance matrix $\underline{\Sigma}_{\mathcal{P}}^{\mathrm{LPCA}}$ has a size of $3n_x \times N$, such that:

$$\underline{\Sigma}_{\mathcal{P}}^{\mathrm{LPCA}} = [\underline{\mu}_{0,1}^{\perp}, \underline{\mu}_{0,2}^{\perp}, \dots, \underline{\mu}_{0,N}^{\perp}] \qquad \in \mathbb{R}^{3n_x \times N}. \tag{6.1.1}$$

The SVD of $\underline{\Sigma}_{\mathcal{P}}^{\mathrm{LPCA}}$ returns $N$ sorted eigenvalues $\lambda_i, i = (1, \dots, N)$ and associated normalized eigenvectors $\underline{m}$. These eigenvectors are known as modes which represent the principal components in the examined initial momenta vector fields collected in $\underline{\Sigma}_{\mathcal{P}}^{\mathrm{LPCA}}$. These modes describe the dominating deformation directions of the cylindrical source $S$ to every AAA shape in the cohort, encoding thus the dominant shape features in the cohort. The shape features can be deduced and visualized from the dominant deformation directions with geodesic shooting. These modes are elements of the dual space $\mathcal{V}^{\perp *}$.

The associated eigenvalues depict the variance along such a mode. The variance indicates the variation of the encoded shape feature in the cohort. If the variance is large, the associated shape feature is represented in the cohort taking a wide range of values [182].

The appropriate number $m$ of principle components sufficient for accurately representing the higher dimensional data is determined by the explained variance $\pi$ which is written as

$$\pi(m) = \frac{\sum_i^m \lambda_i}{\sum_i^N \lambda_i} \tag{6.1.2}$$

and is usually set to $0.98$ to achieve $98\%$ of accuracy.

One significant feature of this approach lies in the structure of resulting momenta vectors which are perpendicular to one another. This leads to their statistical independency.

### Generation of shape descriptors

The shape descriptors $\underline{s}_i \in \mathbb{R}^m$ for every AAA shape $T_i$ result from

$$\underline{s}_i = \left[\langle \underline{\mu}_{0,i}^{\perp}, \underline{m}_1 \rangle_{\mathcal{V}^{\perp *}}, \dots, \langle \underline{\mu}_{0,i}^{\perp}, \underline{m}_m \rangle_{\mathcal{V}^{\perp *}}\right]^{\mathrm{T}} \tag{6.1.3}$$

with scalar products $\langle \cdot, \cdot \rangle_{\mathcal{V}^{\perp *}}$ in $\mathcal{V}^{\perp *}$ of every flattened initial momenta field $\underline{\mu}_{0,i}^{\perp} \in \mathbb{R}^{3n_x}$. This scalar product is equivalent in this case to the dot product.

## Reconstruction of initial momenta from shape descriptors

The original initial momenta vector fields $\underline{\mu}_{0,i}^{\perp} \in \mathbb{R}^{3n_x}$ are approximated with a linear composition of the $m$ basis vectors, following:

$$\tilde{\underline{\mu}}_{0,i}^{\perp} = \underline{s}_i^{\mathrm{T}} \cdot [\underline{m}_1, \dots, \underline{m}_m] \qquad \in \mathbb{R}^{3n_x}. \tag{6.1.4}$$

## 6.1.2. Kernel principal component analysis

In this work, the higher dimensional space to which the input space is mapped to is the RKHS $\mathcal{V}^{\perp}$. The representation of an input initial momenta $\underline{\mu}_0^{\perp}$ in the higher dimensional space RKHS $\mathcal{V}^{\perp}$ becomes the familiar initial velocity $\underline{v}_0^{\perp}$ which equals the mapping result of $\underline{\Phi}(\underline{\mu}_0^{\perp})$ (Equation 5.1.14). The kernel PCA takes place in the RKHS $\mathcal{V}^{\perp}$.

Accordingly, the Gram matrix $\underline{G}$ in Equation 5.1.15 consists of inner products

$$\underline{G} = \begin{bmatrix} \langle \underline{v}_{0,1}^{\perp}, \underline{v}_{0,1}^{\perp} \rangle_{\mathcal{V}^{\perp}} & \cdots & \langle \underline{v}_{0,1}^{\perp}, \underline{v}_{0,N}^{\perp} \rangle_{\mathcal{V}^{\perp}} \\ \vdots & \vdots & \vdots \\ \langle \underline{v}_{0,N}^{\perp}, \underline{v}_{0,1}^{\perp} \rangle_{\mathcal{V}^{\perp}} & \cdots & \langle \underline{v}_{0,N}^{\perp}, \underline{v}_{0,N}^{\perp} \rangle_{\mathcal{V}^{\perp}} \end{bmatrix} \tag{6.1.5}$$

The initial velocity vector field $\underline{v}_{0,i}^{\perp}$ represents with $i = (1, \ldots, N)$ the centered initial momenta $\underline{\mu}_{0,i}^{\perp}$ in RKHS $\mathcal{V}^{\perp}$. The corresponding inner product is defined with kernel $k_{\mathcal{V}^{\perp}}$ according to

$$\langle \underline{v}_{0,i}^{\perp}, \underline{v}_{0,j}^{\perp} \rangle_{\mathcal{V}^{\perp}} = \sum_{k=1}^{n_x} \sum_{l=1}^{n_x} k_{\mathcal{V}^{\perp}}(\underline{q}_k, \underline{q}_l)(\underline{\mu}_{0,i}^{\perp k})^{\mathrm{T}} \underline{\mu}_{0,j}^{\perp l}. \tag{6.1.6}$$

Herein, $\underline{\mu}_{0,j}^{\perp k}$ and $\underline{\mu}_{0,j}^{\perp l}$ denote the $k$-th and $l$-th vector of initial momenta vector field $\underline{\mu}_{0,j}^{\perp}$. In the context of kernel PCA, the *kernel function* $k(\underline{\mu}_{0,i}^{\perp}, \underline{\mu}_{0,j}^{\perp})$ would take the form $k(\underline{\mu}_{0,i}^{\perp}, \underline{\mu}_{0,j}^{\perp}) = a \cdot (\underline{\mu}_{0,i}^{\perp})^{\mathrm{T}} \underline{\mu}_{0,j}^{\perp}$ of input space vectors $\underline{\mu}_{0,i}^{\perp}, \underline{\mu}_{0,j}^{\perp}$, as prescribed for the kernel $k$ in kernel PCA in Equation 5.1.14. In this work, the factor $a > 0 \in \mathbb{R}$ stands for the evaluation of $k_{\mathcal{V}^{\perp}}(\underline{x}_k, \underline{x}_l)$ which is always $> 0$.

The eigendecomposition of $\underline{G}$ delivers with its $N$ eigenvectors $\underline{g} \in \mathbb{R}^N$ the required principal components. According to Equation 5.1.16, these eigenvectors $\underline{g} \in \mathbb{R}^N$ are used to reconstruct the associated $N$ principal deformation modes with

$$\begin{aligned} \underline{m}_{\mathcal{V}^{\perp}} &= \sum_{k=1}^{N} \underline{g}_{[k]} \, \Phi(\underline{\mu}_{0,k}^{\perp}) \qquad\qquad \in \mathbb{R}^{3n_x} \\ &= \sum_{k=1}^{N} \underline{g}_{[k]} \, \underline{K}_{\mathcal{V}^{\perp}} \, \underline{\mu}_{0,k}^{\perp} = \underline{K}_{\mathcal{V}^{\perp}} \sum_{k=1}^{N} \underline{g}_{[k]} \, \underline{\mu}_{0,k}^{\perp}. \end{aligned} \tag{6.1.7}$$

Herein, $\underline{g}_{[k]}$ represents the $k$-th element of eigenvector $\underline{g} \in \mathbb{R}^N$, $\underline{\mu}_{0,k}^{\perp} \in \mathbb{R}^{3n_x}$ represents the $k$-th observation. The reconstructed principal components $\underline{m}_{\mathcal{V}^{\perp}}$ belong to the higher dimensional RKHS $\mathcal{V}^{\perp}$, $\underline{m}_{\mathcal{V}^{\perp}} \in \mathcal{V}^{\perp}$.

Equation 6.1.7 makes use of the dual space relation, the isometric mapping, between $\underline{\mu}_{0}^{\perp} \in \mathcal{V}^{\perp *}$ and the associated $\underline{v}_{0}^{\perp} \in \mathcal{V}^{\perp}$ (review subsection 3.1.2). The mapping $\Phi(\underline{\mu}_{0}^{\perp})$ of $\underline{\mu}_{0}^{\perp}$ to the RKHS $\mathcal{V}^{\perp}$ becomes the isometric mapping realized with operator $\underline{K}_{\mathcal{V}^{\perp}}$ for the spatially discretized case (see Figure 3.1.3). This already existing definition facilitates to a large degree the application of kernel PCA as in the following.
The corresponding representation of $\underline{m}_{\mathcal{V}^{\perp}} \in \mathcal{V}^{\perp}$ in the dual space $\mathcal{V}^{\perp *}$ is consequently

$$\underline{m} = \sum_{k=1}^{N} \underline{g}_{[k]} \, \underline{\mu}_{0,k}^{\perp}. \tag{6.1.8}$$

Having formulated the principal components in the input space $\mathcal{V}^{\perp *}$ as $\underline{m}$, the further analysis and shape descriptor creation are conducted in the input space $\mathcal{V}^{\perp *}$.

In the next step, the constructed eigenvector $\underline{m} \in \mathcal{V}^{\perp *}$ in Equation 6.1.8 needs to be normalized. This is achieved with the factor $m_{\mathrm{norm}}$

$$m_{\mathrm{norm}} = \frac{1}{\|\underline{m}\|_{\mathcal{V}^{\perp *}}^{2}} = \frac{1}{\underline{m}^{\mathrm{T}} \underline{m}} \tag{6.1.9}$$

for an associated reconstructed deformation mode $\underline{m}$. The normalized constructed eigenvector becomes thus

$$\underline{m}^{\mathrm{norm}} = m_{\mathrm{norm}} \cdot \underline{m} = \frac{1}{\underline{m}^{\mathrm{T}} \underline{m}} \sum_{k=1}^{N} \underline{g}_{[k]} \, \underline{\mu}_{0,k}^{\perp}. \tag{6.1.10}$$

As in linear PCA, the number $m$ for required accuracy is determined according to the explained variance $\pi$ in Equation 6.1.2.

## Generation of shape descriptors

The shape descriptor vector $\underline{s} \in \mathbb{R}^m$ is determined by scalar products in the respective space as in Equation 5.1.17. As the principal component is now defined in the input space $\mathcal{V}^{\perp *}$, the shape descriptors are calculated with scalar products in $\mathcal{V}^{\perp}$ with

$$\underline{s} = [\langle \underline{\mu}_0^{\perp}, \underline{m}_1^{\mathrm{norm}} \rangle_{\mathcal{V}^{\perp *}}, \ldots, \langle \underline{\mu}_0^{\perp}, \underline{m}_m^{\mathrm{norm}} \rangle_{\mathcal{V}^{\perp *}}]^{\mathrm{T}} \qquad \in \mathbb{R}^m. \tag{6.1.11}$$

As in Equation 6.1.3, the scalar product is performed as a dot product.

## Reconstruction of initial momenta from shape descriptors

The reconstruction of initial momenta from shape descriptors $\underline{s} \in \mathbb{R}^m$ is also conducted in the input space $\mathcal{V}^{\perp *}$ following

$$\tilde{\underline{\mu}}_0^{\perp} = s_1 \cdot \underline{m}_1^{\mathrm{norm}} + \ldots + s_m \cdot \underline{m}_m^{\mathrm{norm}} \tag{6.1.12}$$

with $s_1, \ldots, s_m$ being the $m$ elements of the shape vector $\underline{s}$ and $\underline{m}_1^{\mathrm{norm}}, \ldots, \underline{m}_m^{\mathrm{norm}}$ the modes. This reconstruction only includes the non-rigid deformation part of the registration, thereby neglecting the translational transformation. The translation vector $\underline{r}(1)$ has to be added respectively to the resulting non-rigid deformation with $\tilde{\underline{\mu}}_0^{\perp}$.

## 6.1.3. Outlier detection

PCA methods are susceptible to outliers. In an inhomogeneous cohort, outlier detection is therefore necessary. A general overview of outlier detection methods can be found in [80].

### Mahalanobis distance for multivariate outlier detection

The Mahalanobis distance $D_M$ represents a common distance measure and has applications in many methods, like Hotelling's $T^2$ test in process control, $k$-Nearest Neighbour Method in pattern recognition and outlier detection in the field of multivariate calibration [36]. The $D_M$ can be determined in a reduced space, like one achieved with a principal component analysis (PCA), or in the original feature space.
In this work, for determining outliers prior to PCA, the $D_M$ shall be applied to the original feature space which is the RKHS $\mathcal{V}^{\perp}$ and $\mathcal{V}^{\perp *}$, respectively.

The Mahalanobis distance was introduced by P.C. Mahalanobis in 1936 [112]. It measures the distance between a vector and a distribution, unlike the Euclidean distance which gives the distance between two distinct vectors. In particular, the $D_M$ takes the correlation among the vector points into consideration. This is achieved with

$$D_M^2 = (\underline{p} - \underline{\bar{p}})^{\mathrm{T}} \cdot \Sigma^{-1} \cdot (\underline{p} - \underline{\bar{p}}) \tag{6.1.13}$$

with $\underline{p}$ as feature vector, $\underline{\bar{p}}$ as the mean of $N$ feature vectors and $\Sigma^{-1}$ the inverse of the covariance matrix of features.
The term $(\underline{p} - \underline{\bar{p}})^{\mathrm{T}} \cdot \Sigma^{-1}$ is equivalent to the regular standardization, but with a multivariate feature space. With this construction, the distance $D_M$ gets smaller if the correlation within the variables is high, and larger, if the correlation is low. This measure reflects not only the distance, but also the correlation relationship.

For all $N$ feature vectors $\underline{p}$, the distance $D_M$ is measured. Thereof, the mean and standard deviation is calculated. The observations which $D_M$ lies out of three standard deviations scope, is considered an outlier according to the empirical rule [147].

### 6.1.4. Visualization of results

The resulting principal deformation modes $\underline{m}^{\mathrm{norm}}$ can be visualized with geodesic shooting. The visualization is possible since the input space for PCA is the shape space characterized by initial momenta vector fields $\underline{\mu}_0^{\perp}$ in the tangent-space. In this geodesic shooting, the translation vector $\tau$ is zero.

The geodesic shooting is realized with forward temporal integration of momenta ODE in Equation 3.1.25, taking as initial momenta vector field the respective modes $\underline{m}^{+}$ and $\underline{m}^{-}$ belonging to eigenvalue $\lambda$ and eigenvector $\underline{m}$. This applies to linear and kernel PCA. The modes are built according to

$$\begin{aligned} \underline{m}^{+} &= \underline{\bar{\mu}}_0^{\perp} + \underline{m}^{\mathrm{norm}}, \\ \underline{m}^{-} &= \underline{\bar{\mu}}_0^{\perp} - \underline{m}^{\mathrm{norm}}. \end{aligned} \tag{6.1.14}$$

The vector $\underline{\bar{\mu}}_0^{\perp}$ denotes the mean vector of $N$ initial momenta vector fields.
The resulting deformed source $\varphi_1^{\underline{m}_i^{+}}(S)$ and $\varphi_1^{\underline{m}_i^{-}}(S)$ at time $t = 1$ are the final shapes representing the maximum shape variations at both ends of the double variance.

## 6.2. Implementation

Both linear PCA and kernel PCA are implemented in Python, making use of already existing functions of the SciPy library. The matrix in linear PCA is built from the flattened feature vectors of momenta $\underline{\mu}_0^{\perp}$ and its eigen-decomposition is performed with SVD. For building the covariance matrix in kernel PCA, the required scalar products in Equation 6.1.5 are computed with the introduced functions in PyTorch and Keops (see subsection 3.3.3).

The implementation of geodesic shooting is part of the Deformetrica project and contains only the forward model computation. The required input is the initial momenta vector field $\underline{\mu}_0^{\perp}$.

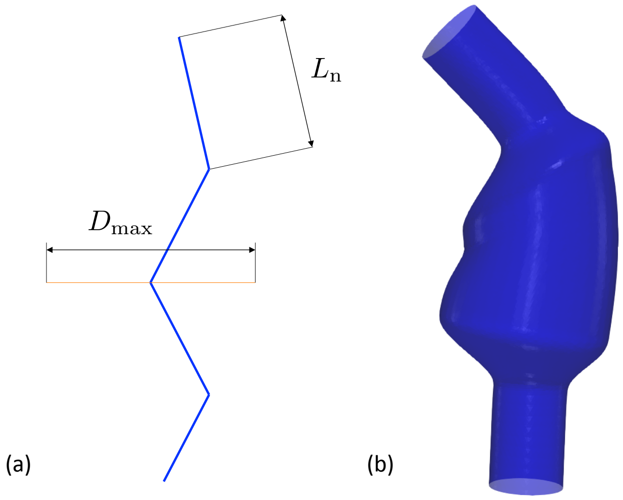

Figure 6.3.1.: (a) the skeleton of the modifiable AAA model with the two relevant parameters for this work, the maximum diameter $D_\mathrm{max}$ and neck length $L_\mathrm{n}$, (b) an example of a resulting parameterized abluminal AAA shape [84].

## 6.3. Explanatory cases

A synthetic cohort of 50 parameterized AAA abluminal surfaces is created with the model presented by Hemmler et. al [84] (see Figure 6.3.1). Therein, on the left, the skeleton of the parameterized surfaces is shown with the two relevant parameters for this work, namely the maximum diameter $D_\mathrm{max}$ and neck length $L_\mathrm{n}$. On the right, an example of a resulting AAA abluminal shape is displayed.
The aim of creating this cohort is to examine and understand the behaviour of principal component analysis methods when applied to the novel non-rigid translation-free initial momenta. That is why - for simplification reasons - the cohort does not depict the real geometrical variation of the patient-specific AAA cohort presented in this work, but varies only in two parameters.

The two parameters $D_\mathrm{max}$ (maximum diameter) and $L_\mathrm{n}$ (neck length) are chosen to create the cohort. They vary according to a Gaussian distribution of mean $\mu$ and variance $\sigma$ with

$$\begin{aligned} D_\mathrm{max} &: \mu = 44\,\mathrm{mm}; \sigma_v = 16\,\mathrm{mm} \\ L_\mathrm{n} &: \mu = 21\,\mathrm{mm}; \sigma_v = 8\,\mathrm{mm}. \end{aligned}$$

The two parameters are chosen such that they do not influence each other when being changed within the created cohort. In the ideal case, if every geometrical parameter of the two parameters controls one shape feature, two principal components are expected when applying linear or kernel PCA on shape-specific initial momenta vector fields. These two principal components shall depict the two main varying geometrical features which are maximum diameter $D_\mathrm{max}$ and neck length $L_\mathrm{n}$.
However, as shown in Figure 6.3.2, when the diameter is changed, some other *hidden* geometrical features get affected and altered too, like the posterior bucket. That is why it is expected

that the main two principal components with biggest eigenvalues reflect $D_{\text{max}}$ and $L_{\text{n}}$, while the remaining principal directions depict these hidden shape variations.
Also, as the maximum diameter $D_{\text{max}}$ possesses the larger variation compared to $L_{\text{n}}$, the first principal axis with the biggest eigenvalue shall belong to this feature.

### Modular registration

As with the patient-specific cohort, the cohort representation in the tangent-space is achieved with the registration of a reference geometry to every AAA abluminal shape in the synthetic cohort using the modular registration. The reference geometry is the same as for the real AAA cases in chapter 4 (see Figure 4.2.1). The registration parameters $\sigma_{\mathcal{W}} = \sigma_{\mathcal{V}^{\perp}} = 18.0\,\text{mm}$ are used for a most accurate registration result.

### Registration results

Figure 6.3.3 shows some registration results of the parameterized cohort for parameters $\sigma_{\mathcal{W}} = \sigma_{\mathcal{V}^{\perp}} = 18.0\,\text{mm}$. The results are expressed with local node-wise distance $d_{cn}$ in $L^2$ and normalized dissimilarity $d_{\mathcal{W}}^{\text{norm}}$. The biggest inaccuracies are located at the inlet. The average error of registration amounts to the following values:

$$\begin{aligned} \text{closest} - \text{node distance}\,\bar{d}_{cn} &: 0.394\,\text{mm} \\ d_{\mathcal{W}}^{\text{norm}} &: 0.00037. \end{aligned}$$

Consequently, the resulting shape-characteristic initial momenta of the non-rigid module are accurate enough and suitable to represent the associated shapes in the following shape analysis. The results of applying such shape analysis methods, here the linear and kernel PCA, are presented in the following.

### Linear PCA

In order to extract the principal shape components in the parameterized cohort, linear PCA is applied to all initial momenta vector fields according to subsection 6.1.1. Taking all cases into consideration, the linear PCA delivers four principal components necessary to represent the shape variability with an accuracy of 98 %. The principal modes are visualized in Figure 6.3.4 after being reconstructed according to Equation 6.1.14. For every eigenvalue $\lambda$, the modes $\underline{m}^{+}$ and $\underline{m}^{-}$ are displayed respectively.
The associated eigenvalues are

$$\lambda_1 = 1.46; \lambda_2 = 1.12; \lambda_3 = 0.14; \lambda_4 = 0.04.$$

The visualized modes $\underline{m}^{+}$ and $\underline{m}^{-}$ in Figure 6.3.4 depict the principal shape variations in the synthetic cohort. The largest two eigenvalues, $\lambda_1$ and $\lambda_2$, correctly exhibit the two varying parameters of the cohort, namely $\lambda_1$ illustrates the changing diameter $D_{\text{max}}$ and $\lambda_2$ the changing length of the neck $L_n$.

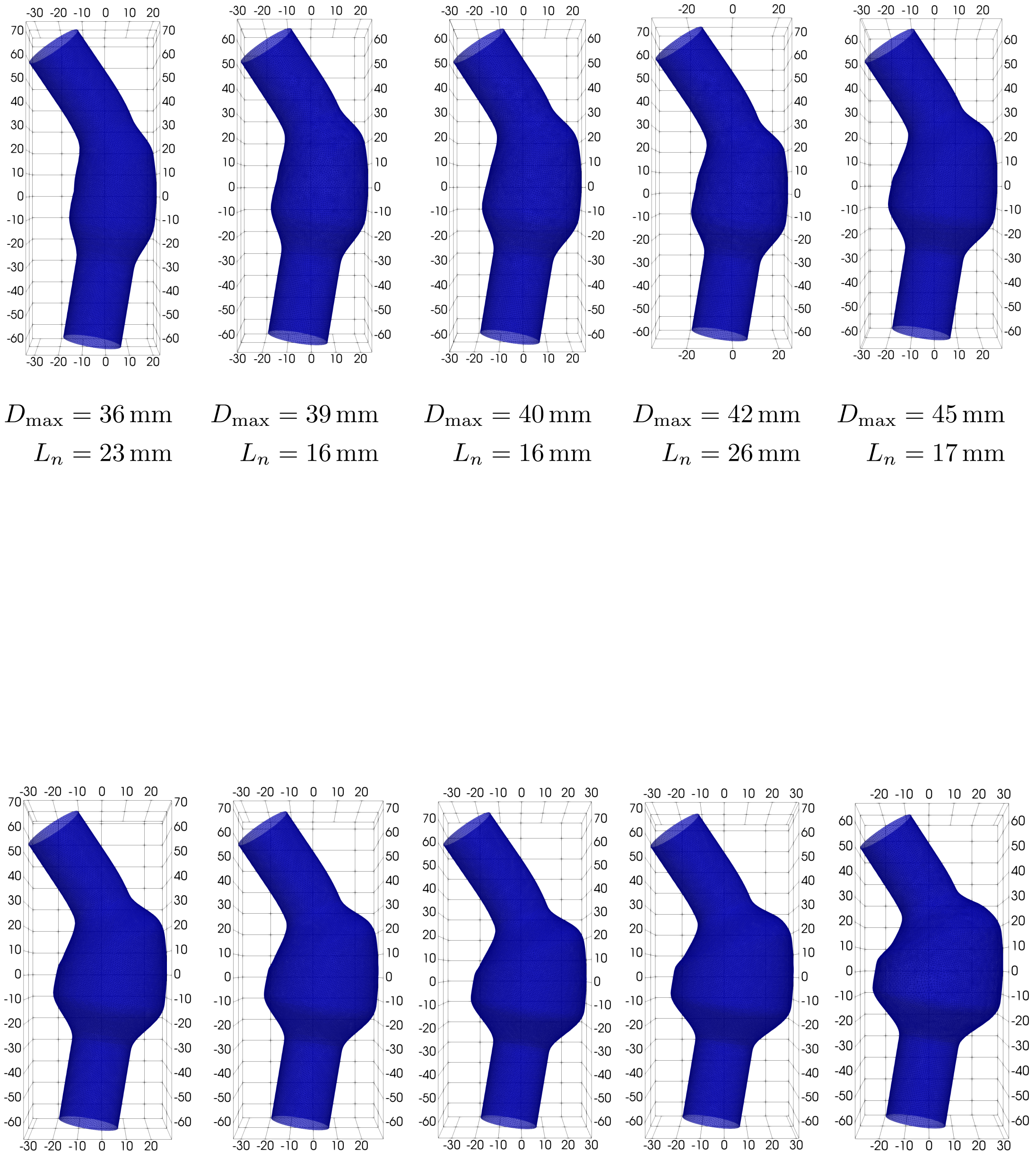

$D_{\max} = 36\,\text{mm}$ $L_n = 23\,\text{mm}$

$D_{\max} = 39\,\text{mm}$ $L_n = 16\,\text{mm}$

$D_{\max} = 40\,\text{mm}$ $L_n = 16\,\text{mm}$

$D_{\max} = 42\,\text{mm}$ $L_n = 26\,\text{mm}$

$D_{\max} = 45\,\text{mm}$ $L_n = 17\,\text{mm}$

$D_{\max} = 46\,\text{mm}$ $L_n = 19\,\text{mm}$

$D_{\max} = 48\,\text{mm}$ $L_n = 22\,\text{mm}$

$D_{\max} = 50\,\text{mm}$ $L_n = 27\,\text{mm}$

$D_{\max} = 52\,\text{mm}$ $L_n = 21\,\text{mm}$

$D_{\max} = 53\,\text{mm}$ $L_n = 15\,\text{mm}$

Figure 6.3.2.: Some shapes of the synthetic cohort of parameterized AAA abluminal shapes. The shapes vary in the two parameters $D_{\max}$ (maximum diameter) and $L_{\mathrm{n}}$ (neck length) and are constructed according to [84].

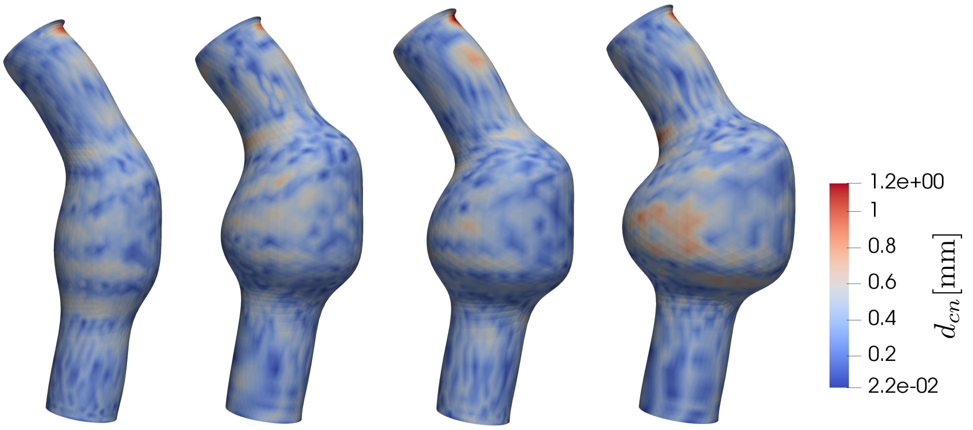

$D_{\max} = 36\,\text{mm}$ $L_n = 23\,\text{mm}$

$D_{\max} = 44\,\text{mm}$ $L_n = 13\,\text{mm}$

$D_{\max} = 48\,\text{mm}$ $L_n = 22\,\text{mm}$

$D_{\max} = 53\,\text{mm}$ $L_n = 15\,\text{mm}$

Figure 6.3.3.: Visualization of registration results. The displayed node-wise $d_{cn}$ distance in mm is measured between the registration result $\varphi_1^{\mu_0^\perp}(S)$ at $t = 1$ and associated original shape $T$.

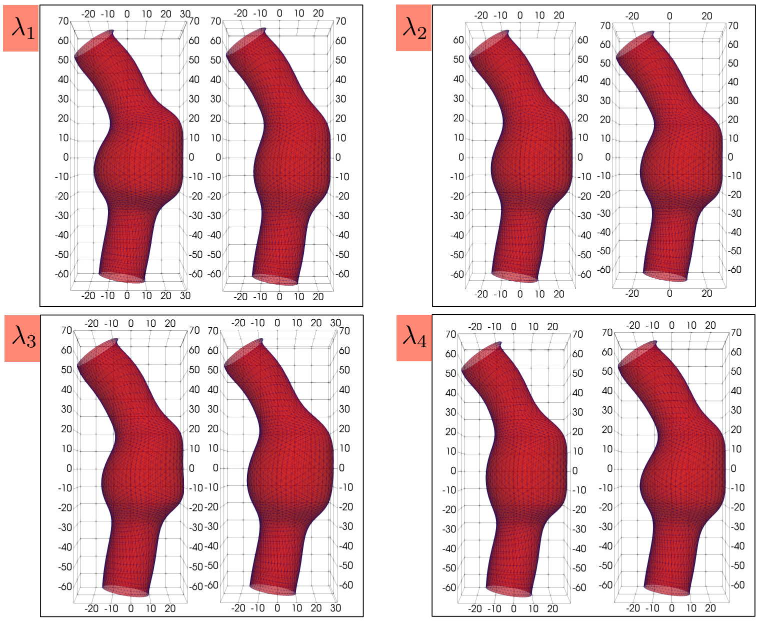

Figure 6.3.4.: Visualization of the four principal components $\underline{m}$ associated with the four eigenvalues generated in linear PCA to represent the shape variability with an accuracy of 98 %. For one eigenvalue $\lambda$ in the Figure, the left shape represents the component $\underline{m}^+$, the right shape $\underline{m}^-$ of Equation 6.1.14.

As can be seen in Figure 6.3.2, the maximum diameter $D_{\text{max}}$ is defined in an off-center fashion. Changing it, creates therefore other implicit diameter-related morphologic features. These are captured in the remaining two modes with eigenvalues $\lambda_3$ and $\lambda_4$: mode 3 highlights the associated change in the posterior sack wall, while mode 4 depicts the anterior curve at the transition to the neck.

The resulting shape vector $\underline{s}$ of a parameterized AAA in the cohort consists of four shape descriptors. Every shape descriptor is calculated according to Equation 6.1.11 by projecting the associated initial momenta vector field $\underline{\mu}_0^\perp$ onto the respective principal component $\underline{m}$. The reduced model is four-dimensional, the shape vector writes $\underline{s} \in \mathbb{R}^4$.

The reconstruction accuracy in the reduced model is retrieved with Equation 6.1.12 where the approximated initial momenta vector field $\underline{\tilde{\mu}}_0^\perp$ is reconstructed from the associated shape vector $\underline{s}$. With this reconstructed $\underline{\tilde{\mu}}_0^\perp$, a geodesic shooting is performed to generate the approximated shape $\tilde{T}$. For the geodesic shooting, the optimal translation vector $\underline{\tau}$ is taken which resulted from the registration step for a synthetic AAA shape.
For this cohort and this parameter choice, the linear PCA achieves a shape reconstruction accuracy of

$$\begin{aligned} \text{closest}-\text{node distance}\, \bar{d}_{cn} &: 0.4074\,\text{mm} \\ d_{\mathcal{W}}^{\text{norm}} &: 0.0009. \end{aligned}$$

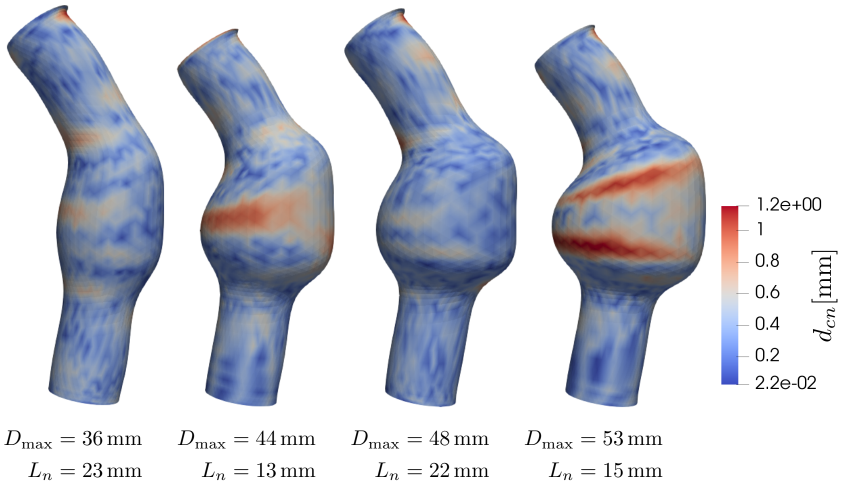

Figure 6.3.5.: Visualization of some reconstructed shapes $\tilde{T}$ in the reduced model generated with linear PCA, the same shapes as in Figure 6.3.3. The displayed node-wise $d_{cn}$ distance in mm is calculated with the $L^2$ norm and is measured between a reconstructed shape $\tilde{T}$ and associated original shape $T$.

Reconstruction results are visualized in Figure 6.3.5 with node-wise $d_{cn}$ distances with $L^2$ norm.

As described in subsection 5.1.3, the quality of the reduced system is determined amongst others by the generalization error. Here, a LOOCV approach is followed to calculate the generalization error of linear PCA applied on the initial momenta vector fields. The error amounts to the following average values, evaluating the difference between the reconstruction of left-out geometries in the reduced system and the original shape:

$$\begin{aligned} \text{closest}-\text{node distance}\,\bar{d}_{cn} &: 0.416\,\text{mm} \\ d_{\mathcal{W}}^{\text{norm}} &: 0.0014. \end{aligned}$$

These values validate the generalization ability of the reduced model generated by linear PCA; unseen data can be represented in the reduced system with high accuracy albeit slightly worse than the registration error of $0.394$ mm.

### Kernel PCA

The kernel PCA delivers three principal components necessary to represent the shape variability with an accuracy of 98 %. The principal modes are visualized in Figure 6.3.6 after being reconstructed also according to Equation 6.1.14. For every eigenvalue $\lambda$, the modes $\underline{m}^{+}$ and $\underline{m}^{-}$ are displayed respectively.
The associated eigenvalues are

$$\lambda_1 = 4.015 \cdot 10^3; \lambda_2 = 1.634 \cdot 10^3; \lambda_3 = 1.414 \cdot 10^2.$$

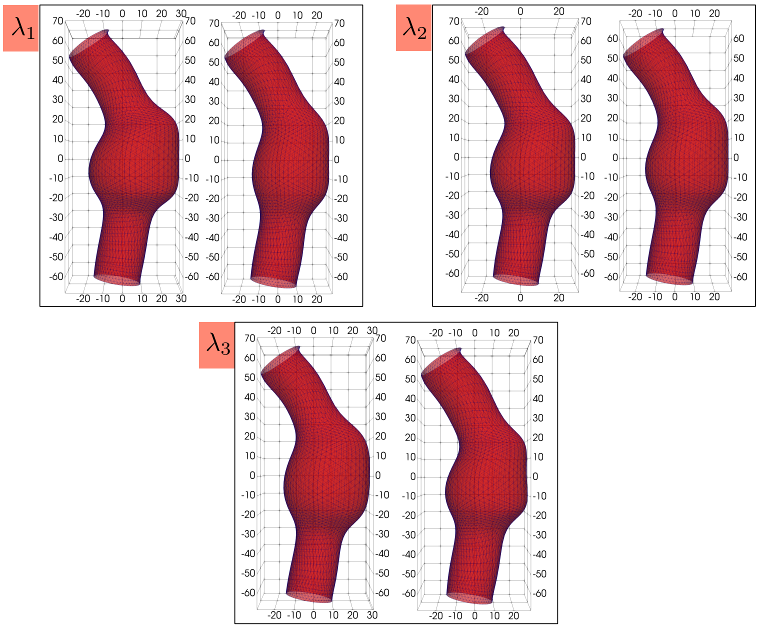

Figure 6.3.6.: Visualization of the three principal components $\underline{m}$ associated to the three eigenvalues generated in kernel PCA to represent the shape variability with an accuracy of 98 %. For one eigenvalue $\lambda$ in the Figure, the left shape represents the component $\underline{m}^+$, the right shape $\underline{m}^-$ of Equation 6.1.14.

The visualized modes $\underline{m}^+$ and $\underline{m}^-$ in Figure 6.3.6 depict the principal shape variations in the synthetic cohort. The largest two eigenvalues, $\lambda_1$ and $\lambda_2$, also correctly exhibit the two varying parameters of the cohort, namely $\lambda_1$ illustrates the changing diameter $D_{\max}$ and $\lambda_2$ the changing length of the neck $L_n$.

As mentioned in the linear PCA application, the remaining third mode associated with $\lambda_3$, depicts the implicit diameter-related shape features. Here, it combines the change in the posterior sack wall and the change of the anterior curve at the transition to the neck.

The resulting shape vector $\underline{s}$ of a parameterized AAA in the cohort consists of three shape descriptors. Every shape descriptor is calculated according to Equation 6.1.11 by projecting the associated initial momenta vector field $\underline{\mu}_0^\perp$ onto the respective principal component $\underline{m}$. The reduced model is three-dimensional and the shape vector writes $\underline{s} \in \mathbb{R}^3$.

The reconstruction accuracy in the reduced model is retrieved with Equation 6.1.12 where the approximated initial momenta vector field $\tilde{\underline{\mu}}_0^\perp$ is reconstructed from the associated shape vector $\underline{s}$. With this reconstructed $\tilde{\underline{\mu}}_0^\perp$, a geodesic shooting is performed to generate the approximated shape $\tilde{T}$. Here also, for the geodesic shooting, the optimal translation vector $\underline{\tau}$ from the registration step is taken.

For this cohort and this parameter choice, the kernel PCA achieves a shape reconstruction accu-

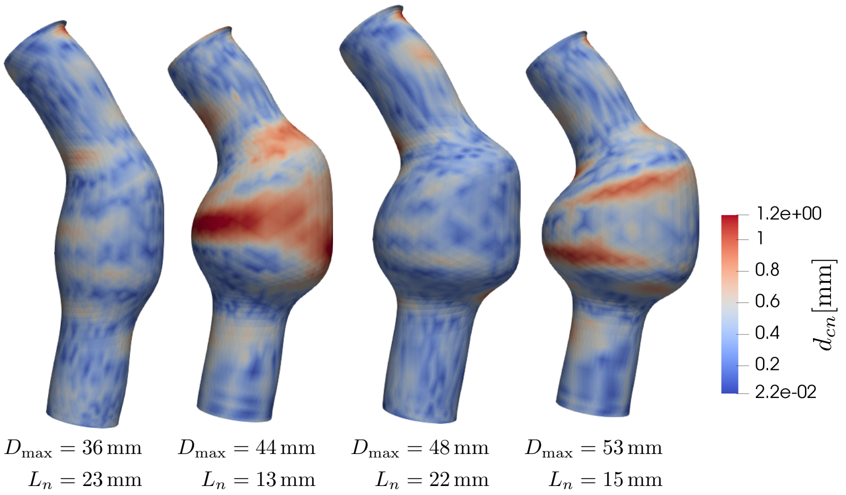

Figure 6.3.7.: Visualization of some reconstructed shapes $\tilde{T}$ in the reduced model generated with kernel PCA, the same shapes as in Figure 6.3.3. The displayed node-wise $d_{cn}$ distance in mm is measured between a reconstructed shape $\tilde{T}$ and associated original shape $T$.

racy of average

$$\begin{aligned} \text{closest}-\text{node distance}\,\bar{d}_{cn} &: 0.434\,\text{mm} \\ d_{\mathcal{W}}^{\text{norm}} &: 0.002. \end{aligned}$$

Reconstruction results with kernel PCA are visualized in Figure 6.3.7 with node-wise $d_{cn}$ distances.

The computed LOOCV results reveal the generalization error of kernel PCA on the parameterized cohort with parameters $\sigma_{\mathcal{W}} = \sigma_{\mathcal{V}^\perp} = 18.0\,\text{mm}$. These amount to the following average values:

$$\begin{aligned} \text{closest}-\text{node distance}\,\bar{d}_{cn} &: 0.444\,\text{mm} \\ d_{\mathcal{W}}^{\text{norm}} &: 0.002. \end{aligned}$$

Also here, with an accuracy slightly worse than the registration results, the kernel PCA shows its ability to represent unseen data in the cohort.

### Linear PCA vs kernel PCA

The application of linear and kernel PCA to the initial momenta vector fields of the synthetic cohort is evaluated first with regard to compactness and generalization error. Regarding compactness, kernel PCA with its three principal components creates a lower dimensional model to capture 98% of shape variability than the linear PCA with four principal components. The largest two eigenvalues, $\lambda_1$ and $\lambda_2$, in both methods express the two varying parameters of the cohort as observed. The greater compactness of kernel PCA is achieved by combining the two implicit diameter-related shape features into one principal component, in contrast to linear PCA that expresses them in two separate components.

However, with these compact principal components, the generality of the model suffers. This is examined with a leave-one-out cross-validation (LOOCV) approach as described before. The LOOCV for the linear PCA delivers with its four principal components the shown accuracy of 0.416 mm, while kernel PCA shows an accuracy of 0.981 mm with three principal components. Apparently, the combination of both implicit diameter-related features costs the kernel PCA some accuracy. An explanation of this behaviour could be the shape data structure and the high-dimensional RKHS space where the shape descriptors are created using the scalar product $\langle \cdot, \cdot \rangle_{\mathcal{V}^\perp}$. As the RKHS is a *smoothing* space, it can be the case that some features are *lost* in the aforementioned scalar product for creating the shape descriptors.

## 6.4. Summary

In this chapter, statistical methods for shape analysis on initial momenta in the tangent-space have been introduced. Additionally, the implementation details have been briefly discussed.
A cohort of 50 synthetic AAA abluminal surfaces was created to which the statistical methods, linear and kernel PCA, were applied and examined. The following conclusions can be made as result:

- The linear and kernel PCA show expected behaviour with regard to detecting the largest shape variances in the synthetic cohort.
- The kernel PCA delivers a more compact reduced model with less principal components to depict 98% shape variability in the cohort than the linear PCA.
- The linear PCA achieves a higher accuracy with regard to the generalization error assessed by LOOCV. The accuracy is almost twice that of kernel PCA.

Depending on the goal of the shape analysis and on the available data structure, linear or kernel PCA can be used, respectively. Both methods have proven to be beneficial and functioning correctly.

In the next chapter, linear and kernel PCA are applied to the real patient-specific AAA cohort to determine the shape variability and obtain the associated shape descriptors. A favourable method is then discussed for the cohort.

# 7. Shape analysis of AAAs

In this chapter, the shape descriptors of the patient-specific AAA shapes are extracted by employing the presented statistical methods in chapter 6, namely the linear and kernel PCA. Also, the shape variability in the examined AAA cohort is assessed, leading to an elementary interpretation of the acquired shape descriptors.
The chapter starts with the prior handling of the available data for statistical analysis.

## 7.1. Data handling

The data in this chapter consist of the resulting initial momenta $(\underline{\mu}_0^\perp, \underline{v}_0^\perp)$ for parameters $\sigma_\mathcal{V} = \sigma_\mathcal{W} = 20.0$ mm that are generated in chapter 4 for all AAA shapes in the examined cohort in chapter 1.

In this section, these initial momenta $(\underline{\mu}_0^\perp, \underline{v}_0^\perp)$ are examined more closely with respect to the subsequent statistical analysis, followed by the outlier detection.

## 7.2. Outlier detection

As described in subsection 6.1.3, both principal component methods are sensitive to outliers. For detecting the outliers of $\underline{\mu}_0^\perp \in \mathcal{V}^{\perp *}$ for linear PCA or $\underline{v}_0^\perp \in \mathcal{V}^\perp$ for kernel PCA, the Mahalanobis distance for multivariate outlier detection is consequently employed as introduced in subsection 6.1.3.

For linear PCA, the outlier detection on $\underline{\mu}_0^\perp \in \mathcal{V}^{\perp *}$ delivers three outliers, namely cases no. 20, 46 and 129, that lie beyond of the three standard deviation window.
For kernel PCA, the outlier detection on $\underline{v}_0^\perp \in \mathcal{V}^\perp$ does not deliver any observations beyond the three standard deviation window.

## 7.3. Principal component analysis

In the context of patient-specific AAA cases, linear PCA is regarded as a data-based method, while kernel PCA represents a patient-based approach, since the comparison in the kernel PCA is based on the patients. In the following, these two approaches are followed to extract the shape descriptors from initial momenta $(\underline{\mu}_0^\perp, \underline{v}_0^\perp)$.

### 7.3.1. Linear principal component analysis

The linear PCA is performed without the identified outliers, generating 76 principal components to describe 98 $\%$ of the cohort's shape variability for parameters $\sigma_{\mathcal{V}} = \sigma_{\mathcal{W}} = 20.0$ mm.

#### Modes

The first ten eigenvalues in descending order are $\lambda_1 = 6.79, \lambda_2 = 5.04, \lambda_3 = 3.78, \lambda_4 = 3.14, \lambda_5 = 2.67, \lambda_6 = 2.31, \lambda_7 = 2.11, \lambda_8 = 1.88, \lambda_9 = 1.64$ and $\lambda_{10} = 1.52$. The corresponding modes $\underline{m}$ are visualized in Figure 7.3.1. The visualization is achieved with geodesic shooting according to subsection 6.1.4.

#### Accuracy

Accordingly, the resulting shape vector $\underline{s}$ of a patient-specific AAA in the cohort consists of 76 shape descriptors. Every shape descriptor is calculated according to Equation 6.1.11 by projecting the associated initial momenta vector field $\underline{\mu}_0^{\perp}$ onto the respective principal component $\underline{m}$. The reduced model is three-dimensional and the shape vector is $\underline{s} \in \mathbb{R}^{76}$.
The reconstruction accuracy in the reduced model is retrieved with Equation 6.1.12 where the approximated initial momenta vector field $\underline{\tilde{\mu}}_0^{\perp}$ is reconstructed from the associated shape vector $\underline{s}$. With this reconstructed $\underline{\tilde{\mu}}_0^{\perp}$, a geodesic shooting is performed to generate the approximated shape $\tilde{T}$. The complementing translational vector $\underline{\tau}$ resulting from the registration step is employed in the geodesic shooting.
For this cohort and this parameter choice, the linear PCA achieves a shape reconstruction accuracy of average values

$$\begin{aligned} \mathrm{closest-node\,distance}\,\bar{d}_{cn} &: 0.748\,\mathrm{mm}, \\ d_{\mathcal{W}}^{\mathrm{norm}} &: 0.261. \end{aligned}$$

Reconstruction results with linear PCA are visualized in Figure 7.3.2 with node-wise $d_{cn}$ distances measured with the $L^2$ norm.

### 7.3.2. Kernel principal component analysis

The kernel PCA generates 39 principal components to describe 98 $\%$ of the cohort's shape variability for parameters $\sigma_{\mathcal{V}} = \sigma_{\mathcal{W}} = 20.0$ mm.

#### Modes

The first ten eigenvalues in descending order are $\lambda_1 = 1.37 \cdot 10^5, \lambda_2 = 7.85 \cdot 10^4, \lambda_3 = 5.44 \cdot 10^4, \lambda_4 = 5.09 \cdot 10^4, \lambda_5 = 3.60 \cdot 10^4, \lambda_6 = 2.85 \cdot 10^4, \lambda_7 = 1.83 \cdot 10^4, \lambda_8 = 1.71 \cdot 10^4, \lambda_9 = 1.65 \cdot 10^4$ and $\lambda_{10} = 1.16 \cdot 10^4$. The corresponding modes $\underline{m}$ are visualized in Figure 7.3.3. The visualization is achieved with geodesic shooting according to subsection 6.1.4.

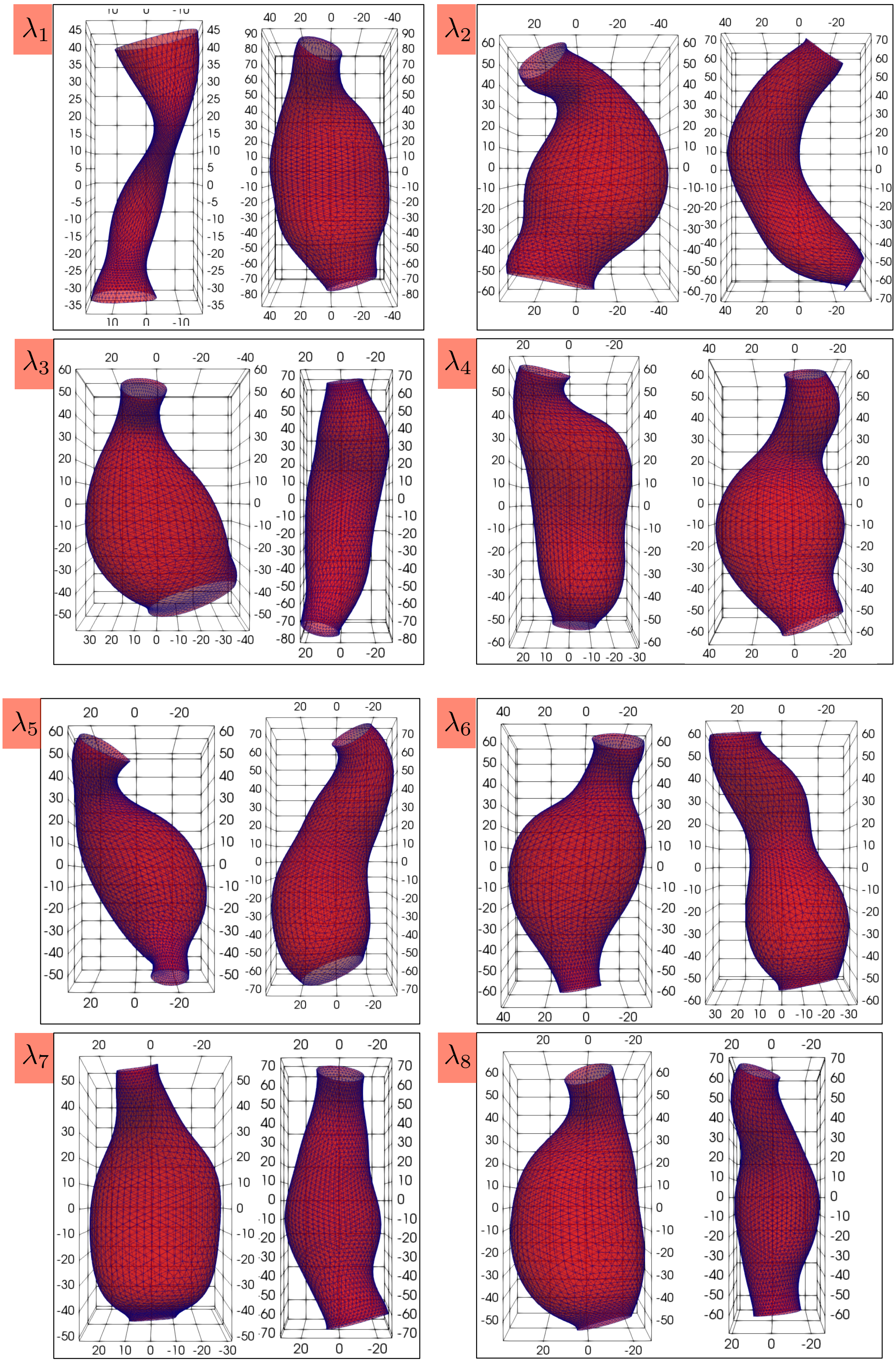

Figure 7.3.1.: First eight principal modes of real AAA cohort extracted with linear PCA, representing the shape variability with an accuracy of 98 %. For one eigenvalue $\lambda$ in the Figure, the left shape represents the component $\underline{m}^+$, the right shape $\underline{m}^-$ of Equation 6.1.14.

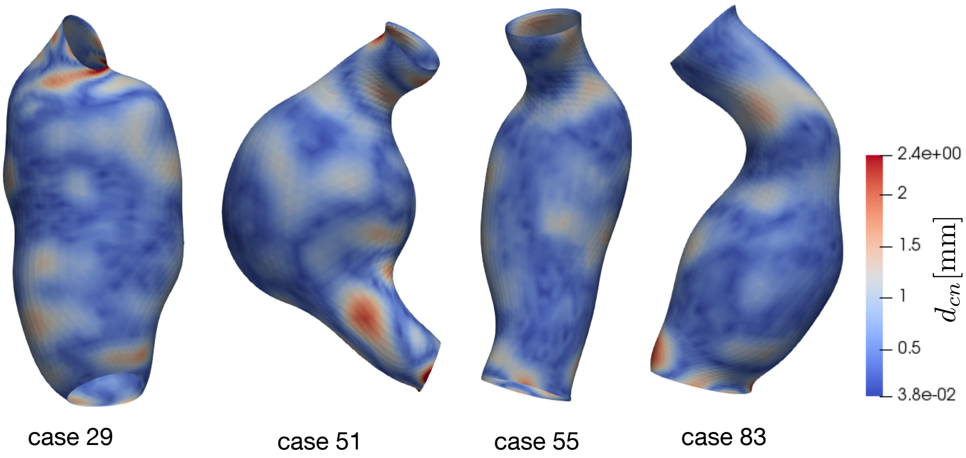

Figure 7.3.2.: Visualization of some reconstructed shapes $\tilde{T}$ in the reduced model generated with linear PCA, with the same shapes as in Figure 4.2.9. The displayed reconstruction accuracy is given with the node-wise distance $d_{cn}$ in mm. The distance is measured between the reconstructed shape $\tilde{T}$ and the associated original shape $T$. The shapes are displayed in the coronal view.

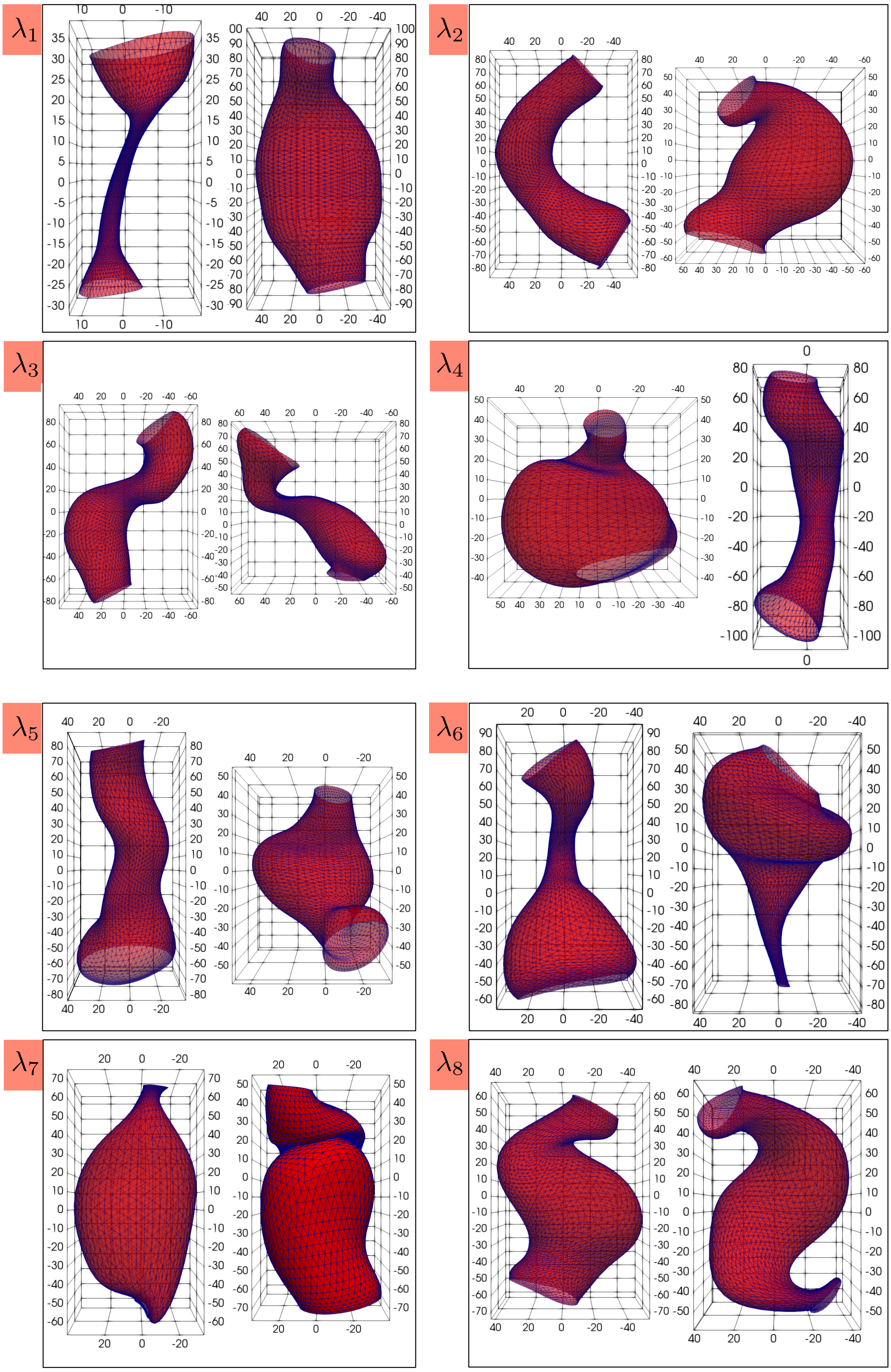

Figure 7.3.3.: First eight principal modes of real AAA cohort extracted with kernel PCA, representing the shape variability with an accuracy of 98 %. For one eigenvalue $\lambda$ in the Figure, the left shape represents the component $\underline{m}^{+}$, the right shape $\underline{m}^{-}$ of Equation 6.1.14.

Table 7.1.: The generalization error of the reduced systems generated by linear and kernel PCA on the initial momenta of AAA shape cohort. The error is computed between the reconstructed and original AAA shapes in an LOOCV approach, using once the closest-node distance $\bar{d}_{cn}$ with the $L^2$ norm and once the normalized similarity measure $d_{\mathcal{W}}^{\text{norm}}$. The displayed values represent the average for each measurement method over the examined AAA shapes.

| | Linear PCA | Kernel PCA |
|---|---|---|
| $\text{closest} - \text{node distance}\, \bar{d}_{cn}$ [mm] | 1.51 | 3.41 |
| $d_{\mathcal{W}}^{\text{norm}}$ [-] | 0.251 | 0.373 |

### Accuracy

Accordingly, the resulting shape vector $\underline{s}$ of a patient-specific AAA in the cohort consists of 39 shape descriptors. Every shape descriptor is calculated according to Equation 6.1.11 by projecting the associated initial momenta vector field $\underline{\mu}_0^{\perp}$ onto the respective principal component $\underline{m}$. The reduced model is three-dimensional and the shape vector is $\underline{s} \in \mathbb{R}^{39}$.
The reconstruction accuracy in the reduced model is retrieved with Equation 6.1.12 where the approximated initial momenta vector field $\underline{\tilde{\mu}}_0^{\perp}$ is reconstructed from the associated shape vector $\underline{s}$. With this reconstructed $\underline{\tilde{\mu}}_0^{\perp}$, a geodesic shooting is performed to generate the approximated shape $\tilde{T}$. Also here, the complementing translational vector $\underline{\tau}$ resulting from the registration step is employed in the geodesic shooting
For this cohort and this parameter choice, the kernel PCA achieves a shape reconstruction accuracy of average

$$\begin{aligned} \text{closest} - \text{node distance}\, \bar{d}_{cn} &: 3.196\,\text{mm}, \\ d_{\mathcal{W}}^{\text{norm}} &: 0.407, \end{aligned}$$

calculated over all AAA shapes. Reconstruction results with kernel PCA are visualized in Figure 7.3.4 with node-wise $d_{cn}$ distances measured with the $L^2$ norm.

## 7.4. Evaluation of statistical model

As described in subsection 5.1.3 and as employed for the synthetic cohort in section 6.3, the quality of the reduced system is determined amongst others by the generalization error. The error is evaluated with the LOOCV approach. Table 7.1 shows the error for the linear and kernel PCA. Therein, for every method, the generalization error is computed between reconstructed and original AAA shapes in a LOOCV approach, once with the closest-node distance $d_{cn}$ with the $L^2$ norm and once with normalized similarity measure $d_{\mathcal{W}}^{\text{norm}}$. The displayed values represent the average for each measurement method over all examined AAA shapes.

The quality of the reduced systems can be also assessed with the compactness. As for the synthetic cohort, the compactness is given by the number of modes necessary to capture a certain variability in the cohort. For capturing $98\%$ variability, the linear PCA generates 76 principal

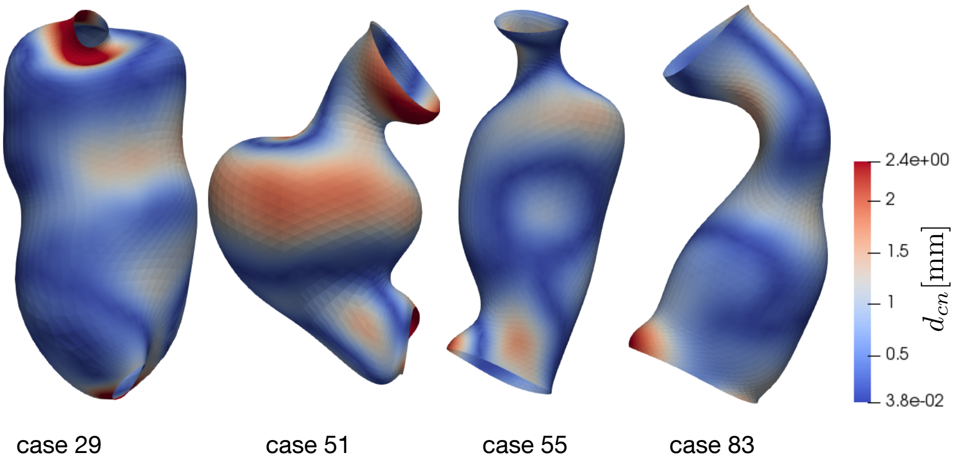

Figure 7.3.4.: Visualization of some reconstructed shapes $\tilde{T}$ in the reduced model generated with kernel PCA, with the same shapes as in Figure 4.2.9. The displayed reconstruction accuracy is given with the node-wise distance $d_{cn}$ in mm. The distance is measured between the reconstructed shape $\tilde{T}$ and the associated original shape $T$. The shapes are displayed in the coronal view.

components, while the kernel PCA requires only 39 principal components.
Consequently, kernel PCA generates a more compact reduced model with higher inaccuracy, while linear PCA produces a higher dimensional reduced model but with superior accuracy.

## 7.5. Summary

In this chapter, a statistical analysis is conducted on the registration parameters $\underline{\mu}_0^\perp$ of the non-rigid space $\mathcal{V}^\perp$ for the patient-specific AAA cohort presented in chapter 1. The statistical analysis is performed once with the linear PCA and once with the kernel PCA method. The outcome of each method is a reduced order system constructed with the identified principal modes. The registration parameters $\underline{\mu}_0^\perp$ are mapped onto these principal modes, resulting in shape vectors $\underline{s}$ of AAA shapes with regard to the reduced system. A shape vector $\underline{s}$ represents the associated $\underline{\mu}_0^\perp$ and thus the associated AAA abluminal shape.

The quality of the reduced order systems of the linear and kernel PCA differ in the number of necessary principal modes and the accuracy of the reduced representations of $\underline{\mu}_0^\perp$ and the associated shapes. The accuracy is determined by comparing the reconstructed shape from the reduced representation to the original AAA shapes. Linear PCA requires 76 principal components to describe $98\%$ of shape variability, while kernel PCA requires only 39 principal components. However, the linear PCA produces a more accurate reduced representation of the AAA shapes. These results are discussed in detail in section 8.2.

# 8. Discussion

In this chapter, the results achieved in the present work are discussed. The discussion includes

- discussion of the modular registration method,
- discussion of its application to the examined AAA cohort,
- discussion of the application of statistical methods, specifically linear and kernel PCA, to the acquired registration parameters of the examined AAA abluminal shapes.

## 8.1. Modular registration method (Part I)

The formulation and implementation of the novel modular registration method in chapter 3 perform as expected and fullfill the requirements of the two-space registration. The resulting registration parameterizations in the rigid and non-rigid components are generated correctly according to the characteristics of the two spaces.

Regarding the accuracy for both the synthetic AAA cohort and the patient-specific AAA cohort, the method delivers an accurate representation of the original shapes with an overall average error of only 0.52 mm for the patient-specific AAA cohort. It is important to note that the method parameters $\sigma_{\mathcal{W}}$ and $\sigma_{\mathcal{V}}$ contribute to the method accuracy. In this work, they represent the pair which produces the best accuracy within an interval of pairs deemed to be reasonable for the mesh size and shape sizes. A more convenient and consistent approach could be to include these parameters in the optimization process by minimizing the following cost function

$$J(\sigma_{\mathcal{W}}, \sigma_{\mathcal{V}}, \underline{M}_0^{\perp}, \underline{T}) = \sum_i^N \|\varphi_1^{\underline{\mu}_{0,i}^{\perp}}(S) - T_i\|^2_{\mathcal{W}^*} + \gamma_E \cdot \sum_i^N \|\underline{v}_{0,i}^{\perp}\|^2_{\mathcal{V}^{\perp}} \tag{8.1.1}$$

with regard to the method parameters $\sigma_{\mathcal{W}}$ and $\sigma_{\mathcal{V}}$, to the $N$ non-rigid registration parameters $\underline{\mu}_0^{\perp}$ summarized in the matrix $\underline{M}_0^{\perp} \in \mathbb{R}^{N \times 3n_x}$ and the $N$ rigid registration parameters $\underline{\tau}_i$ summarized in $\underline{T} \in \mathbb{R}^{N \times 3n_x}$, with $N$ being the number of shapes and $n_x$ the number of vertices of the triangular mesh of the reference shape.

In this spirit, Equation 8.1.1 can be reformulated to

$$J(D_{\text{cyl}}, H_{\text{cyl}}, \underline{M}_0^{\perp}, \underline{T}) = \sum_i^N \|\varphi_1^{\underline{\mu}_{0,i}^{\perp}}(S) - T_i\|^2_{\mathcal{W}^*} + \gamma_E \cdot \sum_i^N \|\underline{v}_{0,i}^{\perp}\|^2_{\mathcal{V}^{\perp}} \tag{8.1.2}$$

where the minimization takes place with regard to $D_{\text{cyl}}$ and $H_{\text{cyl}}$, the diameter and height of the cylindrical reference geometry. In so doing, a *mean* cylindrical shape can be estimated for the underlying cohort which energetically lies closer to the mean non-rigid transformation energy of all shapes in the cohort. This would lead to a more even distribution of the energy in the resulting $\underline{\mu}_0^\perp$ of cohort shapes and might reduce the peaks in the statistical analysis.

The algorithmic implementation and performance were achieved by using PyKeops in Python. The gradient descent scheme also succeeded in finding the optimal registration parameters $\underline{\mu}_0^\perp$ and $\underline{\tau}$ for all AAA shapes in the cohort for method parameters $\sigma_{\mathcal{W}} = \sigma_{\mathcal{V}} = 20\,\mathrm{mm}$.

### AAA discussion

As mentioned above, the application of the modular registration method to the patient-specific AAA shapes yields accurate registration results. The most inaccuracies are located at the in- and outlet boundaries (see subsection 4.2.2). This behaviour is due to the nature of the registered structures.
Due to the great variability in the cohort shapes and the strongly varying sizes of the AAA shapes, the accuracy varies among the individual AAA shapes for the selected parameter pairs $\sigma_{\mathcal{W}} = \sigma_{\mathcal{V}} = 20\,\mathrm{mm}$. However, for the sake of consistency in the subsequent statistical analysis, the method parameters $\sigma_{\mathcal{W}} = \sigma_{\mathcal{V}} = 20\,\mathrm{mm}$must be the same for the entire examined cohort, as otherwise the statistical analysis cannot be performed.
An idea here, would be to divide the cohort into groups based on the volume for instance, to then choose appropriate method parameters $\sigma_{\mathcal{W}}$ and $\sigma_{\mathcal{V}}$ and to then conduct the statistical anylsis separately on the groups.
An outlier detection at this point would be reasonable, too. However, for the statistical analysis, the relevant parameters to determine outliers are the non-rigid $\underline{\mu}_0^\perp$ or $\underline{v}_0^\perp$. An outlier detection at this point would be premature in this case.

In general, applying the method to the patient-specific cohort does not require any special characteristics of the cohort shapes, making the method applicable and functional for other shape types.

## 8.2. Statistical analysis (Part II)

The statistical analysis which covers the second part of the work at hand focuses on the principal component analysis (PCA) method in two different forms: the linear or classic form and the kernel form. These two methods are applied separately on the acquired patient-specific non-rigid registration parameters $\underline{\mu}_0^\perp$ of the cohort, producing dimensionally reduced systems for their description. The representation of every $\underline{\mu}_0^\perp$ in the reduced system provides the shape descriptors for the associated AAA shape.

For the synthetic AAA cohort, both methods behave as expected: The principal modes generated by linear and kernel PCA capture the shape variability in the synthetic cohort, which were basically two main shape features: the length of the neck and the maximum diameter. Due to the construction mechanism of the synthetic shapes, some implicit shape features occurred in the cohort when varying the two main features. These were also captured in the prinicipal modes.

As expected, the kernel PCA generates fewer principal modes than the linear PCA, for the same required $98\%$ of shape variability to be captured and is hence more compact than the linear PCA. To that end, some features are represented with one mode.
With regard to the generalization error, linear and kernel PCA achieve a good generalization with their reduced systems. Additionally, they possess the same reconstruction accuracy which is high.
Subsequently, both methods are validated and prove the usability of the non-rigid registration parameters as intended; the non-rigid parameters contain the information which is needed for the statistical analysis. The employed statistical methods can detect the shape variability and necessary information in the non-rigid parameters. The non-rigid parameters are therefore an appropriate basis for the intended shape analysis.

## AAA discussion

In the same manner, the linear and kernel PCA were applied to the non-rigid registration parameters $\underline{\mu}_0^{\perp}$ of the 142 patient-specific AAA shapes in the examined cohort. Also here, as expected, the kernel PCA achieves a greater compactness than the linear PCA - however, with great losses regarding generalization. Unlike for the synthetic cohort, the linear and kernel PCA generate reduced systems with different generalization abilities for the patient-specific AAA cohort, particularly in terms of reconstruction error. The relatively poor performance of the kernel PCA in this application can be traced back to the following facts:

- In the patient-specific AAA cohort, the shapes which are encoded with the registration parameter $\underline{v}_0^{\perp}$ differ more than in the synthetic cohort where the kernel PCA performed well. Thus, it might be that the large shape differences in the patient-specific AAA cohort reduced the performance of the kernel PCA.

- It is also possible that the selected reconstruction algorithm in Equation 6.1.12 does not accurately reconstruct the original data from their representations in the higher-dimensional space. The reconstruction challenge for kernel PCA was highlighted in subsection 5.1.2. Hence, for a more accurate mapping, solving an optimization problem like described in Equation 5.1.19 would have been more beneficial.

- Another reason for the poor performance of kernel PCA is possibly the smoothing nature of the used Gaussian kernel. In particular, the Gaussian kernel determines the scalar product which is built to construct the gram matrix $\underline{G}$ in Equation 5.1.15 using the initial velocity vector fields $\underline{v}_0^{\perp}$ (see Equation 6.1.6). Subsequently, the scalar product has a smoothing character such that crucial shape features might be eradicated with the scalar product.

Still, depending on the intended application of the shape descriptors, it could be the case that the kernel PCA delivers the neccessary accuracy. There is always a trade-off between dimensionality of the shape vector and the accuracy.

So, the linear PCA delivers 76 principal modes to describe the AAA shapes with an overall accuracy of $1.51$ mm. The identified modes in the cohort depict and combine the maximum diameter, curvature, asymmetry and many other geometric features. An extensive correlation analysis should be performed in order to understand the nature of the modes and what geometric feature each shape descriptor represents.

Since the rigid component of the registration method only comprises rigid translations, rigid rotations can be identified in the modes structure, as expected. However, for the shape analysis of other anatomical regions, the incorporation of rigid rotations in the rigid component could be added.

# 9. Conclusions and outlook

In this work, the following contributions are achieved:

- A modular matching method extends the widely used LDDMM framework for anatomical shape analysis. The method constitutes two transformation modules in two perpendicular spaces and separates hence non-rigid and rigid translational transformations.
- A consistent and expedient preparation of the patient-specific AAA abluminal shapes is demonstrated for shape analysis.
- Two methods for statistical shape analysis are elaborated, namely the linear and kernel PCA. These methods are applied to the patient-specific AAA cohort, generating reduced systems. The AAA shape representation in these reduced systems delivers the required shape descriptors.
- The principal modes of the linear and kernel PCA reduced systems are visualized, giving a first impression as to the shape variability in the AAA cohort.

The introduced modular registration method is used in this work to acquire the initial momenta for the subsequent statistical analysis. The method could be also integrated into growth analysis and prediction, extending these biomechanical models.

In further works, the acquired shape descriptors should be employed for rupture risk prediction and for wall parameter estimation for biomechanical modeling. For the rupture risk prediction, a correlation analysis should be performed to identify existing relations between the shape descriptors and the rupture risk. It must however be noted that this is just a cross-sectional cohort and it does not represent AAA formation over time. Thus, it is not known when the AAA ruptured after the anatomical image was taken.
With regard to the wall parameter estimation, the shape descriptors could be integrated in the Gaussian process, for instance instead of the concrete geometric features.

It would be also interesting to create synthetic AAA shapes based on combinations of the principal modes, create biomechanical models from the resulting shapes with consistent wall thickness and wall properties and then compute the PWS (peak wall stress). The analysis of the relation between the PWS and the principal modes could indicate relevant shape modes with regard to rupture risk estimation.
The generated reduced system could be used for segmentation purposes: The principal modes of the reduced system are constant and the shape descriptors are optimized to minimize a similarity measure on the medical images.

Other statistical methods are partial least squares regression (PLS regression) and canonical-correlation analysis (CCA) could be also applied to the initial momenta. These methods would select the modes that are relevant for an incident or a change in the clinical values directly.

Finally, the registration method and the statistical analysis could be integrated in a clinical workflow, as the computation times and power are minimal and can substitute a cumbersome and imprecise estimation of concrete geometrical features. It may also be possible to apply the novel registration method directly to medical images to match 2D images or even 3D volumes. In such situations, finding an initial position for the target and the source is crucial. With the developed registration method, this dilemma is solved.

# A. Registration results

In this table, the registration results for the chosen parameter pair $\sigma_{\mathcal{W}} = \sigma_{\mathcal{V}} = 20$ mm are presented for all the $N = 142$ AAA abluminal surfaces in the cohort. To that end, the cylindrical surface $S$ of Figure 4.2.1 is mapped to every AAA abluminal shape $T$ with the novel modular registration method in the two orthogonal spaces. The trade-off parameter $\gamma_E$ is $0.0001$.

Herein, the registration results are represented with three parameters: the normalized similarity measure $d_{\mathcal{W}}^{\mathrm{norm}}$, the path energy $\|\underline{v}_0^{\perp}\|^2_{\mathcal{V}^{\perp}}[\frac{\mathrm{mm}}{s}]$ and the average of the closest-node distances $\bar{d}_{cn}$ [mm] measured with the $L^2$ norm.
The parameters $d_{\mathcal{W}}^{\mathrm{norm}}$ and $\bar{d}_{cn}$ are measured between the deformed cylindrical surface $\varphi_1^{\underline{v}_0^{\perp}}(S)$ at $t = 1$ and the original AAA abluminal surface $T$.

Table A.1.: The registration results for parameter pair $\sigma_{\mathcal{W}} = \sigma_{\mathcal{V}} = 20$ mm for all $N = 142$ target AAA surfaces. The registration results include the normalized similarity measure $d_{\mathcal{W}}^{\mathrm{norm}}$, the path energy $\|\underline{v}_0^{\perp}\|^2_{\mathcal{V}^{\perp}}[\frac{\mathrm{mm}}{s}]$ and the average of the closest-node distances $\bar{d}_{cn}$ [mm].

| $n$ | $d_{\mathcal{W}}^{\mathrm{norm}}$ | $\|\underline{v}_0^{\perp}\|^2_{\mathcal{V}^{\perp}}$ | $\bar{d}_{cn}$ |
|---|---|---|---|
| 1 | 0.0005 | 1857.1786 | 4.23E-01 |
| 2 | 0.0002 | 4674.3374 | 4.80E-01 |
| 3 | 0.0002 | 6295.234 | 4.61E-01 |
| 4 | 0.0002 | 2977.1545 | 4.20E-01 |
| 5 | 0.0006 | 4349.9243 | 5.39E-01 |
| 6 | 0.0002 | 5487.911 | 5.46E-01 |
| 7 | 0.0007 | 4287.4497 | 5.55E-01 |
| 8 | 0.0008 | 2764.2778 | 6.05E-01 |
| 9 | 0.0002 | 4127.046 | 4.36E-01 |
| 10 | 0.0003 | 3202.953 | 5.30E-01 |
| 11 | 0.0003 | 3066.1338 | 4.50E-01 |
| 12 | 0.0003 | 13533.792 | 5.10E-01 |
| 13 | 0.0002 | 2538.6868 | 3.84E-01 |
| 14 | 0.0001 | 3166.5942 | 4.17E-01 |
| 15 | 0.0002 | 8790.074 | 5.08E-01 |
| 16 | 0.0001 | 7895.1694 | 4.25E-01 |
| 17 | 0.0005 | 3550.0007 | 5.18E-01 |
| 18 | 0.0003 | 7416.2466 | 4.96E-01 |
| 19 | 0.0003 | 9445.762 | 5.78E-01 |
| 20 | 0.0001 | 18836.59 | 4.51E-01 |

| $n$ | $d_{\mathcal{W}}^{\mathrm{norm}}$ | $\lVert \underline{v}_0^{\perp} \rVert^2_{\mathcal{V}^{\perp}}$ | $\bar{d}_{cn}$ |
|---|---|---|---|
| 21 | 0.0002 | 5490.1084 | 4.13E-01 |
| 22 | 0.0003 | 4754.5327 | 5.16E-01 |
| 23 | 0.0002 | 3908.5288 | 4.64E-01 |
| 24 | 0.0001 | 6483.382 | 4.83E-01 |
| 25 | 0.0003 | 6679.295 | 4.69E-01 |
| 26 | 0.0002 | 3148.4885 | 4.55E-01 |
| 27 | 0.0001 | 5114.35 | 3.97E-01 |
| 28 | 0.0001 | 4199.453 | 4.49E-01 |
| 29 | 0.0001 | 18463.826 | 4.59E-01 |
| 30 | 0.0003 | 6067.6514 | 5.45E-01 |
| 31 | 0.0002 | 2647.4822 | 6.11E-01 |
| 32 | 0.0003 | 4096.875 | 4.20E-01 |
| 33 | 0.0005 | 8703.496 | 6.65E-01 |
| 34 | 0.0001 | 13003.618 | 6.39E-01 |
| 35 | 0.0001 | 2103.994 | 4.87E-01 |
| 36 | 0.0005 | 3896.1658 | 6.09E-01 |
| 37 | 0.0002 | 6984.037 | 4.28E-01 |
| 38 | 0.0002 | 1934.488 | 4.84E-01 |
| 39 | 0.0003 | 14521.733 | 6.13E-01 |
| 40 | 0.0002 | 12969.447 | 5.27E-01 |
| 41 | 0.0003 | 5179.352 | 5.03E-01 |
| 42 | 0.0001 | 2555.163 | 4.60E-01 |
| 43 | 0.0004 | 2700.0217 | 4.61E-01 |
| 44 | 0.0002 | 3741.8235 | 4.34E-01 |
| 45 | 0.0005 | 13493.472 | 1.44E+00 |
| 46 | 0.0003 | 13958.307 | 4.48E-01 |
| 47 | 0.0003 | 4061.6956 | 4.23E-01 |
| 48 | 0.0003 | 6149.7637 | 4.59E-01 |
| 49 | 0.0001 | 1849.1351 | 3.81E-01 |
| 50 | 0.0001 | 2716.1658 | 4.57E-01 |
| 51 | 0.0002 | 9017.605 | 6.04E-01 |
| 52 | 0.0002 | 3442.1333 | 5.80E-01 |
| 53 | 0.0002 | 16856.232 | 4.74E-01 |
| 54 | 0.0002 | 12922.504 | 5.66E-01 |
| 55 | 0.0002 | 6917.2583 | 4.16E-01 |
| 56 | 0.0002 | 17261.207 | 4.76E-01 |
| 57 | 0.0004 | 6408.51 | 4.75E-01 |
| 58 | 0.0001 | 11431.021 | 4.70E-01 |
| 59 | 0.0002 | 8804.433 | 4.74E-01 |
| 60 | 0.0002 | 8683.068 | 5.22E-01 |
| 61 | 0.0002 | 14125.154 | 4.25E-01 |
| 62 | 0.0002 | 3226.8723 | 4.39E-01 |
| 63 | 0.0002 | 6881.6147 | 3.97E-01 |

| $n$ | $d_{\mathcal{W}}^{\mathrm{norm}}$ | $\lVert \underline{v}_0^{\perp} \rVert^2_{\mathcal{V}^{\perp}}$ | $\bar{d}_{cn}$ |
|---|---|---|---|
| 64 | 0.0002 | 2103.9912 | 4.37E-01 |
| 65 | 0.0005 | 3486.5996 | 5.68E-01 |
| 66 | 0.0003 | 3430.366 | 4.71E-01 |
| 67 | 0.0002 | 5131.1445 | 4.94E-01 |
| 68 | 0.0002 | 11016.881 | 4.72E-01 |
| 69 | 0.0002 | 7360.4136 | 4.93E-01 |
| 70 | 0.0003 | 16522.29 | 1.29E+00 |
| 71 | 0.0002 | 6276.3794 | 4.38E-01 |
| 72 | 0.0003 | 2559.6465 | 4.56E-01 |
| 73 | 0.0004 | 4008.432 | 5.44E-01 |
| 74 | 0.0003 | 9409.031 | 4.64E-01 |
| 75 | 0.0002 | 13257.532 | 4.65E-01 |
| 76 | 0.0002 | 16591.016 | 4.18E-01 |
| 77 | 0.0003 | 7372.486 | 5.31E-01 |
| 78 | 0.0002 | 7300.357 | 5.03E-01 |
| 79 | 0.0003 | 3475.2126 | 4.41E-01 |
| 80 | 0.0004 | 8244.989 | 5.03E-01 |
| 81 | 0.0001 | 13207.685 | 4.13E-01 |
| 82 | 0.0008 | 10675.137 | 7.52E-01 |
| 83 | 0.0002 | 2808.5042 | 4.49E-01 |
| 84 | 0.0002 | 2676.56 | 4.93E-01 |
| 85 | 0.0003 | 13650.519 | 5.89E-01 |
| 86 | 0.0003 | 18052.262 | 5.48E-01 |
| 87 | 0.0002 | 6495.4897 | 4.22E-01 |
| 88 | 0.0002 | 4725.2554 | 4.24E-01 |
| 89 | 0.0002 | 3165.4175 | 5.65E-01 |
| 90 | 0.0001 | 5272.72 | 4.44E-01 |
| 91 | 0.0003 | 4590.854 | 4.93E-01 |
| 92 | 0.001 | 2107.8423 | 5.00E-01 |
| 93 | 0.0007 | 9508.215 | 6.75E-01 |
| 94 | 0.0001 | 13457.504 | 3.89E-01 |
| 95 | 0.0004 | 10532.513 | 6.07E-01 |
| 96 | 0.0002 | 5095.771 | 4.36E-01 |
| 97 | 0.0006 | 4438.778 | 6.05E-01 |
| 98 | 0.0005 | 5082.488 | 5.40E-01 |
| 99 | 0.0002 | 6585.152 | 4.66E-01 |
| 100 | 0.0001 | 10885.041 | 3.65E-01 |
| 101 | 0.0004 | 11591.346 | 6.09E-01 |
| 102 | 0.0003 | 3287.9587 | 4.46E-01 |
| 103 | 0.0001 | 18044.043 | 4.07E-01 |
| 104 | 0.0003 | 2496.918 | 4.63E-01 |
| 105 | 0.0002 | 7661.8115 | 6.38E-01 |
| 106 | 0.0001 | 13545.529 | 1.41E+00 |

| $n$ | $d_{\mathcal{W}}^{\mathrm{norm}}$ | $\|\underline{v}_0^{\perp}\|_{\mathcal{V}^{\perp}}^{2}$ | $\bar{d}_{cn}$ |
|---|---|---|---|
| 107 | 0.0003 | 14232.663 | 5.22E-01 |
| 108 | 0.0004 | 17817.475 | 5.48E-01 |
| 109 | 0.0002 | 4225.7236 | 3.87E-01 |
| 110 | 0.0001 | 8360.858 | 4.25E-01 |
| 111 | 0.0004 | 2374.5999 | 4.85E-01 |
| 112 | 0.0002 | 3691.1597 | 5.03E-01 |
| 113 | 0.0001 | 6185.8296 | 4.45E-01 |
| 114 | 0.0002 | 11109.864 | 5.17E-01 |
| 115 | 0.0002 | 9649.335 | 4.63E-01 |
| 116 | 0.0002 | 2834.7263 | 4.14E-01 |
| 117 | 0.0003 | 5087.6426 | 4.77E-01 |
| 118 | 0.0003 | 14271.812 | 9.20E-01 |
| 119 | 0.0003 | 14994.739 | 5.14E-01 |
| 120 | 0.0002 | 5164.3403 | 4.87E-01 |
| 121 | 0.0003 | 15163.254 | 5.39E-01 |
| 122 | 0.0002 | 2244.4788 | 4.94E-01 |
| 123 | 0.0001 | 20847.662 | 4.71E-01 |
| 124 | 0.0001 | 5155.613 | 4.18E-01 |
| 125 | 0.0002 | 5563.2515 | 5.65E-01 |
| 126 | 0.0003 | 9330.3 | 5.33E-01 |
| 127 | 0.0006 | 15995.216 | 1.35E+00 |
| 128 | 0.0004 | 4698.488 | 5.05E-01 |
| 129 | 0.0005 | 19610.809 | 6.54E-01 |
| 130 | 0.0002 | 7611.4243 | 5.26E-01 |
| 131 | 0.0004 | 18177.53 | 5.38E-01 |
| 132 | 0.0001 | 19342.562 | 4.36E-01 |
| 133 | 0.0002 | 5060.6035 | 3.86E-01 |
| 134 | 0.0006 | 5451.1694 | 6.59E-01 |
| 135 | 0.0002 | 10738.782 | 5.24E-01 |
| 136 | 0.0002 | 3115.562 | 4.56E-01 |
| 137 | 0.0002 | 6415.0044 | 4.35E-01 |
| 138 | 0.0001 | 5343.7085 | 4.41E-01 |
| 139 | 0.0003 | 4300.8477 | 5.50E-01 |
| 140 | 0.0002 | 6788.549 | 5.16E-01 |
| 141 | 0.0006 | 2279.511 | 5.08E-01 |
| 142 | 0.0005 | 10073.159 | 7.06E-01 |

# Bibliography

[1] D. C. Adams, Methods for shape analysis of landmark data from articulated structures Evolutionary Ecology Research, *Evol. Ecol. Res.* 1, 959–970, 1999.

[2] S. Arguillère and E. Trélat, Sub-Riemannian structures on groups of diffeomorphisms, *Proc. Am. Math. Soc.* 11, 559, 2006.

[3] S. Arguillère, M. Miller, and L. Younes, Diffeomorphic Surface Registration with Atrophy Constraints, *SIAM J. Imaging Sci.* 9, 975–1003, 2016.

[4] S. Arguillère, E. Trélat, A. Trouvé, and L. Younes, Shape deformation analysis from the optimal control viewpoint, *J. des Math. Pures Appl.* 104, 139–178, 2015.

[5] N. Aronszajn, Theory of Reproducing Kernels, *Trans. Am. Math. Soc.* 68, 1950.

[6] V. Arsigny, O. Commowick, X. Pennec, and N. Ayache, A Log-Euclidean Framework for Statistics on Diffeomorphisms, pages 924–931, 2006.

[7] K. S. Arun, T. S. Huang, and S. D. Blostein, Least-Squares Fitting of Two 3-D Point Sets, *IEEE Trans. Pattern Anal. Mach. Intell.* 9, 698–700, 1987.

[8] J. Augoustides and A. T. Cheung, Aneurysms and dissections, In *Perioper. Transesophageal Echocardiogr.*, pages 191–217, 2014.

[9] M. Bäck, T. C. Gasser, J. B. Michel, and G. Caligiuri, Biomechanical factors in the biology of aortic wall and aortic valve diseases, *Cardiovasc. Res.* 99, 232–241, 2013.

[10] R. Bajcsy and C. Broit, Matching of deformed images, In *VIth Int. Conf. Pattern Recognit.*, pages 351–353, 1982.

[11] R. Bajcsy, Multiresolution elastic matching, *Comput. Vision, Graph. Image Process.* 46, 1–21, 1989.

[12] S. Banerjee and A. Roy, *Linear Algebra and Matrix Analysis for Statistics*, Chapman & Hall/CRC Texts in Statistical Science, CRC Press, 2014.

[13] A. Bellaiche and J.-J. Risler, *Sub-Riemannian Geometry*, Birkhäuser Basel, 1996.

[14] S. Bergman, Über die Entwicklung der harmonischen Funktionen der Ebene und des Rümes nach Orthogonal Functionen, *Math. Ann.* 86, 238–271, 1922.

[15] A. Berlinet and C. Thomas-Agnan, *Reproducing Kernel Hilbert Spaces in Probability and Statistics*, Springer US, 1 Edition, 2004.

[16] J. Biehler, S. Kehl, M. W. Gee, F. Tanios, J. Pelisek, A. Maier, C. Reeps, H. H. Eckstein, and W. Wall, Non-Invasive Prediction of Wall Properties of Abdominal Aortic Aneurysms Using Bayesian Regression, *Biomech. Model. Mechanobiol.* 16, 45–61, 2017.

[17] C. M. Bishop, *Pattern Recognition and Machine Learning*, Springer-Verlag New York, 2006.

[18] M. K. Bode, Y. Soini, J. Melkko, J. Satta, L. Risteli, and J. Risteli, Increased amount of type III pN-collagen in human abdominal aortic aneurysms: Evidence for impaired type III collagen fibrillogenesis, *J. Vasc. Surg.* 32, 1201–1207, 2000.

[19] A. Bône, M. Louis, B. Martin, and S. Durrleman, Deformetrica 4: An Open-Source Software for Statistical Shape Analysis, *Lect. Notes Comput. Sci. (including Subser. Lect. Notes Artif. Intell. Lect. Notes Bioinformatics)*, 3–13, 2018.

[20] F. Bookstein, *The measurement of biological shape and shape changes*, Volume 24, Springer-Verlag Berlin Heidelberg New-York, 1978.

[21] F. L. Bookstein, Morphometric Tools for Landmark Data. Geometry and Biology, *Biometrical J.*, 1991.

[22] I. Borg and P. J. F. Groenen, *Modern Multidimensional Scaling - Theory and Applications*, Springer-Verlag New York, 2 Edition, 2005.

[23] C. G. Broyden, A Class of Methods for Solving Nonlinear Simultaneous Equations, *Math. Comput.* 19, 577–593, 1965.

[24] J. L. Bruse, K. McLeod, G. Biglino, H. N. Ntsinjana, C. Capelli, T. Y. Hsia, M. Sermesant, X. Pennec, A. M. Taylor, S. Schievano, A. Taylor, A. Giardini, S. Khambadkone, M. de Leval, E. Bove, A. Dorfman, G. H. Baker, A. Hlavacek, F. Migliavacca, G. Pennati, G. Dubini, A. Marsden, I. Vignon-Clementel, R. Figliola, and J. McGregor, A statistical shape modelling framework to extract 3D shape biomarkers from medical imaging data: Assessing arch morphology of repaired coarctation of the aorta, *BMC Med. Imaging* 16, 1–19, 2016.

[25] M. Carmo, L. Colombo, A. Bruno, F. R. Corsi, L. Roncoroni, M. S. Cuttin, F. Radice, E. Mussini, and P. G. Settembrini, Alteration of elastin, collagen and their cross-links in abdominal aortic aneurysms, *Eur. J. Vasc. Endovasc. Surg.* 23, 543–549, 2002.

[26] E. L. Chaikof, R. L. Dalman, M. K. Eskandari, B. M. Jackson, W. A. Lee, M. A. Mansour, T. M. Mastracci, M. Mell, M. H. Murad, L. L. Nguyen, G. S. Oderich, M. S. Patel, M. L. Schermerhorn, and B. W. Starnes, The Society for Vascular Surgery practice guidelines on the care of patients with an abdominal aortic aneurysm, *J. Vasc. Surg.* 67, 2–77.e2, 2018.

[27] B. Charlier, J. Feydy, J. A. Glaunès, F.-D. Collin, and G. Durif, Kernel operations on the GPU, with autodiff, without memory overflows, *arXiv preprint arXiv:2004.11127*, 2020.

[28] G. E. Christensen, R. D. Rabbitt, and M. I. Miller, 3D brain mapping using a deformable neuroanatomy, *Phys. Med. Biol.* 39, 609–618, 1994.

[29] G. E. Christensen, R. D. Rabbitt, and M. I. Miller, Deformable templates using large deformation kinematics, *IEEE Trans. Image Process.* 5, 1435–1447, 1996.

[30] L. Chu, P. Johnson, H. Dietz, B. Brooke, G. Arnaoutakis, J. r. Black, and E. Fishman, Vascular complications of EhlersDanlos syndrome: CT findings., *AJR Am J Roentgenol.* 198, 482–487, 2012.

[31] T. F. Cootes, C. J. Taylor, D. H. Cooper, and J. Graham, Active Shape Models -Their Training and Application, *Comput. Vis. Image Underst.* 61, 38–59, 1995.

[32] C. J. Cotter, A. Clark, and J. Peiró, A Reparameterisation Based Approach to Geodesic Constrained Solvers for Curve Matching, *Int. J. Comput. Vis.* 99, 103–121, 2012.

[33] E. S. Crawford, The Diagnosis and Management of Aortic Dissection, *JAMA* 264, 2537–2541, 1990.

[34] C. Cury, J. A. Glaunès, R. Toro, M. Chupin, G. Schumann, V. Frouin, J. B. Poline, and O. Colliot, Statistical shape analysis of large datasets based on diffeomorphic iterative centroids, *Front. Neurosci.* 12, 1–18, 2018.

[35] R. Darling, C. Messina, D. Brewster, and L. Ottlinger, Autopsy study of unoperated abdominal aortic aneurysms. The case for early resection., *Circulation* 54, 1977.

[36] R. De Maesschalck, D. Jouan-Rimbaud, and D. L. Massart, The Mahalanobis distance, *Chemom. Intell. Lab. Syst.* 50, 1–18, 2000.

[37] S. de Putter, F. N. van de Vosse, M. Breeuwer, and F. A. Gerritsen, Local influence of calcifications on the wall mechanics of abdominal aortic aneurysm, *Med. Imaging 2006 Physiol. Funct. Struct. from Med. Images* 6143, 61432E, 2006.

[38] G. DeRham, *Variétés différentiables, formes, courants, formes harmoniques.*, Hermann, Paris, 1960.

[39] M. P. Do Carmo, *Differential Forms and Applications*, Springer-Verlag Berlin Heidelberg, 1994.

[40] B. J. Doyle, A. Callanan, P. E. Burke, P. A. Grace, M. T. Walsh, D. A. Vorp, and T. M. McGloughlin, Vessel asymmetry as an additional diagnostic tool in the assessment of abdominal aortic aneurysms, *J. Vasc. Surg.* 49, 443–454, 2009.

[41] B. Doyle, P. Grace, E. Kavanagh, P. Burke, F. Wallis, M. Walsh, and T. McGloughlin, Improved assessment and treatment of abdominal aortic aneurysms: the use of 3D reconstructions as a surgical guidance tool in endovascular repair, *Ir. J. Med. Sci.* 178, 2009.

[42] P. Dupuis, U. Grenander, and M. I. Miller, Variational problems on flows of diffeomorphisms for image matching, *Q. Appl. Math.* 56, 587–600, 1998.

[43] S. Durrleman, M. Prastawa, G. Gerig, and S. Joshi, Optimal Data-Driven Sparse Parameterization of Diffeomorphisms for Population Analysis, *Inf Process Med Imaging* 22, 123–134, 2011.

[44] S. Durrleman, *Statistical models of currents for measuring the variability of anatomical curves, surfaces and their evolution*, PhD thesis, Universite de Nice - Sophia Antipolis, Ecole Doctorale STIC Sciences et technologies de l'information et de la communication, 2010.

[45] S. Durrleman, X. Pennec, A. Trouvé, P. M. Thompson, and N. Ayache, Inferring brain variability from diffeomorphic deformations of currents: an integrative approach, *Med Image Anal.* 12, 626–637, 2008.

[46] S. Durrleman, X. Pennec, A. Trouvé, and N. Ayache, Statistical models of sets of curves and surfaces based on currents, *Med. Image Anal.* 13, 793–808, 2009.

[47] S. Durrleman, P. Fillard, X. Pennec, A. Trouvé, and N. Ayache, Registration, atlas estimation and variability analysis of white matter fiber bundles modeled as currents, *Neuroimage* 55, 1073–1090, 2011.

[48] S. Durrleman, M. Prastawa, N. Charon, J. R. Korenberg, S. Joshi, G. Gerig, and A. Trouvé, Morphometry of anatomical shape complexes with dense deformations and sparse parameters, *Neuroimage* 101, 35–49, 2014.

[49] H. H. Eckstein, D. Böckler, I. Flessenkämper, T. Schmitz-Rixen, S. Debus, and W. Lang, Ultraschall-screening abdominaler aortenaneurysmen, *Dtsch. Arztebl.* 106, 657–663, 2009.

[50] M. Faber and G. Moller-Hou, The human aorta. V. Collagen and elastin in the normal and hypertensive aorta, *Acta Pathol Microbiol Scand.* 31, 377–382, 1952.

[51] M. F. Fillinger, M. L. Raghavan, S. P. Marra, J. L. Cronenwett, and F. E. Kennedy, In vivo analysis of mechanical wall stress and abdominal aortic aneurysm rupture risk, *J. Vasc. Surg.* 36, 589–597, 2002.

[52] M. F. Fillinger, S. P. Marra, M. L. Raghavan, and F. E. Kennedy, Prediction of rupture risk in abdominal aortic aneurysm during observation: Wall stress versus diameter, *J. Vasc. Surg.* 37, 724–732, 2003.

[53] M. F. Fillinger, J. Racusin, R. K. Baker, J. L. Cronenwett, A. Teutelink, M. L. Schermerhorn, R. M. Zwolak, R. J. Powell, D. B. Walsh, and E. M. Rzucidlo, Anatomic characteristics of ruptured abdominal aortic aneurysm on conventional CT scans: Implications for rupture risk, *J. Vasc. Surg.* 39, 1243–1252, 2004.

[54] E. A. Finol, K. Keyhani, and C. H. Amon, The Effect of Asymmetry in Abdominal Aortic Aneurysms Under Physiologically Realistic Pulsatile Flow Conditions, *J. Biomech. Eng.* 125, 207, 2003.

[55] S. H. Forsdahl, K. Singh, S. Solberg, and B. K. Jacobsen, Risk factors for abdominal aortic aneurysms: a 7-year prospective study: the tromsø study, 1994 2001, *Circulation* 119, 2202–2208, 2009.

[56] O. Fritze, B. Romero, M. Schleicher, M. P. Jacob, D. Y. Oh, B. Starcher, K. Schenke-Layland, J. Bujan, and U. A. Stock, Age-related changes in the elastic tissue of the human aorta, *J. Vasc. Res.* 49, 77–86, 2011.

[57] J. Gallier, Basics of Classical Lie Groups: The Exponential Map, Lie Groups, and Lie Algebras, In *Geom. Methods Appl. Texts Appl. Math. vol 38*, pages 367–414, Springer, New York, NY, 2001.

[58] S. Gallot, D. Hulin, and J. Lafontaine, *Riemannian Geometry*, Springer-Verlag Berlin Heidelberg, 3 Edition, 2004.

[59] T. C. Gasser, M. Auer, F. Labruto, J. Swedenborg, and J. Roy, Biomechanical rupture risk assessment of abdominal aortic aneurysms: Model complexity versus predictability of finite element simulations, *Eur. J. Vasc. Endovasc. Surg.* 40, 176–185, 2010.

[60] J. Gee and R. Bajcsy, Elastic matching: Continuum mechanical and probabilistic analysis, In *IN BRAIN WARPING*, pages 18–3. Academic Press, 1999.

[61] M. Gee, C. Reeps, H. H. Eckstein, and W. Wall, Prestressing in finite deformation abdominal aortic aneurysm simulation, *J. Biomech.* 42, 1732–1739, 2009.

[62] E. Georgakarakos, C. V. Ioannou, Y. Kamarianakis, Y. Papaharilaou, T. Kostas, E. Manousaki, and A. N. Katsamouris, The Role of Geometric Parameters in the Prediction of Abdominal Aortic Aneurysm Wall Stress, *Eur. J. Vasc. Endovasc. Surg.* 39, 42–48, 2010.

[63] German Federal Statistical Office Wiesbaden, Table (23211-0002) of causes of death statistics in 2019 in Germany, Technical report, 2020.

[64] G. Giannoglou, G. Giannakoulas, J. Soulis, Y. Chatzizisis, T. Perdikides, N. Melas, G. Parcharidis, and G. Louridas, Predicting the risk of rupture of abdominal aortic aneurysms by utilizing various geometrical parameters: Revisiting the diameter criterion, *Angiology* 57, 487–494, 2006.

[65] J. Glaunès, A. Trouvé, and L. Younes, Diffeomorphic Matching of Distributions: A New Approach for Unlabelled Point-sets and Sub-manifolds Matching, In *Proc. 2004 IEEE Comput. Soc. Conf. Comput. Vis. Pattern Recognit.*, CVPR'04, pages 712–718, Washington, DC, USA, 2004, IEEE Computer Society.

[66] J. Glaunès, A. Trouvé, and L. Younes, Modeling Planar Shape Variation via Hamiltonian flows of curves, *Model. Simul. Sci. Eng. Technol.*, 335–361, 2006.

[67] G. Golub and C. Reinsch, Singular Value Decomposition and Least Squares Solutions, *Numer. Math.* 14, 403–420, 1970.

[68] C. Goodall, Procrustes Methods in the Statistical Analysis of Shape, *J. R. Stat. Soc. B* 53, 285–339, 1991.

[69] S. Greenberg, The association of medial collagenous tissue with atheroma formation in the aging human aorta as revealed by a special technique., *Histol Histophatol.* 1, 323–326, 1986.

[70] U. Grenander, A unified approach to pattern analysis, *Adv. Comput.* 10, 175–188, 1970.

[71] U. Grenander, *General pattern theory: A mathematical study of regular structures*, Clarendon Press, 1994.

[72] U. Grenander, M. I. Miller, C. Dafermos, W. Freiberger, and D. Mumford, Computational anatomy: an emerging discipline, Technical Report 4, 1998.

[73] B. Gris, S. Durrleman, and A. Trouvé, A sub-Riemannian modular framework for diffeomorphism based analysis of shape ensembles, *SIAM J. Imaging Sci. Soc. Ind. Appl. Math.*, 2017.

[74] R. T. Grundmann, *Etiology, Pathogenesis and Pathophysiology of Aortic Aneurysms and Aneurysm Rupture*, IntechOpen, 2012.

[75] T. Halme, T. Savunen, H. Aho, T. Vihersaari, and R. Penttinen, Elastin and collagen in the aortic wall: changes in the Marfan syndrome and annuloaortic ectasia, *Exp. Mol. Pathol.* 43, 1–12, 1985.

[76] K. Hamaoui, A. Riaz, A. Hay, and A. Botha, Massive spontaneous diaphragmatic rupture in Ehlers-Danlos syndrome, *Ann. R. Coll. Surg. Engl.* 94, 5–7, 2012.

[77] J. D. Hamilton, M. Kumaravel, M. L. Censullo, A. M. Cohen, D. S. Kievlan, and O. C. West, Multidetector CT evaluation of active extravasation in blunt abdominal and pelvic trauma patients, *Radiographics* 28, 1603–1616, 2008.

[78] L. P. Harter, B. H. Gross, P. W. Callen, and R. A. Barth, Ultrasonic evaluation of abdominal aortic thrombus, *J. Ultrasound Med.* 1, 315–318, 1982.

[79] T. Hatakeyama, H. Shigematsu, and T. Muto, Risk factors for rupture of abdominal aortic aneurysm based on three-dimensional study, *J. Vasc. Surg.* 33, 453–461, 2001.

[80] C. Hayward and A. Madill, A Survey of Outlier Detection Methodologies, *Artif. Intell. Rev.* 22, 85–126, 2004.

[81] C. M. He and M. R. Roach, The composition and mechanical properties of abdominal aortic aneurysms, *J. Vasc. Surg.* 20, 6–13, 1994.

[82] R. He, B. G. Hu, W. S. Zheng, and X. W. Kong, Robust principal component analysis based on maximum correntropy criterion, *IEEE Trans. Image Process.* 20, 1485–1494, 2011.

[83] P. Heider, O. Wolf, C. Reeps, M. Hanke, A. Zimmermann, H. Berger, and H. H. Eckstein, Aneurysmen und Dissektionen der thorakalen und abdominellen Aorta, *Der Chir.* 78, 600–610, 2007.

[84] A. Hemmler, B. Lutz, C. Reeps, and M. W. Gee, In silico study of vessel and stent-graft parameters on the potential success of endovascular aneurysm repair, *Int. j. numer. method. biomed. eng.* 35, 2019.

[85] M. S. Heng, M. J. Fagan, J. W. Collier, G. Desai, P. T. McCollum, and I. C. Chetter, Peak wall stress measurement in elective and acute abdominal aortic aneurysms, *J. Vasc. Surg.* 47, 17–22, 2008.

[86] T. Hofmann, B. Schölkopf, and A. J. Smola, Kernel methods in machine learning, *Ann. Stat.* 36, 1171–1220, 2008.

[87] D. D. Holm, J. E. Marsden, and T. S. Ratiu, Euler-poincaré models of ideal fluids with nonlinear dispersion, *Phys. Rev. Lett.* 80, 4173–4176, 1998.

[88] H. A. Hong and U. U. Sheikh, Automatic detection, segmentation and classification of abdominal aortic aneurysm using deep learning, *Proceeding - 2016 IEEE 12th Int. Colloq. Signal Process. its Appl. CSPA 2016*, 242–246, 2016.

[89] G. N. Hounsfield, Computed medical imaging. Nobel lecture, Decemberr 8, 1979., *J. Comput. Assist. Tomogr.* 4, 665–674, 1980.

[90] M. Hubert and S. Engelen, Robust PCA and classification in biosciences, *Bioinformatics* 20, 1728–1736, 2004.

[91] A. Hyvärinen, J. Karhunen, and E. Oja, *Independent Component Analysis*, John Wiley and Sons, Inc., 2001.

[92] R. Jenssen, Kernel Entropy Component Analysis, *IEEE Trans. Pattern Anal. Mach. Intell.* 32, 847–860, 2010.

[93] S. C. Joshi and M. I. Miller, Landmark Matching via Large Deformation Diffeomorphisms, *J. Math. Imaging Vis.* 9, 179–200, 2000.

[94] S. Kehl, *Bayesian Calibration of Nonlinear Cardiovascular Models for the Predictive Simulation of Arterial Growth*, PhD thesis, Technische Universität München, 2017.

[95] S. Kehl and M. W. Gee, Calibration of parameters for cardiovascular models with application to arterial growth, *Int. j. numer. method. biomed. eng.* 33, 1–13, 2017.

[96] K. C. Kent, Clinical Practice. Abdominal aortic aneurysms., *N. Engl. J. Med.* 371, 2101–8, 2014.

[97] Kibaek Leea, Junjun Zhua, Judy Shumb, Yongjie Zhanga, Satish C. Mulukc, Ankur Chandrad, Mark K. Eskandarie, and Ender A. Finolf, Surface Curvature as a Classifier of Abdominal Aortic Aneurysms: A Comparative Analysis, *Ann. Biomed. Eng.* 100, 130–134, 2012.

[98] M. Kimura, K. Hoshina, K. Miyahara, J. Nitta, M. Kobayashi, S. Yamamoto, and M. Ohshima, Geometric analysis of ruptured and nonruptured abdominal aortic aneurysms, *J. Vasc. Surg.* 69, 86–91, 2019.

[99] A. Kitagawa, T. M. Mastracci, R. Von Allmen, and J. T. Powell, The role of diameter versus volume as the best prognostic measurement of abdominal aortic aneurysms, *J. Vasc. Surg.* 58, 258–265, 2013.

[100] C. Kleinstreuer and Z. Li, Analysis and computer program for rupture-risk prediction of abdominal aortic aneurysms, *Biomed. Eng. Online* 5, 1–13, 2006.

[101] N. Kontopodis, D. Pantidis, A. Dedes, N. Daskalakis, and C. V. Ioannou, The Not So Solid 5.5 cm Threshold for Abdominal Aortic Aneurysm Repair: Facts, Misinterpretations, and Future Directions, *Front. Surg.* 3, 1–6, 2016.

[102] R. Kramme, *Medizintechnik - Verfahren Systeme Informationsverarbeitung*, Springer-Verlag Berlin Heidelberg, 2 Edition, 2002.

[103] J. B. Kruskal, Multidimensional scaling by optimizing goodness of fit to a nonmetric hypothesis, *Psychometrika* 29, 1–27, 1964.

[104] J. B. Kruskal, Nonmetric multidimensional scaling: A numerical method, *Psychometrika* 29, 115–129, 1964.

[105] K. Landsman, *Foundations of Quantum Theory, From Classical Concepts to Operator Algebras*, Springer, Cham, 1 Edition, 2017.

[106] G. J. Langewouters, K. H. Wesseling, and W. J. Goedhard, The static elastic properties of 45 human thoracic and 20 abdominal aortas in vitro and the parameters of a new model, *J. Biomech.* 17, 425–435, 1984.

[107] E. L. Leemans, T. P. Willems, C. H. Slump, M. J. van der Laan, and C. J. Zeebregts, Additional value of biomechanical indices based on CTa for rupture risk assessment of abdominal aortic aneurysms, *PLoS One* 13, 1–12, 2018.

[108] L. Liang, M. Liu, C. Martin, J. A. Elefteriades, and W. Sun, A machine learning approach to investigate the relationship between shape features and numerically predicted risk of ascending aortic aneurysm, *Biomech. Model. Mechanobiol.* 16, 1519–1533, 2017.

[109] B. S. Lie, The foundations of the theory of infinite continuous transformation groups II., 1–33, 1891.

[110] J. S. Lindholt, S. Vammen, S. Juul, E. W. Henneberg, and H. Fasting, The validity of ultrasonographic scanning as screening method for abdominal aortic aneurysm, *Eur. J. Vasc. Endovasc. Surg.* 17, 472–475, 1999.

[111] M. Lorenzi and X. Pennec, Geodesics, Parallel Transport and One-parameter Subgroups for Diffeomorphic Image Registration, *Int. J. Comput. Vis.* 105, 111–127, 2013.

[112] P. C. Mahalanobis. On the general distance in statistics, 1936.

[113] A. Maier, M. W. Gee, C. Reeps, J. Pongratz, H. H. Eckstein, and W. A. Wall, A comparison of diameter, wall stress, and rupture potential index for abdominal aortic aneurysm rupture risk prediction, *Ann. Biomed. Eng.* 38, 3124–3134, 2010.

[114] A. Maier, *Computational Modeling of Rupture Risk in Abdominal Aortic Aneurysms*, PhD thesis, Technische Universität München, 2012.

[115] G. Malandin and J.-m. Rocchisani, Matching of 3D medical images with a potential based method, Technical report, 1993.

[116] B. J. Manning, T. Kristmundsson, B. Sonesson, and T. Resch, Abdominal aortic aneurysm diameter: A comparison of ultrasound measurements with those from standard and three-dimensional computed tomography reconstruction, *J. Vasc. Surg.* 50, 263–268, 2009.

[117] T. Mansi, I. Voigt, B. Leonardi, X. Pennec, S. Durrleman, M. Sermesant, H. Delingette, A. M. Taylor, Y. Boudjemline, G. Pongiglione, and N. Ayache, A statistical model for quantification and prediction of cardiac remodelling: Application to tetralogy of fallot, *IEEE Trans. Med. Imaging* 30, 1605–1616, 2011.

[118] T. Mansi, *Image-based physiological and statistical models of the heart : application to tetralogy of Fallot*, PhD thesis, l ' École nationale supérieure des mines de Paris Modèles physiologiques et statistiques du cœur guidés par imagerie médicale, 2010.

[119] S. Marsland and R. McLachlan, A hamiltonian particle method for diffeomorphic image registration, *Lect. Notes Comput. Sci. (including Subser. Lect. Notes Artif. Intell. Lect. Notes Bioinformatics)*, 396–407, 2007.

[120] G. Martufi, M. Auer, J. Roy, J. Swedenborg, N. Sakalihasan, G. Panuccio, and T. C. Gasser, Multidimensional growth measurements of abdominal aortic aneurysms, *J. Vasc. Surg.* 58, 748–755, 2013.

[121] G. Martufi, M. Lindquist Liljeqvist, N. Sakalihasan, G. Panuccio, R. Hultgren, J. Roy, and T. C. Gasser, Local Diameter, Wall Stress, and Thrombus Thickness Influence the Local Growth of Abdominal Aortic Aneurysms, *J. Endovasc. Ther.* 23, 957–966, 2016.

[122] S. Mika, B. Schölkopf, A. Smola, K. R. Müller, M. Scholz, and G. Rätsch, Kernel PCA and de-noising in feature spaces, *Adv. Neural Inf. Process. Syst.*, 536–542, 1999.

[123] M. Miller, G. E. Christensen, Y. Amit, and U. Grenander, Mathematical textbook of deformable neuroanatomies, In *Proc Natl Acad Sci U S A*, Volume 90, pages 11944–11948, 1993.

[124] M. I. Miller, Computational anatomy: Shape, growth, and atrophy comparison via diffeomorphisms, *Neuroimage* 23, 19–33, 2004.

[125] M. I. Miller, A. Trouvé, and L. Younes, On the Metrics and Euler-Lagrange Equations of Computational Anatomy, *Annu. Rev. Biomed. Eng.* 4, 375–405, 2002.

[126] M. I. Miller, A. Trouvé, and L. Younes, Geodesic shooting for computational anatomy, *J. Math. Imaging Vis.* 24, 209–228, 2006.

[127] M. I. Miller, L. Younes, and A. Trouvé, Diffeomorphometry and geodesic positioning systems for human anatomy, *Technol. (Singap World Sci)* 02, 36–43, 2014.

[128] W. Mower, L. Baraff, and J. Sneyd, Stress distributions in vascular aneurysms: factors affecting risk of aneurysm rupture, *J Surg Res.* 55, 155–161, 1993.

[129] W. Mower, W. Quinones, and S. Gambhir, Effect of intraluminal thrombus on local abdominal aortic aneurysm wall strength, *J. Vasc. Surg.* 26, 602–608, 1997.

[130] M. Müller, Gefäßchirurgie - arterielle Aneurysmen, In *Chir. für Stud. und Prax.*, pages 58–61, 2005.

[131] D. Mumford and P. W. Michor, On Euler's equation and 'EPDiff', *J. Geom. Mech.* 5, 319–344, 2013.

[132] A. J. d. S. Neto, O. L. Santiago, and G. N. Silva, *Mathematical Modeling and Computational Intelligence in Engineering Applications*, 2016.

[133] P. Netrapalli, N. U N, S. Sanghavi, A. Anandkumar, and P. Jain, Non-convex Robust PCA, In Z. Ghahramani, M. Welling, C. Cortes, N. D. Lawrence, and K. Q. Weinberger (eds.), *Adv. Neural Inf. Process. Syst. 27*, pages 1107–1115, Curran Associates, Inc., 2014.

[134] C. Nienaber, R. Clough, N. Sakalihasan, T. Suzuki, R. Gibbs, F. Mussa, M. Jenkins, M. Thompson, A. Evangelista, J. Yeh, N. Cheshire, U. Rosendahl, and J. Pepper, Aortic dissection, *Nat. Rev. Dis. Prim.* 2, 2016.

[135] J. A. Niestrawska, P. Regitnig, C. Viertler, T. U. Cohnert, A. R. Babu, and G. A. Holzapfel, The role of tissue remodeling in mechanics and pathogenesis of abdominal aortic aneurysms, *Acta Biomater.* 88, 149–161, 2019.

[136] S. Ockert, D. Böckler, J. Allenberg, and H. Schumacher, Rupturiertes abdominelles Aortenaneurysma, *Gefässchirurgie* 12, 379–391, 2007.

[137] B. Owen, N. Bojdo, A. Jivkov, B. Keavney, and A. Revell, Structural modelling of the cardiovascular system, *Biomech. Model. Mechanobiol.* 17, 1217–1242, 2018.

[138] A. Pai, S. Sommer, L. Sorensen, S. Darkner, J. Sporring, and M. Nielsen, Kernel Bundle Diffeomorphic Image Registration Using Stationary Velocity Fields and Wendland Basis Functions, *IEEE Trans. Med. Imaging* 35, 1369–1380, 2016.

[139] S. A. Parikh, R. Gomez, M. Thirugnanasambandam, S. S. Chauhan, V. De Oliveira, S. C. Muluk, M. K. Eskandari, and E. A. Finol, Decision Tree Based Classification of Abdominal Aortic Aneurysms Using Geometry Quantification Measures, *Ann. Biomed. Eng.* 46, 2135–2147, 2018.

[140] M. R. Partin, A. Shaukat, D. B. Nelson, A. Gravely, S. Nugent, Z. F. Gellad, and J. F. Burgess, Reply, *Clin. Gastroenterol. Hepatol.* 14, 486, 2016.

[141] A. Paszke, S. Gross, S. Chintala, G. Chanan, E. Yang, Z. DeVito, Z. Lin, A. Desmaison, L. Antiga, and A. Lerer, Automatic differentiation in PyTorch, In *31st Conf. Neural Inf. Process. Syst. (NIPS), Long Beach, CA, USA*, Volume 22, pages 2–8, 2017.

[142] A. Paszke, S. Gross, F. Massa, A. Lerer, J. Bradbury, G. Chanan, T. Killeen, Z. Lin, N. Gimelshein, L. Antiga, A. Desmaison, A. Köpf, E. Yang, Z. DeVito, M. Raison, A. Tejani, S. Chilamkurthy, and S. Chintala, PyTorch: An Imperative Style, High-Performance Deep Learning Library, *33rd Conf. Neural Inf. Process. Syst.*, 8024–8035, 2019.

[143] K. Pearson, LIII. On lines and planes of closest fit to systems of points in space, *London, Edinburgh, Dublin Philos. Mag. J. Sci.* 2, 559–572, 1901.

[144] E. A. Perez, L. R. Rojas-Solorzano, and E. Finol, Geometric Predictors of Abdominal Aortic Aneurysm Maximum Wall Stress, *Chem Eng Trans* 49, 73–78, 2016.

[145] S. Polzer and T. C. Gasser, Biomechanical rupture risk assessment of abdominal aortic aneurysms based on a novel probabilistic rupture risk index, *J. R. Soc. Interface* 12, 2015.

[146] M. Postnikov, *Geometry VI Riemannian Geometry*, Springer-Verlag Berlin Heidelberg, 2001.

[147] F. Pukelsheim, The Three Sigma Rule, *Am. Stat.* 48, 88–91, 1994.

[148] M. L. Raghavan, B. Ma, and R. E. Harbaugh, Quantified aneurysm shape and rupture risk, *J. Neurosurg.* 102, 355–362, 2009.

[149] A. Rakotomamonjy and S. Canu, Frames, reproducing kernels, regularization and learning, *J. Mach. Learn. Res.* 6, 1485–1515, 2005.

[150] Y. Rathi, S. Dambreville, and A. Tannenbaum, Statistical shape analysis using kernel PCA, *Image Process. Algorithms Syst. Neural Networks, Mach. Learn.* 6064, 60641B, 2006.

[151] S. S. Raut, S. Chandra, J. Shum, and E. A. Finol, The role of geometric and biomechanical factors in abdominal aortic aneurysm rupture risk assessment, *Ann. Biomed. Eng.* 41, 1459–1477, 2013.

[152] C. Reeps, A. Maier, J. Pelisek, F. Härtl, V. Grabher-Meier, W. A. Wall, M. Essler, H. H. Eckstein, and M. W. Gee, Measuring and modeling patient-specific distributions of material properties in abdominal aortic aneurysm wall, *Biomech. Model. Mechanobiol.* 12, 717–733, 2013.

[153] C. Reeps, M. Gee, A. Maier, M. Gurdan, H. H. Eckstein, and W. A. Wall, The impact of model assumptions on results of computational mechanics in abdominal aortic aneurysm, *J. Vasc. Surg.* 51, 679–688, 2010.

[154] B. Rengarajan, W. Wu, C. Wiedner, D. Ko, S. C. Muluk, M. K. Eskandari, P. G. Menon, and E. A. Finol, A Comparative Classification Analysis of Abdominal Aortic Aneurysms by Machine Learning Algorithms, *Ann. Biomed. Eng.* 48, 1419–1429, 2020.

[155] J. Rodriguez, C. Ruiz, M. Doblaré, and G. A. Holzapfel, Mechanical stresses in abdominal aortic aneurysms: influence of diameter, asymmetry, and material anisotropy, *J. Biomech. Eng.* 130, 2008.

[156] S. Saitoh and Y. Sawano, *Theory of Reproducing Kernels and Applications*, Volume 44, Springer Singapore, 1 Edition, 2016.

[157] T. J. Schlatmann and A. E. Becker, Histologic changes in the normal aging aorta: Implications for dissecting aortic aneurysm, *Am. J. Cardiol.* 39, 13–20, 1977.

[158] B. Schölkopf, C. Burges, and A. Smola., Support Vector Learning, *Adv. Kernel Methods*, 2–5, 1999.

[159] B. Schölkopf and A. J. Smola, *Learning with Kernels: Support Vector Machines, Regularization, Optimization, and Beyond*, MIT Press, Cambridge, MA, USA, 2001.

[160] B. Schölkopf, A. Smola, and K.-R. Müller, Nonlinear Component Analysis as a Kernel Eigenvalue Problem, Technical report, 1996.

[161] H. Schumacher, H. H. Eckstein, F. Kallinowski, and J. R. Allenberg, Morphometry and classification in abdominal aortic aneurysms: patient selection for endovascular and open surgery., *J. Endovasc. Surg. Off. J. Int. Soc. Endovasc. Surg.* 4, 39–44, 1997.

[162] L. Schwartz, Sous-espaces hilbertiens d'espaces vectoriels topologiques et noyaux associés (Noyaux reproduisants), *J. d'Analyse Mathématique* 13, 115–256, 1964.

[163] R. A. P. Scott, The multicentre aneurysm screening study (MASS) into the effect of abdominal aortic aneurysm screening on mortality in men: a randomised controlled trial, *Lancet* 360, 1531–1539, 2002.

[164] R. Scott, P. Tisi, H. Ashton, and D. Allen, Abdominal aortic aneurysm rupture rates: a 7-year follow-up of the entire abdominal aortic aneurysm population detected by screening, *J. Vasc. Surg.* 28, 124–128, 1998.

[165] C. M. Scotti, A. D. Shkolnik, S. C. Muluk, and E. A. Finol, Fluid-structure interaction in abdominal aortic aneurysms: Effects of asymmetry and wall thickness, *Biomed. Eng. Online* 4, 1–22, 2005.

[166] J. Shawe-Taylor and N. Cristianini, *Kernel methods for Pattern Analysis*, 2004.

[167] J. Shum, G. Martufi, E. Di Martino, C. B. Washington, J. Grisafi, S. C. Muluk, and E. A. Finol, Quantitative assessment of abdominal aortic aneurysm geometry, *Ann. Biomed. Eng.* 39, 277–286, 2011.

[168] S. Sternberg, *Lectures on Differential Geometry*, Prentice Hall Mathematics Series. Prentice Hall Inc., 1964.

[169] G. Szegö, Über orthogonale Polynome, die zu einer gegebenen Kurve der komplexen Ebene gehören, *Math. Zeitschrift* 9, 218–270, 1921.

[170] A. Tang, C. Kauffmann, S. Tremblay-Paquet, S. Elkouri, O. Steinmetz, F. Morin-Roy, L. Cloutier-Gill, and G. Soulez, Morphologic evaluation of ruptured and symptomatic abdominal aortic aneurysm by three-dimensional modeling, *J. Vasc. Surg.* 59, 894–902.e3, 2014.

[171] M. Tenenbaum and H. Pollard, *Ordinary Differential Equations*, Dover Publications Inc, 1986.

[172] The UK Small Aneurysm Trial Participants, The U.K. small aneurysm trial: Design, methods and progress, *Eur. J. Vasc. Endovasc. Surg.* 9, 42–48, 1995.

[173] D. W. Thompson, *On Growth and Form*, Cambridge University Press, England, 1917.

[174] P. M. Thompson, J. N. Gledd, R. P. Woods, D. MacDonald, A. C. Evans, and A. W. Toga, Growth patterns in the developing brain detected by using continuum mechanical tensor maps, *Nature* 404, 190–193, 2000.

[175] W. P. Thurston, *Three-Dimensional Geometry and Topology, Volume I*, Princeton University Press, 1997.

[176] A. Trouvé, Action de groupe de dimension infinie et reconnaissance de formes, *C. R. Séances Acad. Sci., Sér. 1 Math.* 321, 1031–1034, 1995.

[177] A. Trouvé, Diffeomorphisms Groups and Pattern Matching in Image Analysis, *Int. J. Comput. Vis.* 28, 213–221, 1998.

[178] M. Truijers, J. A. Pol, L. J. SchultzeKool, S. M. van Sterkenburg, M. F. Fillinger, and J. D. Blankensteijn, Wall Stress Analysis in Small Asymptomatic, Symptomatic and Ruptured Abdominal Aortic Aneurysms, *Eur. J. Vasc. Endovasc. Surg.* 33, 401–407, 2007.

[179] A. Tsamis, A. Rachev, and N. Stergiopulos, A constituent-based model of age-related changes in conduit arteries, *Am. J. Physiol. - Hear. Circ. Physiol.* 301, 1286–1301, 2011.

[180] A. Tsamis, J. T. Krawiec, and D. A. Vorp, Elastin and collagen fibre microstructure of the human aorta in ageing and disease: A review, *J. R. Soc. Interface* 10, 2013.

[181] S. Umeyama, Least-Squares Estimation of Transformation Parameters Between Two Point Patterns, *IEEE Trans. Pattern Anal. Mach. Intell.* 13, 376–380, 1991.

[182] M. Vaillant, M. I. Miller, L. Younes, and A. Trouvé, Statistics on diffeomorphisms via tangent space representations, *Neuroimage* 23, 161–169, 2004.

[183] M. Vaillant and J. Glaunès, Surface Matching via Currents, *Proc. Inf. Process. Med. Imaging Lect. Notes Comput. Sci.* 3565, 2005.

[184] D. C. Van Essen, H. A. Drury, S. Joshi, and M. I. Miller, Functional and structural mapping of human cerebral cortex: solutions are in the surfaces, In *Proc Natl Acad Sci U S A*, Volume 95, pages 788–795, 1998.

[185] J. P. Vande Geest, D. H. Wang, S. R. Wisniewski, M. S. Makaroun, and D. A. Vorp, Towards a noninvasive method for determination of patient-specific wall strength distribution in abdominal aortic aneurysms, *Ann. Biomed. Eng.* 34, 1098–1106, 2006.

[186] . VanRossum, GuidoandDrakeJr, *Pythonreferencemanual*.

[187] A. K. Venkatasubramaniam, M. J. Fagan, T. Mehta, K. J. Mylankal, B. Ray, G. Kuhan, I. C. Chetter, and P. T. McCollum, A comparative study of aortic wall stress using finite element analysis for ruptured and non-ruptured abdominal aortic aneurysms, *Eur. J. Vasc. Endovasc. Surg.* 28, 168–176, 2004.

[188] F.-X. Vialard, L. Risser, D. Rueckert, and C. J. Cotter, Diffeomorphic 3D Image Registration via Geodesic Shooting Using an Efficient Adjoint Calculation, *Int. J. Comput. Vis.* 97, 229–241, 2012.

[189] G. Vilalta, F. Nieto, C. Vaquero, J. A. Vilalta, and M. Á. Pérez, Patient-Specific Clinical Assessment of Abdominal Aortic Aneurysm Rupture Risk based on its Geometric Parameters 4, 404–408, 2011.

[190] P. Virtanen, R. Gommers, T. E. Oliphant, M. Haberland, T. Reddy, D. Cournapeau, E. Burovski, P. Peterson, W. Weckesser, J. Bright, S. J. van der Walt, M. Brett, J. Wilson, K. J. Millman, N. Mayorov, A. R. J. Nelson, E. Jones, R. Kern, E. Larson, C. J. Carey, İ. Polat, Y. Feng, E. W. Moore, J. VanderPlas, D. Laxalde, J. Perktold, R. Cimrman, I. Henriksen, E. A. Quintero, C. R. Harris, A. M. Archibald, A. H. Ribeiro, F. Pedregosa, P. van Mulbregt, and SciPy 1.0 Contributors, SciPy 1.0: Fundamental Algorithms for Scientific Computing in Python, *Nature Methods* 17, 261–272, 2020.

[191] D. A. Vorp, M. L. Raghavan, and M. W. Webster, Mechanical wall stress in abdominal aortic aneurysm: Influence of diameter and asymmetry, *J. Vasc. Surg.* 27, 632–639, 1998.

[192] M. Y. Wang, B. S. Peterson, and L. H. Staib, 3D brain surface matching based on geodesics and local geometry, *Comput. Vis. Image Underst.* 89, 252–271, 2003.

[193] P. N. Watton and N. A. Hill, Evolving mechanical properties of a model of abdominal aortic aneurysm, *Biomech. Model. Mechanobiol.* 8, 25–42, 2009.

[194] M. A. Whittle, A. C. Gibbs, P. S. Hasleton, and J. C. Anderson, Collagen in dissecting aneurysms of the human thoracic aorta: Increased collagen content and decreased collagen concentration may be predisposing factors in dissecting aneurysms, *Am. J. Cardiovasc. Pathol.* 3, 311–319, 1993.

[195] World Health Organization, [Fact sheet] Cardiovascular diseases, Technical report, 2017.

[196] W. Wu, B. Rengarajan, M. Thirugnanasambandam, S. Parikh, R. Gomez, V. De Oliveira, S. C. Muluk, and E. A. Finol, Wall Stress and Geometry Measures in Electively Repaired Abdominal Aortic Aneurysms, *Ann. Biomed. Eng.*, 2019.

[197] L. Younes, Computable Elastic Distances between Shapes, *SIAM J. Appl. Math.* 58, 565–586, 1998.

[198] L. Younes, Constrained Diffeomorphic Shape Evolution, *Found. Comput. Math.* 12, 295–325, 2012.

[199] N. Young, *An introduction to Hilbert space*, Cambridge University Press, 1988.

[200] E. Zeidler, Applied Functional Analysis: Applications to Mathematical Physics, page 481, Springer-Verlag New York, 1 Edition, 1995.

[201] M. A. Zullinger and N. Stergiopulos, Structural strain energy function applied to the ageing of the human aorta, *J. Biomech.* 40, 3061–3069, 2007.